UC Irvine
UC Irvine Electronic Theses and Dissertations

Title
Treatment of inherited retinal degenerations through viral and non-viral delivery of precision genome editors

Permalink
https://escholarship.org/uc/item/92t500hs

ISBN
9798173722867

Author
Du, Samuel Wang

Publication Date
2025-11-03

Copyright Information
This work is made available under the terms of a Creative Commons Attribution-NonCommercial License, available at https://creativecommons.org/licenses/by-nc/4.0/

Peer reviewed|Thesis/dissertation

eScholarship.org Powered by the California Digital Library
University of California

UNIVERSITY OF CALIFORNIA, IRVINE

Treatment of inherited retinal degenerations through viral and non-viral delivery of precision genome editors

DISSERTATION

Submitted in partial satisfaction of the requirements for the degree of

DOCTOR OF PHILOSOPHY

in Biomedical Sciences

Samuel W. Du

Dissertation Committee:

Donald Bren Professor Krzysztof Palczewski, Chair

Professor Todd C. Holmes

Associate Professor Philip D. Kiser

Professor Chang C. Liu

Professor Rachel W. Martin

2025

Portions of Chapter 1 © 2023 Elsevier

Portions of Chapter 2 © 2024 the National Academy of Sciences of the United States of America

Portions of Chapter 3 © 2022 Elsevier

Portions of Chapter 4 © 2024 Nature Publishing Group

Portions of Chapter 5 © 2025 Cell Press

Portions of Chapter 6 © 2024 Nature Publishing Group

All other materials © 2025 Samuel W. Du

DEDICATION

This work is dedicated to my life partner TJ. My deepest thanks and gratitude to you, without whom I could not have completed my research. Thank you for your unwavering support, belief, and feedback. You enable me to pursue my dreams and strive for excellence.

Many thanks to my entire family – both the one I was born into and the ones I became a member of. Thank you for your flexibility and understanding.

I will be eternally grateful to the mentorship, support, and advocacy from my mentor, Dr. Krzysztof Palczewski, who continually pushes me to achieve greater things and to realize my potential. Thank you for being my friend during our journey together.

“It does not matter how slowly you go as long as you do not stop.”

- *Confucius*

TABLE OF CONTENTS

Page

LIST OF FIGURES iv

LIST OF TABLES v

ACKNOWLEDGEMENTS vi

VITA vii

ABSTRACT OF THE DISSERTATION viii

CHAPTER 1: Introduction 1
- 1.1 DNA and RNA as substrates and targets 2
- 1.2 Discovery and characterization of CRISPR systems 4
- 1.3 Genetics and biochemistry of CRISPR/Cas systems 5
- 1.4 Classical genome editing with CRISPR-Cas9 nucleases 9
- 1.5 Extending Cas9 Functionality with base editors 12
- 1.6 CRISPR 3.0: Prime editing 15
- 1.7 New developments in genome editing tools 19
- 1.8 The eye as a testbed for genetic therapies 20
- 1.9 Challenges of gene augmentation therapy for the treatment of IRDs 21
- 1.10 Delivery of gene therapies to the eye 24

CHAPTER 2: *In vivo* base editing in the rhodopsin E150K retinitis pigmentosa mouse 33
- 2.1 Introduction 34
- 2.2 Results 37
- 2.2.1 Development of an adenine base-editing strategy for Rho-E150K 37
- 2.2.2 Expression of characterization of *Rho* base-editing variants 38
- 2.2.3 Development of a prime editing strategy for Rho-E150K 39
- 2.2.4 Base editing of rhodopsin in arRP mice 40
- 2.3 Discussion 42
- 2.4 Methods 45

CHAPTER 3: Development of engineered virus-like particles (eVLPs) 67
- 3.1 Introduction 68
- 3.2 Development of base editor VLPs 69
- 3.3 Application of BE-eVLPs in the CNS and liver 71
- 3.4 Application of BE-eVLPs to the *rd12* model of inherited retinal degeneration 72
- 3.5 Discussion 76
- 3.6 Selected methods 77

CHAPTER 4: Development of eVLPs to facilitate prime editing 91
- 4.1 Prime editing in the eye 92
- 4.2 Development of PE-eVLPs 92
- 4.3 Application of PE-eVLPs to the *rd6* and *rd12* IRD models 94

4.4 Discussion 97
4.5 Selected methods 98

CHAPTER 5: Development of ENVLPE VLPs as an alternative to eVLPs 113
5.1 Development of ENVLPE VLPs 114
5.2 Delivering mRNA to study ENVLPE biodistribution *in vivo* 116
5.3 PE_{Csy4} $ENVLPE^{+}$ in inherited retinal degeneration mouse models 116
5.4 Discussion 118
5.5 Selected methods 119

CHAPTER 6: Development of lipid nanoparticles to deliver CRISPR RNPs 131
6.1 Introduction 132
6.2 Results 135
6.2.1 Expression and characterization of Cre, ABE, and PE 135
6.2.2 CPPs enable efficient delivery of Cre *in vitro* and *in vivo* 136
6.2.3 CPPs are unable to efficiently deliver ABE and PE in vitro and in vivo 138
6.2.4 Optimized LNPs enable the effective delivery of ABE and PE RNPs 139
6.2.5 *In vivo* ABE and PE editing in the *rd12* mouse model restores visual chemistry and physiology 144
6.3 Discussion 145
6.4 Methods 153

CHAPTER 7: Conclusions and future directions 210
7.1 Summary of the work 211
7.2 Ethics of genome editing 211
7.3 Challenges in scaling genome editing 213
7.4 Immunogenicity of gene editing 214
7.5 Challenges of delivery and promising new technologies 215
7.6 Further development of base and prime editors 216

REFERENCES 218

LIST OF FIGURES

Page

CHAPTER 1: Introduction
Figure 1.1 Summary of CRISPR/Cas9-based common genome editing strategies 28
Figure 1.2 DNA deamination reaction mechanism 30
Figure 1.3 Selected mutations in the eye that lead to inherited retinal diseases targetable by gene augmentation 31
Figure 1.4 Precision genome editing formulation and delivery 32

CHAPTER 2: *In vivo* base editing in the rhodopsin E150K retinitis pigmentosa mouse
Figure 2.1 Establishment of rhodopsin-E150K cell line and base-editing screening *in vitro*. 54
Figure 2.2 Characterization of bystander-edited variants of E150K-rhodopsin. 56
Figure 2.3 *In vivo* adenine base editing of E150K mice treated at P21. 58
Figure 2.4 *In vivo* adenine base editing of E150K mice treated at P15. 60
Figure 2.5 Rhodopsin expression in E150K mice after base editing at P15. 62
Figure 2.6 Screening of alternate base-editing strategies *in vitro*. 63
Figure 2.7 Tandem MS/MS spectra of purified peptides from rhodopsin variants. 65
Figure 2.8 *In vitro* screening of epegRNAs for correction of Rho-E150K. 66

CHAPTER 3: Development of engineered virus-like particles (eVLPs)
Figure 3.1 Summary of eVLP development from v1 to v4. 84
Figure 3.2 *In vivo* delivery of VSV-G psueodtype Cre-eVLPs 86
Figure 3.3 *In vivo* base editing by v4 BE-eVLPs in a mouse model of genetic blindness. 87
Figure 3.4 Sequencing analysis of RPE cDNA after BE-eVLP or lentivirus treatment. 89

CHAPTER 4: Development of eVLPs to facilitate prime editing
Figure 4.1 Summary of PE-eVLP architectures and PEmax/pegRNA/ngRNA recruitment strategies. 106
Figure 4.2 Retinal disease correction *in vivo* with PE-eVLPs. 107
Figure 4.3 A fluorescent reporter *Mfrp*^{rd6} cell line. 110
Figure 4.4 Immunohistochemistry blot on eye cryosections of *rd6* mice. 111
Figure 4.5 Off-target analysis in *rd12* mice. 112

CHAPTER 5: Development of ENVLPE VLPs as an alternative to eVLPs
Figure 5.1 Assembly and RNP recruitment mechanisms in ENVLPE and eVLP variants. 124
Figure 5.2 Subretinal injection of ENVLPE particles for mRNA delivery into Cre-reporter mice and for PE RNP delivery to mouse models of inherited retinal degeneration. 125
Figure 5.3 Delivery of CreNLS mRNA to activate a red/green-reporter locus. 127
Figure 5.4 Quantification of VLP titers using anti-p24 (HIV-1) or anti-p30 (MMLV) ELISA. 128
Figure 5.5 eVLP versus ENVLPE anti-Cas9 Western blot. 129
Figure 5.6 Correlation of *in vivo* editing of *Rpe65* in *rd12* mice with corresponding b-waves. 130

CHAPTER 6: Development of lipid nanoparticles to deliver CRISPR RNPs
Figure 6.1 Purification and characterization of genome-editing proteins. 177
Figure 6.2 Direct protein delivery of Cre recombinase mediated by cell-penetrating peptides. 179
Figure 6.3 Cell-penetrating peptide-mediated delivery of ABE in vitro and in vivo. 182
Figure 6.4 Lipid nanoparticle delivery of ABE RNPs. 184
Figure 6.5 Lipid nanoparticle delivery of PE. 187
Figure 6.6 *In vivo* physiology and chemistry of *Rpe65* correction. 189

Extended Data Figure 6.1 Delivery of PE RNP into *rd12* reporter cells. 191
Extended Data Figure 6.2 Delivery of ABE using Lipofectamine 3000. 193
Extended Data Figure 6.3 Optimization of ABE RNP LNPs. 195
Extended Data Figure 6.4 Treatment with editor-containing nanoparticles restores visual responses in *rd12* mice. 197
Supplementary Figure 6.1 Differential-scanning fluorimetry profiles of ABE and PE. 198
Supplementary Figure 6.2 Titration of HEK293-loxP-GFP-RFP cells with CPP-fused Cre. 199
Supplementary Figure 6.3 Titration of HEK293-loxP-GFP-RFP cells with Cre and 6xHis-CM18-PTD4 peptide. 201
Supplementary Figure 6.4 Minus-enzyme controls for HEK293-loxP-GFP-RFP cells with 6xHis-CM18-PTD4 peptide. 203
Supplementary Figure 6.5 Structures of lipids used in this study. 204
Supplementary Figure 6.6 Mass spectrometric quantification of ABE and PE. 205
Supplementary Figure 6.7 Off-target analysis of *rd12* mice treated with ABE- and PE RNP LNP. 207
Supplementary Figure 6.8 Non-targeting ABE and PE RNP LNPs do not result in correction of *Rpe65* or restore scotopic flash ERG responses. 208
Supplementary Figure 6.9 Flow cytometry gating strategies. 209

LIST OF TABLES

Page

Table 1.1 Commonly used and upcoming genome editors 26

ACKNOWLEDGMENTS

I am grateful to the entire administrative and support staff at the University of California, Irvine in the Department of Ophthalmology and Department of Physiology & Biophysics. I am especially grateful to Tim Dinh, Anna Kiker, and Dziyana Aydin for the work you did to enable my focus on discovery and research. I am grateful for the mentorship and assistance I received from everyone in lab, with special recognition to Dr. Susie Suh and Dr. Elliot H. Choi. I am grateful for all of the faculty collaborators, students, and staff, whose expertise strengthened my projects and added valued new perspective. I would also like to acknowledge Dr. Zhiqian Dong and Xiuli Ma for their assistance with the management of my animal colonies and research animals. Special thanks to the entire faculty of the Center for Translational Vision Research for their mentorship and support.

I gratefully acknowledge the faculty who served on my thesis committee and for their guidance throughout this process: Dr. Todd C. Holmes, Dr. Philip D. Kiser, Dr. Chang C. Liu, and Dr. Rachel W. Martin.

The text of portions of Chapter 1 of this dissertation is an adaptation of the material as it appears in Yan, A. L., Du, S. W. & Palczewski, K. Genome editing, a superior therapy for inherited retinal diseases. *Vision Research* 206, 108192 (2023), used with permission from Elsevier. Krzysztof Palczewski directed and supervised research which forms the basis for part of this dissertation.

The text of portions of Chapter 2 of this dissertation is an adaptation of the material as it appears in Du, S. W. *et al*. In vivo photoreceptor base editing ameliorates rhodopsin-E150K autosomal-recessive retinitis pigmentosa in mice. *Proceedings of the National Academy of Sciences* 121, e2416827121 (2024), used with permission from the National Academy of Sciences. The co-authors listed in this publication are Gregory A. Newby, David Salom, Fangyuan Gao, Carolline Rodrigues Menezes, Susie Suh, Elliot H. Choi, Paul Z. Chen, and David R. Liu. Krzysztof Palczewski directed and supervised research which forms the basis for part of this dissertation.

The text of portions of Chapter 3 is an adaptation of the material as it appears in Banskota, S. *et al*. Engineered virus-like particles for efficient in vivo delivery of therapeutic proteins. *Cell* 185, 250-265 e216 (2022), used with permission from Elsevier. The co-authors listed in this publication are Aditya Raguram, Susie Suh, Jessie R. Davis, Elliot H. Choi, Xiao Wang, Sarah C. Nielsen, Gregory A. Newby, Peyton B. Randolph, Mark J. Osborn, and Kiran Musunuru. Krzysztof Palczewski and David R. Liu directed and supervised research which forms the basis for part of this dissertation.

The text of portions of Chapter 4 is an adaptation of the material as it appears in An, M. et al. Engineered virus-like particles for transient delivery of prime editor ribonucleoprotein complexes in vivo. *Nature Biotechnology* (2024), used with permission from Nature Publishing Group. The co-authors listed in this publication are Aditya Raguram, Samagya Banskota, Jessie R. Davis, Gregory A. Newby, and Paul Z. Chen. Krzysztof Palczewski

and David R. Liu directed and supervised research which forms the basis for part of this dissertation.

The text of portions of Chapter 5 is an adaptation of the material as it appears in Geilenkeuser, J. *et al*. Engineered nucleocytosolic vehicles for loading of programmable editors. *Cell* 188, 1–19 (2025), used with permission from Elsevier. The co-authors listed in this publication are Julian Geilenkeuser, Niklas Armbrust, Emily Steinmaßl, Sebastian Schmidt, Eva Binder, Yuchun Li, Niklas Warsing, Stephanie Victoria Wendel, Florian von der Linde, Elisa Schiele, Xiya Niu, Luisa Stroppel, Oleksandr Berezin, Tobias Santl, Tanja Orschmann, Keith Nel-son, Christoph Gruber, Grazyna Palczewska, Carolline Rodrigues Menezes, Eleonora Risaliti, Zachary J. Engfer, Naile Koleci, Andrea Schmidts, and Arie Geerlof. Gil Gregor Westmeyer, Dong-Jiunn Jeffery Truong, and Krzysztof Palczewski directed and supervised research which forms the basis for part of this dissertation.

The text of portions of Chapter 6 is an adaptation of the material as it appears in Holubowicz, R. *et al*. Safer and efficient base editing and prime editing via ribonucleoproteins delivered through optimized lipid-nanoparticle formulations. *Nature Biomedical Engineering* (2024), used with permission from Nature Publishing Group. The co-authors listed on this publication are Jiin Felgner, Roman Smidak, Elliot H. Choi, Grazyna Palczewska, Carolline Rodrigues Menezes, Zhiqian Dong, Fangyuan Gao, Omar Medani, Alexander L. Yan, Maria W. Holubowicz, Paul Z. Chen, Marco Bassetto, Eleonora Risaliti, David Salom, J. Noah Workman, Philip D. Kiser, Andrzej T. Foik, David C. Lyon, Gregory A. Newby, David R. Liu, and Philip L. Felgner. Krzysztof Palczewski directed and supervised research which forms the basis for part of this dissertation.

Financial support for this dissertation was provided in part by grants from the National Institutes of Health to S.W.D. numbered T32GM008620 and F30EY033642.

VITA

Samuel W. Du

2016	B.A. in Molecular Biology, Pomona College
2016-2018	Research Assistant, Seattle Children's Research Institute
2018-2020	M.D. Candidate, University of California, Irvine School of Medicine
2020-2025	Graduate Student Researcher, Department of Physiology and Biophysics, Center for Translational Vision Research, Department of Ophthalmology, University of California, Irvine School of Medicine
2021-2026	National Eye Institute, National Research Service Award Fellow
2025	Ph.D. in Biomedical Sciences, University of California, Irvine

FIELD OF STUDY

Treatment of inherited retinal degenerations through viral and non-viral delivery of precision genome editors

PUBLICATIONS

Arkatkar, T. et al. B cell-derived IL-6 initiates spontaneous germinal center formation during systemic autoimmunity. J Exp Med 214, 3207-3217 (2017). https://doi.org/10.1084/jem.20170580

Arkatkar, T. et al. TACI deletion protects against progressive murine lupus nephritis induced by BAFF overexpression. Kidney Int 94, 728-740 (2018). https://doi.org/10.1016/j.kint.2018.03.012

Benayahu, Y. et al. The Octocorals of Dongsha Atoll (South China Sea): An Iterative Approach to Species Identification Using Classical Taxonomy and Molecular Barcodes. Zool Stud 57, e50 (2018). https://doi.org/10.6620/ZS.2018.57-50

Du, S. W., Jacobs, H. M., Arkatkar, T., Rawlings, D. J. & Jackson, S. W. Integrated B Cell, Toll-like, and BAFF Receptor Signals Promote Autoantibody Production by

Transitional B Cells. J Immunol 201, 3258-3268 (2018). https://doi.org/10.4049/jimmunol.1800393

Raso, F. et al. alphav Integrins regulate germinal center B cell responses through noncanonical autophagy. J Clin Invest 128, 4163-4178 (2018). https://doi.org/10.1172/JCI99597

Du, S. W. et al. Functional Characterization of CD11c(+) Age-Associated B Cells as Memory B Cells. J Immunol 203, 2817-2826 (2019). https://doi.org/10.4049/jimmunol.1900404

Du, S. W., Arkatkar, T., Jacobs, H. M., Rawlings, D. J. & Jackson, S. W. Generation of functional murine CD11c(+) age-associated B cells in the absence of B cell T-bet expression. Eur J Immunol 49, 170-178 (2019). https://doi.org/10.1002/eji.201847641

Santos, P. M. et al. Impact of checkpoint blockade on cancer vaccine-activated CD8+ T cell responses. J Exp Med 217 (2020). https://doi.org/10.1084/jem.20191369

Chiang, K. et al. Cutting Edge: A Threshold of B Cell Costimulatory Signals Is Required for Spontaneous Germinal Center Formation in Autoimmunity. J Immunol 207, 2217-2222 (2021). https://doi.org/10.4049/jimmunol.2100548

Jacobs, H. M. et al. TACI haploinsufficiency protects against BAFF-driven humoral autoimmunity in mice. Eur J Immunol 51, 2225-2236 (2021). https://doi.org/10.1002/eji.202149244

Banskota, S. et al. Engineered virus-like particles for efficient in vivo delivery of therapeutic proteins. Cell 185, 250-265 e216 (2022). https://doi.org/10.1016/j.cell.2021.12.021

Choi, E. H. et al. In vivo base editing rescues cone photoreceptors in a mouse model of early-onset inherited retinal degeneration. Nat Commun 13, 1830 (2022). https://doi.org/10.1038/s41467-022-29490-3

Du, S. W. & Palczewski, K. MicroRNA regulation of critical retinal pigment epithelial functions. Trends Neurosci 45, 78-90 (2022). https://doi.org/10.1016/j.tins.2021.10.008

Du, S. W. & Palczewski, K. Eye on genome editing. J Exp Med 220 (2023). https://doi.org/10.1084/jem.20230146

Yan, A. L., Du, S. W. & Palczewski, K. Genome editing, a superior therapy for inherited retinal diseases. Vision Res 206, 108192 (2023). https://doi.org/10.1016/j.visres.2023.108192

An, M. et al. Engineered virus-like particles for transient delivery of prime editor ribonucleoprotein complexes in vivo. Nat Biotechnol (2024). https://doi.org/10.1038/s41587-023-02078-y
Du, S. W. et al. Conditional deletion of miR-204 and miR-211 in murine retinal pigment epithelium results in retinal degeneration. J Biol Chem 300, 107344 (2024). https://doi.org/10.1016/j.jbc.2024.107344

Du, S. W. et al. In vivo photoreceptor base editing ameliorates rhodopsin-E150K autosomal-recessive retinitis pigmentosa in mice. Proc Natl Acad Sci U S A 121, e2416827121 (2024). https://doi.org/10.1073/pnas.2416827121

Holubowicz, R. et al. Safer and efficient base editing and prime editing via ribonucleoproteins delivered through optimized lipid-nanoparticle formulations. Nat Biomed Eng (2024). https://doi.org/10.1038/s41551-024-01296-2

Hong, J. D. et al. Retinylidene chromophore hydrolysis from mammalian visual and non-visual opsins. J Biol Chem 300, 105678 (2024). https://doi.org/10.1016/j.jbc.2024.105678

Liu, S. et al. NADPH oxidase exerts a B cell-intrinsic contribution to lupus risk by modulating endosomal TLR signals. J Exp Med 221 (2024). https://doi.org/10.1084/jem.20230774

Geilenkeuser, J. et al. Engineered nucleocytosolic vehicles for loading of programmable editors. Cell 188, 1–19 (2025). https://doi.org/10.1016/j.cell.2025.03.015

ABSTRACT OF THE DISSERTATION

Treatment of inherited retinal degenerations through viral and non-viral delivery of precision genome editors

by

Samuel W. Du

Doctor of Philosophy in Biomedical Sciences

University of California, Irvine, 2025

Professor Krzysztof Palczewski, Chair

Inherited retinal degenerations (IRDs), leading to vision loss, are caused by mutations in genes or regulatory elements critical for retinal structure and function. Despite extensive research, effective IRD therapy is still lacking due to the large pool of genes involved and the fact that multiple mutations in a single gene can cause different phenotypes, requiring distinct treatments. Recent genome-editing advances, like CRISPR-Cas9, base editors (BE), and prime editors (PE), have shown feasibility by correcting mutated genes in vitro, but significant obstacles remain for translating these approaches to clinical applications. A key challenge is efficient delivery of these editors due to their large size and negatively charged guide RNA. Thus, advancement of BE and PE into the eye and for other genetic diseases requires novel delivery mechanisms. In this work, we demonstrated the correction of blindness-causing mutations in the mouse equivalents of *RHO*, *MFRP*, and *RPE65* following subretinal injection. Efficient editing was observed, which restored

protein expression and physiological function within the eye. This was achieved through the development of new *in vivo* delivery modalities of BE and PE, including split adeno-associated viruses, two types of virus-like particles, and lipid nanoparticles. The transient, safe, and efficient delivery of BE and PE is thus poised to create new solutions for the treatment of IRDs and other genetic disorders.

CHAPTER 1

Introduction

This chapter is derived in part from the following manuscript published in *Vision Research:*

Yan, A. L., Du, S. W. & Palczewski, K. Genome editing, a superior therapy for inherited retinal diseases. Vision Research 206, 108192 (2023).

© 2023 Elsevier Ltd.

CHAPTER 1: Introduction

1.1 DNA and RNA as substrates and targets

The complexity of life on Earth is encoded by the nucleic acids deoxyribonucleic acid (DNA) and ribonucleic acid (RNA). DNA and RNA possess many qualities which allow them to store the information of life. This necessitates machinery to copy, read, interpret, transmit, and interfere with this information.

While the transmission of genetic information from an individual to its progeny can be remarkably accurate, errors and mutations can also be passed down. These can be inherited, occur during the processes of mitosis and meiosis, or arise *de novo* within the offspring. Alternatively, while recessive alleles can be phenotypically silent in a mutation carrier, this phenotype can be revealed when two copies of a mutated allele (in a diploid organism) are inherited or generated.

Thus, the question arises: how do we detect the presence of deleterious mutations and intervene when appropriate? With the advent of sequencing technologies, including those by Fred Sanger[1], Walter Gilbert, and Allan Maxam[2], genes and genomes could now be investigated and mapped at single base resolution, with individual genes of interest such as those encoding hemoglobin, CFTR, and visual opsins being cloned. Combined with advances in DNA/RNA manipulation, sequence interpretation and computation, whole genomes were sequenced, starting with single-cell organisms, to multicellular organisms, and finally to *Homo sapiens,* with the first draft of the human genome released in 2001[3]. Of note, an entire human genome, including heterochromatin, centromeres, and telomeres, was not completely sequenced until 2022 due to technical difficulties sequencing polymeric DNA, and even this assembly lacked a Y chromosome[4].

In parallel with the sequencing of genes and genomes that identified causative genes and mutations, scientists began to investigate if genetic conditions caused by gene mutations could

be treated by complementation with healthy, wildtype DNA. By exploiting the abilities of viruses to transfer nucleic acids to host cells, patient cells could be transduced with viruses encoding potentially curative genes, as demonstrated for patients with adenosine deaminase (ADA) deficiency starting in 1990[5].

One of the first tools discovered and exploited to manipulate DNA in vitro was the restriction enzyme. Found in bacteria, these enzymes recognize and cleave specific DNA sequences with a double-stranded break (DSB) and allow scientists to cut and paste DNA in a controlled way[6].

While restriction enzymes can be useful, they have limitations. Not all DNA sequences have restriction sequences that can target them, or the enzyme does not cut in the correct place. As well, most restriction enzyme recognition sequences are relatively short – with a genome that is over a billion bases long, instead of targeting one specific location in the genome, dozens, hundreds, or thousands of sequences could be simultaneously targeted. One solution is to increase the length of the DNA recognition sequence. Two classes of DNA-binding proteins include zinc finger nucleases (ZFNs) and transcription factor-like effector nucleases (TALENs).

The zinc finger is a protein domain that utilizes a zinc (Zn^{2+}) cofactor to recognize and bind a 3 basepair (bp) sequence[7]. By fusing multiple zinc fingers together, a zinc finger complex can recognize longer sequences. A nuclease is also fused to the zinc fingers, as zinc fingers do not have any intrinsic cleavage ability. The non-specific type IIS nuclease FokI is commonly used, and because FokI operates as a dimer, two ZFN are often used to specify a DNA target[8]. Commonly, pairs of 9 bp recognizing ZFNs are used, resulting in an 18 bp recognition sequence, though longer ZFNs can be used as well. Difficulties of using ZFNs are in the engineering of the protein complexes – while multiple zinc fingers have been described that cover the sequence space of possible 3 bp combinations, interactions between zinc finger protein domains, as well as sequence context specific interactions between the DNA and protein can all influence binding selectivity and specificity *in vivo*[9]. Thus, ZFNs need to be carefully validated *in vitro* and *in vivo*,

and must be reoptimized *de novo* for new targets. TALENs operate on similar principles to ZFNs, but TALE subunits recognize single bases, and TALE arrays are modular and can be assembled to recognize DNA sequences with high specificity[10]. Similarly to ZFNs, TALE arrays are then fused with a FokI nuclease and designed as a dimer.

To summarize, by engineering discrete DNA binding domains, ZFNs and TALENs can recognize custom and specific DNA sequences. They can also be programmably engineered to recognize a custom sequence, instead of relying on naturally occurring restriction sites or performing directed evolution on restriction enzymes. However, ZFNs and TALENs are difficult to optimize and engineer. While TALEN arrays are somewhat more modular than ZFNs, they must still be optimized and tested for each sequence. Both ZFNs and TALENs are also difficult to multiplex to simultaneously edit multiple sites, though they have some advantages due to their all-protein design that does not require the use of DNA or RNA for activity.

1.2 Discovery and characterization of CRISPR systems

As single celled organisms, bacteria lack the complex, cell-driven immune systems associated with multicellular organisms, but they are not defenseless against bacteriophages. In 1987, researchers described repeated sequences in the *Escherichia coli* genome that were interspaced with additional sequences[11]. Additional clues to the function of these sequences came in 2007, when these repetitive sequences, also known as clustered regularly interspaced short palindromic repeats (CRISPR), were used by bacteria to integrate phage genomic sequences as a form of acquired anti-phage immunity upon subsequence challenge[12]. The integrated sequences were processed into targeting RNAs that, in complex with CRISPR-associated systems (Cas) proteins, targeted and degraded bacteriophage genomes to provide resistance to infection.

Landmark papers in 2012 and 2013 demonstrated the mechanism of DNA cleavage by the Cas9 protein from *Streptococcus pyogenes*[13-15]. Collectively, these works also showed that productive and programmable DNA cutting could be achieved *in vitro*, as well as within a

mammalian cell, which was a critical hurdle for the translation of gene editing to humans. They also elucidated the function of the CRISPR RNA (crRNA) that encodes the protospacer (the targeted genomic sequence) in combination with the transactivating CRISPR RNA (tracRNA) and showed that the crRNA and tracRNA could be combined into a single guide RNA (sgRNA) for ease of use[13]. Other features of genomic targeting include the protospacer adjacent motif (PAM), which is a sequence directly adjacent to the protospacer and is recognized by the Cas protein, allowing for greater specificity and the avoidance of self-targeting by the Cas complex[13].

Major advantages of the CRISPR system are that the DNA targeting is programmably achieved by a guide RNA. Instead of designing a new protein *de novo* for each new target, a new site can be targeted by a simple exchange of the guide RNA. This simplifies screening of editing strategies and could additionally assist in safety studies and regulatory approval. Additionally, a single Cas protein can be multiplexed with multiple guide RNAs to target sites simultaneously, a boon when multiple genes need to be knocked out or altered, such as in immune cell engineering and creating models for xenotransplantation[16,17]. Other than their use in creating DNA single and double stranded breaks, CRISPR targeting has been repurposed for other applications where DNA needs to be targeted, such as high throughput CRISPR screening, gene activation, gene inactivation, and epigenome rewriting[18].

1.3 Genetics and biochemistry of CRISPR/Cas systems

In opposition to pathways such as metabolism and DNA replication, pathways that are involved in “attack” and “defense” (e.g. antiviral immunity) are often the fastest evolving and most divergent regions of genomes between species. The evolutionary arms race to detect and thwart attacks from other individuals leads to an extraordinarily fast mutagenesis of attack and defense genes. Therefore, as researchers began to analyze the genomes of bacteria and archaea for CRISPR genes, they realized that different organisms encode vastly different systems and varieties of CRISPR proteins, and the DNA and protein sequences are highly divergent as well. CRISPR systems are thus categorized by their function and common features.

Modules common to all Cas systems include Cas1, Cas2, and Cas4, which work cooperatively to capture and insert new spacers into the Cas array, interspaced with the CRISPR sequences[19]. Specifically, Cas1 is an integrase, Cas2 is a structural adapter, and Cas4 is an endonuclease. Then, the systems that are used to recognize and interfere with pathogens, often termed the “interference” or “effector” system, can be classified into class I or class II systems. In class I systems, multiple proteins form an interference complex (any combination of Cas3, Cas5-8, Cas10, and Cas11), as opposed to class II systems, where one large protein handles multiple roles in recognition and interference (Cas9, Cas12, or Cas13)[19]. These classes can be further subdivided into multiple subtypes (at least types I through VI), depending on the combination of effector proteins, targets, and roles. As phages or mobile genetic elements, such as transposons and retrotransposons, can have genomes of either DNA or RNA, different Cas effector modules can target either DNA or RNA.

Of course, phages can also fight back. Anti-CRISPR proteins (Acrs) are a feature of many phage genomes. These have many diverse functions that interfere with multiple steps of the CRISPR system. One of these is molecular mimicry, where Acrs can mimic double-stranded DNA and act as decoys for CRISPR ribonucleoproteins (RNPs) due to their structure and charge[20]. Other mechanisms include covalent and enzymatic modification of Cas effectors, including acetylation of Cas proteins and endonuclease cleavage of crRNAs[20]. Yet another form of anti-CRISPR is the degradation of second messengers and signaling molecules used by the bacterium to signal invasion[20]. Similarly to the complexity of the vertebrate immune system, each innovation in CRISPR or anti-CRISPR can lead to a commensurate adaptation and compensatory mechanism, which invites its own response, and so on. In terms of genome editing, the exploitation of Acrs and anti-CRISPR strategies could be a useful tool to control and limit genome editing or prevent unwanted editing byproducts.

As the first to be characterized, the Cas9 from the bacterium *Streptococcus pyogenes* (SpCas9) has been the best studied and understood. SpCas9 also has one of the least restrictive

PAMs (NGG, where N is any nucleotide), which theoretically allows for the targeting of 1/16th of genome sequences. SpCas9, however, is one of the larger Cas9 effectors (1,368 amino acids, or ~4.1 kb), which poses problems in terms of delivery.

As a class II enzyme, SpCas9 contains multiple modules necessary for its function identifying and degrading foreign genetic material. The two major domains are the alpha-helical DNA recognition domain (REC domain) and the nuclease domain (NUC), which is further subdivided into the HNH and RuvC nuclease domains[21]. The REC domain contains three alpha helices and a PAM recognition domain. Interestingly, the REC domain is less structured when not bound to the guide RNA, further supporting the idea that Cas9 requires binding of the guide RNA for its function. The nuclease subdomains each cleave one strand of the target DNA, allowing for selective inactivation of the enzyme to create a Cas9 nickase, where only one strand of the target DNA is nicked. The RuvC domain cleaves the strand non-targeted by the guide RNA, while the HNH domain cleaves the targeted strand, and SpCas9 creates a blunt, symmetrical cut, while other Cas nucleases can either make one cut or make staggered cuts. The creation of the nickase thus enables more fine control of DNA damage, as blunt double-stranded breaks can be highly genotoxic, which is ideal when targeting a pathogen, but suboptimal when applied in genome editing.

SpCas9 cannot cover all use cases for genome editors, whether due to size, delivery, PAM restrictions, immunogenicity, or intellectual property, among other reasons. Substantial effort has been invested, therefore, into the discovery of Cas9 orthologues and other novel nucleases that may offer advantages over SpCas9 for generalized or niche gene editing use cases. These are often performed by deep metagenomic mining for CRISPR arrays and similar Cas proteins, though this has been challenging due to rapid sequence diversification during evolution. Examples include Cas9 from *Parasutterella secunda* (PsCas9) which showed equivalent editing to SpCas9, but with far fewer off-target editing events *in vitro* and *in vivo*[22]. Another nuclease and its cognate guide RNA, Cas12f from an archaeon, was engineered for editing in mammalian cells,

which the wildtype protein did not have[23]. An alternative approach to sequence-based mining, the Doudna group used structure-based search to identify a novel Cas13an[24]. Searching closer to eukaryotes, the transposon systems IS200, IS605, and IS607 were found to encode RNA guided nucleases called TnpB that were programmable, indicating that programmable RNA guided nucleases can be found more widely than just in prokaryotes[25,26]. TnpB and its guide RNA, called an omega RNA (ωRNA) has been further engineered and optimized to improve its activity and specificity in mammalian cells[27-29]. This class of proteins has been called OMEGA, for Obligate Mobile Element-guided Activity. Even more excitingly, an OMEGA family protein called Fanzor is encoded within eukaryotic genomes and could be reprogrammed for RNA-guided nuclease activity[30]. Characterization of Fanzor from *Spizellomyces punctatus* was performed, and its structure showed similarities to TnpB and Cas12, indicating a shared common function or origin[30]. Thus, further search and characterization of both eukaryotes and prokaryotes can result in the discovery of new programmable RNA-guided nucleases.

Another route to modifying SpCas9 is through directed evolution or rational engineering of Cas9 to create high-fidelity or less PAM-constrained variants. SpCas9 has been subjected to multiple kinds of directed evolution and rational engineering, as NGG PAMs are not evenly distributed through the genome, and some NGG PAMs cannot reach mutation sites or place base and prime editors too far away from the target base to be useful. Thus, there have been efforts to make more flexible PAMs, such as the phage-assisted continuous evolution (PACE) variant xCas9, recognizing NG, GAA and GAT PAMs[31]. Other variants of note include the NG SpCas9, which shows relaxed targeting[32], and the SpG/SpRY SpCas9s that are theoretically PAMless[33]. Another approach has been to decrease the off-target capabilities of SpCas9 by modulating Cas9 interactions with target DNA, creating a high-fidelity Cas9 with greatly decreased off-target editing[34]. Other studies have also demonstrated that it is possible to decrease off-target editing with additional mutations in Cas9[35].

There is a concern that relaxing PAM requirements for Cas9 could make them less active or increase their off-target editing. Thus, another approach is to make them more specific for certain PAMs or create a bespoke Cas9 for each specific mutation. This was demonstrated with the generation of a novel SpCas9-NRCH in combination with the ABE8e deaminase to create a custom editor capable of converting the sickle cell hemoglobin B to the Makassar variant[36,37]. Similarly, the ABE8e-SpRY editor was selected to perform base editing of *SMN2* after screening multiple combinations of deaminase and editor pairs[38].

1.4 Classical genome editing with CRISPR-Cas9 nucleases

Considering the many drawbacks of gene augmentation therapy, genome editing therapies have emerged as the most promising treatments for IRDs. Although genome editing with zinc finger nucleases (ZFNs) and transcription activator-like effector nucleases (TALENs) have existed for some time, they are limited by many disadvantages, such as time-consuming and expensive construct design as well as large assemblies that form barriers to certain delivery modalities [39]. However, the discovery of RNA-guided CRISPR (clustered-regularly interspaced short palindromic repeats) nucleases in 2012 has made ZFNs and TALENs largely irrelevant for further *in vivo* genome editing applications. The most commonly used CRISPR platform for genome editing therapeutics is the CRISPR associated protein 9, Cas9, which when complexed with an engineered single guide RNA (sgRNA), can recognize specific DNA sequences and generate a double-strand break (DSB) at that sequence [40]. Although ZFNs and TALENs also generate DSBs, the advantage of CRISPR-Cas9 is that only the sgRNA sequence needs to be changed to recognize a different genetic locus, rather than completely reengineering the protein domains [41,42].

After Cas9 introduces a double stranded break, there are two main methods of repair – non-homologous end-joining (NHEJ) and homology-directed repair (HDR) (**Figure 1.1A**) [43]. End-joining pathways directly re-ligate the double stranded break and often result in misaligned repair, which includes a random mixture of insertions and deletions (indels); these often lead to frameshift

mutations and gene knockout [41]. On the other hand, the HDR repair pathway inserts a donor DNA molecule containing the correct gene sequence directly into the genome as the cell repairs the DSB. In theory, HDR can precisely correct mono-allelic mutations involved in IRDs, and researchers have demonstrated that targeted *in vivo* gene-integration can rescue mutations in the *PDE6B, NR2E3, RPGR, USH1C, RHO,* and *RPE65* genes [44-51]. However, HDR has several drawbacks that preclude it from efficiently introducing precise gene corrections in the retina. Cas9-induced DSBs often result in substantial indels that nullify the potential therapeutic benefits of HDR [42]. In addition, the HDR pathway is predominantly active in dividing cells, so the efficiency of homologous recombination in post-mitotic cells, such as photoreceptors and RPE cells, is drastically reduced [52]. Thus, HDR is largely unsuitable for precise genome editing in the eye.

On the other hand, end-joining methods have considerable therapeutic potential for treating inherited retinal diseases. NHEJ is active throughout the cell cycle and across several different cells, which is especially useful for applications of gene disruption, where indels are desired [52]. Using NHEJ repair, Suzuki *et al.* developed a strategy for homology-independent targeted integration (HITI), which results in targeted transgene integration (**Figure 1.1A**) [53]. The DNA template used in HITI is flanked by Cas9 cleavage sites rather than homology domains as in HDR. Using this approach, researchers improved rod-cone response by restoring a 1.9 kb deletion from the *Mertk* gene in a mouse model of autosomal dominant retinitis pigmentosa (adRP) [53]. Because NHEJ is active in post-mitotic cells and HDR is not, HITI could greatly expand the scope of nuclease-mediated genome editing in the retina.

An alternative DSB repair pathway, microhomology-mediated end-joining (MMEJ), functions by annealing microhomologies (5-25 complementary base pairs) upstream and downstream of the DSB [54]. The MMEJ pathway most often results in short deletions of the microhomologous sequence, which makes it effective for gene knockout. Recently, Sakuma *et al.* developed a system for MMEJ-assisted gene knock-in by delivering Cas9 nuclease in conjunction with a donor DNA vector including two different microhomology arms [55]. Cleaving between the

microhomologies allows targeted gene integration by MMEJ. Although MMEJ has not yet been applied in the eye, it serves as a promising alternative pathway to HDR and NHEJ for gene knock-in treatments.

Researchers have also developed an approach to preferentially ablate the mutant *Rho* allele carrying either a P23H or S334ter mutation in mouse models of adRP, thereby preserving the wild-type allele and ameliorating disease phenotypes [56,57]. In some cases, this gene disruption approach induces haploinsufficiency, which then requires cells to be supplemented with an exogenous cDNA copy of the wild-type gene. The main drawback of this approach is the genetic heterogeneity in *Rho* that causes adRP, which poses an economic challenge when designing sgRNAs to target each mutation, especially in conjunction with the delivery of exogenous cDNA. To alleviate these costs, researchers have used Cas9 to eliminate both copies of the endogenous *Rho* gene before supplementation with an exogenous wild-type copy of *Rho* [58]. This ablate-and-replace strategy rescued photoreceptor structure and function in adRP mice [58]. Although this approach eliminates potential cellular stress from products of the mutant allele, there are still concerns of waning transgene expression over time, the same as those in gene augmentation therapy, as well as genotoxicity from DSB formation.

Multiplex nuclease-mediated editing is enabled by delivery of several sgRNAs targeting different sites. This approach was used by Maeder *et al*. to correct a deep-intronic recessive mutation (IVS26) in the *CEP290* gene, which results in erroneous protein splicing and is implicated in LCA type 10 (LCA10) [59]. Employing *Staphylococcus aureus* Cas9 (SaCas9), the group was able to restore normal splicing of *CEP290* transcription products by excising or inverting the mutation [59]. In experiments involving human retinal explants, editing efficiency reached the desired level for therapeutic effect and there was no detected off-target editing [60]. In addition, this study demonstrated that human G protein-coupled receptor kinase 1(*GRK1)*-promoter-driven expression of SaCa9 is specific to photoreceptors, and there appears to be limited immunogenicity towards SaCas9. Based on the favorable nature of these results, Editas

Medicine initiated a phase 1/2 trial of EDIT-101 to correct a *CEP290* mutation in patients with LCA10. EDIT-101 uses a single AAV to deliver *GRK1*-driven SaCas9 along with two sgRNAs to target the IVS26 point mutation in intron 26 of the *CEP290* gene (NCT03872479). By introducing DSBs at both ends of the mutation, the mutated sequence is excised, and normal protein splicing is restored. While post-treatment assessment is still ongoing, EDIT-101 repairs the mutation and solves many of the problems of gene augmentation, as the effects of editing are permanent and there is little risk with cellular toxicity of mutant gene products. Overall, nuclease-mediated editing has pushed gene therapy away from gene augmentation and towards genome editing approaches.

1.5 Extending Cas9 Functionality with Base Editors

Because of the risk of creating double-stranded breaks and the heterogeneity of editing outcomes when correcting point mutations, a new form of genome editor needed to be made to perform precision chemistry on the genome. Cas9's main strength is the use of a programmable and easily interchangeable sgRNA to direct the nuclease to a site in the genome. Thus, if the DNA modification could be performed with another enzyme, then the advantages of Cas9 could be maintained in combination with a more targeted DNA modification. In 2016, the first base editors were reported. These were the first cytosine base editors (CBEs), which fuse a dead or nickase Cas9 to a cytosine deaminase, both of which exist in mammalian genomes to convert C•G base pairs to U•G base pairs through removal of an amine group from cytosine (**Figure 1.2**). The uracil created by the deamination is then read as a thymine when the DNA is repaired. When the sgRNA forms an RNA-DNA duplex with the target strand, the non-targeted strand is exposed in an R-loop and chemistry can be performed on this exposed DNA strand. The Liu group utilized the rat APOBEC1 enzyme, known for performing C>T RNA editing for their CBE[61]. They also noted that uracils are commonly repaired quickly in cells through base excision repair and the involvement of the enzyme uracil DNA glycosylase (UDG), and thus they added an uracil DNA glycosylase inhibitor (UGI), which boosted editing efficiencies[61]. Another important observation was that by

nicking the target strand in complex with the sgRNA, the cellular repair machinery is then biased toward using the non-target edited strand as the template for repair[61]. Thus, the SpCas9 used in base editing experiments is the D10A nickase, which only nicks the target strand. Similarly, the Kondo group fused activation-induced cytosine deaminase (AID), an enzyme critical for somatic hypermutation in B and T cells, to Cas9 and reported a similar CBE[62].

The deamination of adenine (A•T) base pairs to inosine (I•T) base pairs is repaired similarly to C>T conversions, where inosines are read as guanines during DNA repair, except there is no equivalent of UDG, and thus there is no need for an equivalent to a UGI (**Figure 1.2**). While the CBEs could utilize naturally occurring enzymes, no such enzyme existed for the deamination of adenine DNA. There were adenine deaminases, such as the ADAR enzymes, that only worked on RNA or double stranded DNA, and they were not capable of single stranded DNA editing in mammalian cells. Thus, the Liu group opted to use directed evolution to reengineer the tRNA adenine deaminase TadA found in *E. coli* to redirect its substrate specificity from RNA to DNA[63]. Through seven rounds of directed evolution, they generated a TadA variant that was capable of binding and deaminating single-stranded DNA. This best variant was TadA 7.10, which, when fused as a dimer of wildtype TadA and TadA 7.10 to the N-terminus of Cas9, was termed the adenine base editor (ABE) 7.10. Further optimization of the codon usage and nuclear localization sequences (NLS) for ABE7.10 and the CBE BE4 led to the “max” versions of these base editors (ABE7.10max/ABEmax and BE4max) [64]. Further development and evolution of the deaminase led to a hyperactive deaminase, which showed an improvement in kinetics and efficiency of editing, though at the cost of increased bystander editing due to the processivity of the enzyme[65]. Follow-up structural and biochemical studies elaborated on the mechanisms and insights into TadA activity and how to improve the editor[66,67]. Lastly, as CBEs demonstrate more off-target editing, more transcriptome RNA editing, and more sequence context bias than ABEs, directed evolution of the TadA deaminase toward CBE activity, rather than ABE activity, led to the development of the TadCBEs[68].

CBEs and ABEs can theoretically correct all transition mutations within the human genome, which account for approximately 30% of all known human pathogenic variants [69]. Recent developments of C•G to G•C base editors (CGBEs) have further expanded the scope of mutations that base editors can target (**Fig. 2B**) [70,71]. As a result, base editors are an extremely attractive technology for the treatment of IRDs, especially when gene augmentation therapies fall short. Base editors are particularly suitable for correcting mutations in large genes that exceed the AAV cargo limit for exogenous cDNA delivery, like *ABCA4* (6.8 kb) and *USH2A* (15.5 kb); these are the two most implicated genes across all IRD cases in the U.S. [72].

Base editing has significant advantages over conventional gene augmentation in the treatment of IRDs. Because base editors directly correct endogenous DNA, there is no expression of the mutant protein, which greatly reduces the potential toxicity of the dysfunctional protein. This is especially important in the context of IRDs with dominant modes of inheritance, as gene augmentation may not be sufficient to negate the effect of the mutant allele. In addition, correcting the endogenous locus allows expression of the corrected gene to be driven by the endogenous promoter, which enables cell-specific, physiological regulation of expression. Gene augmentation strategies often rely on exogenous promoters to drive gene expression, which faces the risk of DNA methylation and waning transgene expression over time [73,74]. Such risks are alleviated in base editing treatments, as base editors install permanent corrections in the genome which are regulated by endogenous transcription factors [63].

In 2021, Suh *et al.* demonstrated the first *in vivo* application of base editing to treat an IRD. Through subretinal delivery of a lentiviral vector expressing an ABE and sgRNA, the research group corrected the nonsense mutation in the *Rpe65* gene of the autosomal recessive *rd12* mouse model for LCA type 2 (LCA2) [75]. With the appropriate sgRNA, the target mutation was precisely corrected with up to 29% efficiency, with less than 0.5% indel formation and no off-target editing at the top ten potentially mutable genomic sites [75]. Base editing rescued *Rpe65* expression and restored visual function, as the treated mice exhibited nearly 50% recovery of retinal function

in scotopic electroretinography (ERG) recordings and demonstrated strong responses to visual changes in orientation, spatial and temporal frequency, size, and contrast [75]. A later study found that using base editing to restore *Rpe65* expression in *rd12* mice resolved many of the problems associated with *RPE65* gene augmentation therapy. Choi *et al.* showed that base editing could induce long lasting improvements in cone function while preventing photoreceptor degeneration [76]. As opposed to near-complete degeneration of the retina in untreated mice, mice treated with the base editor displayed improved cone function and survival 6 months following the treatment. Further, the researchers found that restoring *Rpe65* gene expression through base editing downregulated the expression of genes that potentially confer cell death [76]. Thus, base editing has demonstrated its potential to overcome the shortcomings of today's gene augmentation therapies and provide a method for permanent gene correction, which raises the prospect of permanent improvement in visual acuity [73,77,78]. In a separate study of genome editing in the same *rd12* mouse model of LCA, Jang *et al.* demonstrated non-viral delivery of base editors *via* subretinal injection. By injecting lipofectamine in conjunction with ABE/sgRNA ribonucleoproteins (RNPs), they observed delivery of the ABE-sgRNA complexes and up to 5.7% correction efficiency, which resulted in rescued *Rpe65* mRNA and protein expression without risk of lentiviral integration into the genome [79]. These studies raise the prospect of permanent rescue of photoreceptor degeneration *via* genome editing, which was demonstrated in the mouse model of LCA2. While these results are not directly translatable to human LCA2 patients, genome editing seems to provide a clear path to restoration of photoreceptor health that is unaddressed by voretigene neparvovec (Luxturna), though further investigation is needed to assess long-term outcomes of base editing. However, restoration of physiological protein expression may be sufficient to overcome these challenges.

1.6 CRISPR 3.0: Prime editing

Prime editors (PEs) are the most recent advances among the CRISPR-Cas9-derived genome editing technologies. Consisting of a reverse transcriptase fused to a Cas9 nickase, PEs

can theoretically correct all transition and transversion mutations as well as generate small indels (**Figure 1.1**). PEs use prime editing guide RNAs (pegRNAs), which serve both as the sequence that guides Cas9 to the target genomic locus as well as the RNA template for reverse transcription [69]. This innovation allows PEs to precisely write mutations directly into genomic DNA, without the risk of bystander editing.

Although base editors offer multiple advantages over nuclease-based genome editing, they suffer from several major drawbacks. One is the level of Cas9-independent off-target effects by the deaminase, which can lead to deamination across different target sites and in the transcriptome. Another disadvantage is the phenomenon of bystander editing, where multiple potential adenines or cytosines are present within the activity window of the deaminase. Multiply deaminated bases could lead to nonfunctional proteins, which is problematic when the target is a single base[80]. Lastly, and most critically, base editors can only perform transition mutations (A>G and C>T). While these are the most common types of point mutations, transversion mutations and insertions/deletions (indels) still comprise a substantial proportion of disease-causing mutations. Therefore, a new technology was needed.

An innovative new approach, also from the laboratory of David R. Liu, envisioned the use of the guide RNA to both specify the genomic location for Cas9, as well as to contain the genetic information for the new edit. By utilizing a different nickase that nicked the non-target strand to expose one end of the DNA, a reverse transcriptase (RT) could then be primed from the genomic strand to reverse transcribe from the guide RNA into new DNA. The fusion of RT from Moloney murine leukemia virus (MMLV) to a H840A SpCas9 nickase led to low, but detectable reverse transcription of new DNA from the guide RNA[81]. This new guide RNA, termed a prime editing guide RNA (pegRNA), contains an sgRNA with a 3' extension, with a RT template (RTT) and a primer binding site (PBS) with homology upstream of the nicked genomic DNA. Encouraged by this result, they next incorporated five mutations previously described to increase MMLV RT activity (D200N/L603W/T330P/T306K/W313F) to create a more active PE, termed PE2.

Excitingly, PE2 was able to create every type of single base substitution, as well as insertions up to 44 bp and deletions up to 80 bp [81].

Base editors utilize a Cas9 nickase to nick the non-edited strand to promote DNA repair from the edited strand. To apply this same strategy to PE2, they introduced a nicking sgRNA (ngRNA) that nicks the non-edited strand 3' downstream of the templated edit to favor the edited strand. This strategy that they termed PE3 (PE2 protein + pegRNA + ngRNA) increased editing efficiency, but also increased indel rates[81]. This is probably due to the fact that two strands of the DNA are nicked, creating a staggered DSB – while not as toxic as a blunt DSB, it could still lead to unwanted indels. One strategy around this to have the protospacer of the ngRNA match the edited sequence, but not the wildtype sequence, also known as the PE3b strategy.

Further development of prime editing occurred when David Liu's group investigated how to make prime editing more efficient. They utilized a CRISPR inhibition (CRISPRi) assay called Repair-seq[82] that knocked down 476 genes involved in DNA repair and co-transfected a PE/pegRNA pair encoding a single nucleotide change to assess how each of the 476 genes impacted prime editing efficiency[83]. Knockdown of *MSH2*, *MSH6*, *MLH1*, and *PMS2*, proteins that are involved in DNA mismatch repair (MMR) all increase editing efficiency; knockdown of *EXO1*, an exonuclease that is also involved in MMR, also increased efficiencies[83]. Two genes, *LIG1* and *FEN1*, involved in DNA ligation and flap processing, respectively, decreased editing efficiencies when knocked down. Together, these data suggest that MMR antagonizes PE of point mutation installation, and that DNA ligation and flap excision are required for PE[83]. Another editing byproduct that was noted in both studies was the reverse transcription of the pegRNA scaffold and insertion of part of the scaffold into the edit site, and this increased in frequency when MMR was knocked down. Therefore, to boost editing efficiencies, they screened catalytically inactive forms of MMR proteins and found that deactivated MLH1 improved PE the most. They installed additional mutations into MLH1, named this more potent version MLH1dn, and expressed it in the PE plasmid *via* a ribosomal skipping P2A sequence. This created the PE4 and PE5 improvements

on PE2 and PE3, respectively, where P2A-MLH1dn was added to the transfection mixture[83]. It was also noted that installation of additional silent mutations increased PE efficiencies by evading MMR, which primarily repairs singly mismatched bases, as opposed to multiple mismatches. Lastly, they re-optimized PE with codon optimization, the installation of additional SpCas9 mutations, various NLS, and linkers between RT and SpCas9 to create PEmax[83].

On the pegRNA side, as the 3' end of the pegRNA is exposed to the cytosol, in contrast to sgRNAs where the entire scaffold is protected by Cas9, the 3' end of the pegRNA is thus vulnerable to exonuclease degradation, potentially leading to decreased editing efficiencies. In support of this, when the Liu group tested PE with varying mixes of full length and truncated pegRNAs, PE efficiency decreased[84]. Thus, they tested several RNA motifs and knots to protect the 3' end of the pegRNA and selected the truncated evoPreQ1 (tevoPreQ1) to be added to the pegRNA. This was then called the engineered pegRNA, or epegRNA. Of note, the addition of the tevoPreQ1 increased epegRNA stability, but decreased SpCas9 affinity toward the guide[84]. They also found that these improvements translated to increased prime editing whether delivered on plasmids or as chemically synthesized epegRNAs.

More recent improvements of PE include additional directed evolution on the RT domains to increase processivity or decrease size and the installation of additional Cas9 mutations, leading to the PE6 family of editors[85]. Another improvement of the epegRNA-PE interaction was reported with "PE7", where La, a small RNA-binding protein, could interact with the 3' end of the epegRNA and further protect it from degradation, leading to improved pegRNAs and a PEmax fused to La[86]. To assist with the resolution of PE editing, the Westmeyer group fused an exonuclease to the PE to promote flap excision to form exo-PE[87]. Lastly, the Liu group optimized the PE architecture to be packaged into dual AAV vectors, partially by removal of the RNaseH domain[88]. Further insights into the mechanisms of prime editing and its resolution by DNA repair will undoubtably improve PE constructs and boost editing efficiencies to closer parity with base editors.

The first *in vivo* application of prime editing in the eye was demonstrated soon after its development. In this case the *rd12* mouse model of LCA2 was again used, although it was already shown to be precisely corrected by ABE. However, PEs hold a significant advantage over BEs, as BEs can potentially deaminate multiple bases within its catalytic window while PEs exhibit very low bystander editing. Jang *et al.* subretinally administered dual-AAVs of PE and pegRNA, which resulted in about 6.4% correction efficiency without any detectable indels, unintended substitutions, bystander effects, or off-target effects [89]. They also observed improved dark-adapted ERG responses, up to 67% of the wild-type amplitude. As PEs also install permanent corrections directly in the genome, the rescued visual function is expected to be long-lasting. In addition to their ability to generate all point mutations as well as short indels, successful delivery by AAV, a proven clinical approach, makes prime editing an extremely promising new strategy for the treatment of IRDs.

1.7 New developments in genome editing tools

Aside from the progress made in developing and refining base and prime editors, new forms of genome editors have recently been described in various stages of applicability to *in vivo* genome editing. Prime editing of large insertions is limited by the length of the templated insertion, as described in the twin PE[90] and dual pegRNA strategies[91]. For genome engineering and for treatment or replacement of multiple mutations or defective genes, large insertions could be valuable. One way around this is to, instead, use PE to code an integrase recombination site and then use a site-specific recombinase or integrase to knock in large payloads. This was demonstrated by the Liu group and others to integrate DNA templates up to 10 kb long[90,92-94]. However, this has not yet been translated *in vivo*, and there may be substantial difficulty to deliver both the integrase and the cargo with the kinetics of editing and integration. Similarly, different Cas systems also have programmable integrases, and these CRISPR-associated transposases could be leverage for site-specific and targeted integration of large payloads[95,96].

Another alternative to prime editing is the click editor (CE), which fuses a DNA polymerase and an HUH endonuclease to the nickase Cas9[97]. This has theoretical advantages over PEmax, as DNA, rather than RNA, can be covalently and irreversibly attached to the CE, and takes advantage of the higher speed and lower error rate of DNA polymerases compared to RT. As DNA chemical synthesis is much faster and cheaper than RNA chemical synthesis, this could facilitate more rapid screening of editing strategies *in vitro*, as well as lead to improve delivery through an irreversible association of the insertion template DNA to the Cas9 complex. Lastly, the most recent description leverages programmable integrases derived from mobile genetic element transposons, called bridge RNAs. Uniquely, these bridge RNAs bind themselves to their protein product and can be reprogrammed to perform insertions, though this has only been demonstrated in *E. coli* at this time[98,99]. Further optimization of these and other strategies for genome editing will widen the toolbox for genome engineering and potential translation into human clinical trials.

1.8 The eye as a testbed for genetic therapies

Vision is the dominant modality by which we perceive the world. Throughout our daily lives, we are culturally dependent on vision to read, write, and navigate, among many other functions. Thus, people with visual impairment are often severely disadvantaged. Inherited retinal diseases (IRDs) are a class of diseases that damage the retina, often leading to severe visual deterioration or blindness. IRDs affect approximately 200 thousand people in the United States and about 4.5 million people around the world. The genetic diversity of IRDs is broad, as they are caused by mutations in over 280 different genes, with multiple mutations in each gene capable of causing severe disease (**Figure 1.3A**) [100]. Mutations associated with key enzymes of the retinoid cycle are especially devastating, as they lead to impaired synthesis of the visual chromophore or accumulation of cytotoxic retinoid byproducts, which cause retinal dystrophy [101,102]. Hundreds of these different mutations are implicated in several distinct diseases, such as Leber congenital amaurosis (LCA), retinitis pigmentosa (RP), Stargardt disease, choroideremia, and age-related macular degeneration (AMD) [103]. Although all characterized as IRDs, these diseases manifest

with various modes of inheritance and times of onset and affect different areas of the retina, which makes them especially challenging to treat [104,105].

Thus far, treatments for the vast majority of IRDs are only supportive, which require expensive and persistent care [106]. Recently, much progress involving gene augmentation therapy and genome editing has been made towards treating IRDs. The retina is a particularly attractive tissue for developing gene augmentation therapy and genome editing treatments, as it is relatively accessible by surgery and can be imaged noninvasively to assess treatment safety and efficacy [105].

Most genetic therapies for IRDs currently in development consist of gene augmentation strategies, which involve delivering a wild-type cDNA to retinal cells [107]. Yet, due to rapid advances in genome editing strategies, several potential gene disruption and gene correction treatments have been taken to clinical trials. Currently, clinical trials using CRISPR-Cas technology to treat various cancers, sickle cell disease, misfolded protein diseases, and cardiovascular disease have already begun [108-110]. With the advent of even newer genome editing technologies such as base editors and prime editors, which can install permanent precise gene corrections, CRISPR-Cas technologies have become more attractive as approaches to treat IRDs [69].

1.9 Challenges of gene augmentation therapy for the treatment of IRDs

In 2017, the U.S. Food and Drug Administration (FDA) approved voretigene neparvovec (brand name Luxturna) as a gene augmentation therapy for patients with biallelic missense or nonsense mutations in the RPE65 protein (retinal pigment epithelium-specific 65 kDa protein), a key protein in the pathway for regenerating visual pigment [111]. As the first FDA approved gene therapy, Luxturna engendered a new wave of optimism for gene augmentation strategies to treat monogenic IRDs. Currently, most clinical trials for IRDs involve gene augmentation, spanning a broad range of disorders including LCA, achromatopsia, choroideremia, Stargardt disease, and RP [112]. Despite the enthusiasm for gene augmentation therapy, there are several serious challenges, including: 1) delivery effectiveness, 2) variable expression of the transgene, and 3)

waning expression of the transgene over time [113]. These shortcomings have raised concerns regarding the potential of gene augmentation therapy as a truly curative treatment.

The efficacy of gene therapy depends on the effectiveness of the delivery vector to reliably transduce target cells. The most promising vehicle for transgene delivery is the adeno-associated virus (AAV) due to its favorable safety profile, low immunogenicity, and broad tropism [114]. Luxturna is administered *via* a subretinal injection of recombinant AAV serotype 2 (rAAV2) containing a wild-type copy of the *RPE65* gene; the loaded rAAV2 then transduces the *RPE65* transgene into retinal pigment epithelium (RPE) cells (**Figure 1.3B**). Two clinical trials for X-linked retinoschisis (NCT02317887 and NCT02416622) are exploring intravitreal delivery of AAV, which would theoretically allow for a broader region of therapeutic effect and supplant the need for the invasive surgery involved in subretinal injections. However, early clinical data suggest that intravitreal injection of rAAV2 has limited therapeutic benefit, and intravitreal injection of rAAV8 produced ocular inflammation [115,116]. Moreover, Xiong *et al*. recently found that certain AAV promoters are correlated with RPE toxicity; in particular, the cytomegalovirus immediate-early promoter (CMV) and chicken beta actin promoter (CAG), which are the promoters used by Luxturna to drive *RPE65* expression [74].

Due to the ocular inflammation that can result from AAV administration, Luxturna is limited to a small dose that minimizes toxicity and potential efficacy [78]. Moreover, typically only half of the delivered volume is available to transduce the retina, because the subretinal injection forms a bleb which depresses the retina into the vitreous [117]. As a result, Luxturna administration results in delivery to only ~10% of retinal cells [74]. Although *RPE65* is highly expressed in RPE cells and the rAAV2 targets RPE cells, Luxturna also delivers the transgene to some photoreceptors [118]. As *RPE65* was previously shown to be naturally expressed in mammalian cones, but not in rods, there is concern that unnatural expression of *RPE65* in rods may have adverse effects [119].

Moreover, another shortcoming of AAVs is their limited packaging capacity (5 kb). Consequently, gene augmentation therapies seeking to deliver larger cDNA sequences, such as

the *ABCA4* gene (6.8 kb) implicated in some forms of Stargardt disease must utilize other delivery vectors or strategies. In the past, a phase I/II clinical trial (NCT01367444) using a lentiviral vector to deliver the *ABCA4* transgene was terminated due to loss of sponsorship, but a long-term safety study is presently ongoing [120]. However, delivery by lentiviral vectors is not ideal for gene therapy, as it risks insertional mutagenesis of the transgene [121].

Despite evident short-term improvement in visual acuity for Luxturna-treated patients, clinical follow-up studies of these patients for 3 to 6 years after treatment reported diminution of visual sensitivity and unabated advancement of photoreceptor deterioration [73,77,78]. Given the short history of Luxturna use, the reason for continuous retinal degeneration is yet unknown. In 2013, Cideciyan *et al.* published a 3-year follow-up study of patients who received *RPE65* gene augmentation therapy, which showed sustained improvements in visual function, but also progressive retinal atrophy and photoreceptor death [77]. The researchers postulated that biochemical changes in photoreceptors as a result of *RPE65* deficiency place cells into a spectrum of functionally silent pre-apoptotic states, which suggests that advancing retinal generation results from photoreceptors that are already on the verge of cell death [77]. In another 3-year study of *RPE65* gene augmentation patients, Bainbridge *et al.,* reported a decline in retinal sensitivity 12 months after treatment along with uninterrupted retinal degeneration [78]. They also found that maximal retinal sensitivity was only achieved after extended periods of dark adaption, hypothesizing that *RPE65* expression is insufficient to meet the threshold 11-*cis*-retinal supply for normal visual function [78]. Similar visual decline in *RPE65* gene augmentation patients was reported in a 6 year follow up study by *Jacobson et al,* which found that after reaching a peak visual sensitivity 1-3 years after treatment, there was a progressive diminution in retinal sensitivity in parallel with retinal thinning [73]. While it is not known why there is an eventual contraction in visual function, Jacobson and coworkers speculate that many factors contribute: 1) many photoreceptors were already in a pre-apoptotic state at the time of treatment and degenerated shortly after; 2) waning transgene expression due to methylation of the exogenous promoter failed

to meet the physiological requirement; and 3) insufficient transgene expression in RPE cells at the edges of the subretinal bleb, which causes them to degenerate [73]. More recent clinical trials concluded that improved visual acuity is sustained for at least 4 to 7.5 years, but the evidence for eventual relapse provided by the previous studies is especially concerning [122,123]. Nevertheless, the variable durability of transgene expression and episomal persistence that accompany existing gene therapy approaches make gene augmentation a less favorable treatment strategy for inherited diseases.

1.10 Delivery of gene therapies to the eye

At present, several methods for viral and non-viral delivery strategies are being developed for gene therapy and gene editing in the eye (**Figure 1.4**). Lipid nanoparticles (LNPs) are relatively non-immunogenic, highly scalable, and have large delivery capacities capable of encapsulating gene-editor cargos. LNP systems have successfully delivered and expressed Cas9 mRNAs/sgRNA to rodent skeletal muscle and liver tissue [124-127]. In addition, mRNAs encoding ABEs and sgRNA targeting the *PCSK9* gene were delivered *via* LNP to the livers of NHPs in two separate studies [128,129]. Using two different LNP formulations, *PCSK9* expression was significantly knocked down, and researchers were able to achieve on average 66% and 28% A-to-G editing with 0.2% and 0.3% indel frequency, respectively [128,129]. In one study, the induced phenotypic and genomic changes remained stable up to 8 months after treatment [129]. mRNA delivery overcomes the risk of transgene integration present in DNA delivery and often has higher efficiency, as it avoids the necessity of nuclear entry. Also, mRNA-driven gene-editor expression is faster relative to DNA, although the expression is still prolonged. Further, lipofectamine has been shown to deliver Cas9 RNPs and, as previously discussed, ABE RNPs *in vivo* with clinically significant efficiency [79,130]. RNPs are an ideal cargo for genome editing applications, as there is no risk of gene insertion and RNPs typically degrade after 3 days in the RPE [131]. Despite the many advantages of RNP delivery, the large size and negative charge of the RNP-sgRNA makes intracellular delivery cumbersome. Cell-penetrating peptides (CPPs) can also transiently deliver

protein or nucleic acid cargos to the retina with even lower immunogenicity [132-134]. CPPs and gene-editors can potentially be conjugated or expressed as fusion proteins, but CPP-mediated delivery is often achieved through endocytosis, which results in entrapment of the protein cargo in endosomes and subsequent lysosomal degradation [135]. A new strategy to avoid endosomal entrapment was recently developed, which involves the coupling of CPPs to endosomal leakage domains that destabilize endosomal membranes, allowing direct translocation of the gene-editor to the cytosol [136]. Further development of CPP-mediated delivery is exciting due to its favorable safety profile, rapid delivery, and convenient packaging, which circumvents the need to encapsulate the gene-editor cargo in a viral capsid or liposome.

The first genome editing clinical trial, EDIT-101, dosed its first patients with AAV in 2020, and the results of this phase I/II trial will be essential to guide the development of safer high-efficiency modes of delivery to minimize the temporal activity window of gene-editors and the need for invasive surgery. Optimizing therapies for different routes of administration will also ensure sufficient drug delivery to enough target cells. By adopting these strategies, it is possible to broaden the therapeutic range of genome editing and unleash their true potential. The development of genome editing therapies will pave the way for achieving truly innovative, permanent cures for IRD patients.

Table 1. Commonly used and upcoming genome editors.

Editor	*Brief description and mechanism*	*Landmark papers*
Zinc finger nuclease (ZFN)	Zinc finger protein domains recognize 3 bp sequences; multiple zinc fingers are placed in an array and fused with FokI for DNA cleavage.	Kim, Cha, and Chandrasegaran, *PNAS* 1996. "Hybrid restriction enzymes: zinc finger fusions to Fok I cleavage domain."[137]
Transcription factor-like effector nuclease (TALEN)	TALEs recognize 1 bp sequences; multiple TALEs are placed in an array and fused with FokI for DNA cleavage.	Boch *et al*., *Science* 2009. "Breaking the code of DNA binding specificity of TAL-type III effectors."[138]
Clustered regularly interspaced palindromic repeat (CRISPR)	CRISPR-associated system (Cas) proteins are guided to genomic sites by guide RNAs, which utilize a protospacer for targeting. Nuclease domains of Cas proteins can then make single or double stranded DNA breaks in a predictable fashion.	Jinek *et al*., *Science* 2012. "A programmable dual-RNA-guided DNA endonuclease in adaptive bacterial immunity."[13] Cong *et al*., *Science* 2013. "Multiplex genome engineering using CRISPR/Cas systems."[14] Mali *et al., Science* 2013. "RNA-guided human genome engineering via Cas9."[15]
Base editors	A partially inactivated Cas9 nickase is used to guide a fused deaminase to a target site. Deamination of DNA leads to C>G and A>T changes. Other types of nucleotide changes and RNA editing are also possible with base editors.	Komor *et al., Nature* 2016. "Programmable editing of a target base in genomic DNA without double-stranded DNA cleavage."[61] Gaudelli *et al., Nature* 2017. "Programmable base editing of A*T to G*C in genomic DNA without DNA cleavage."[139]
Prime editors	A partially inactivated Cas9 nickase is used to guide a fused reverse transcriptase to a target site. An extended guide RNA encodes a genome binding fragment and a reverse transcriptase template, allowing for the installation of every point mutation and small insertions and deletions.	Anzalone *et al., Nature* 2019. "Search-and-replace genome editing without double-strand breaks or donor DNA."[81]
Click editors	A partially inactivated Cas9 nickase is used to guide a fused DNA polymerase to a target site. A HUH endonuclease is used to tether a DNA, rather than RNA, substrate to the editor. The click DNA template allows for the installation of every point mutation and small	Ferreira da Silva *et al., Nature Biotechnology* 2024. "Click editing enables programmable genome writing using DNA polymerases and HUH endonucleases."[97]

	insertions and deletions. Has yet to be translated *in vivo*.	
CRISPR-associated transposases	Alternative Cas proteins do not have nuclease action. Some of these Cas systems can be used for directed insertion of large sequences in a transposon-like manner, and could be reprogrammed to insert DNA in a site-specific manner. Has yet to be translated *in vivo*.	Strecker *et al., Science* 2019. "RNA-guided DNA insertion with CRISPR-associated transposases."[95] Klompe *et al., Nature* 2019. "Transposon-encoded CRISPR–Cas systems direct RNA-guided DNA integration."[96]
Bridge RNA transposons	Mobile genetic elements, such as DNA and RNA transposons, can insert themselves into genomes. A family of bridge RNAs binds itself to its encoded recombinase and was recently shown to be reprogrammable to insert a cargo sequence in a site-specific manner. Has yet to be translated *in vivo*.	Durrant *et al., Nature* 2024. "Bridge RNAs direct programmable recombination of target and donor DNA."[98] Hiraizumi *et al., Nature* 2024. "Structural mechanism of bridge RNA-guided recombination."[99]

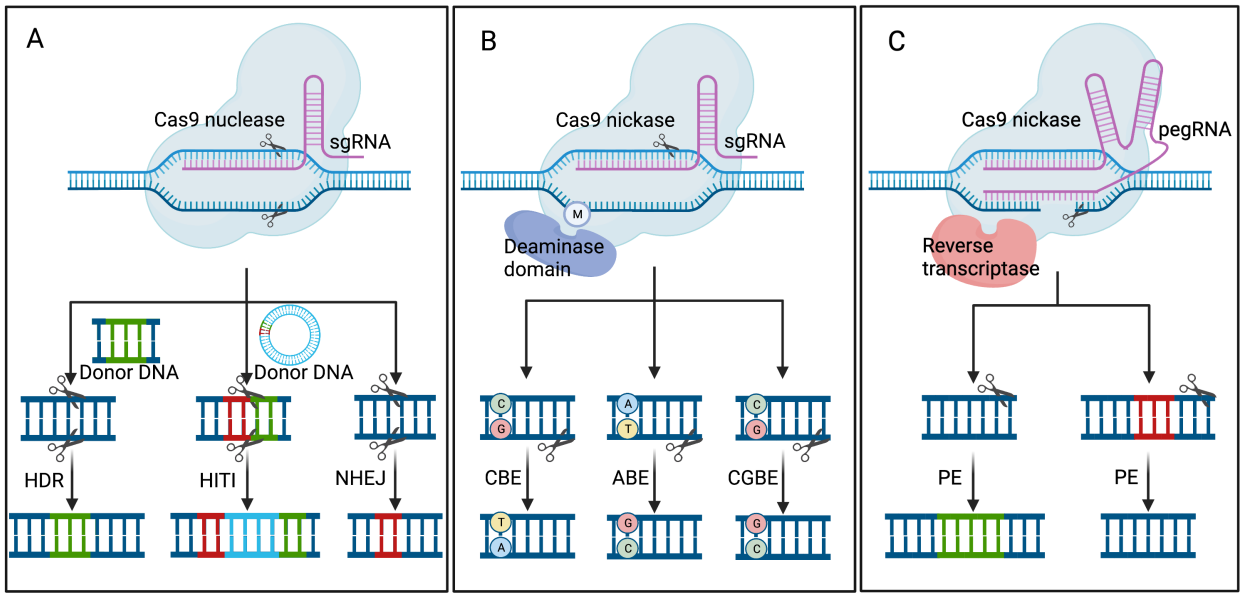


Figure 1.1. Summary of common CRISPR/Cas9-based genome editing strategies. (A) CRISPR/Cas9 nuclease treatment uses a single guide RNA (sgRNA) to direct a Cas9 nuclease to a selected site in the genome. Cas9 then induces a double-stranded DNA break, which the cell repairs *via* two dominant mechanisms, homology-directed repair (HDR) and non-homologous end joining (NHEJ). HDR is commonly employed to edit DNA through donor DNA incorporation, and NHEJ is often used to knockout gene expression. Another reported strategy to incorporate a transgene using Cas9 nuclease is homology-independent targeted integration (HITI). (B) Base editing utilizes a sgRNA and Cas9 to target specific sites in the genome, but the Cas9 is mutated to cleave only the targeted strand (Cas9 nickase). The fused deaminase domain deaminates target bases on the non-target strand, and cellular repair machinery finishes the conversion. Cytosine base editors (CBEs, left) convert cytosines to thymines, adenine base editors (ABEs, center) convert adenines to guanines, and cytosine to guanine base editors (CGBEs, right) convert cytosines to guanines. (C) Prime editing also utilizes a Cas9 nickase, but the sgRNA is further modified into a prime editing guide RNA (pegRNA) that binds to the cleaved strand and provides a template encoding the desired edit. Instead of a fused deaminase domain, a reverse transcriptase is fused to Cas9 nickase, and reverse transcribes the pegRNA; the created DNA

flap is either ligated into the genome for successful editing or excised when editing is unsuccessful. Prime editing can notably be used to correct all point mutations, insert DNA (left, green), or remove DNA (right, red). Figure generated in part in Biorender.

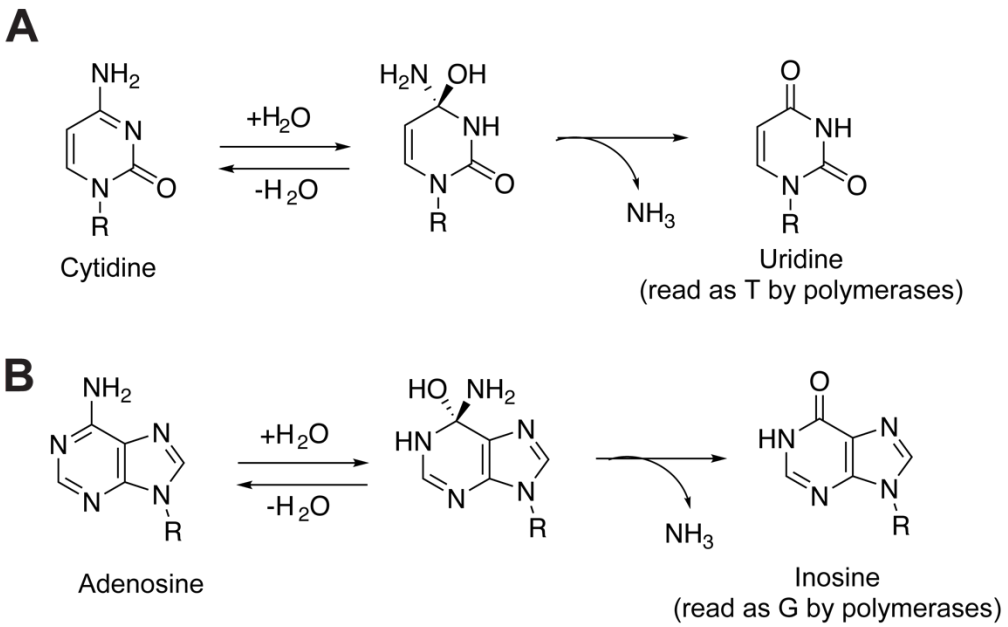


Figure 1.2 DNA deamination reaction mechanism. (A) Deamination of cytidine to uridine by cytosine base editors. (B) Deamination of adenosine to inosine by adenine base editors.

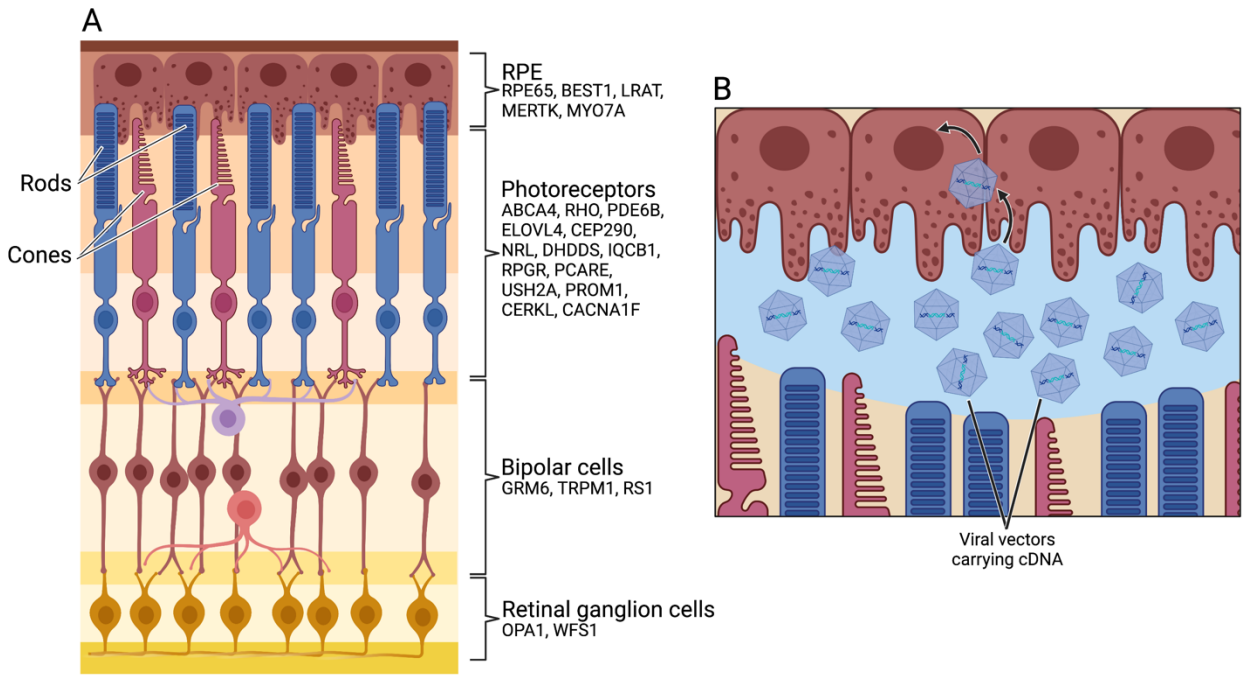


Figure 1.3 Selected mutations in the eye that lead to inherited retinal diseases targetable by gene augmentation. The retinal pigment epithelium (RPE) and neural retina compose numerous cell types that support image-forming vision. (A) Selected cell types and inherited mutations in cell-specific genes that lead to inherited retinal diseases (IRDs) are highlighted here. Numerous mutations have been identified in the RPE, rod and cone photoreceptors, bipolar cells, and retinal ganglion cells. Furthermore, different mutations in the same gene can lead to different IRDs (e.g. *RPE65* mutations lead to either Leber congenital amaurosis or retinitis pigmentosa). (B) Gene augmentation for inherited retinal diseases is performed by the delivery of wildtype gene cDNA delivered to the target cell *via* administration of a viral vector. Figure generated in part in Biorender.

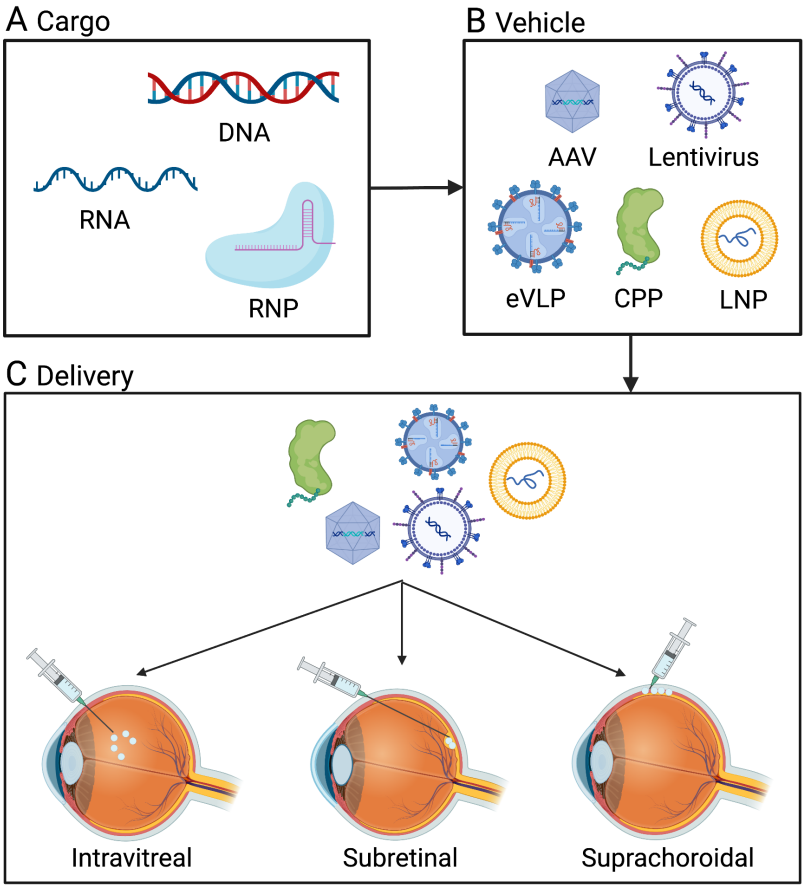


Figure 1.4 Precision genome editing formulation and delivery. (A) Cas9 nucleases, base editors, and prime editors can be delivered as DNA in the form of plasmids or viral genomes, synthetic mRNA and sgRNA, or ribonucleoproteins (RNPs), composed of Cas9 protein precomplexed with an sgRNA. (B) Depending on the formulation, different delivery vehicles for genome editing cargos can be considered. These include adeno-associated viruses (AAVs) and lentiviruses (LVs) for DNA delivery, engineered virus-like particles (eVLP) and cell-penetrating peptides (CPPs) for RNP delivery, and lipid nanoparticles (LNPs) for mRNA delivery, among others. (C) Depending on the formulation and vehicle, different routes of administration can be considered. For instance, AAV capsids which have been reported to transduce the outer retina from an intravitreal injection can be injected intravitreally, while other delivery modalities would likely be injected subretinally. Alternatively, treatments which target the RPE or choroid could be injected suprachoroidally. Figure generated in part in Biorender.

CHAPTER 2

In vivo base editing in the rhodopsin E150K retinitis pigmentosa mouse

This chapter is derived in part from the following manuscript published in *Proceedings of the National Academy of Sciences:*

Du, S. W. *et al*. In vivo photoreceptor base editing ameliorates rhodopsin-E150K autosomal-recessive retinitis pigmentosa in mice. *Proceedings of the National Academy of Sciences* 121, e2416827121 (2024).

© 2024 the Authors.

CHAPTER 2

In vivo base editing in the rhodopsin E150K retinitis pigmentosa mouse[140]

2.1 Introduction

Image-forming vision depends on inputs from the light-sensitive neurons called rod and cone photoreceptors, which sense dim and bright light, respectively [141]. Photoreceptors, in turn, depend on light-sensitive proteins known as opsins located in their outer segments to capture and transduce photons of light. The rod opsin, known as rhodopsin, was discovered by Böll in 1876, subsequently determined to be a G-protein coupled receptor (GPCR), and the first GPCR crystallized and structurally solved [142-144]. Comprised of seven transmembrane domains, rhodopsin binds the chromophore 11-*cis*-retinal through a protonated Schiff-base linkage to the Lys^{296} residue [145]; upon stimulation by a photon, the 11-*cis*-retinal photoisomerizes to all-*trans*-retinal, thus inducing a conformational change and propagating the signal [146] .

Rhodopsin is not only a sensory protein but also plays a major structural role in the rod photoreceptor. Rods utilize a modified primary cilium, termed the rod outer segment (ROS), in which the phototransduction proteins are assembled [147,148]. Depending on the species, the ROS is composed of varying numbers of separate layered and regularly spaced membranous discs within its plasma membrane; for example, mouse ROS have around 800 discs, while amphibians have much larger rods with a corresponding increase in ROS disc number. Rhodopsin, at an approximate concentration of 3-5 mM, is the most abundant protein within the ROS disc, representing over 90% of the protein content and 50% of the ROS surface area [149]. In mice, each disc contains approximately 8×10^4 rhodopsin molecules, totaling ~4×10^{14} molecules per eye (~650 pmol/eye) [150,151]. Within the disc, rhodopsin has been shown to form dimers and higher order multimers and is essential for overall ROS morphogenesis[152-154]. Thus, *Rho*$^{-/-}$ mice do not form the ROS and undergo rod degeneration, while *Rho*$^{+/-}$ mice exhibit ROS which have ~60% of

the volume of ROS in *Rho*$^{+/+}$ mice [151]. Rhodopsin is also rapidly turned over, as the entire ROS in each rod is phagocytosed and completely replaced roughly every ten days in rodents [155,156], and at a similar frequency in primates [157]. Accordingly, sustained high expression of rhodopsin is critical for maintaining the structure and function of the ROS.

The first genetic mutation linked to retinitis pigmentosa (RP) was the P23H-rhodopsin mutation, causative for autosomal dominant RP (adRP) [158]. This mutation is responsible for a substantial number of adRP cases, accounting for roughly 40% of *RHO*-associated adRP in the United States, and it is one of the best-characterized rhodopsin mutants [159,160]. Subsequently, over 150 adRP-causing mutations have been identified. Collectively, these mutant rhodopsins impact fundamental cellular processes such as Golgi trafficking, outer segment targeting, protein folding and endoplasmic reticulum stress, as well as vision-specific processes such as constitutive phototransduction activity and activation of rhodopsin's cognate G protein, transducin [101,161]. Notably, there are fewer rhodopsin mutants that are linked to autosomal recessive RP (arRP), including two nonsense mutants (W161X and E249X), and two missense mutants (E150K and M253I) [161]. In each of these cases, heterozygous carriers of the respective mutations appear to be mostly normal with little or no visual deficits. The relative abundance of adRP mutations compared to arRP mutations suggests that rhodopsin is highly sensitive to mutation, and mutations in rhodopsin tend to be pathogenic.

No treatments are currently available for *RHO*-associated RP. As *RHO* mutations are responsible for a large proportion of inherited retinal diseases, there has been great interest in developing genetic therapies for halting or reversing rhodopsin-mediated degeneration. These approaches include gene-replacement therapy, although this approach proves to be a particular challenge with dominant mutations, as simple augmentation of the wild-type gene will not suppress the dominant-negative allele [162]. An alternative approach is the use of gene editing to correct the mutation *in vivo*, though correction of a dominant allele may still require close to 100% efficiency to prevent cell loss [105]. Another gene-editing approach called "knockout and replace"

utilizes AAVs to disrupt both wild-type and mutant genomic *Rho* alleles and simultaneously provide a replacement wild-type *Rho* cDNA. Multiple approaches can achieve this goal, either by using a short hairpin RNA (shRNA) to knock down *Rho*, CRISPR/Cas9 to disrupt endogenous *Rho,* an allele specific knockdown approach, or by using CRISPR/Cas13 to knock down mutant alleles by RNA editing [163-166]. While this approach is mutation-independent, substantial challenges include efficacy of knockout, stoichiometry, and control of *Rho* expression, which is toxic if overexpressed, or potentially ineffective if underexpressed. Additionally, the use of nucleases that function by creating double-strand DNA breaks (DSBs) results in highly heterogeneous mixtures of potentially toxic indel outcomes [167], AAV integration into the genome [168-170], chromosomal abnormalities, and other undesired cellular consequences of DSBs. Lastly, disruption of one or both alleles responsible for recessive diseases is unlikely to result in significant therapeutic benefit.

In a seminal pair of papers, Suh and Choi and colleagues utilized a lentiviral vector to deliver ABE to the RPE, correcting a nonsense mutation in *Rpe65*[80,171]. Other studies that used base editing to correct genes involved in RPE or photoreceptors in mice often used dual-AAVs to target genes such as *Rpe65*[172], *Pde6a*[173], *Pde6b*[174,175], and *Abca4*[176]. The majority of other nonviral approaches deliver RNPs of base editors[177-179]. A notable nonviral approach used silica nanocapsules to deliver ABE8e mRNA to correct a W53X mutation in *Kcnj13*[180].

To study gene-editing strategies for the treatment of arRP, we used the *Rho*-E150K knock-in mouse model of arRP [181]. This rare rhodopsin mutation was reported to cause arRP in three families [182-185]. Knock-in *Rho*-E150K mice were generated to study the mechanisms of rhodopsin-mediated retinal degeneration in an autosomal recessive manner, though it was noted that in contrast to human patients, the heterozygous mouse exhibited a mild and delayed retinal degeneration [181]. However, we reasoned that in an autosomal recessive disease such as E150K-arRP, therapeutic rescue could be achieved from reasonably efficient editing, and that in a clinical

setting, correction of a subset of rod photoreceptors should arrest the progression of retinal degeneration and provide some benefit to patients.

In this study, we employed CRISPR/Cas9-derived precision base editing strategies [186] to correct the rhodopsin-E150K mutation *in vivo* without requiring double-stranded DNA breaks. Because of bystander editing near the target adenine, we expressed and biochemically characterized all the bystander-edited rhodopsin protein variants. We then demonstrated efficient editing *in vivo*; however, partial electrophysiological rescue of retinal function was achieved when mice were treated at post-natal day 15 but not at later time points due to progressive retinal degeneration. Histology of treated eyes revealed that *in vivo* base editing arrested photoreceptor degeneration and preserved rhodopsin expression. In contrast to vision-associated enzymes such as *Rpe65* [80] and *Pde6b* [174], our results suggest that restoration of visual function and retinal structure by gene editing is more challenging for proteins such as rhodopsin that serve both signaling and structural functions. Nevertheless, with careful application and optimization, including treatment timing, gene editing approaches hold promise as future treatment approaches for *RHO*-associated RP.

2.2 RESULTS

2.2.1 Development of an adenine base-editing strategy for Rho-E150K

Rhodopsin is a key structural and sensory protein within the rod photoreceptor. The majority of rhodopsin protein is found within the rod outer segment (ROS) (**Figure 1A**). Mutations within rhodopsin are linked to several inherited retinal degenerations. Previously, we generated and characterized a mouse model for Rho-E150K autosomal-recessive retinitis pigmentosa [181]. A single-nucleotide G>A mutation results in the change of Glu^{150} to Lys^{150} on the intracellular side of transmembrane helix IV of the protein (c.448G>A, p.E150K) (**Figure 1A**). This G>A mutation could be addressed by CRISPR/Cas9-derived adenine base editing (ABE) to revert Lys^{150} to the wild-type Glu^{150} (**Figure 1B**). Accordingly, we screened three single-guide RNAs (sgRNAs), placing the target mutated adenine at position 5, 6, or 7 in the protospacer within the activity

window of ABEmax (sgRNA A5, A6, and A7, respectively) (**Figure 1C**). To facilitate screening of ABE strategies to correct the Rho-E150K variant, we created a HEK293T cell line which carries a fragment of *Rho* DNA, termed HEK-E150K (**Figure 1D**). When we co-transfected wild-type *Streptococcus pyogenes* Cas9-ABEmax and the A5, A6, and A7 sgRNAs, we noted that only A5 resulted in productive editing, with an average of 12% total editing of the on-target base (on-target plus bystander) and 9.0% precise correction (on-target single-base editing only) (**Figure 1E**). We also investigated the use of alternative ABE variants, such as ABE8e, SpRY-ABEmax and SpRY-ABE8e, along with alternative sgRNAs that placed the target adenine at positions 5, 7, 9, 10, and 11 in the protospacer, but none of these combinations matched the precision or efficiency of ABEmax in combination with the A5 sgRNA (**Figure 1F, Figure S1**).

2.2.2 Expression and characterization of Rho *base-editing variants*

Our ABE strategy revealed that in addition to target base editing by ABEmax, additional editing outcomes arose from bystander editing of other adenines besides the target adenine within the activity window of ABEmax. The resulting bystander-mutated rhodopsins might lead to altered retinal function (**Figure 2A**). Therefore, we generated mammalian expression vectors of wild-type rhodopsin, E150K rhodopsin, and eight other rhodopsin variants that were observed as editing byproducts in the *in vitro* editing transfection experiments, and expressed them in HEK293T cell culture (**Figure 2A, B**). When the ten rhodopsins were reconstituted with 11-*cis*-retinal and purified, the UV-vis absorbance spectra of all ten exhibited rhodopsin's characteristic λ_{max} at 500 nm, indicating successful reconstitution of the rhodopsin with its chromophore (**Figure 2C**). We also assessed the ability of the photoactivated rhodopsin to activate transducin ($G_{t\alpha}$) with a fluorescence assay that measures the increase of intrinsic fluorescence of tryptophan (Trp) in $G_{t\alpha}$ upon binding of GTPγS. The kinetic data are represented in **Figure 2D** for mRho WT and for the most frequent mutant E150K, and the rate constant for WT is compared with those for all nine mutants in **Supplementary Table 3**. The results suggest that all of the mutants characterized are

functional and able to activate transducin in a manner similar to that of WT mRho, consistent with previously reported measures of E150K and WT mRho [187]. Lastly, we characterized and confirmed the identities of the rhodopsin variants by tandem mass spectrometry (MS/MS) (**Figure 2E, Figure S2**).

2.2.3 Development of a prime editing strategy for Rho-E150K

Our *in vitro* biochemical characterization of the bystander-edited rhodopsin variants indicated that bystander editing would not affect reconstitution with visual chromophore or G-protein signaling. If behavior of these mutant rhodopsins were different *in vivo*, a more precise editing strategy that avoids bystander editing would be required. Accordingly, we developed a prime editing (PE) strategy to correct the E150K mutation. We first chose to screen prime editing guide RNAs (pegRNAs) and nicking-guide RNAs (ngRNAs) with PE-SpRY, as previously demonstrated in a *Pde6b* PE strategy [188]. We screened 14 pegRNAs targeting spacers around the intended editing site, with a 13-nucleotide primer-binding sequence (PBS) and a 13-nucleotide reverse-transcriptase template, along with 6 ngRNAs. Our editing outcomes *in vitro* indicated that several combinations of pegRNA and ngRNA resulted in precise correction (**Figure S3A**). We opted to further optimize pegRNA-5 in combination with ngRNA-4. We determined that a RTT length of 13 nucleotides and a PBS length of 12 nucleotides was optimal for maximizing editing (**Figure S3B, C**). However, because evolved Cas9 variants can suffer from decreased efficiency compared to wild-type Cas9, we also investigated the use of PEmax with a wild-type Cas9. We used a machine-learning tool (PRIDICT) [189] to design a pegRNA and noted that editing efficiency with PEmax was substantially higher with the PRIDICT pegRNA compared to the PE-SpRY editor with optimized p5, both with and without ngRNA-4: PE-SpRY reached 10.4% editing without ngRNA-4 and 16.4% editing with ngRNA-4, PEmax achieved 13.6% editing without ngRNA-4 and 20.8% editing with ngRNA-4 (**Figure S3D**). PEmax editing also resulted in lower indel formation than PE-SpRY in combination with ngRNA-4, with indel rates of 3.1% versus 6.4%, respectively

(**Figure S3D**). While more recent developments in prime editing systems would likely increase the efficiency of PE outcomes and enable *in vivo* PE, including a dual-AAV system to deliver PEmax that was developed after the *in vitro* and *in vivo* BE studies described here [84-86,88,190], given the high efficiency of base editing and the data above suggesting that the observed *RHO* bystander base editing outcomes did not abrogate rhodopsin function, we advanced our base editing strategy into studies *in vivo*.

2.2.4 Base editing of rhodopsin in arRP mice

As demonstrated in other studies targeting photoreceptors, we generated dual-AAV vectors that each encoded part of ABEmax fused to N- and C-terminal inteins to mediate restoration of full-length base editor after dual transduction [191]. We produced two AAV vectors with Cbh promoters driving N-terminal ABEmax on one genome and C-terminal ABEmax on a separate genome, which also contains a U6 sgRNA expression cassette (**Figure 3A**). These genomes were then packaged into AAV2/8 viral vectors. To perform base editing *in vivo*, we injected a 1:1 mix of the dual AAV8s subretinally into homozygous Rho-E150K mice at post-natal day 21 and assessed electroretinography (ERG) and sequencing data 10 weeks post-injection (**Figure 3A**). We reasoned that this post-treatment period would allow sufficient time for AAV expression, editing, and assessment of phenotypic rescue. At 10 weeks post-injection, we collected neural retinas from dual-AAV8-treated animals. Along with genomic DNA, we also collected RNA from the retinas. As there are over 100 other cell types found within the retina, but *Rho* is expressed only within rod photoreceptors, analysis of both genomic DNA and complementary DNA (cDNA) synthesized from RNA enabled us to assess editing outcomes in our cell type of interest [192]. In the genomic DNA, we noted an average of 10.5% total editing at the on-target base, with an average of 4.6% precise single-base correction, and a maximal precise correction rate of 11.4% (**Figure 3B**). In the cDNA, the average of total editing of the on-target base was 18.2%, with an average of 11.9% precise correction, and a maximum precise correction rate of 44.2% (**Figure**

3C). However, we did not notice a phenotypic rescue of the ERG a-wave, attributable to photoreceptor activation, as ERG a-wave amplitudes were lower in dual AAV8 treated animals compared to a phosphate-buffered saline-injected control (**Figure 3D**). Lastly, to assess off-target effects of ABEmax, we performed CIRCLE-seq analysis [193] of retinas from treated and untreated Rho-E150K mice. We noted no difference in indels or A>G base editing within the activity window, or indels at the top ten nominated sites (**Figure 3E, F**).

In conjunction with our biochemical characterization of rhodopsins, we had hypothesized that our editing rates would have been sufficient to rescue the degeneration phenotype. We reasoned that the incomplete phenotypic rescue could be due to a delay in the timing of editing relative to what would be required for functional rescue. We previously reported that untreated homozygous E150K mice had already lost >20% of their photoreceptors at post-natal day 30, and two-month-old homozygous E150K mice were >60% degenerated [181]. Therefore, we next treated homozygous Rho-E150K mice 6 days earlier at post-natal day 15 with the same dual AAV8 strategy (**Figure 4A**). 10 weeks post-injection, we noted a trend toward rescue of the ERG a- and b-wave phenotypes with higher amplitudes recorded from dual-AAV8 treated mice compared to untreated controls (**Figure 4B**). Therefore, we remeasured ERG amplitudes at 14 weeks post-injection, at which untreated homozygous mice have lost nearly all photoreceptors and ERG responses, while a rescue of the phenotype would result in preservation of the ERG wave [181]. As we predicted, the treated animals retained some of the ERG a- and b-wave, while the untreated animals continued to degenerate (**Figure 4C, D**). To examine the anatomical rescue of the retinas, we assessed eyes from dual AAV8 treated mice and untreated controls along the superior-inferior axis to measure the outer nuclear layer (ONL) where the photoreceptor nuclei reside (**Figure 4E**). As the gene-editing therapy may not evenly treat the entire retina, we evaluated the entire retina and quantified the number of photoreceptor nuclei at the thickest and thinnest points of each retina. We discovered that treatment with dual AAV8 led to preservation of the ONL, with a greater number of photoreceptor nuclei per column in the thickest part of each retina, whereas the thinnest

part of the retina, likely untreated by dual AAV8, did not show a difference in the photoreceptor-nuclei count (**Figure 4F**).

To confirm that we restored rhodopsin expression in dual AAV8-treated mice, we performed immunohistochemistry on WT mice, untreated E150K mice, and E150K mice treated with dual AAV8 at P15. Staining with DAPI and 1D4 revealed robust rhodopsin expression in the outer segment of retinas from WT mice that was absent in the retinas from untreated E150K mice, while dual AAV8 treatment restored rhodopsin expression in the retinas of treated E150K mice (**Figure 5A**). Correlating with the expression of rhodopsin, retinas from untreated E150K mice only exhibited one single column of ONL nuclei, while retinas from treated E150K mice exhibited multiple ONL nuclei per column.

2.3 Discussion

In this report, we provide evidence that genetic mutations in rhodopsin can be corrected to provide modest therapeutic benefit in a mouse model of retinitis pigmentosa. We also demonstrate two precision-editing approaches, adenine base-editing and prime-editing. Many previous studies on precision editing in the mouse retina focused on correction of mutations which affect enzymes, including *Rpe65* [80] and *Pde6b* [188], which catalyze biochemical reactions critical for light detection and phototransduction. To our knowledge, fewer studies have focused on proteins that provide structural support to photoreceptors, such as *Cep290* [194]; fewer still have investigated proteins such as rhodopsin which provide both structural and signaling properties to the cell. Our study highlights both the promise and potential challenge in reaching a therapeutic threshold for rhodopsin and other structural and signaling proteins in photoreceptors and other cell types.

We showed that rhodopsin could be edited productively, with a maximum of 44% transcript editing. Treatment of E150K mice with dual AAV8 at post-natal day 15 was able to rescue the ERG photoresponse compared to untreated E150K mice, which did not show the a- or b-waves

in response to photostimulation. The dual AAV8 treatment also prevented the complete loss of photoreceptor nuclei in the ONL. In the untreated animals, the remaining cells in the ONL did not express rhodopsin; thus, likely they are residual cone photoreceptors. Cone photoreceptors have been shown to persist in patients with RP and mouse models of RP after the death of rod photoreceptors, though the surviving cone bodies are often dysfunctional and eventually die [195,196]. As rod photoreceptors support the survival of cone photoreceptors, which mediate high-acuity daytime vision, the rescue of rod photoreceptors is expected also to improve cone function and maintain vision for RP patients. While we did observe a preserved ERG response in the treated animals, the amplitudes were modest compared to wild type. This is likely due to the fact that the rescue was uneven across the retina, which some areas of treated retinas demonstrating strong rescue, while other areas of treated retinas showing no rescue (**Figure 4F**). Further optimization of dosing and surgical technique could increase the total rescued area in mice or in patients.

Based on the known volume and concentration of rhodopsin within the ROS, it is possible to calculate the number of rhodopsin molecules per rod photoreceptor, which is approximately 6.4 x 10^7 [151,197,198]. In the mammalian retina, roughly 10% of the ROS is turned over every day; thus, 10% of the rhodopsin content must be replaced every day. As each molecule of mRNA, on average, creates between 2,800 and 4,200 protein molecules [199,200], each rod photoreceptor generates roughly 3,400 to 5,000 molecules of *Rho* mRNA per day, or at least one *Rho* mRNA molecule every 25 seconds; thus, for a mouse retina with 6.4 million rods, about 250,000 mRNA molecules are generated every second. An alternative approach to estimating the rhodopsin concentration in the eye is by analysis of its chromophore, 11-*cis*-retinal, which in a dark-adapted mouse retina amounts to at least 500 pmol, nearly all bound to rhodopsin stoichiometrically [201,202]. This calculation estimates at least 3 x 10^{14} rhodopsin molecules, within a factor of three of our calculation above [(1.4 x 10^8 per rod) X (6.4 X 10^6 rods) = 9 x 10^{14} Rho molecules] [151,203]. These estimates indicate that the phenotypic changes observed are a result of significant alterations of

Rho transcript and protein production that persists post-treatment. Indeed, as heterozygous *E150K-Rho* mice exhibit altered ROS morphology, ROS number, and phototransduction kinetics, alterations in *Rho* expression can lead to dramatic changes in visual physiology [151]. Edited genomic DNA would be expected to provide sufficient wild-type rhodopsin within two weeks of successful editing, though we only noted significant phenotypic rescue after treatment at post-natal day 15 and not at post-natal day 21. This timing difference may be due to the kinetics of ABE expression. AAV8 has been shown to express as soon as 7 days post-injection, though maximal expression of the cargo occurs around 30 days post-injection [204]. In animal models and patients where degeneration begins early and progresses quickly, the kinetics of gene editor delivery and treatment may play a crucial role. Thus, earlier diagnosis and treatment could be critical for therapeutic benefit where the degeneration and structural loss is relatively rapid.

Knowledge of the mechanisms of retinal degeneration in E150K-associated arRP and other forms of arRP remains limited. It has been hypothesized that the E150K mutation impacts protein trafficking and higher-order oligomerization of rhodopsin in the outer segment, and we reasoned that non-productive or bystander editing could still disrupt ROS organization; however, our biochemical characterization of bystander-edited rhodopsin variants showed that they remained functional, so elimination of the E150K mutation by on-target or bystander editing could restore proper dimerization. It is also possible that the bystander-edited mutants were unable to traffic correctly to the plasma membrane due to a disruption of electrostatics that need to be compensated, similarly to the E150K variant previously characterized *in vitro* [205]. With the exception of the A6 bystander edit (Lys^{150} to Arg^{150}), productive or bystander editing results in the removal of the positive charge on Lys^{150}. This could be sufficient to prevent degeneration in the E150K mouse, as we had previously proposed that Lys^{150} disrupts higher-order packing and multimerization in the mouse ROS [181]. Thus, future *in vivo* studies utilizing the PE approach proposed here could result in therapeutic benefit to eliminate the possibility of bystander editing causing *de novo* or unarrested degeneration (**Supplemental Figure 3**). Though heterozygous

carriers of *Rho*-E150K did not exhibit any retinal abnormalities, homozygous mice exhibited delayed retinal degeneration [181]. This delayed degeneration could result from differences in the physiology and structure of the mouse proteins and cells and may indicate that a greater fraction of accurate-editing outcomes may be required to rescue the homozygous-mouse Rho-E150K phenotype relative to the threshold potentially required for humans.

The *RHO*-E150K and other mutations are individually rare, so it may be difficult to bring a candidate therapy through clinical trials and approval. Subsequent to this work, another study reported *in vivo* base editing of *Rho* for the Q344ter and T17M mutations, though these are also rare mutations[206]. Accordingly, innovative mutation-agnostic editing strategies using a combination of complementary therapies that extend the therapeutic window, as demonstrated for other gene-editing strategies [94,207], or a simplified regulatory framework [208], could be critical to provide RP patients with a molecularly targeted therapy.

2.4 Methods

Animals

Rho-E150K knock-in animals were previously described (32). The animals were housed at the University of California, Irvine, where they were maintained on an unrestricted regular diet and a 12 h light/12 h dark cycle. Mouse experiments were approved by the Institutional Animal Care and Use Committee of the University of California, Irvine, were performed in accordance with the NIH Guidelines for the Care and Use of Laboratory Animals, and with the ARVO Statement for the Use of Animals in Ophthalmic and Visual Research.

Expression and purification of mRho variants

To express mRho variants, HEK293T/17 cells were seeded into 15-cm tissue-culture dishes the day before transfection. 20 µg of plasmid was transfected into cells *via* PEI max (3:1 ratio PEI:plasmid complexed in OptiMEM, Polysciences #24765-100). 48 h post-transfection, cells were collected by trypsinization and pelleted for protein purification.

Cells expressing rhodopsin mutants were subjected to hypotonic shock with 10 mM HEPES pH 7.5 plus protease inhibitor cocktail (Roche), 1 mM $MgCl_2$ and benzonase. After centrifugation, the pellet was resuspended in 10 mM HEPES pH 7.5, 0.25 M NaCl plus protease inhibitor cocktail (Roche), 1 mM $MgCl_2$ and benzonase. Then, each sample was incubated in the dark with 90 μM of 11-*cis*-retinal for 15 min at room temperature. Next, the membranes were solubilized in 6 mM LMNG for 2 h at 4 °C and centrifuged at 21,000 x g for 20 min. Then, rhodopsin in the supernatant was immunopurified using immobilized 1D4 antibody as previously described (67, 68). In brief, solubilized membranes were incubated for 2 h with the 1D4-Sepharose, and then the medium was washed with 40 column volumes of washing buffer (0.2 mM LMNG in 20 mM HEPES, pH 7.4, 0.15 M NaCl). The rhodopsin mutants were then eluted by competition with 1 mg/mL peptide TETSQVAPA in washing buffer.

G_t activation assay

Activation of G_t was assessed by the increase in intrinsic tryptophan fluorescence upon nucleotide exchange catalyzed by photoactivated Rho. G_t was extracted from frozen bovine ROS membranes as described elsewhere (69, 70). The time course of intrinsic-fluorescence change from $G_{t\alpha}$ was measured with an L55 luminescence spectrophotometer (PerkinElmer Life Sciences) operating at excitation and emission wavelengths of 300 and 345 nm, respectively. Rhodopsin (25 nM) was mixed with G_t (500 nM) in 20 mM BTP pH 7.0, 120 mM NaCl, 2 mM $MgCl_2$, 0.5 mM LMNG. Then, rhodopsin was photoactivated for 30 sec with 505-nm fiber light (625 μW) and the fluorescence emission was measured for 5 min. This was followed by the addition of 5 μM GTPγS to induce Rho/G_t complex dissociation and increase in $G_{t\alpha}$ fluorescence. The pseudo first-order rate constants (k) of G_t activation were determined from the first 1500 s of the assay.

***In vitro* plasmid transfection and cell culture genomic DNA isolation**

The day before transfection, HEK-E150K cells were seeded into 48- or 96-well plates to achieve ~70% confluency on the day of transfection. Plasmids were transfected with Lipofectamine 3000 (Thermo #L3000001) according to manufacturer instructions. 48 h post-

transfection, cells were lysed as previously described (71). Briefly, culture medium was removed and the cells were incubated in lysis buffer (10 mM pH 8 Tris-HCl, 0.05% SDS, 1:1,000 proteinase K (NEB #P8107S)) at 37 ºC for 1 h. Then, the proteinase K was inactivated by incubation at 80 ºC for 30 min. Crude lysates were stored at -20 ºC.

AAV preparation

AAV2 genomes were generated as previously described (48) and propagated in Stbl3 *E. coli* (Thermo #C737303). AAVs were packaged by SignaGen Laboratories (Frederick, MD) into AAV8 capsids at a final titer of 1.53×10^{13} genome copies (GC) mL^{-1} (N-terminus) and 1.72×10^{13} GC mL^{-1} (C-terminus). AAVs were mixed at a 1:1 particle ratio and stored at -80 ºC until injection. Mixed AAVs were injected in a 1 µl solution, containing 7.65×10^{9} total GC each of N- and C-terminus AAVs.

Subretinal injections

Mice were bilaterally dilated, first with topical administration of 1% tropicamide ophthalmic solution (Akorn, 17478-102-12), followed by 10% phenylephrine ophthalmic solution (MWI Animal Health, 054243). Mice were then anesthetized by intraperitoneal administration of 20 mg ml^{-1} ketamine and 1.60 mg ml^{-1} xylazine in PBS at a dose of 100 mg kg^{-1} of ketamine and 8 mg kg^{-1} of xylazine. To maintain corneal hydration, a drop of GenTeal Severe Lubricant Eye Gel was applied (0.3% Hypromellose, Alcon). Subretinal injections were performed under an ophthalmic surgical microscope (Zeiss). Using a 27G beveled needle, an incision was made in the cornea proximal to the limbus at the nasal side. A 34G needle with a blunt tip (World Precision Instruments, NF34BL-2), connected to an Nanofil injection holder (World Precision Instruments, NFINHLD) with SilFlex tubing (World Precision Instruments, SILFLEX-2), was inserted through the corneal incision into the anterior chamber and advanced into the subretinal space without touching the lens. Each mouse received a 1 µl injection in each eye at 70 nl s^{-1}, controlled by a UMP3 UltraMicroPump (World Precision Instruments, UMP3-4). After surgery, the mice were placed on a heating pad and anesthesia was reversed with intraperitoneal 2.5 mg kg^{-1} atipamezole

in PBS , (MWI Animal Health, #032800). Triple antibiotic ophthalmic ointment (neomycin, polymyxin, and bacitracin) was administered to the cornea to promote recovery.

Electroretinography (ERG)

Prior to ERG recording, mice were dark adapted overnight. Under a safety light, mice were bilaterally dilated, first with topical administration of 1% tropicamide ophthalmic solution (Akorn, 17478-102-12), followed by 10% phenylephrine ophthalmic solution (MWI Animal Health, 054243). Mice were then anesthetized by isoflurane inhalation. To maintain corneal hydration, a drop of GenTeal Severe Lubricant Eye Gel was applied (0.3% Hypromellose, Alcon). The mouse was placed on a Diagnosys Celeris rodent-ERG device preheated to 37 ºC (Diagnosys LCC, Lowell, MA, USA). Ocular stimulator and recording electrodes were placed to cover the corneas, a reference electrode was placed subdermally between the ears, and a ground electrode was positioned subdermally in the left rear thigh. The mice were stimulated with 544 nm light at an intensity of -0.3 log (cd s m^{-2}) (160 nm bandwidth). Voltage recordings for 10 repeated stimuli, with 10 s between each stimulus, were combined to form the averaged ERG waveform in Espion V6 software (Diagnosys LLC). A- and b-wave amplitudes and annotations were verified before analysis.

Retina dissociation and genomic DNA and total RNA isolation

Mouse eyes were dissected under a light microscope to remove the anterior segment. Then retina was then separated from the RPE, choroid, sclera. Each retina was immediately immersed in RLT-Plus (Qiagen), disrupted with a motorized pestle (Fisher #12-141-361), and then homogenized in a QiaShredder (Qiagen # 79656). The lysate was then processed for genomic DNA and RNA with the AllPrep DNA/RNA Micro kit according to manufacturer instructions (Qiagen #80284).

Next-generation sequencing

Complementary DNA (cDNA) was synthesized from RNA with the SuperScript III First-Strand Synthesis SuperMix (Thermo Fisher #18080400), according to manufacturer's instructions. 0.5 – 1 µl of the isolated genomic DNA or cDNA was used as input for the first of two PCR reactions (PCR1). Genomic loci were amplified in PCR1, using Phusion Plus polymerase (Thermo Fisher Scientific F631S). PCR1 primers for genomic loci are listed in **Supplemental Table 1**. PCR1 was performed as follows: 98 °C for 30 sec; 30 cycles at 98 °C for 10 sec, 60 °C for 20 sec, and 72 °C for 30 sec; 72 °C for 5 min. PCR1 products were confirmed on a 1% agarose gel. One microliter of PCR1 was used as input for PCR2 to install Illumina barcodes. PCR2 was conducted for nine cycles of amplification using a Phusion HS II kit (Life Technologies). Following PCR2, samples were pooled, and gel-purified in a 1% agarose gel using a Qiaquick Gel Extraction Kit (Qiagen). Library concentration was quantified using the Qubit High-Sensitivity Assay Kit (Thermo Fisher Scientific). Samples were sequenced on an Illumina MiSeq instrument (paired-end read, read 1: 200–280 cycles, read 2: 0 cycles), using an Illumina MiSeq 300 v2 Kit (Illumina).

Histology

Mice were euthanized by CO_2 inhalation before whole eye enucleation. Excess tissues were removed by microdissection before eyes were placed into Hartman's fixative (Sigma-Aldrich #H0290) and fixed for 24 h at 4 ºC. The eyes were then stored in 70% ethanol before paraffin embedding. Sections were cut to 8 µm thickness onto Superfrost Plus slides (Thermo #12-550-15) before hematoxylin and eosin (H&E) staining by standard procedures. Images were acquired on a Keyence BZ-X810 All-in-One fluorescence microscope.

Immunohistochemistry

Hartman's-fixed and paraffin-embedded sections were rehydrated with sequential washes of xylene, ethanol, and PBS before blocking with 5% normal donkey serum (NDS) in 0.2% Triton X-100 in PBS at room temperature for 1 h. Sections were then incubated with primary antibodies with 2.5% NDS in 0.1% Triton X-100 in PBS overnight in the dark at 4 ºC (mouse 1D4 anti-rhodopsin-Alexa Fluor 488, 1:500, in-house). The sections were then washed with 0.1% Triton X-

100 in PBS at room temperature in the dark 3 times, with each wash being 10 min, before sections were mounted with VectaShield HardSet Antifade Mounting Medium with DAPI (Vector Labs, #H-1500-10) and a coverslip. Images were acquired on a Leica Stellaris SP8 confocal microscope.

Molecular cloning

All plasmids for transfection were prepared by endotoxin-free mini-, midi-, or maxi-prep (Thermo #K210002, K210014, or K210016). To generate hU6-sgRNA expression vectors, oligos corresponding to the protospacer were used to PCR-mutagenize and KLD-clone (NEB #M0554S) the hU6-rd12-A6 sgRNA-expression vector (1). To generate mammalian expression vectors for mouse rhodopsin (mRho), Rho-E150K retinal cDNA was subjected to PCR with primers appending EcoRI and NotI restriction sites. Then, a pcDNA3.1 vector was double digested with EcoRI and NotI, the backbone was purified by QiaQuick MinElute gel extraction (Qiagen #28604), the fragments were assembled by InFusion Gibson assembly (Takara #638945), and the assembly was transformed into Mach1 competent *E. coli* (Thermo #C862003) to generate pcDNA3.1-mRho-E150K. The vector pcDNA3.1-mRho-E150K was then PCR-mutagenized and KLD-cloned (NEB #M0554S) to generate the other 9 mRho variants.

Generation of HEK293T cell line expressing Rho-E150K

A HEK293T cell line stably expressing a fragment of Rho-E150K (HEK-E150K) was generated by transduction of naïve HEK293T cells with helper-free retrovirus collected from Phoenix-Ampho cells transfected with pMXs-E150K-IRES-GFP, as previously described (2). To generate pMXs-E150K-IRES-GFP, a 279bp fragment of the murine *Rho* (rhodopsin) gene was PCR-amplified and then double digested with EcoRI and NotI and inserted into the MCS of pMX-IRES-GFP (a gift from T. Kitamura at the University of Tokyo). Downstream of the *Rho* fragment, the IRES-GFP allows for cell sorting by flow cytometry. GFP+ cells were collected on a FACSAria Fusion cell sorter (BD Biosciences) to enrich transduced cells. Cells were clonally isolated by sequential limiting dilution, and the construct was sequenced. Cells were maintained in DMEM with glutamine (Thermo Fisher, 11965092), 10% FBS (Genesee Scientific, San Diego, CA, USA,

25-514H), and optional 100 U ml^{-1} penicillin-streptomycin (Thermo Fisher, 15140122), in a humidified incubator at 37 °C with 5% CO_2.

Mass spectrometry sample preparation

The purified rhodopsin samples were digested by the filter-aided sample-preparation (FASP) method. Briefly, the sample was diluted with 50 mM NH_4HCO_3 and then transferred into a Amicon Ultra 0.5 spin-filter column (30 kDa). Afterwards, the concentrated proteins were reduced by 10 mM DTT at 56 ºC for 1 h and alkylated by 20 mM IAA at room temperature in the dark for 1 h. Then, the protein solution was washed with 50 mM NH_4HCO_3 three times *via* dilution-concentration cycles. Lys-C was added into the samples from the E150K, WT, E150G, E150K/N151S E150K/N151D, N151D, E150G/N151D, E150G/N151G, and N151S rhodopsin samples, and Arg-C was added into the samples from the E150R rhodopsin sample at a ratio of 1:50 (protease:protein) and incubated at 37 ºC for 4 h. Then, 1 volume of 200 mM Tris-HCl, 20 mM $CaCl_2$ was added before chymotrypsin was spiked at a ratio of 1:50 (protease:protein) and incubated at room temperature overnight. The digests were recovered by centrifugation as flow-through 30-kDa MW-cutoff filters, the filters washed with water, and the filtrates were combined. The resultant supernatant solution was vacuum-dried and then adjusted to 200 µL with 0.5% acetic acid. Then the peptide mixture was subjected to C18 solid-phase extraction (Nest Group, Inc.) for desalting, and subsequently vacuum-dried.

Mass spectrometry data acquisition.

Proteomics data were acquired *via* LC-MS/MS using an UltiMate 3000 UHPLC (Thermo Fisher Scientific) coupled in-line with an Orbitrap Fusion Lumos mass spectrometer (Thermo Fisher Scientific) with an ESI nanospray source. Mobile phase (buffer B) was comprised of 0.1% formic acid in acetonitrile. The total flow rate was 300 nL min^{-1}, and peptides were separated over a 57-min gradient from 4% to 25% buffer B (total run time 90 min per sample) on an Acclaim PepMap RSLC column (50cm x 75 µm). Survey (MS) scans were acquired in Orbitrap (FT) with automated gain control (AGC) target 8E5, maximum injection time 50 ms, and dynamic exclusion

of 30 s across the scan range of 375-1800 m/z. MS/MS spectra were acquired in data-dependent acquisition mode at top speed for 3 s per cycle; the AGC target was set to 1E4 with maximum injection time of 35 ms. Ions were subjected to stepped-energy higher-energy collision dissociation (seHCD) fragmentation at a normalized collision energy (NCE) of 20±5%.

Label-free quantification analysis

The raw LC-MS/MS data files were analyzed using MaxQuant (version 2.0.3.1), with the spectra searched against the wild-type and mutant rhodopsin sequences. For identification of the peptides, the mass tolerances were 20 ppm for initial precursor ions, and 0.5 Da for fragment ions. Two missed cleavages in tryptic digests were allowed. Cysteine residues were set as static modifications. Oxidation of methionine was set as the variable modification. Filtering for the peptide identification was set at a 1% false discovery rate (FDR).

CIRCLE-seq off-target analysis

CIRCLE-seq off-target editing analysis was performed as previously described (3, 4). Genomic DNA from Rho-E150K mouse liver was isolated using Gentra Puregene Kit (Qiagen #158845), following the manufacturer's instructions. Purified genomic DNA was sheared with a Covaris S2 instrument to an average length of 300 bp. The fragmented DNA was end-repaired, A-tailed and ligated to a uracil-containing stem–loop adaptor, using the KAPA HTP Library Preparation Kit, PCR Free (KAPA Biosystems #KK8235). Adaptor-ligated DNA was treated with Lambda Exonuclease (New England Biolabs #M0262) and *E. coli* Exonuclease I (New England Biolabs #M0293); and then with USER enzyme (New England Biolabs #M5505) and T4 poly-nucleotide kinase (New England Biolabs #M0201). Intramolecular circularization of the DNA was performed with T4 DNA ligase (New England Biolabs #M0202), and residual linear DNA was degraded by Plasmid-Safe ATP-dependent DNase (Lucigen #E3110). Synthetic guide RNAs were ordered from IDT with standard 2′-*O*-methyl modification at the first three and last three bases. The synthetic guide RNAs were resuspended to 9 μM in nuclease-free water, denatured at 90 °C for 5 min and slowly annealed while cooling at 0.1 °C s^{-1} to 25 °C. *In vitro* cleavage reactions were

performed with 125 ng Plasmid-Safe-treated circularized DNA, 90 nM Cas9 nuclease protein (New England Biolabs #M0386) and 270 nM synthetic guide RNA in a 50 µl volume for 1 h. Cleaved products were treated with proteinase K as described, A-tailed, ligated with a hairpin adaptor (New England Biolabs #E7600S), treated with USER enzyme (New England Biolabs #M5505), and amplified by PCR with barcoded universal primers (New England Biolabs #E7600S), using Kapa HiFi Polymerase (KAPA Biosystems #KK4824). Libraries were sequenced with 150-bp/150-bp paired-end reads with an Illumina MiSeq instrument. CIRCLE-seq data analyses were performed using open-source CIRCLE-seq analysis software and recommended default parameters. The top ten nominated off-target sites for the Rho-E150K sgRNA were analyzed by HTS from the retinas of untreated or dual-AAV8 treated mice. Insertions or deletions at sgRNA-associated off-target sites were analyzed as a percentage of discarded reads divided by the total reference-aligned reads.

High-throughput sequencing data analysis

Sequencing reads were demultiplexed using the MiSeq Reporter software (Illumina), and were analyzed using CRISPResso2 (5). Batch analysis mode (one batch for each unique amplicon and sgRNA combination analyzed) was used in all cases. Reads were filtered according to minimum average quality score (Q > 30) prior to analysis. The following quantification window parameters were used: -w 20, -wc -10. Base-editing efficiencies are reported as the percentage of sequencing reads containing a given base conversion at a specific position.

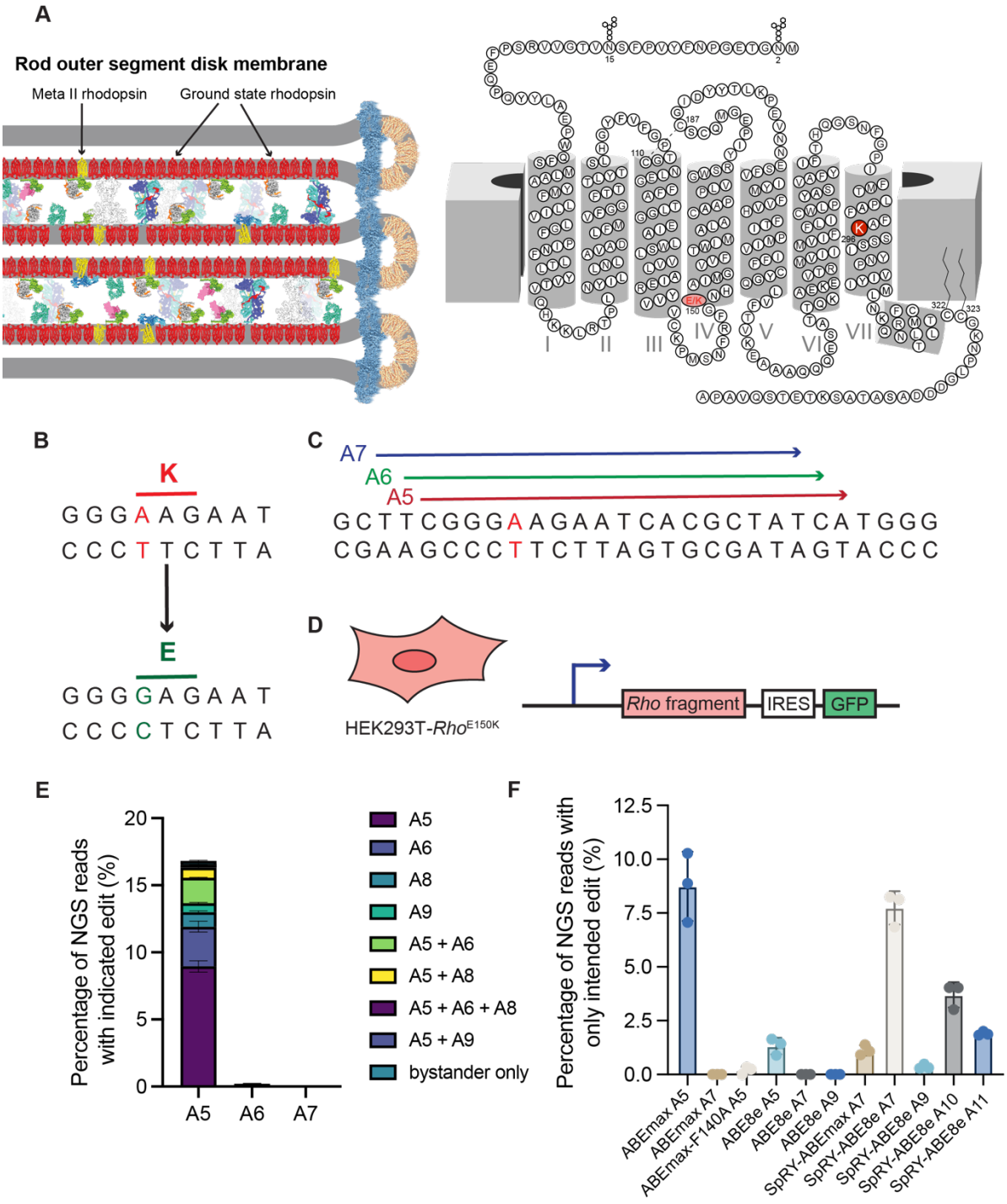


Figure 2.1. Establishment of rhodopsin-E150K cell line and base-editing screening *in vitro*.

(**A**) Left, the rod outer segment is composed of stacked disc membranes with a high concentration of rhodopsin (red) (adapted from Gulati and Palczewski)[141]. When rhodopsin encounters photons

of light, it is photoactivated (yellow) and initiates phototransduction. Right, 2-D protein structure of mouse rhodopsin. Locations of Schiff-base Lys^{296} and E150K mutation are indicated in red. (**B**) Coding sequence of the E150K rhodopsin mutation. (**C**) Design of base-editing SpCas9 single-guide RNAs (sgRNAs), each named for the location where the adenine of interest is positioned within the protospacer. (**D**) Schematic diagram of the HEK293T-Rho^{E150K} (HEK-E150K) cell line generated by retroviral transduction, used for *in vitro* screening. IRES-GFP downstream of the *Rho* fragment enables FACS purification of transduced cells. (**E**) Base-editing outcomes *via* next-generation sequencing (NGS) after co-transfection of HEK-E150K cells with plasmids expressing ABEmax and sgRNAs. (**F**) Base-editing outcomes *via* NGS after co-transfection of HEK-E150K cells with various ABEs and sgRNAs with the target adenine placed at positions 5, 7, 9, 10, or 11 within the protospacer. Data generated in part with assistance from Susie Suh and Elliot H. Choi.

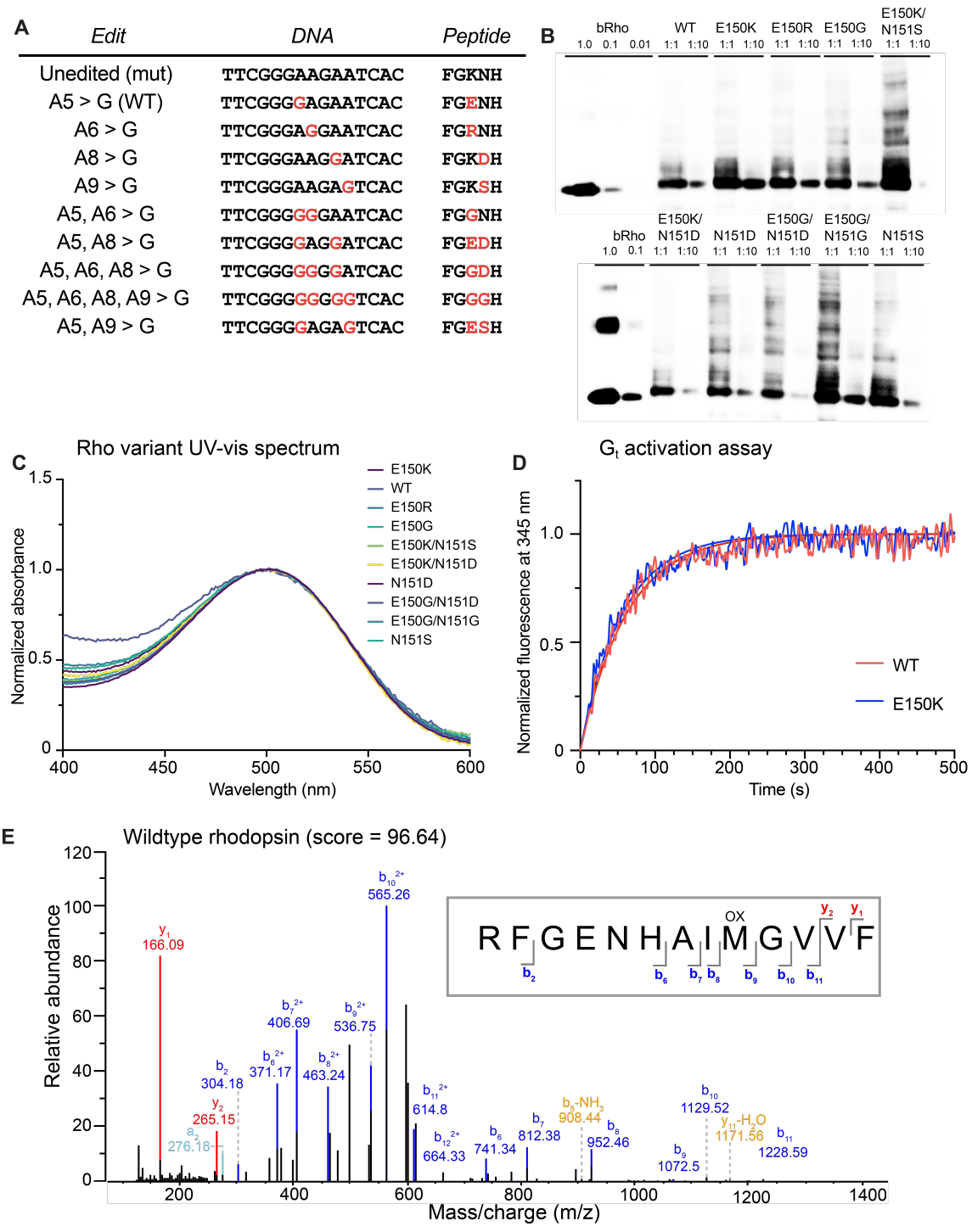
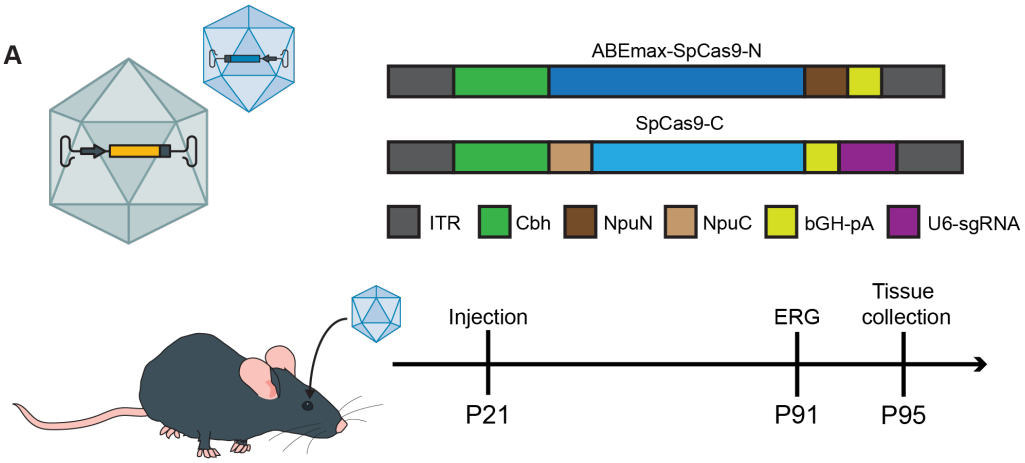
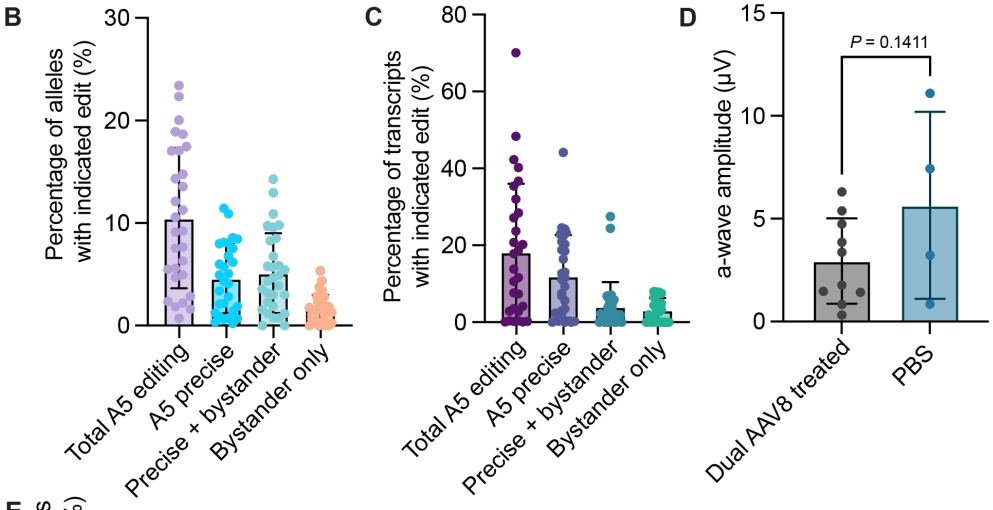


Figure 2.2. Characterization of bystander-edited variants of E150K-rhodopsin. (**A**) List of all potential coding variants of rhodopsin resulting from on-target and bystander editing observed by next-generation sequencing. (**B**) Anti-1D4 Western blot of HEK293T cells transfected with expression plasmids for all rhodopsin variants, loaded either undiluted (1:1) or diluted (1:10).

Purified bovine rhodopsin is used as a positive control (concentration indicated in μg/mL). (**C**) UV-vis absorbance spectra of purified rhodopsin variants in LMNG after reconstitution with 11-*cis*-retinal. Absorbances are normalized to the absorbance of rhodopsin at its λ_{max}, 500 nm. (**D**) G_t activation assay of WT rhodopsin and the E150K mutant. The results are plotted as normalized increase of fluorescence intensity at 345 nm of G_t upon addition of GTPγS. The curves represent the fitting of a pseudo first-order association model. In this experiment, the rate constants (turnover numbers) were determined to be $16.2 \pm 0.4 \times 10^{-3}$ s^{-1} for WT and $17.8 \pm 0.4 \times 10^{-3}$ s^{-1} for the E150K mutant. (**E**) Tandem MS/MS spectrum of a unique peptide from purified wildtype-rhodopsin and its fragmentation pattern. Data generated in part with assistance from Alexander L. Yan, David Salom, and Fangyuan Gao.


A
ABEmax-SpCas9-N
SpCas9-C
ITR
Cbh
NpuN
NpuC
bGH-pA
U6-sgRNA
Injection
ERG
Tissue collection
P21
P91
P95


B
Percentage of alleles with indicated edit (%)
Total A5 editing
A5 precise
Precise + bystander
Bystander only
C
Percentage of transcripts with indicated edit (%)
D
a-wave amplitude (μV)
P = 0.1411
Dual AAV8 treated
PBS

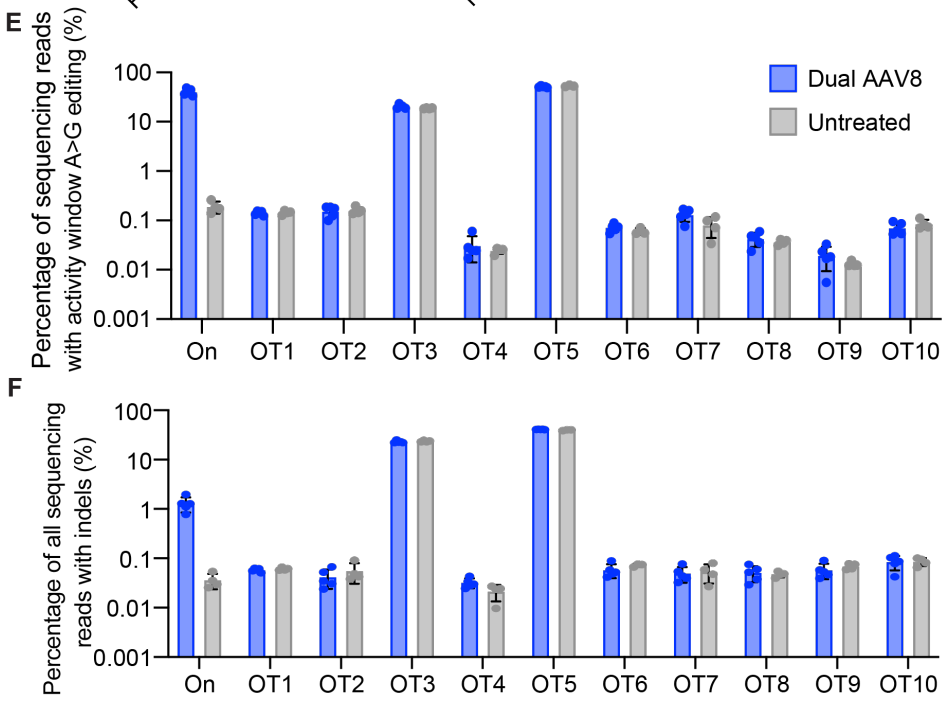

E
Percentage of sequencing reads with activity window A>G editing (%)
Dual AAV8
Untreated
On
OT1
OT2
OT3
OT4
OT5
OT6
OT7
OT8
OT9
OT10
F
Percentage of all sequencing reads with indels (%)

Figure 2.3. *In vivo* adenine base editing of E150K mice treated at P21. (**A**) Schematic diagram (upper) depicting the dual-AAV strategy for *in vivo* base editing. The gene coding for ABEmax and the sgRNA are split into a N-terminal and a C-terminal AAV. When a cell is transduced by both AAVs, the full-length ABEmax is reconstituted *via* Npu intein splicing. Schematic diagram (lower) illustrating the P21 animal-treatment protocol: E150K mice were treated at post-natal day 21 (P21) by subretinal injection of dual-AAV8 and analyzed by electroretinography (ERG) 10 weeks later (P91). Retinas were then collected and analyzed by NGS. (**B**) NGS analysis of bulk retinal genomic DNA for base-editing outcomes after dual-AAV8 treatment. (**C**) NGS analysis of bulk retinal cDNA (synthesized from retinal RNA) for base editing outcomes after dual-AAV8 treatment. (**D**) ERG a-wave amplitudes from E150K mice after dual AAV8 treatment, compared with E150K mice treated with PBS (controls). $P = 0.1411$ by Student's t-test. (**E**) CIRCLE-seq analysis of A>G editing of on- and off-target genomic DNA within the ABE activity window (protospacer positions 4-8) for retinas from E150K dual AAV8-treated mice *versus* untreated mice. (**F**) CIRCLE-seq analysis of all indels within the entire NGS amplicon for retinas from E150K dual-AAV8 treated mice *versus* untreated mice. All results are represented as mean ± S.D. Data generated in part with assistance from Carolline R. Menezes, Gregory A. Newby and Paul Z. Chen.

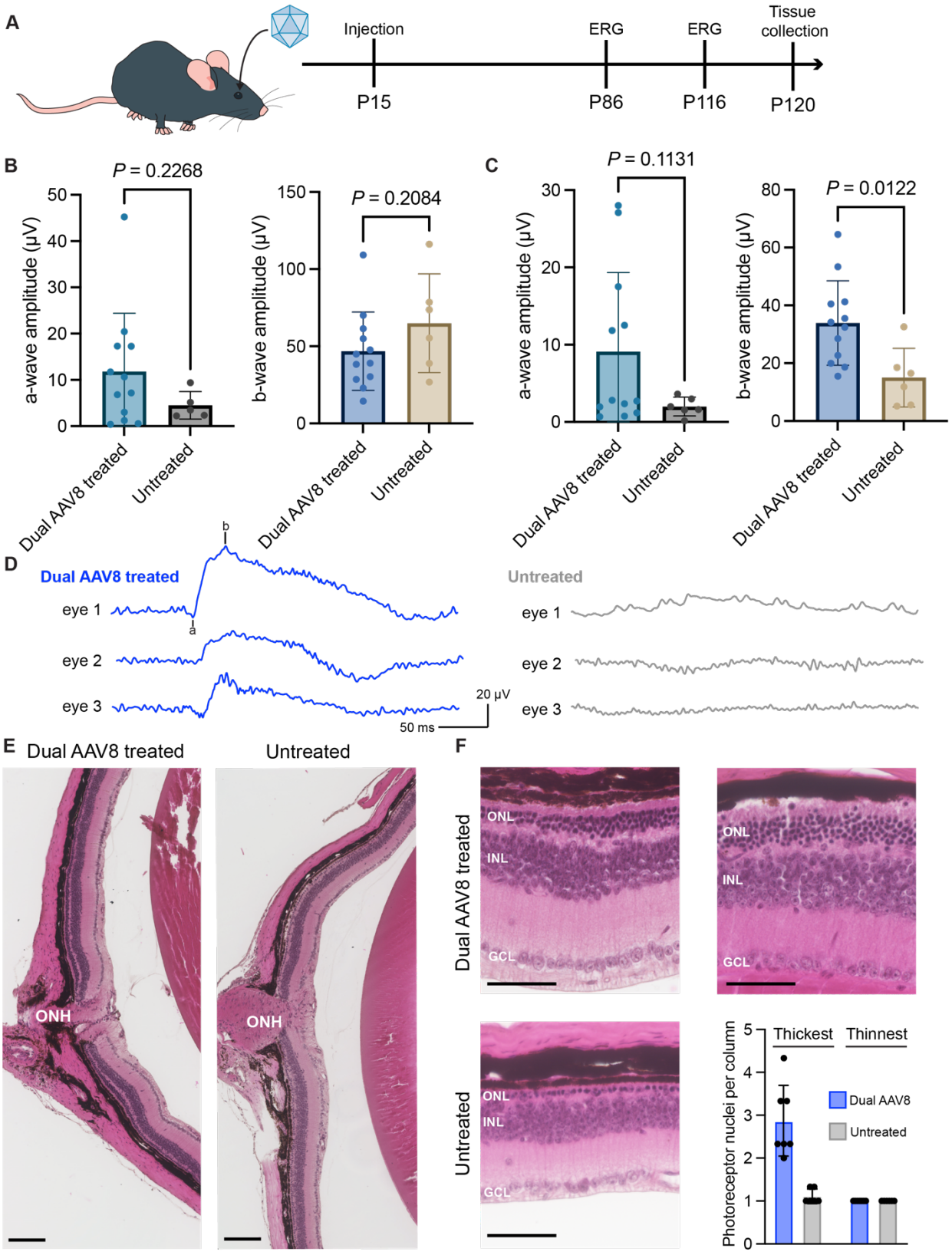

A
Injection
ERG
ERG
Tissue collection
P15
P86
P116
P120
B
P = 0.2268
a-wave amplitude (μV)
Dual AAV8 treated
Untreated
P = 0.2084
b-wave amplitude (μV)
C
P = 0.1131
P = 0.0122
D
Dual AAV8 treated
Untreated
eye 1
eye 2
eye 3
20 μV
50 ms
E
Dual AAV8 treated
Untreated
ONH
F
ONL
INL
GCL
Thickest
Thinnest
Dual AAV8
Untreated
Photoreceptor nuclei per column

Figure 2.4. In vivo adenine base editing of E150K mice treated at P15. (**A**) Schematic diagram of P15 treatment protocol: E150K mice were treated at post-natal day 15 (P15) by subretinal injection of dual-AAV8, and analyzed by electroretinography after 10 weeks (P86) or 14 weeks (P116). Retinas were then collected and analyzed by NGS. (**B**) ERG a-wave (left) and b-wave (right) amplitudes from E150K mice 10 weeks after dual-AAV8 treatment. P = 0.2268 and 0.2084 by Student's t-test. (**C**) ERG a-wave (left) and b-wave (right) amplitudes from E150K mice 14 weeks after dual AAV8 treatment. P = 0.1131 and 0.0122 by Student's t-test. (**D**) Representative ERG waveforms at -0.3 log cd s m−2 from three dual AAV8-treated mice (left) and three untreated mice (right). The ERG a- and b-wave markers are indicated on trace 1 (treated mice). (**E**) Representative hematoxylin and eosin sections from dual AAV8-treated mice (left) and untreated mice (right). ONH, optic nerve head. Scale bar represents 100 μm. (**F**) Representative hematoxylin and eosin sections from the thickest region of the retina from dual AAV8-treated and untreated mice. Quantification of photoreceptor nuclei per outer nuclear layer, from thickest and thinnest regions of retinas. Scale bar represents 50 μm. ONL, outer nuclear layer; INL, inner nuclear layer; GCL, ganglion cell layer. All results are represented as mean +/- S.D. Data generated in part with assistance from Carolline R. Menezes.

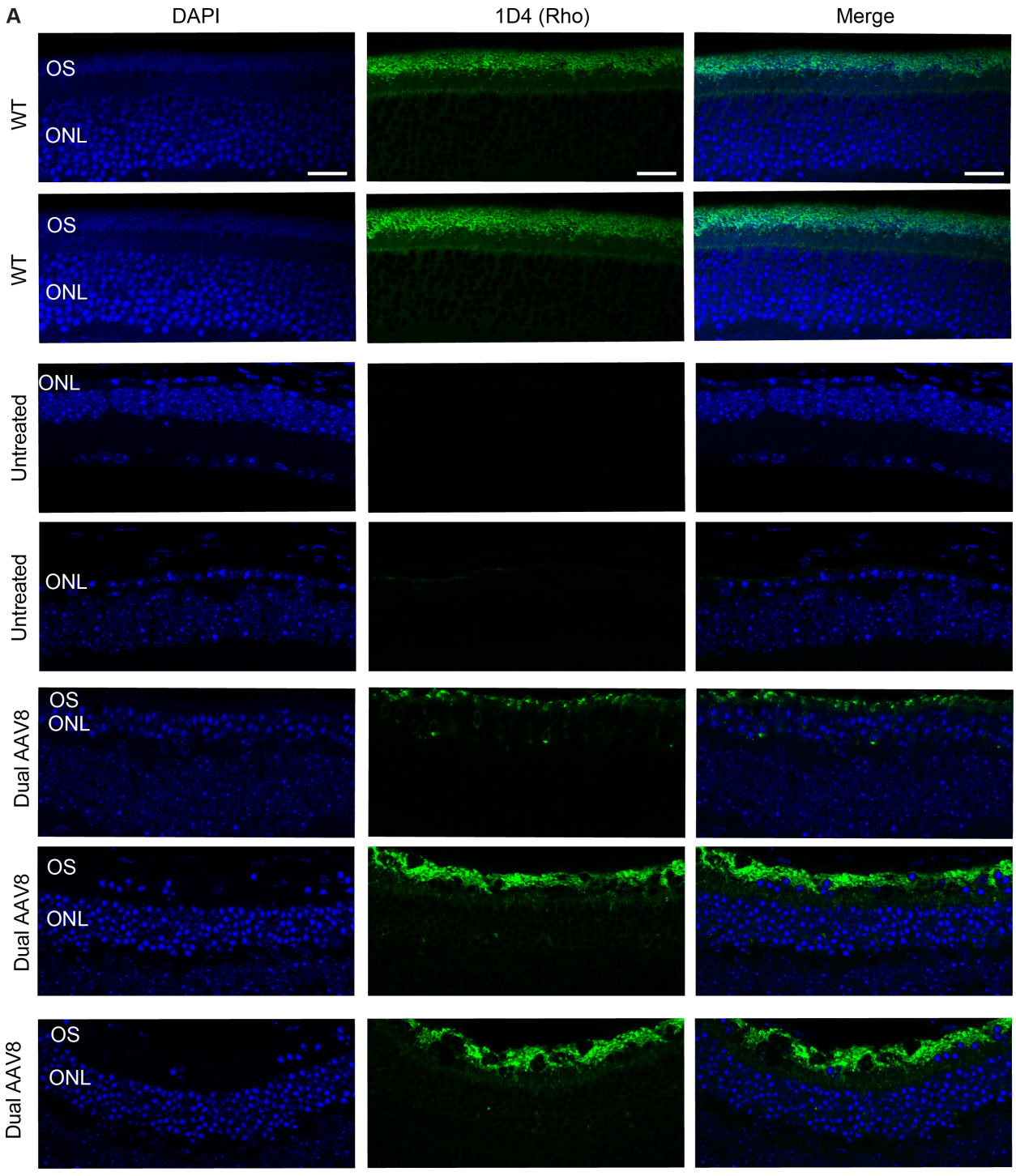


Figure 2.5. Rhodopsin expression in E150K mice after base editing at P15. (**A**) Representative immunohistochemistry of sections stained with DAPI and 1D4 (anti-Rho) of WT, untreated E150K mice, and E150K mice treated with dual AAV8 at P15. ONL, outer nuclear layer; OS, outer segment. Scale bar represents 20 μm.

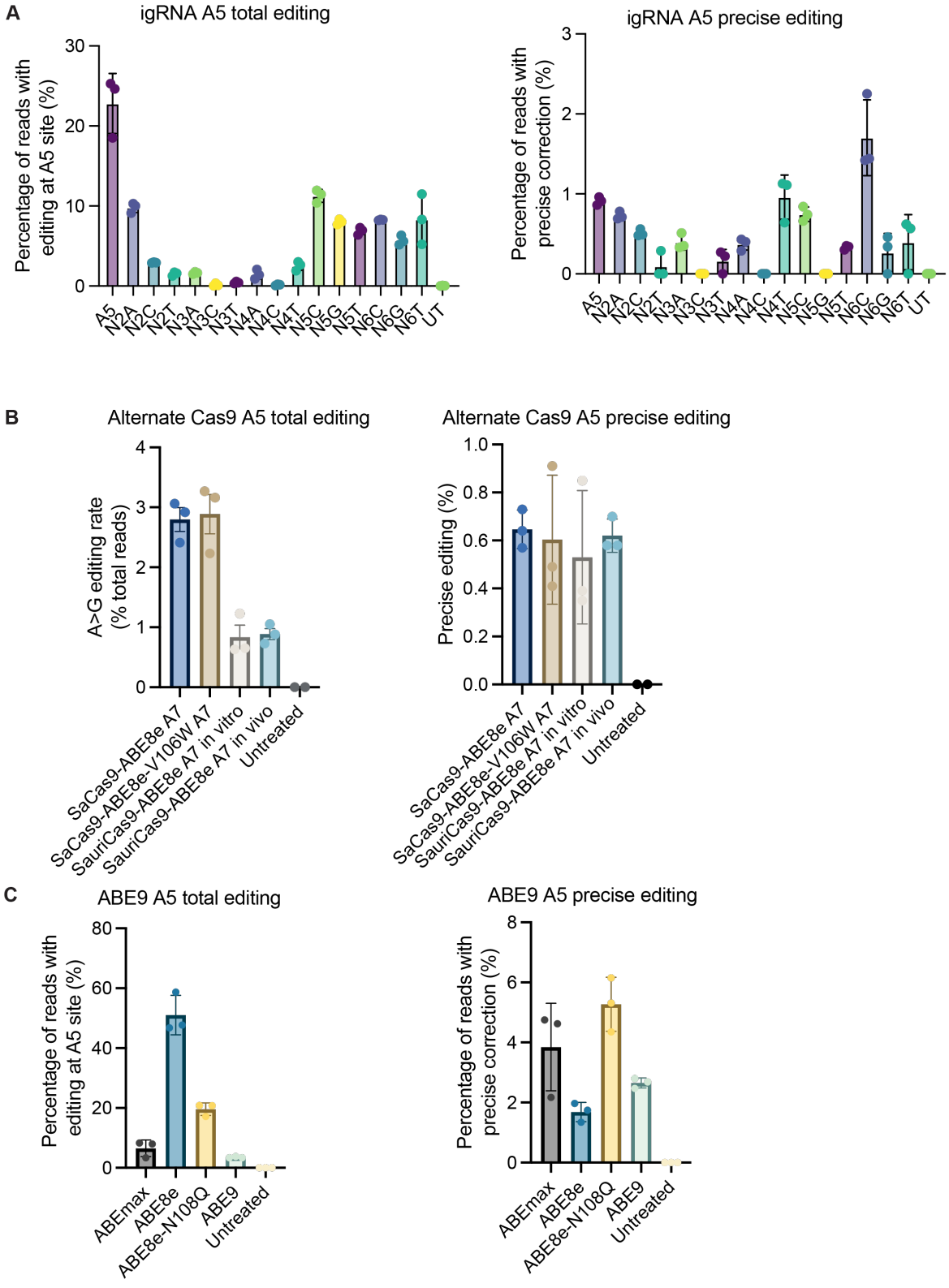

A
igRNA A5 total editing
Percentage of reads with editing at A5 site (%)
30
20
10
0
A5
N2A
N2C
N2T
N3A
N3C
N3T
N4A
N4C
N4T
N5C
N5G
N5T
N6C
N6G
N6T
UT
igRNA A5 precise editing
Percentage of reads with precise correction (%)
3
2
1
0
B
Alternate Cas9 A5 total editing
A>G editing rate (% total reads)
4
3
2
1
0
SaCas9-ABE8e A7
SaCas9-ABE8e-V106W A7
SauriCas9-ABE8e A7 in vitro
SauriCas9-ABE8e A7 in vivo
Untreated
Alternate Cas9 A5 precise editing
Precise editing (%)
1.0
0.8
0.6
0.4
0.2
0.0
C
ABE9 A5 total editing
Percentage of reads with editing at A5 site (%)
80
60
40
20
0
ABEmax
ABE8e
ABE8e-N108Q
ABE9
Untreated
ABE9 A5 precise editing
Percentage of reads with precise correction (%)
8
6
4
2
0

Figure 2.6. Screening of alternate base-editing strategies *in vitro*. (**A**) NGS results of imperfect guide RNA (igRNA) plus ABE8e, screening with total-target base editing (left) and precise-target base editing (right). igRNAs are denoted by position in the protospacer (N) and the mutated base. UT, untreated. (**B**) NGS results of alternative Cas9-ABEs, screening with total-target base editing (left) and precise-target base editing (right). (**C**) NGS results of ABE9-variant screening with total-target base editing (left) and precise-target base editing (right). All results are represented as mean ± S.D. Data generated in part with assistance from Gregory A. Newby and Paul Z. Chen.

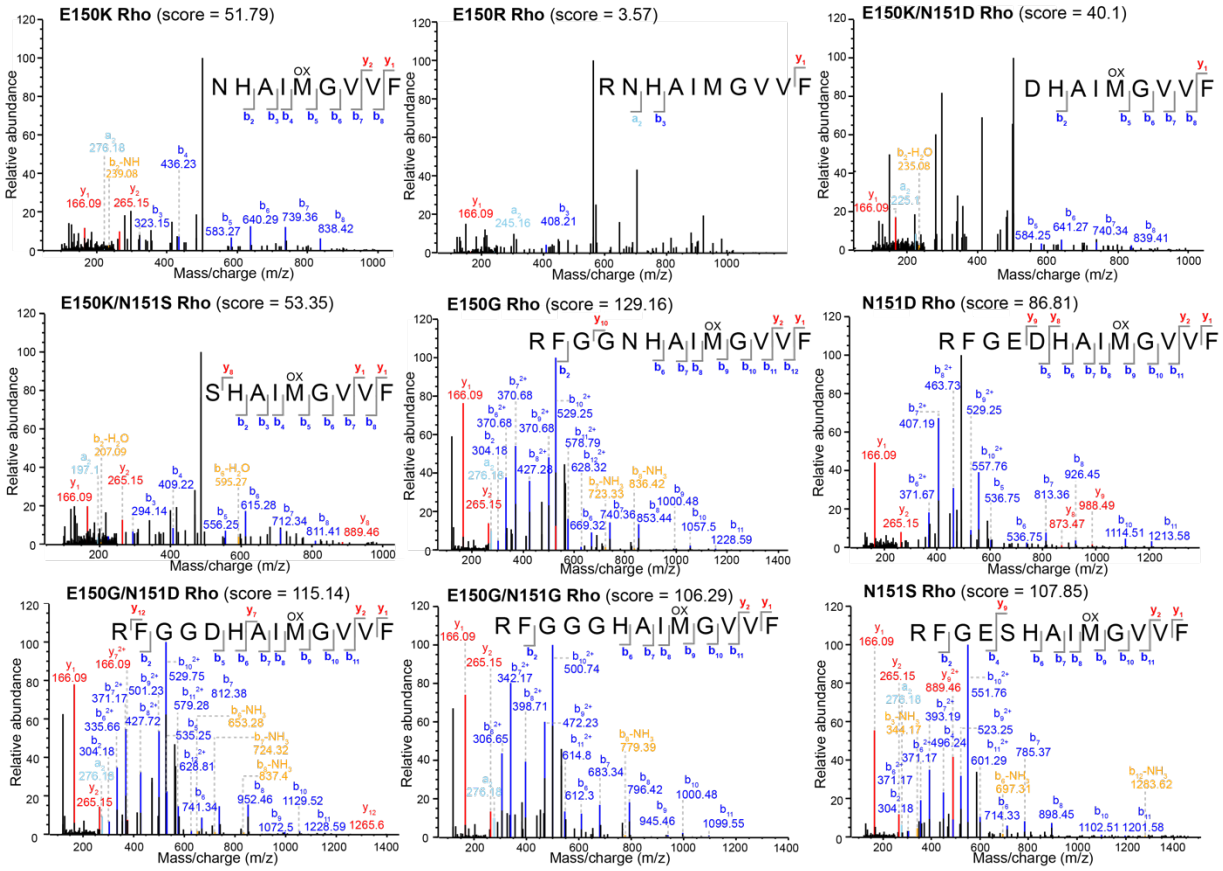


Figure 2.7. Tandem MS/MS spectra of purified peptides from rhodopsin variants. Spectra for each unique rhodopsin variant and their respective peptide fragmentation patterns. Data generated in part with assistance from Fangyuan Gao.

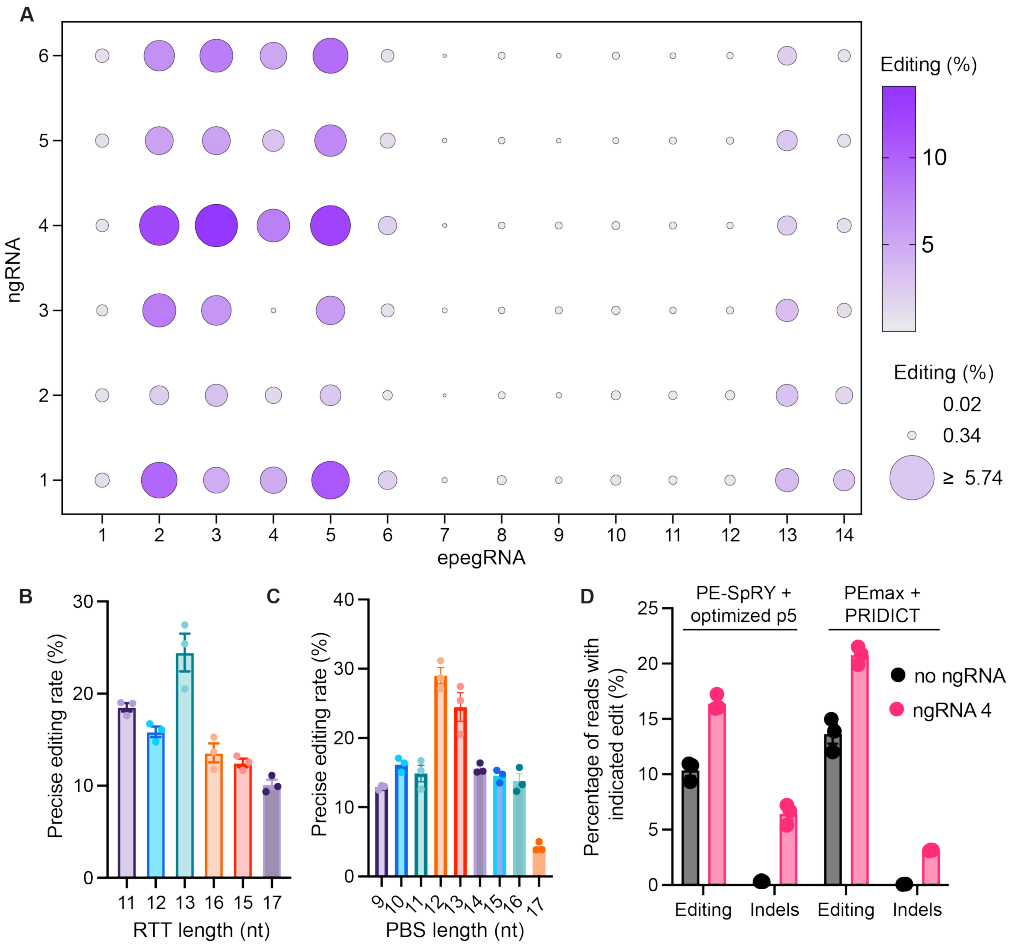


Figure 2.8. *In vitro* screening of epegRNAs for correction of Rho-E150K. (**A**) Bubble plot of epegRNA and nicking guide RNA (ngRNA) screening for PE-SpRY. Bubbles are colored and sized according to precise A>G editing rate. (**B, C**) Optimization of lengths of p5 epegRNA reverse-transcriptase template (RTT, left) and primer binding site (PBS, middle). (**D**) Comparison of PE-SpRY and optimized p5 epegRNA with PEmax and PRIDICT epegRNA. Results are represented as mean ± S.D. Data generated in part with assistance from Gregory A. Newby and Paul Z. Chen.

CHAPTER 3

Development of engineered virus-like particles (eVLPs)

This chapter is derived in part from the following manuscript published in *Cell:*

Banskota, S. et al. Engineered virus-like particles for efficient in vivo delivery of therapeutic proteins. *Cell* 185, 250-265 e216 (2022).

© 2022 the Authors.

CHAPTER 3

Development of engineered virus-like particles (eVLPs)[209]

3.1 Introduction

In contrast with the delivery of base editors, such as ABEmax, by dual AAV as demonstrated for the rhodopsin E150K mutation (Chapter 2), an optimal delivery strategy for translational genome editing in humans would ideally be transient in nature. Despite the highly efficient delivery of viruses, such as AAV, prolonged expression of CRISPR/Cas9 components could lead to off-target and increased bystander editing. A viral genome expresses the cargo for a prolonged period and additionally adds the possibility of oncogenic or disruptive viral genome integration into the host genome. To avoid this, transient expression or residence of CRISPR/Cas9 could be accomplished with controllable AAV promoters or self-targeting AAVs. Another strategy would be transient delivery of CRISPR/Cas9 ABE or PE as ribonucleoprotein (RNP) complexes or messenger RNA (mRNA).

While direct delivery of RNPs and mRNA is possible, RNPs and mRNA are vulnerable to degradation. Additionally, there are not many uptake mechanisms for the direct intracellular delivery of RNPs and mRNA; thus, they will often require an additional delivery mechanism. Multiple systems have been proposed, including the use of lipid nanoparticles (LNPs), other nanoparticles such as gold and silica, and small molecule facilitators.

One promising solution is the use of virus-like particles (VLPs). VLPs exploit many favorable characteristics of enveloped viruses, such as large cargo capacity, low immunogenicity, and targetable tissue tropism by modification of envelope glycoproteins. Instead of packaging a viral genome, the viral production lifecycle can be modified so that VLPs package therapeutic proteins of interest instead of a viral genome. This allows for the VLP to deliver RNPs, which has the shortest lifetime in the cell.

One of the first descriptions of VLPs utilized the Moloney murine leukemia virus (MMLV) framework, which tolerates C-terminal fusion to the gag nucleocapsid protein. As MMLV gag tolerates C-terminal fusion, proteins of interest can be covalently linked, packaged into MMLV VLPs, and subsequently cleaved from gag following VLP maturation. This system was able to deliver Cre recombinase and caspase intracellularly to cells in culture and was able to induce cell death[210].

Nuclease CRISPR/Cas9 was then delivered via Friend murine leukemia virus (FMLV) VLPs as RNPs. This system was termed Nanoblades[211]. By fusing Cas9 downstream of FMLV gag with a protease cleavage site, they demonstrated packaging of Cas9 RNPs loaded with sgRNAs, CRISPR activation (CRISPRa), and homology-directed repair by complexation with ssDNA donor templates. They were also active *in vivo,* as they reported productive editing in mouse zygotes and in the liver after retroorbital injection. These demonstrated the power of VLPs to deliver Cas9 RNPs *in vivo* without off-target editing. VLPs were then further developed in subsequent work and shown to be targetable to different cell types of interest through substitution of envelope glycoproteins from naturally occurring viruses, or through the use of conjugated antibodies to direct VLP delivery[212,213].

3.2 Development of base editor VLPs

The laboratory of David R. Liu hypothesized that the FMLV VLP framework could also support the packaging of base editor RNPs. When they used this previously described framework to deliver ABE8e (termed v1 VLPs), they observed efficient base editing in HEK293T cells at the *HEK2, HEK3*, and *BCL11A* loci at the highest doses tested, but noticed a steep drop-off in efficiency with decreasing dosage. Thus, further improvements in efficiency could be made, which would be critical for *in vivo* and clinical applications.

In the first improvement, they switched the retroviral framework from FMLV to MMLV, which improved efficiencies. Additionally, inefficient linker cleavage between gag and ABE8e may decrease editing efficiency, as ABE8e may need to be fully freed from the VLP for maximal editing

efficiency. By screening four previously characterized endogenous protease cleavage sites, they selected an optimal cleavage sequence that balanced maturation times and cleavage effiency, PLQVLTLNIERR. Interestingly, another cleavage sequence, TSTLLMENSS, was more efficient in cleavage, but demonstrated lower editing efficiency. This indicates that if the cleavage was too efficient, then ABE8e would be cleaved prematurely before recruitment into a mature VLP *via* covalent linkage, and thus less ABE8e would be packaged into the final VLP. These improved VLPs were termed v2 VLPs and showed that the gag-cargo linker strongly influences delivery efficiency.

Another bottleneck in VLP maturation could be improper subcellular localization. For optimal editing, BEs often fuse nuclear localization sequences (NLS) to both the N- and C-termini to encourage proper localization of genome-modifying reagents within the nucleus. However, MMLV gag must be located within the cytoplasm to be packaged into the maturing VLP. In the next step of optimization, v3 VLPs were created by the insertion of nuclear export sequences (NES) into the gag gene to facilitate the export to the cytoplasm. By screening multiple insertion sites, the v3.4 architecture was identified, which places the NES directly upstream of the v2 protease cleavage site, and this improved the editing rate even further. These demonstrate that careful consideration of subcellular localization and understanding of the VLP maturation process can improve VLP efficiencies.

Lastly, the gag-ABE and gag-pro-pol stoichiometry was optimized for a v4 VLP and found to be 1:3. The inclusion of gag-ABE is insufficient for high titer VLP production, as the gag-ABE fusion is bulky – the addition of wildtype gag-pro-pol not only spatially separates the gag-ABE fusions, but the wildtype gag-pro-pol additionally provides the proteases (pro) required to cleave and mature the VLPs. Through engineering of the linker cleavage, NES/NLS optimization, and transfection stoichiometry, the Liu lab greatly improved the efficiency of the MMLV VLP system, and thus termed their final v4 architecture as engineered virus-like particles (eVLPs), which improved editing efficiencies by over 8-fold compared to v1 VLPs.

Because an important advantage of VLPs is their transient nature, the Liu lab then produced and transduced HEK293T cells with v4 BE-eVLPs that target the *HEK2, HEK3*, and *BCL11A* loci with sgRNAs with known off-target sites, compared with plasmid transfection of the same ABE and sgRNAs. They noted similar on-target editing, but off-target editing was substantially lower in the eVLP treated cells. Additionally, with the R-loop assay, an off-target assay that analyzes Cas9-independent off-target editing, BE-eVLPs resulted in barely detectable or absent R-loop activity, in comparison with plasmid transfected cells. Collectively, these results indicate that eVLPs are highly efficient and result in a more favorable safety profile compared to viruses due to their transient nature, with high on-target and minimal off-target editing.

3.3 Application of BE-eVLPs in the CNS and liver

The Liu group then investigated the use of VLPs for *in vivo* delivery. After intracerebroventricular injections in post-natal day 0 mice, they noted up to 55% base editing in cells that were co-labeled with a GFP-expressing lentivirus. However, transduction efficiency was relatively low and limited to the local area under the injection site.

They next investigated the use of BE-eVLPs for the treatment of liver diseases. As intravenous injection of Cas9 delivery vehicles often targets the liver, base editing of therapeutic loci could be an ideal application for eVLPs. The *PCSK9* locus, encoding for proprotein convertase subtilisin/kexin type 9 was first described in families that had abnormally low serum cholesterol and low-density lipoproteins in the blood. People with homozygous inactivating mutations in PCSK9 were strongly protected against cardiovascular disease with no apparent side effects from the absence of this pathway. Subsequent research and clinical trials showed that monoclonal antibodies targeting PCSK9 were protective for patients with familial hypercholesterolemia, culminating in the FDA approval of several PCSK9 monoclonal antibody therapies, including evolocumab and alirocumab. However, repeated administrations of monoclonal antibodies by intravenous infusion are burdensome on the patient and could lead to high lifetime healthcare costs, as patients with high cardiovascular risk would need to be on anti-PCSK9 therapy for life.

Other PCSK9 drugs in the pipeline, including Alnylam's inclisiran, an RNAi agent, also must be readministered periodically[214]. In contrast, gene editing inactivation of PCSK9 could be a well-tolerated permanent intervention, as demonstrated by the families with homozygous inactivating mutations in *PCSK9.*

Therefore, the Liu group produced eVLPs that target the splice donor site between exon 1 and intron 1 in *PCSK9*, which was previously described to decrease PCSK9 expression. Deamination of the splice donor site from A to G would result in aberrant splicing and a non-functional protein. Indeed, after intravenous injection of eVLPs through the retro-orbital sinus, they observed 64% editing in the liver 1 week post-injection. This editing was also therapeutic, with a 4.5-fold decrease in the serum concentrations of PCSK9 and no detectable toxicity or liver damage. To assess the safety of BE-eVLPs delivered *in vivo*, they also performed CIRCLE-seq on livers treated with either BE-eVLPs or dual AAVs packaging identical BE/sgRNA sets. In agreement with the *in vitro* data, BE-eVLP treatment did not result in off-target editing at the top fourteen experimentally nominated off-target sites, while dual AAV treatment led to detectable off-target editing at 3 sites. These results indicate that BE-eVLPs result in therapeutically relevant liver editing without off-target effects observed with AAV delivery of base editors.

3.4 Application of BE-eVLPs to the rd12 model of inherited retinal degeneration

In collaboration with David Liu's group, we applied BE-eVLPs to correct a disease-causing point mutation in an adult mouse model of a genetic retinal disorder. First, to assess tissue tropism and biodistribution of eVLPs within the retina, we produced eVLPs with a gag-Cre fusion to deliver Cre recombinase. These were injected subretinally into mT/mG Cre reporter mice, which constitutively express membrane-tagged tdTomato (mT) in all tissues of the body[215]. Upon Cre-mediated excision of the lox-stop-lox cassette, tdTomato expression is replaced with membrane-tagged eGFP (mG). 1 week post subretinal injection, the mT/mG mice were imaged by two-photon excitation. We noted efficient conversion of mT to mG in the RPE, with no gross morphological changes, indicating that the eVLPs were efficient and non-toxic (**Figure 3.2**). This supported the

application of eVLPs to the correction of therapeutically relevant genes within the eye, especially those that are expressed predominantly in the RPE.

Next, we moved to a model of inherited retinal disease. Loss-of-function mutations in multiple genes are associated with various forms of Leber congenital amaurosis (LCA), a family of monogenic retinal disorders that involve retinal degeneration, early-onset visual impairment, and eventual blindness [216,217]. Genome editing approaches hold promise to treat and cure congenital blindness; an ongoing clinical trial (NCT03872479) uses AAV-delivered Cas9 nucleases to disrupt an aberrant splice site in *CEP290* that is associated with rare Leber congenital amaurosis 10 (LCA10). Loss-of-function mutations in other genes, including the retinoid isomerohydrolase *RPE65*, are also candidates for *in vivo* correction using precision genome editing agents [80,218].

We investigated whether v4 BE-VLPs can restore visual function in a mouse model of LCA. *rd12* mice harbor a nonsense mutation in exon 3 of *Rpe65* (c.130C > T; p.R44X) that causes a near-complete loss of visual function [80,219]. A homologous mutation responsible for LCA has recently been identified in people [220], highlighting the clinical relevance of the *rd12* model.

We designed and produced v4 BE-VLPs encapsulating ABE8e-NG RNPs and an sgRNA (**Figure 3.3A**) that targets the *Rpe65*(R44X) mutation (hereafter referred to as ABE8e-NG-VLPs). ABE8e-NG-VLPs were pseudotyped with VSV-G to enable them to efficiently transduce retinal pigment epithelium (RPE) cells [80,221]. We injected ABE8e-NG-VLPs subretinally into 4-week-old *rd12* mice. In a separate cohort, we also subretinally injected replication-incompetent lentivirus encoding the identical ABE8e-NG and sgRNA constructs (ABE8e-NG-LV). We previously reported that lentiviral delivery of ABEs can successfully restore visual function in *rd12* mice [80].

Five weeks post-injection, we harvested RPE tissue and performed high-throughput sequencing of RPE genomic DNA (**Figure 3.3B**). NGS revealed that the VLPs and LV had an editing efficiency of 21% and 11.5%, respectively (**Figure 3.3C**). Notably, ABE8e-NG-VLPs

achieved 1.8-fold higher editing at the target base compared to ABE8e-NG-LV, even though BE-VLP delivery is transient.

Although we observed highly efficient correction of the target mutation, we also observed that both ABE8e-NG-VLP and ABE8e-NG-LV induced substantial levels of bystander editing (**Figure 3.3C**) due to the wide editing window of ABE8e-NG [222]. Indeed, the vast majority of edited alleles contained conversions at A_3, A_6, and/or A_8 as opposed to A_6 alone (**Figure 3.3D**). These bystander edits at positions A_3 and A_8 lead to *Rpe65* missense mutations C45R and L43P respectively, and we previously showed that the L43P mutation renders the *Rpe65* enzyme inactive [80]. Indeed, after performing scotopic electroretinography (ERG) to assess retinal cell response, we observed less than expected rescue of visual function in both ABE8e-NG-VLP-injected and ABE8e-NG-LV-injected eyes (**Figure 3.3E**). These results suggested that the wide base editing window of ABE8e-NG is not well suited to precisely correct the *Rpe65*(R44X) mutation.

To address this limitation, we designed and produced v4 BE-VLPs that encapsulate ABE7.10-NG, which exhibits a narrower editing window compared to ABE8e-NG [223]. Subretinal injection of ABE7.10-NG-VLPs into adult *rd12* mice led to 12% correction of the R44X mutation in RPE genomic DNA with virtually no bystander editing (**Figure 3.3F**). Specifically, we observed that ABE7.10-NG-VLP treatment resulted in 11% perfect R44X correction without bystander edits, a 9-fold improvement in perfect correction relative to ABE8e-NG-VLP treatment (**Figure 3.3G**). Furthermore, treatment with ABE7.10-NG-VLPs resulted in a 1.4-fold improvement in bystander-free correction relative to treatment with ABE7.10-NG-LV (a lentivirus encoding the identical ABE7.10-NG and sgRNA constructs), an additional demonstration that v4 BE-VLP transient delivery can achieve comparable or higher editing efficiencies compared to lentiviral BE delivery (**Figure 3.3G**).

We confirmed via Western blot that ABE7.10-NG-VLP treatment restored the expression of Rpe65 protein. Notably, lentiviral ABE7.10-NG-LV-treated eyes still expressed BE protein 5-

weeks post-injection, while eVLP ABE7.10-NG-VLP-treated eyes did not (**Figure 3.3I**), demonstrating the transient exposure of cells *in vivo* to base editors delivered using BE-VLPs. Importantly, ABE7.10-NG-VLPs successfully rescued visual function to similar levels relative to ABE7.10-NG-LV as measured by ERG of the treated eyes (**Figure 3.3H, J**). We previously showed that this level of ERG rescue corresponds to other improvements in visual function, including restoration of the visual chromophore and recovery of visual cortical responses [80]. These results demonstrate that BE-VLPs can mediate efficient correction of a pathogenic mutation in the mouse RPE with amelioration of the disease phenotype.

To further analyze editing outcomes, we extracted RNA from treated eyes and performed targeted high-throughput sequencing of specific cDNAs. As expected, in the BE-VLP treated eyes, we observed up to 64% of A•T-to-G•C conversion of the target adenine (A_6) in the on-target *Rpe65* transcript (**Figure 3.4A**). The higher proportion of corrected *Rpe65* transcripts compared to *Rpe65* genomic loci potentially reflects nonsense-mediated decay of uncorrected mRNAs.

BEs are known to exhibit low levels of transcriptome-wide Cas-independent off-target RNA editing [224]. To investigate this possibility, we assessed off-target RNA editing by ABE-VLPs and ABE-LVs by sequencing the *Mcm3ap* and *Perp* transcripts from treated eyes, two transcripts that were previously identified as potential candidates for off-target RNA editing based on their sequence similarity to the native TadA deaminase substrate [225]. We observed RNA off-target editing by ABE8e-NG-LV in both transcripts and low but detectable RNA off-target editing by ABE7.10-NG-LV at one adenine in *Perp* (**Figure 3.4B, C**). Notably, we did not detect any RNA off-target editing above background in these two transcripts by ABE8e-NG-VLPs or ABE7.10-NG-VLPs (**Figure 3.4B, C**). Collectively, these findings highlight the therapeutic utility of BE-VLPs as a DNA-free method for transiently delivering BE RNPs *in vivo* with high on-target editing and minimal off-target editing.

3.5 Discussion

Excitingly, non-viral delivery of BE RNPs was shown in this model to be equivalently efficient as viral vectors, the previous gold standard for *in vivo* delivery of genome editors. Non-viral delivery was previously hampered by low editing efficiencies, but in the *rd12* mouse, eVLPs effected equivalent on-target editing, increased purity of editing products with fewer bystander edits, and had no detectable off-target editing. Indeed, when we examined the RPE 3 weeks post-treatment, we only noted ABE expressed in the lentivirus treated group. This supports the use and increased safety of eVLP-mediated RNP delivery for the treatment of IRDs.

Although these are promising results, several additional features of eVLPs must be considered and addressed before they are further translated into human applications. One, the purification of eVLPs needs to be improved to create a GMP or pharmacological grade material. Ultracentrifugation pelleting of eVLPs greatly improved the purity, but other materials, such as organelles, may co-pellet with the particles. Additionally, it is unclear whether other human cell materials or DNA derived from the HEK293-based Gesicle cells are present. To address this, the considerable investment into lentiviral vector production for gene therapy can be leveraged and applied here. Secondly, it is unclear if eVLPs can be used to treat diseases of photoreceptors. VSV-G pseudotyped particles show excellent tropism toward the RPE, but photoreceptor transduction with retroviral particles is much more difficult and has yet to be demonstrated conclusively. Third, the immune response to retroviral particles was not investigated. In particular, people with pre-existing immunity to either MMLV or VSV-G could show decreased editing efficiency or unacceptable inflammation in response to dosing with eVLP. In a related point, the residence time and half-life of Cas9 and other MMLV proteins were not investigated *in vivo*, and an increase time could increase the risk of immunogenic responses.

However, in its totality, the developments reported here combine the one-time treatment potential of gene editing agents with the transient nature of RNPs to minimize the opportunity for unwanted off-target editing or DNA integration with the efficient, tissue-targeted nature of viral

transduction. Our findings thus suggest eVLPs as an attractive alternative to other delivery strategies for *in vivo* delivery of BEs for potent therapeutic effect.

3.6 Selected methods

BE-VLP production and purification

BE-VLPs were produced by transient transfection of Gesicle Producer 293T cells. Gesicle cells were seeded in T-75 flasks (Corning) at a density of 5×10^6 cells per flask. After 20–24 h, cells were transfected using the jetPRIME transfection reagent (Polyplus) according to the manufacturer's protocols. For producing v1–v3 BE-VLPs, a mixture of plasmids expressing VSV-G (400 ng), MLVgag-pro-pol (2,800 ng), MLVgag–ABE8e (1,700 ng), and an sgRNA (4,400 ng) were co-transfected per T-75 flask. For MLVgag–ABE8e:MLVgag-pro-pol stoichiometry optimization, the total amount of plasmid DNA for these two components was fixed at 4,500 ng and the relative amounts of each were varied. For producing v4 BE-VLPs, a mixture of plasmids expressing VSV-G (400 ng), MMLVgag-pro-pol (3,375 ng), MMLVgag–3xNES–ABE8e (1,125 ng), and an sgRNA (4,400 ng) were co-transfected per T-75 flask.

40–48 h post-transfection, producer cell supernatant was harvested and centrifuged for 5 min at 500 *g* to remove cell debris. The clarified VLP-containing supernatant was filtered through a 0.45 μm PVDF filter. For BE-VLPs that were used in cell culture, unless otherwise stated, the filtered supernatant was concentrated 100-fold using PEG-it Virus Precipitation Solution (System Biosciences; LV825A-1) according to the manufacturer's protocols. For BE-VLPs that were injected into mice, the filtered supernatant was concentrated 1000–3000-fold by ultracentrifugation using a cushion of 20% (w/v) sucrose in PBS. Ultracentrifugation was performed at 26,000 rpm for 2 h (4ºC) using either an SW28 rotor in an Optima XPN Ultracentrifuge (Beckman Coulter) or an AH-629 rotor in a Sorvall WX+ Ultracentrifuge (Thermo Fisher Scientific). Following ultracentrifugation, BE-VLP pellets were resuspended in cold PBS (pH 7.4) and centrifuged at 1,000 *g* for 5 min to remove debris. BE-VLPs were frozen at a rate of 1ºC/min and stored at -80ºC. BE-VLPs were thawed on ice immediately prior to use.

High-throughput sequencing

Following genomic DNA isolation, 1 µL of the isolated DNA (1–10 ng) was used as input for the first of two PCR reactions. Genomic loci were amplified in PCR1 using PhusionU polymerase (Thermo Fisher Scientific). PCR1 was performed as follows: 95 °C for 3 min; 30–35 cycles of 95 °C for 15 s, 61 °C for 20 s, and 72 °C for 30s; 72°C for 1 min. PCR1 products were confirmed on a 1% agarose gel. 1 µL of PCR1 was used as an input for PCR2 to install Illumina barcodes. PCR2 was conducted for nine cycles of amplification using a Phusion HS II kit (Life Technologies). Following PCR2, samples were pooled and gel purified in a 1% agarose gel using a Qiaquick Gel Extraction Kit (Qiagen). Library concentration was quantified using the Qubit High-Sensitivity Assay Kit (Thermo Fisher Scientific). Samples were sequenced on an Illumina MiSeq instrument (paired-end read, read 1: 200–280 cycles, read 2: 0 cycles) using an Illumina MiSeq 300 v2 Kit (Illumina).

High-throughput sequencing data analysis

Sequencing reads were demultiplexed using the MiSeq Reporter software (Illumina) and were analyzed using CRISPResso2[226]. Batch analysis mode (one batch for each unique amplicon and sgRNA combination analyzed) was used in all cases. Reads were filtered by minimum average quality score (Q > 30) prior to analysis. The following quantification window parameters were used: -w 20 -wc -10. Base editing efficiencies are reported as the percentage of sequencing reads containing a given base conversion at a specific position. Prism 9 (GraphPad) was used to generate dot plots and bar plots.

Lentiviral vector cloning and production

Lentiviral vectors were constructed via USER cloning into the lentiCRISPRv2 backbone (Addgene #135955). Lentiviral transfer vectors were propagated in NEB Stable Competent *E. coli* (New England Biolabs). HEK293T/17 (ATCC CRL-11268) cells were maintained in antibiotic-free DMEM supplemented with 10% fetal bovine serum (v/v). On day 1, 5×10^6 cells were plated in 10 mL of media in T75 flasks. The following day, cells were transfected with 6 µg of VSV-G

envelope plasmid, 9 µg of psPAX2 (plasmid encoding viral packaging proteins) and 9 µg of transfer vector plasmid (plasmid encoding the gene of interest) diluted in 1,500 µL Opti-MEM with 70 µL of FuGENE. Two days after transfection, media was centrifuged at 500 *g* for 5 min to remove cell debris following filtration using 0.45-µm PVDF vacuum filter. The lentiviruses were further concentrated by ultracentrifugation with a 20% (w/v) sucrose cushion as described above for eVLP production.

Animals

All mouse experiments were approved by the Broad Institute, the University of California, Irvine, and the University of Pennsylvania institutional animal care and use committees. Timed pregnant C57BL/6J mice for P0 studies were purchased from Charles River Laboratories (027). Wild-type adult C57BL/6J mice (000664) and pigmented *rd12* mice (005379) were purchased from the Jackson Laboratory. All mice were housed in a room maintained on a 12 h light and dark cycle with *ad libitum* access to standard rodent diet and water. Animals were randomly assigned to various experimental groups.

CIRCLE-seq

Circularization for In vitro Reporting of Cleavage Effects by sequencing (CIRCLE-seq) was performed and analyzed as described previously [193] save for the following modifications: For the Cas9 cleavage step, guide denaturation, incubation, and proteinase K treatment was conducted using the more efficient method described in the CHANGE-seq protocol [227]**.** Specifically, the sgRNA with the guide sequence “GCCCATACCTTGGAGCAACGG” was ordered from Synthego with their standard chemical modifications, 2’O-Methyl for the first three and last three bases, and phosphorothioate bonds between the first three and last two bases. A 5’ “G” nucleotide was included with the 20-nucleotide specific guide sequence to recapitulate the sequence expressed and packaged into VLPs. The sgRNA was diluted to 9 µM in nuclease-free water and re-folded by incubation at 90^{o}C for 5 min followed by a slow annealing down to 25^{o}C at a ramp rate of 0.1 ^{o}C/second. The sgRNA was complexed with Cas9 nuclease (NEB; M0386T) via a 10 min room

temperature incubation after mixing 5 µL of 10x Cas9 Nuclease Reaction Buffer provided with the nuclease, 4.5 µL of 1 µM Cas9 nuclease (diluted from the 20µM stock in 1x Cas9 Nuclease Reaction Buffer), and 1.5 µL of 9 µM annealed sgRNA. Circular DNA from mouse N2A cells was added to a total mass of 125 ng and diluted to a final volume of 50 µL. Following 1 h of incubation at 37°C, Proteinase K (NEB; P8107S) was diluted 4-fold in water and 5 µL of the diluted mixture was added to the cleavage reaction. Following a 15 min Proteinase K treatment at 37°C, DNA was A-tailed, adapter ligated, and USER-treated, and PCR-amplified as described in the CIRCLE-seq protocol [193]. Following PCR, samples were loaded on a preparative 1% agarose gel and DNA was extracted between the 300bp and 1kb range to eliminate primer dimers before sequencing on an Illumina MiSeq. Data was processed using the CIRCLE-seq analysis pipeline and aligned to the human genome Hg19 (GRCh37) with parameters: “read_threshold: 4; window_size: 3; mapq_threshold: 50; start_threshold: 1; gap_threshold: 3; mismatch_threshold: 6; merged_analysis: True”.

Amplicon sequencing of off-target sites nominated by CIRCLE-seq

We observed in prior work that exhaustively assessed ABE8e off-target sites nominated by CIRCLE-seq that off-target editing efficiency did not track well with the CIRCLE-seq read count [37]. However, nominated off-target sites where editing was observed shared some striking similarities. Namely, over 90.7% of the 54 off-target sites with validated off-target editing had zero mismatches or one mismatch to the guide in the 9 nucleotides proximal to the PAM. The few sites with more than 1 mismatch in this region were all edited with low efficiency (the bottom half of sites, when ranked by editing efficiency). Based on this knowledge, we chose to assess 14 off-target sites in our CIRCLE-seq list that showed one or fewer mismatches in the 9 nucleotides of the protospacer proximal to the PAM to increase the chance that we sequence a true off-target site.

Mouse subretinal injection

Mice were anesthetized by intraperitoneal injection of a cocktail consisting of 20 mg/mL ketamine and 1.75 mg/mL xylazine in phosphate-buffered saline at a dose of 0.1 mL per 20 g body weight, and their pupils were dilated with topical administration of 1% tropicamide ophthalmic solution (Akorn; 17478-102-12). Subretinal injections were performed under an ophthalmic surgical microscope (Zeiss). An incision was made through the cornea adjacent to the limbus at the nasal side using a 25-gauge needle. A 34-gauge blunt-end needle (World Precision Instruments; NF34BL-2) connected to an RPE-KIT (World Precision Instruments, no. RPE-KIT) by SilFlex tubing (World Precision Instruments; SILFLEX-2) was inserted through the corneal incision while avoiding the lens and advanced through the retina. Each mouse was injected with 1 µL of experimental reagent (lentivirus or VLP) per eye. Lentivirus titer was >$1x10^9$ TU/mL as measured by the QuickTiter™ Lentivirus Titer Kit (Cell Biolabs; VPK-107-5). BE-VLPs were normalized to a titer of $4x10^{10}$ VLPs/µL, corresponding to an encapsulated BE protein content of 3 pmol/µL. After injections, pupils were hydrated with the application of GenTeal Severe Lubricant Eye Gel (0.3% Hypromellose, Alcon) and kept for recovery.

RPE dissociation and genomic DNA and RNA preparation

Under a light microscope, mouse eyes were dissected to separate the posterior eyecup (containing RPE, choroid and sclera) from the retina and anterior segments. Each posterior eyecup was immediately immersed in 350 µl of RLT Plus tissue lysis buffer provided with AllPrep DNA/RNA Mini Kit (Qiagen; 80284). After 1 min incubation, RPE cells were detached in the lysis buffer from the posterior eyecup by gentle pipetting, followed by a removal of the remaining posterior eyecup. The lysis buffer containing RPE cells was further processed for DNA and RNA extraction using the AllPrep DNA/RNA Mini Kit protocol. The final DNA and RNA were eluted in 30 µL and 15 µL water, respectively. cDNA synthesis was performed using the SuperScript™ III First-Strand Synthesis SuperMix (Thermo Fisher; 18080400).

Western blot analysis of mouse RPE tissue extracts

To prepare the protein lysate from the mouse RPE tissue, the dissected mouse eyecup, consisting of RPE, choroid, and sclera, was transferred to a microcentrifuge tube containing 30 µL of RIPA buffer with protease inhibitors and homogenized with a motor tissue grinder (Fisher Scientific; K749540-0000) and centrifuged for 30 min at 20,000 *g* at 4°C. The resulting supernatant was pre-cleared with Dynabeads Protein G (Thermo Fisher; 10003D) to remove contaminants from blood prior to gel loading. Twenty µL of RPE lysates pre-mixed with NuPAGE LDS Sample Buffer (Thermo Fisher; NP0007) and NuPAGE Sample Reducing Agent (Thermo Fisher; NP0004) was loaded into each well of a NuPAGE 4-12% Bis-Tris gel (Thermo Fisher; NP0321BOX), separated for 1 h at 130 V and transferred onto a PVDF membrane (Millipore; IPVH00010). After 1 h blocking in 5% (w/v) non-fat milk in PBS containing 0.1% (v/v) Tween-20 (PBS-T), the membrane was incubated with primary antibody, mouse anti-RPE65 monoclonal antibody (1:1,000; in-house production) [228], diluted in 1% (w/v) non-fat milk in PBS-T overnight at 4°C. After overnight incubation, membranes were washed three times with PBS-T for 5 min each and then incubated with goat anti-mouse IgG-HRP antibody (1:5,000; Cell Signaling Technology; 7076S) for 1 h at room temperature. After washing the membrane three times with PBS-T for 5 min each, protein bands were visualized after exposure to SuperSignal West Pico Chemiluminescent substrate (Thermo Fisher; 34580). Membranes were stripped and reprobed for ABE and β-actin expression using mouse anti-Cas9 monoclonal antibody (1:1,000; Invitrogen; MA523519) and rabbit anti-β-actin polyclonal antibody (1:1,000; Cell Signaling Technology; 4970S), following the same protocol. Corresponding secondary antibodies were goat anti-mouse IgG-HRP antibody (1:5,000; Cell Signaling Technology; 7076S) and goat anti-rabbit IgG-HRP antibody (1:5,000; Cell Signaling Technology; 7074S).

Electroretinography

Prior to recording, mice were dark adapted for 24 h overnight. Under a safety light, mice were anesthetized by intraperitoneal injection of a cocktail consisting of 20 mg/mL ketamine and 1.75 mg/mL xylazine in phosphate-buffered saline at a dose of 0.1 mL per 20 g body weight, and

their pupils were dilated with topical administration of 1% tropicamide ophthalmic solution (Akorn; 17478-102-12) followed by 2.5% hypromellose (Akorn; 9050-1) for hydration. The mouse was placed on a heated Diagnosys Celeris rodent ERG device (Diagnosys LCC). Ocular electrodes were placed on the corneas, and the reference electrode was positioned subdermally between the ears. The eyes were stimulated with a green light (peak emission 544 nm, bandwidth ~160 nm) stimulus of -0.3 log ($cd \cdot s/m^2$). The responses for 10 stimuli with an inter-stimulus interval of 10 s were averaged together, and the a- and b-wave amplitudes were acquired from the averaged ERG waveform. The ERGs were recorded with the Celeris rodent electrophysiology system (Diagnosys LLC) and analyzed with Espion V6 software (Diagnosys LLC).

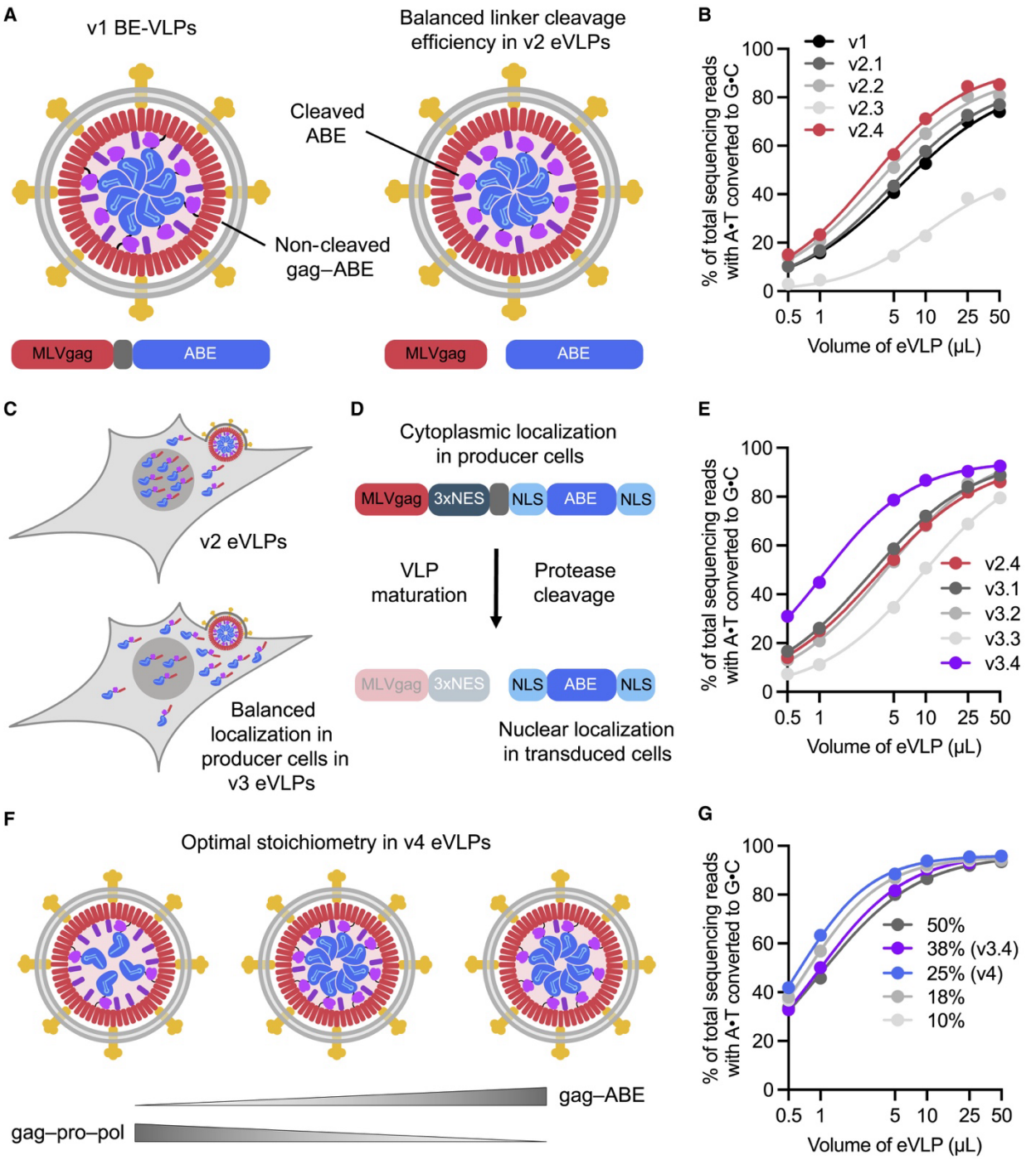


Figure 3.1 Summary of eVLP development from v1 to v4. (A) More efficient linker cleavage leads to improved cargo release after VLP maturation. (B) Adenine base editing efficiencies of v1 and v2 BE-eVLPs at position A_7 of the *BCL11A* enhancer site in HEK293T cells. (C) Improved localization of cargo in producer cells leads to more efficient incorporation into eVLPs. (D) Installing a 3xNES motif upstream of the cleavable linker encourages cytoplasmic localization of

gag–3xNES–cargo in producer cells but nuclear localization of free ABE cargo in transduced cells. (E) Adenine base editing efficiencies of v2.4 and v3 BE-eVLPs at position A_7 of the *BCL11A* enhancer site in HEK293T cells. (F) The optimal gag–cargo:gag–pro–pol stoichiometry balances the amount of cargo protein per particle with the amount of MMLV protease required for efficient particle maturation. (G) Adenine base editing efficiencies of v3.4 eVLPs with different gag–ABE:gag–pro–pol stoichiometries at position A_7 of the *BCL11A* enhancer site in HEK293T cells. Legend denotes % gag–ABE plasmid of the total amount of gag–ABE and gag–pro-pol plasmids. (B, E, and G) Values and error bars reflect mean ± SEM of n = 3 biological replicates. Data were fitted to four-parameter logistic curves using nonlinear regression. Figure adapted from Banskota *et al* and generated in David R. Liu's laboratory.

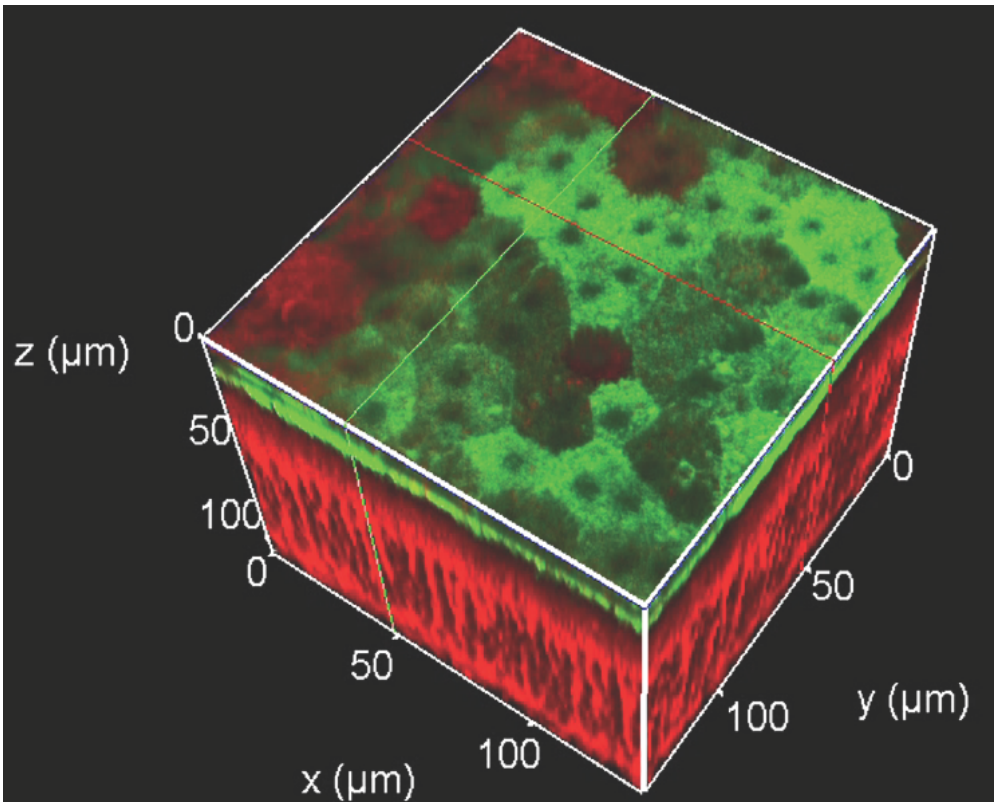


Figure 3.2 *In vivo* delivery of VSV-G pseudotyped Cre-eVLPs. Cre-eVLPs pseudotyped with VSV-G were produced and injected subretinally into mT/mG Cre reporter mice. 1 week post-treatment, eyes were enucleated and imaged *via* two-photon excitation. The RPE is found at z = 0 μm. Efficient conversion of mT (red) to mG (green) was observed with no apparent toxicity. Data generated in part by Grazyna Palczewska.

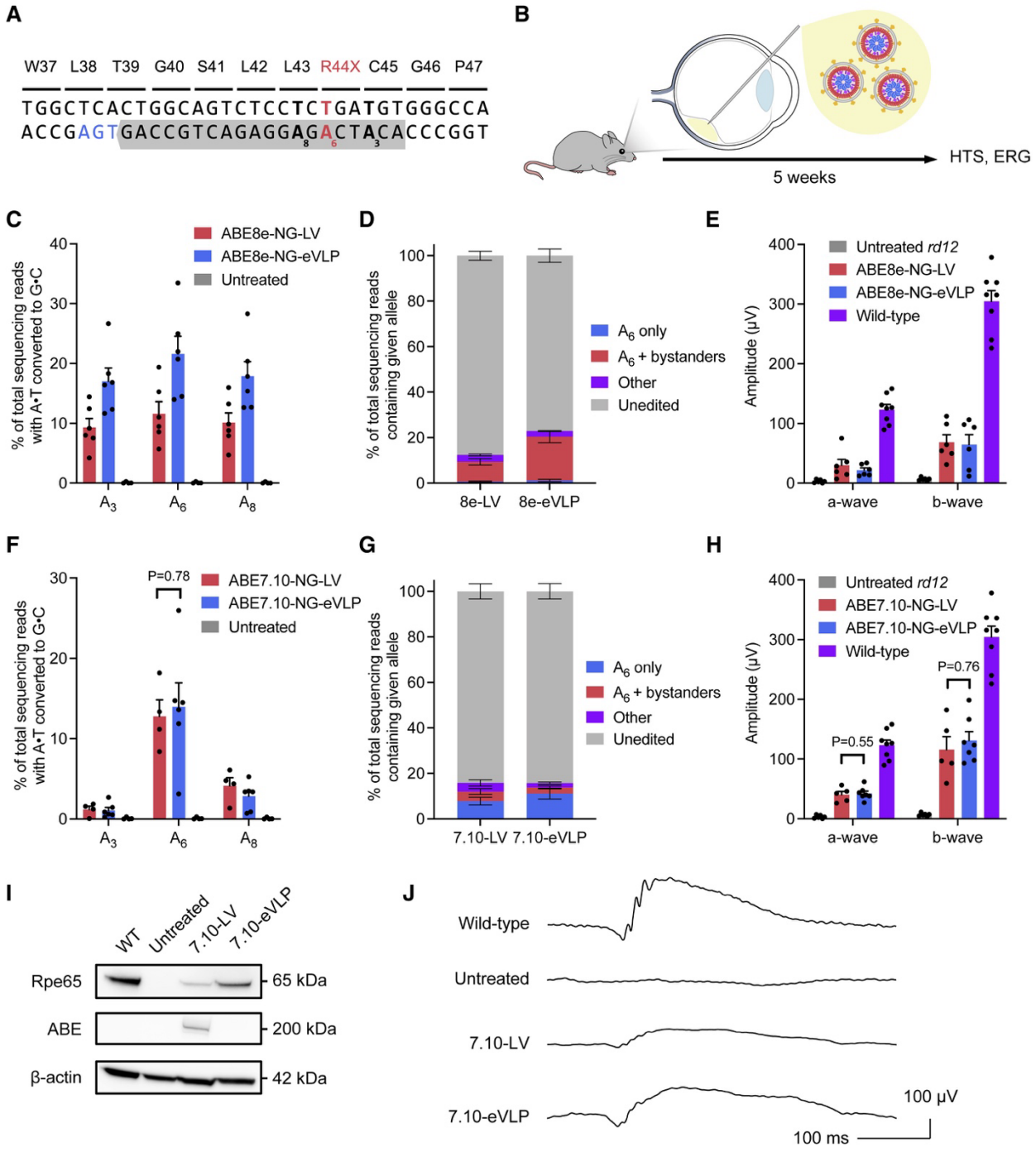


Figure 3.3 *In vivo* base editing by v4 BE-eVLPs in a mouse model of genetic blindness. (A) Schematic of *Rpe65* exon 3 surrounding the R44X mutation (in red), which can be corrected by an A·T-to-G·C conversion at position A_6 in the protospacer (shaded gray, PAM in blue). (B) Schematic of subretinal injections. Five weeks post-injection, phenotypic rescue was assessed via ERG and tissues were subsequently harvested for sequencing. HTS, high-throughput

sequencing; ERG, electroretinography. (C) Adenine base editing efficiencies at positions A_3, A_6, and A_8 of the protospacer in genomic DNA harvested from *rd12* mice. Data are shown as individual data points and mean ± SEM for n = 6 mice (both treated groups) or n = 4 mice (untreated). (D) Allele frequency distributions of genomic DNA harvested from treated *rd12* mice. Data are shown as mean ± SEM for n = 6 mice. 8e-LV, ABE8e-NG-LV; 8e-eVLP, v4 ABE8e-NG-eVLP. (E) Scotopic a- and b-wave amplitudes measured by ERG following overnight dark adaptation. Data are shown as individual data points and mean ± SEM for n = 8 mice (wild-type), n = 6 mice (ABE8e-NG-LV and v4 ABE8e-NG-eVLP) or n = 4 mice (untreated). (F) Adenine base editing efficiencies at positions A_3, A_6, and A_8 of the protospacer in genomic DNA harvested from *rd12* mice. Data are shown as individual data points and mean ± SEM for n = 6 mice (v4 ABE7.10-NG-eVLP) or n = 4 mice (ABE7.10-NG-LV and untreated). p values were calculated using a two-sided t test. (G) Allele frequency distributions of genomic DNA harvested from treated *rd12* mice. Data are shown as mean ± SEM for n = 6 mice (v4 ABE7.10-NG-eVLP) or n = 4 mice (ABE7.10-NG-LV and untreated). 7.10-LV, ABE7.10-NG-LV; 7.10-eVLP, v4 ABE7.10-NG-eVLP. (H) Scotopic a- and b-wave amplitudes measured by ERG following overnight dark adaptation. Data are shown as individual data points and mean ± SEM for n = 8 mice (wild-type), n = 7 mice (v4 ABE7.10-NG-eVLP), n = 5 mice (ABE7.10-NG-LV), or n = 4 mice (untreated). p values were calculated using a two-sided t test. (I) Western blot of protein extracts from RPE tissues of wild-type, untreated, v4 ABE7.10-NG-eVLP-treated, and ABE7.10-NG-LV-treated mice. (J) Representative ERG waveforms from wild-type, untreated, ABE7.10-NG-LV-treated, and v4 ABE7.10-NG-eVLP-treated mice. Figure adapted from Banskota *et al* and generated in David R. Liu and Krzysztof Palczewski's laboratory.

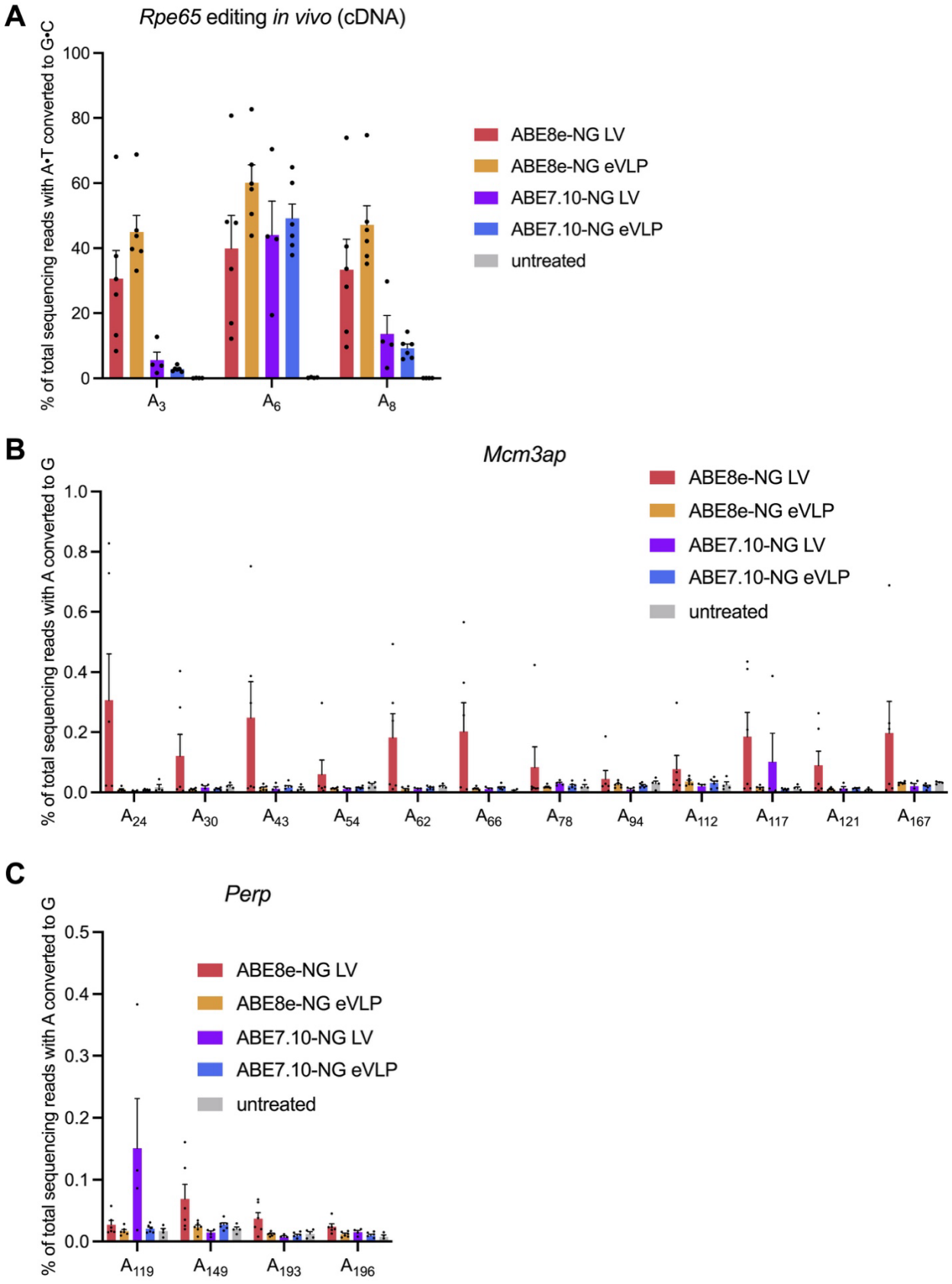

A
Rpe65 editing in vivo (cDNA)
% of total sequencing reads with A•T converted to G•C
100
80
60
40
20
0
A3
A6
A8
ABE8e-NG LV
ABE8e-NG eVLP
ABE7.10-NG LV
ABE7.10-NG eVLP
untreated
B
Mcm3ap
% of total sequencing reads with A converted to G
1.0
0.8
0.6
0.4
0.2
0.0
A24
A30
A43
A54
A62
A66
A78
A94
A112
A117
A121
A167
ABE8e-NG LV
ABE8e-NG eVLP
ABE7.10-NG LV
ABE7.10-NG eVLP
untreated
C
Perp
% of total sequencing reads with A converted to G
0.5
0.4
0.3
0.2
0.1
0.0
A119
A149
A193
A196
ABE8e-NG LV
ABE8e-NG eVLP
ABE7.10-NG LV
ABE7.10-NG eVLP
untreated

Figure 3.4 Sequencing analysis of RPE cDNA after v4 BE-eVLP or lentivirus treatment. (A) v4 BE-eVLP and lentivirus treatment led to 50%–60% of A·T-to-G·C conversion at the target adenine (A_6) of the *Rpe65* transcript. Data are shown as individual data points and mean values ± SEM for n = 6 (ABE8e-NG-LV, ABE8e-NG-eVLP, and ABE7.10-NG-eVLP), or n = 4 (ABE7.10-NG-LV and untreated) mice. (B and C) Off-target A-to-G RNA editing by v4 BE-eVLPs and lentiviruses as measured by high-throughput sequencing of the (B) *Mcm3ap* and (C) *Perp* transcripts. Data are shown as individual data points and mean values ± SEM for n = 6 (ABE8e-NG-LV, ABE8e-NG-eVLP, and ABE7.10-NG-eVLP), or n = 4 (ABE7.10-NG-LV and untreated) mice. Figure adapted from Banskota *et al* and generated in David R. Liu's laboratory.

CHAPTER 4

Development of eVLPs to support prime editing

This chapter is derived in part from the following manuscript published in *Nature Biotechnology:*

An, M. *et al*. Engineered virus-like particles for transient delivery of prime editor ribonucleoprotein complexes in vivo. *Nature Biotechnology* (2024).

© 2024 the Authors.

CHAPTER 4

Development of eVLPs to support prime editing[229]

4.1 Prime editing in the eye

The application of PEs retinal genes and diseases has moved quickly. Notable therapeutically relevant genes that were targeted in the mouse include *Pde6a*[173], *Pde6b*[188], *Vegfr2*[230], and *Rpe65*[231,232]. These were all delivered *via* dual-AAVs, which has been proven to be efficacious in installing base and prime edits *in vivo.* However, virally-expressed base editors have been shown to increase off-target editing *in vivo*; therefore, clinical translation of PE would likely require transient, non-viral delivery methods, such as the eVLPs previously developed for base editors[209]. Because prime editors can address virtually all of the mutations that lead to IRDs, as well as opening the possibility for large insertions of DNA and other forms of genetic engineering, efficient delivery of PEs as RNPs or in other non-viral forms could prove transformative for IRD treatment.

4.2 Development of PE-eVLPs

As base editors were successfully delivered *in vivo* with the eVLP architecture, the laboratory of David R. Liu applied the same architecture for the delivery of prime editors (PE). However, they observed very low editing efficiencies (<1% editing) *in vitro* with this v1.1 PE-eVLP at the highest doses tested. Thus, further optimization of eVLPs would be required to support therapeutic *in vivo* prime editing.

The first series of modifications made were to exchange the prime editing guide RNA (pegRNA) with an engineered pegRNA (epegRNA) for a v1.2 PE-eVLP. These epegRNAs were demonstrated to improve pegRNA stability with the inclusion of a 3' pseudoknot (evoPreQ1 pseudoknot) that protects the 3' end of the pegRNA from exonucleolytic degradation[84]. The second change was to replace the PE2 protein with PEmax, which included additional mutations in Cas9, an improved linker, codon optimization, and improved NLS compared to PE2 to create

the v1.3 PE-eVLP[83]. Both of these changes modestly improved PE efficiencies compared to v1.1 PE-eVLPs.

As the MMLV gag polyprotein requires protease cleavage to mature, and because the reverse transcriptase (RT) domain of PEmax is derived from MMLV, they hypothesized that the RT was being cleaved by MMLV protease. Thus, they created a v2.1 PE-eVLP by removing the protease recognition site from the RT, which improved PE efficiency. In contrast with dual-AAV approaches to package PEmax, deletion of the RNaseH domain in PE-eVLPs lowered editing efficiencies[88]. The next improvement made was to relocate the NES within the gag subdomain to improve PE packaging by eliminating unproductive cleavage products, creating the v2.2 PE-eVLP. Lastly, they added additional GGS linkers around the protease cleavage sites to improve protease access to the site for processing, creating the v2.3 PE-eVLP.

A series of *in vitro* assays showed that epegRNAs, and not PEmax proteins, were limiting in the PE-eVLP packaging and negatively impacted PE efficiency. As well, epegRNAs, with their 3' extensions compared to sgRNAs, demonstrate considerably less affinity for the Cas9 apoprotein[84]. Thus, improvements in epegRNA recruitment and stability would likely improve PE efficiencies. To improve epegRNA recruitment, the Liu group exploited aptamer systems, which have specified RNA-protein interactions. With the MCP-MS2 system, the MS2 RNA motif is bound by the MS2 coat protein (MCP)[233]. They inserted the MCP module into the gag-pol polyprotein and the MS2 motif into the ST2 loop of the epegRNA scaffold and then reoptimized the plasmid transfection stoichiometry, as WT gag-pol, gag-MCP-pol, and gag-PEmax could compete against each other in PE-eVLP packaging. These changes created the v3 PE-eVLP, which further improve efficiency. Lastly, as the PE3 strategy utilizes a nicking sgRNA (ngRNA) alongside the epegRNA, the addition of MS2-tagged ngRNAs in a 1:4 ratio with MS2-tagged epgRNAs together in the same PE-eVLP particle further improved editing efficiencies. Thus, through a series of rationally driven changes to eliminate bottlenecks in PEmax and guide RNA packaging and loading, the Liu group created a v3 PE-eVLP that greatly improved efficiencies over the original v1.1 PE-eVLP

based on the v4 BE-eVLP architecture, indicating that PE has unique considerations compared to the simpler packaging of base editors.

Though the v3 PE-eVLP was greatly improved, they noted that the absolute number of PE particles packaged per eVLP was half that of the ABE particles packaged per eVLP. Thus, they investigated an alternative recruitment strategy for PE RNPs. Utilizing an alternative mechanism for PE recruitment that does not rely on gag-PE fusion, they chose to utilize the P3-P4 coil-coil peptide system, where two alpha-helices strongly interact with each other noncovalently. Inserting the P3 sequence in the gag-pol polypeptide and fusing P4 to the N-terminus of PEmax, they demonstrated successful and increased recruitment of PEmax into the PE-eVLP. However, a dual fusion of gag-MCP-P3-pol was not efficient, so they introduced the COM-Com apatamer system for epegRNA/ngRNA recruitment. Collectively, these changes resulted in a v3b PE-eVLP system. They also noted a sequence dependent difference in editing efficiency, with some edits and sites comparably edited with v3 or v3b systems, while v3b outperformed v3 at selected sites with select edits. A summary of the different PE-eVLP architectures can be found in **Figure 4.1.**

4.3 Application of PE-eVLPs to the rd6 *and* rd12 *IRD models*

Next, to test the therapeutic utility of *in vivo* delivery of prime editors via PE-eVLPs, we sought to correct mutations that cause retinal diseases in mice. The *rd6* mouse[234] is a model of autosomal recessive retinal degeneration that contains a 4-bp deletion in the splice donor of the membrane-type frizzled-related protein (*Mfrp*) gene, resulting in skipping of exon 4[235] (**Figure 4.2a**). The mutation leads to early onset, but slowly progressive, retinal degeneration that leads to a loss of detectable electroretinography (ERG) responses by 70 weeks of age[235]. *rd6* mice show scattered white retinal dots, which are characteristic of human flecked retinal diseases, and genetic defects in *MFRP* in humans have been shown to lead to syndromes of microphthalmos and retinitis pigmentosa[236]. Given the unique ability of prime editing to directly and precisely correct a 4-bp deletion, and the potential of prime editing to treat congenital blindness[162], we

investigated whether PE-eVLPs could achieve efficient correction of the pathogenic mutation in the *rd6* model.

The Liu group developed a PE3b strategy—in which the ngRNA is designed to nick only after the desired prime edit is installed into the edited strand[81,237]—to correct this 4-bp deletion in *Mfrp* (**Figure 4.2a**). First, they generated an N2A cell line containing the pathogenic *Mfrp* mutation (N2A^{Mfrp}) by installing the 4-bp deletion at the endogenous locus using prime editing, and clonally expanding cells homozygous for the mutation. Similarly, we generated a fluorescent reporter that has a frameshifted eGFP downstream of mCherry and a fragment of the *rd6* genomic locus (**Figure 4.3**). Using plasmid transfection in N2A^{Mfrp} cells, they screened three epegRNA protospacer sequences coupled with varying PBS (9-13 nt) and RTT (9-25 nt) lengths as well as eleven candidate ngRNAs. The best PE3b strategy yielded on average 18% correction of the mutation with 0.66% indels following plasmid transfection in N2A^{Mfrp} cells Encouraged by this result, they produced v3 PE3b-eVLPs pseudotyped with VSV-G to efficiently transduce the retinal pigment epithelium (RPE) cells[80,209,221], where MFRP is most abundantly expressed[235].

To characterize these eVLPs *in vivo*, we performed subretinal injections into 5-week-old *rd6* mice to administer the mutation-correcting v3 PE3b-eVLPs (**Figure 4.2b**), harvested the RPE tissue 3 weeks after injection, and performed high-throughput sequencing (HTS) on the extracted genomic DNA. Sequencing analysis revealed on average 15% bulk retinal editing with v3 PE3b-eVLPs (**Figure 4.2c**). Western blot revealed that MFRP expression was restored in the v3 PE3b-eVLP treated eyes (**Figure 4.2d**). We performed immunohistochemistry on the RPE flatmounts and confirmed robust restoration of MFRP expression in the RPE (**Figure 4.2e**). To assess off-target prime editing from v3 PE3b-eVLP treatment, we performed CIRCLE-seq[193] using the genomic DNA extracted from liver cells of *rd6* mice to nominate potential off-target sites using Cas9 complexed with the epegRNA or the ngRNA used to correct *Mfrp*. We then performed HTS on the genomic DNA extracted from retina tissue of untreated or v3 PE3b-eVLP-treated *rd6* mice at the top 10 candidate off-target sites nominated by CIRCLE-seq. We did not detect any off-

target editing in PE-eVLP-treated samples (>0.1%, the limit of detection of the targeted high-throughput sequencing method used) (**Figure 4.2f, g**), consistent with the inherently high DNA specificity of prime editing[81,238-248] and transient exposure of cells to the editors from PE-eVLP treatment. PE-eVLP treatment additionally did not induce any morphological changes or signs of toxicity as assessed by histology of treated and untreated eye cryosections (**Figure 4.4**).

Finally, to further test the ability of PE-eVLPs to mediate therapeutic *in vivo* prime editing, we applied PE-eVLPs to treat the *rd12* mouse model[219], which displays more severe retinal degeneration that allows evaluation of disease phenotype rescue. The *rd12* model contains a nonsense mutation in exon 3 of the *Rpe65* gene (c.130C > T; p.R44X) that leads to premature termination of the RPE65 protein (**Figure 4.2h**). The mutation leads to relatively slow retinal anatomical degeneration, but physiological ERG responses are severely diminished from 3 weeks of age[219]. The corresponding mutation in humans has been identified and in homozygous form causes Leber congenital amaurosis (LCA)[220]. We previously demonstrated partial rescue of this disease phenotype using BE-eVLPs[209]. However, base editing at this site generates bystander edits at nearby A•T base pairs that may inactivate the *RPE65* enzyme and cause adverse effects[80], whereas the mechanism of prime editing inherently avoids bystander editing[81].

We developed a PE3b strategy to correct the *Rpe65* R44X mutation (**Figure 4.2h**) by screening a panel of epegRNAs with varying PBS lengths (8-11 nt) and RTT lengths (11-25 nt) and seven candidate ngRNAs via plasmid transfection in an engineered NIH 3T3 cell line[80] containing the corresponding mutation. The most promising PE3b strategy yielded 46% precise correction with 0.58% indels. We performed subretinal injection of 5-week-old *rd12* mice with mutation-correcting v3 PE3b-eVLPs. We harvested RPE tissues 5 weeks after injection and performed HTS on the extracted genomic DNA. We observed on average 7.2% correction of the mutation in bulk RPE tissue (**Figure 4.2i**). This editing efficiency is higher than the reported value from triple-AAV[232] and low-dose dual-vector AAV mediated PE delivery[231], and comparable to that

achieved by high-dose dual-vector AAV mediated PE delivery[231], but using a virus-free, single-particle delivery method.

We further analyzed *Rpe65* transcripts in the extracted RNA by sequencing the cDNA. Editing was enriched at the transcript level, achieving on average 14% correction of the target mutation (**Figure 4.2j**), presumably due to nonsense-mediated decay accelerating the degradation of uncorrected transcripts and enrichment of the major *RPE65*-expressing RPE cells that are preferentially transduced by PE-eVLPs among other cell types co-collected from tissue dissection. We confirmed robust expression of full-length Rpe65 in v3 PE3b-eVLP-treated eyes by western blot (**Figure 4.2k**). ERG of the v3 PE3b-eVLP-treated animals indeed showed substantial rescue of visual function in response to the stimuli compared to the untreated eyes (**Figure 4.2l, m**). We nominated potential off-target sites associated with the *rd12* epegRNA or ngRNA again by performing CIRCLE-seq with the genomic DNA extracted from liver cells of *rd12* mice. We assessed the off-target prime editing at the top 10 CIRCLE-seq-nominated off-target sites associated with the *rd12* epegRNA or ngRNA, by performing HTS on genomic DNA extracted from retinal tissue of untreated or v3 PE3b-eVLP treated *rd12* mice. Once again, we did not detect any off-target prime editing above the 0.1% limit of detection (**Figure 4.5**). Together, these results demonstrate that *in vivo* application of optimized PE-eVLPs can correct a pathogenic mutation and partially rescue disease phenotype.

4.4 Discussion

In the mouse retina, a single injection of v3 PE3-eVLPs precisely corrected a pathogenic 4-bp deletion in *Mfrp* in the *rd6* model of retinal degeneration, restoring production of full-length MFRP protein. In the *rd12* mouse model of genetic blindness, v3 PE3-eVLPs achieved comparable levels of prime editing as a recently reported triple-vector AAV-PE system[232], but using a non-viral, single-particle delivery vehicle, resulting in partial rescue of visual function. These findings demonstrate that v3 and v3b PE-eVLPs can achieve prime editing efficiency comparable to that attained using an AAV-PE delivery system, while avoiding other drawbacks of

viral delivery systems such as prolonged editor expression that increases off-target editing and the risk of oncogenic DNA integration[249,250]. To our knowledge, these findings also represent the first use of prime editor RNPs to achieve phenotypic rescue of an animal model of genetic disease.

While v3 and v3b PE-eVLPs demonstrated therapeutically relevant levels of editing in *in vivo* applications, PE-eVLP systems would benefit from the continued engineering effort for the next-generation prime editors as well as VLP packaging and transduction systems with improved potency. Furthermore, the engineering of envelope proteins that have specific tissue tropisms could expand the scope of PE-eVLP applications to additional tissues and organs. Especially for CNS editing, envelope protein engineering to facilitate either broad transduction or cell-type specific transduction targeting cell populations implicated in disease will be instrumental to advancing the PE-eVLPs for therapeutic applications in the CNS editing. The possibility that single-dose, transient delivery of prime editor RNPs by PE-eVLPs may mitigate clinically relevant immunogenicity[251] warrants further investigation. Lastly, future optimization of large-scale eVLP production, including the adoption of suspension producer cells, scalable purification methods, and high-throughput quality control and titering methods, will be necessary to fully realize the therapeutic potential of eVLPs. Nonetheless, the PE-eVLP system reported here offers unique advantages of non-viral, single-particle delivery of prime editors in their most transient form as RNPs rather than DNA or mRNA, with associated safety and target specificity benefits.

4.5 Selected methods

Animals

Retinal degeneration mouse models *rd6* (003684) and *rd12* (005379) were purchased from the Jackson Laboratory. All experiments involving live animals were approved by the Broad Institute and the University of California, Irvine. Mouse housing facilities were maintained on a 12 h light/ 12 h dark cycle with ad libitum access to standard rodent diet and water. Animals were randomly assigned to various experimental groups.

PE-eVLP production

eVLPs were produced as previously described[209]. Briefly, Gesicle Producer 293T cells were plated at a density of 5 x 10^6 cells per flask in 10 mL of DMEM + 10% FBS media in T75 flask (Corning). 18-24 h after seeding, a mixture of plasmids was transfected to producer cells with jetPRIME transfection reagent (Polyplus) following the manufacturer's protocol. For production of v3 PE-eVLPs, plasmids expressing VSV-G (400 ng), wild-type MMLV gag-pol (2813 ng), gag-MCP-pol (1125 ng), gag-PE (563 ng) and MS2-guide RNA (4400 ng MS2-epegRNA for v3 PE2-eVLP; 3520 ng MS2-epegRNA and 880 ng MS2-ngRNA for v3 PE3-eVLP) were co-transfected to each T75 flask. For production of v3b PE-eVLPs, plasmids expressing VSV-G (400 ng), wild-type MMLV gag-pol (2813 ng), gag-COM-pol (2000 ng), gag-P3-pol (422 ng), P4-PE (422 ng) and COM-gRNAs (4400 ng COM-epegRNA for v3b PE2-eVLP; 3520 ng COM-epegRNA and 880 ng COM-ngRNA for v3b PE3-eVLP) were co-transfected to each T75 flask. 40-48 h after transfection, supernatants were collected and centrifuged at 500 g for 5 min. Then the supernatant was filtered through 0.45-μm PVDF filter. For PE-eVLPs used with cultured cells, 5x PEG-it Virus Precipitation Solution (System Biosciences; LV825A-1) was subsequently added to the supernatant to precipitate eVLPs overnight at 4°C. The next day, the eVLPs were pelleted by centrifugation at 1,500 g for 30 min at 4 °C and were concentrated 100-fold by resuspending in 100 μL of Opti-MEM (Life Technologies). All eVLPs tested for optimization experiments in cell culture were concentrated uniformly using the above mentioned method to facilitate direct comparison of PE-eVLP potency at the same volume of eVLPs transduced. PE-eVLPs concentrated by this method contain approximately 2.5 x10^8 eVLPs per μL. For PE-eVLPs used *in vivo*, eVLPs were concentrated using a 20% (w/v) sucrose in PBS cushion solution via ultracentrifugation at 26,000 rpm for 2 h at 4 °C using an SW28 rotor in an Optima XPN Ultracentrifuge (Beckman Coulter). The eVLP pellets were resuspended in cold PBS solution following ultracentrifugation. The eVLP solution was further centrifuged at 1,000 g for 5 min on a fixed-angle tabletop centrifuge to remove debris. eVLPs purified by ultracentrifugation and used for *in vivo* applications were resuspended in a minimum volume of PBS solution to maximize the

dose of PE-eVLPs within the permitted volume of injection. For short-term storage, eVLPs were stored at 4 °C for up to one week. For long-term storage, eVLPs were stored at -80 °C and thawed on ice immediately prior to use. Repeated freeze-thaw was avoided.

High-throughput sequencing of genomic DNA samples

High-throughput sequencing was performed as described previously[81]. Primers used for the amplification of genomic loci and corresponding amplicons are listed in Supplementary Table 2. Briefly, 1-5 μL of cell lysate containing genomic DNA described above was used directly for the amplification of the target locus in the first round of PCR (PCR1). For base substitution edits, the target locus was amplified using Phusion U Green Multiplex PCR Master Mix (Thermo Fisher Scientific) under the following condition: 98 °C (3 min); 30 cycles of 98 °C (10 s), 61 °C (20 s), 72 °C (40 s); 72 °C (2 min). For insertion and deletion edits that are more susceptible to PCR bias, PCR1 was monitored using SYBR Green fluorescence with quantitative PCR (qPCR) and the reaction was stopped at the exponential phase to avoid over-amplification of the target locus. Subsequently, 1-2 μL of PCR1 product was used as a template for the second round of PCR (PCR2) to append unique Illumina barcodes. PCR2 was conducted using Phusion U Green Multiplex PCR Master Mix under the following condition: 98 °C (3 min); 10 cycles of 98 °C (10 s), 61 °C (20 s), 72 °C (30 s); 72 °C (2 min). PCR2 products were pooled and purified on 1.5 % agarose gel by gel extraction using QIAquick Gel Extraction Kit (Qiagen). The library was quantified by Qubit dsDNA HS Assay Kit (Thermo Scientific) and was sequenced using Illumina MiSeq 300 v2 Kit (Illumina) on Illumina MiSeq instrument.

High-throughput sequencing data analysis

High-throughput sequencing reads were demultiplexed using the MiSeq Reporter software (Illumina). Data analysis was conducted using CRISPResso2 as previously described[83]. Briefly, reads were filtered by minimum average quality score (Q > 30) prior to analysis. CRISPResso2 analysis was performed with “discard_indel_reads” on, and the quantification window was set to encompass at least 10 nucleotides upstream and downstream of the pegRNA

and/or ngRNA nick site. Prime editing efficiency was calculated as the percentage of reads with the desired editing without indels divided by the total number of reference-aligned reads. Indel frequency was calculated as the number of discarded reads divided by the total number of reference-aligned reads. The lower limit of detection is assumed to be 0.1%, defined by the error rate of the high-throughput sequencing method used.

Subretinal injection

The injection mix for subretinal injection was prepared immediately before injection by mixing 15-20 µL of PE-eVLP with 0.3 µL AAV-GFP (Addgene; 105530-AAV1). Mice were anesthetized by intraperitoneal injection of a cocktail consisting of 20 mg/mL ketamine and 1.75 mg/mL xylazine in phosphate-buffered saline at a dose of 0.1 mL per 20 g body weight, and their pupils were dilated with topical administration of 1% tropicamide ophthalmic solution (Akorn; 17478-102-12) and 10% phenylephrine (Valeant # 42702-0103-05). Subretinal injections were performed under an ophthalmic surgical microscope (Zeiss). The corneas were hydrated with the application of GenTeal Severe Lubricant Eye Gel (0.3% hypromellose, Alcon). An incision was made through the cornea adjacent to the limbus at the nasal side using a 27-gauge needle. A 34-gauge blunt-end needle (World Precision Instruments; NF34BL-2) connected to an RPE-KIT (World Precision Instruments, no. RPE-KIT) by SilFlex tubing (World Precision Instruments; SILFLEX-2) was inserted through the corneal incision while avoiding the lens and advanced through the retina. Each mouse was injected with 1 µL of PE-eVLP (containing approximately 4.2x1010 eVLPs)+AAV1-GFP mixture per eye. After injections, the gel was reapplied, anesthesia was reversed with intraperitoneal atipamezole (2.5 mg/kg, MWI Animal Health #032800) and mice were allowed to recover on a heat pad. Two weeks after injection, GFP signal was assessed by scanning laser ophthalmoscopy as a marker for injection efficiency and retinas that showed >80% GFP+ were collected for downstream analysis.

Electroretinography

Prior to recording, mice were dark adapted for 24 h overnight. Under a safety light, mice were anesthetized by intraperitoneal injection of a cocktail consisting of 20 mg/mL ketamine and 1.75 mg/mL xylazine in phosphate-buffered saline at a dose of 0.1 mL per 20 g body weight, and their pupils were dilated with topical administration of 1% tropicamide ophthalmic solution (Akorn; 17478-102-12) and 10% phenylephrine (Valeant # 42702-0103-05). The corneas were hydrated with the application of GenTeal Severe Lubricant Eye Gel (0.3% hypromellose, Alcon). The mouse was placed on a heated Diagnosys Celeris rodent ERG device (Diagnosys LCC). Ocular electrodes were placed on the corneas, the reference electrode was positioned subdermally between the ears, and the ground electrode was placed in the rear leg. The eyes were stimulated with a green light (peak emission 544 nm, bandwidth ~160 nm) stimulus of -0.3 log (cd·s/m2). The responses for 10 stimuli with an inter-stimulus interval of 10 s were averaged together, and the a- and b-wave amplitudes were acquired from the averaged ERG waveform. The ERGs were recorded with the Celeris rodent electrophysiology system (Diagnosys LLC) and analyzed with Espion V6 software (Diagnosys LLC).

RPE dissociation and genomic DNA and RNA preparation

Under a light microscope, mouse eyes were dissected to separate the posterior eyecup (containing RPE, choroid and sclera) from the retina and anterior segments. Each posterior eyecup was immediately immersed in PBS. RPE, choroid, and scleral cells were detached in PBS from the posterior eyecup by gentle pipetting, followed by a removal of the remaining posterior eyecup. Cells from rd6 mice were then processed for genomic DNA using the DNeasy Blood & Tissue Kit (Qiagen, #69504) and cells from rd12 mice were processed with the AllPrep DNA/RNA Micro Kit (Qiagen, #80284).

Western blot analysis of mouse RPE tissue extracts

To prepare the protein lysate from the mouse RPE tissue, the dissected mouse eyecup, consisting of RPE, choroid, and sclera, was transferred to a microcentrifuge tube containing 40 µL of RIPA buffer with protease inhibitors and homogenized with a motorized grinder (Fisher

Scientific; K749540-0000), incubated on ice for 20 min, and then centrifuged for 20 min at 21,000 g at 4°C. The resulting supernatant was pre-cleared with Dynabeads Protein G (Thermo Fisher; 10003D) to remove immunoglobulin contaminants from the blood prior to gel loading. 10 µL of RPE lysates pre-mixed with NuPAGE LDS Sample Buffer (Thermo Fisher; NP0007) and NuPAGE Sample Reducing Agent (Thermo Fisher; NP0004) and denatured at 70°C for 10 min was loaded into each well of a NuPAGE 4-12% Bis-Tris gel (Thermo Fisher; NP0321BOX), separated for 1 h at 130 V and transferred onto a PVDF membrane (Millipore; IPVH00010). After 1 h blocking in 5% (w/v) non-fat milk in PBS containing 0.1% (v/v) Tween-20 (PBS-T), the membrane was incubated with primary antibody, goat anti-mouse MFRP monoclonal antibody (1:1,000; R&D Systems #AF3445) or mouse anti-mouse RPE65 (1:1,000, in house production90) diluted in 1% (w/v) non-fat milk in PBS-T overnight at 4°C. After overnight incubation, membranes were washed three times with PBS-T for 5 min each and then incubated with donkey anti-goat IgG-HRP antibody (1:10,000; Abcam; ab97110) or goat anti-mouse IgG-HRP antibody (1:5,000; Cell Signaling Technology; 7076S) for 1 h at room temperature. After washing the membrane three times with PBS-T for 5 min each, protein bands were visualized after exposure to SuperSignal West Pico Plus Chemiluminescent substrate (Thermo Fisher; 34577). Membranes were stripped (Thermo Fisher; 21059), re-blocked, and re-probed for β-actin expression using rabbit anti-β-actin polyclonal antibody (1:1,000; Cell Signaling Technology; 4970S), following the same protocol. The corresponding secondary antibody was goat anti-rabbit IgG-HRP antibody (1:5,000; Cell Signaling Technology; 7074S).

Immunohistochemistry of RPE flatmounts and cryosections

Mouse eyes were enucleated and fixed with 4% paraformaldehyde in PBS for 20 min at room temperature and washed three times in PBS for 5 min each. To make RPE flatmounts (RFMs), the anterior segment and retina were removed from the posterior eyecup under a dissecting microscope, and four radial cuts were made toward the optic nerve to flatten the eyecup into an RFM. Samples were permeabilized and blocked in 0.1% Triton X-100 (Sigma–Aldrich;

T8532) with 3% normal donkey serum (NDS) in PBS for 30 min and incubated with the appropriate primary antibody in PBS, 0.1% Triton X-100, and 3% NDS, including goat anti-MFRP antibody (1:100; R&D Systems #AF3445) and rabbit anti-ZO-1 polyclonal antibody (1:100; Invitrogen #61-7300), overnight at 4 °C. The next day, samples were washed three times in PBS for 5 min each and then incubated with the appropriate secondary antibody in PBS + 0.1% Triton X-100 and 3% NDS, including Alexa Fluor 594-conjugated donkey anti-rabbit IgG (1:200; Thermo Fisher; A21207) and Alexa Fluor 647-conjugated donkey anti-goat IgG (1:200; Thermo Fisher A32849) for 2 h at room temperature in the dark. Cryosection samples were incubated in 1 µg/mL DAPI (Thermo Fisher; 62248) in PBS for 10 min. Samples were washed three times in PBS for 5 min each. The samples were then mounted with VECTASHIELD HardSet Antifade Mounting Medium (Vector Labs H-1400-10) and imaged on a Keyence BZ-X800 All-in-One fluorescence microscope.

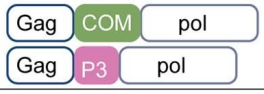
CIRCLE-seq nomination of off-target sites for the rd6 and rd12 models

CIRCLE-seq off-target editing analysis was performed as previously described83,91. Genomic DNA from rd6 mouse liver was isolated using Gentra Puregene Kit (Qiagen) following the manufacturer's instructions. Purified genomic DNA was sheared with a Covaris S2 instrument to an average length of 300 bp. The fragmented DNA was end repaired, A-tailed, and ligated to a uracil-containing stem-loop adaptor, using the KAPA HTP Library Preparation Kit, PCR Free (KAPA Biosystems). Adaptor-ligated DNA was treated with Lambda Exonuclease (NEB) and Escherichia coli Exonuclease I (NEB) and then with USER enzyme (NEB) and T4 poly- nucleotide kinase (NEB). Intramolecular circularization of the DNA was performed with T4 DNA ligase (NEB) and residual linear DNA was degraded by Plasmid-Safe ATP-dependent DNase (Lucigen). Synthetic guide RNAs were ordered from IDT with standard 2'O-Methyl modification at first three and last three bases. The synthetic guide RNAs were resuspended to 9 µM in nuclease-free water, denatured at 90 °C for 5 min and slowly annealed at 0.1 oC per second to 25 °C. In vitro cleavage reactions were performed with 125 ng Plasmid-Safe-treated circularized DNA, 90 nM

Cas9 nuclease protein (NEB), Cas9 nuclease buffer (NEB) and 270 nM synthetic guide RNA (Synthego), in a 50 µL volume for 1 hour. Cleaved products were treated with proteinase K (NEB) as described91, A-tailed, ligated with a hairpin adaptor (NEB), treated with USER enzyme (NEB) and amplified by PCR with barcoded universal primers (NEBNext Multiplex Oligos for Illumina (NEB)), using Kapa HiFi Polymerase (KAPA Biosystems). Libraries were sequenced with 150-bp/150-bp paired-end reads with an Illumina MiSeq instrument. CIRCLE-seq data analyses were performed using open-source CIRCLE-seq analysis software and default recommended parameters (https://github.com/tsailabSJ/circleseq). The top 10 nominated off-target sites for epegRNA used for the rd6 and rd12 models were analyzed by high-throughput sequencing from the RPE tissue of untreated or v3 PE3b-eVLP treated mice. Off-target editing for epegRNA-associated off-target sites was analyzed as described above as the sum of (pegRNA-mediated off-target editing frequency)+(indel frequency at the Cas9 nick site). Insertions or deletions at ngRNA-associated off-target sites was analyzed as a percentage of discarded reads divided by the total reference-aligned reads.

Statistical analysis

Data are presented as mean and standard error of the mean (SEM). Comparisons of different versions of PE-eVLPs were made with eVLPs produced and transduced in parallel in one large experiment. Biological replicates are obtained by treating three independently maintained cell lines and/or three or more animals with a single batch of eVLPs. The sample size and the statistical tests used for each experiment are described in the figure legends. No statistical methods were used to predetermine sample size. Statistical analysis was performed using GraphPad Prism software.

	Accessory proteins	Cargo proteins	Guide RNAs	Improvements from the previous version
v1.1	N/A			
v1.2	N/A			epegRNA
v1.3	N/A			PEmax
v2.1	N/A			MMLV RT truncation
v2.2	N/A			NES optimization
v2.3	N/A			Linker optimization
v3				gRNA recruitment via MCP:MS2 interaction
v3b				Cargo recruitment via P3-P4 interaction; gRNA recruitment via COM:Com interaction

Key: 3xNES NLS Engineered protease site Linker

*Schematics shown in the table represent PE2-eVLPs. For PE3-eVLPs, additional ngRNAs are pacakged.

Figure 4.1 Summary of PE-eVLP architectures and PEmax/pegRNA/ngRNA recruitment strategies. Schematic of accessory proteins, cargo proteins, guide RNA designs, and description of improvements from the previous version for successive generations of PE-eVLPs. Envelope protein VSV-G, and capsid protein MMLV Gag–Pol that are common in all versions of PE-eVLPs are omitted from the table. Schematics shown in the table represent PE2-eVLPs. For PE3-eVLPs, additional ngRNAs are packaged at a ratio of 4:1 for pegRNAs and ngRNAs with corresponding scaffold modification and aptamer insertion. Figure adapted from An *et al* and generated in David R. Liu's laboratory.

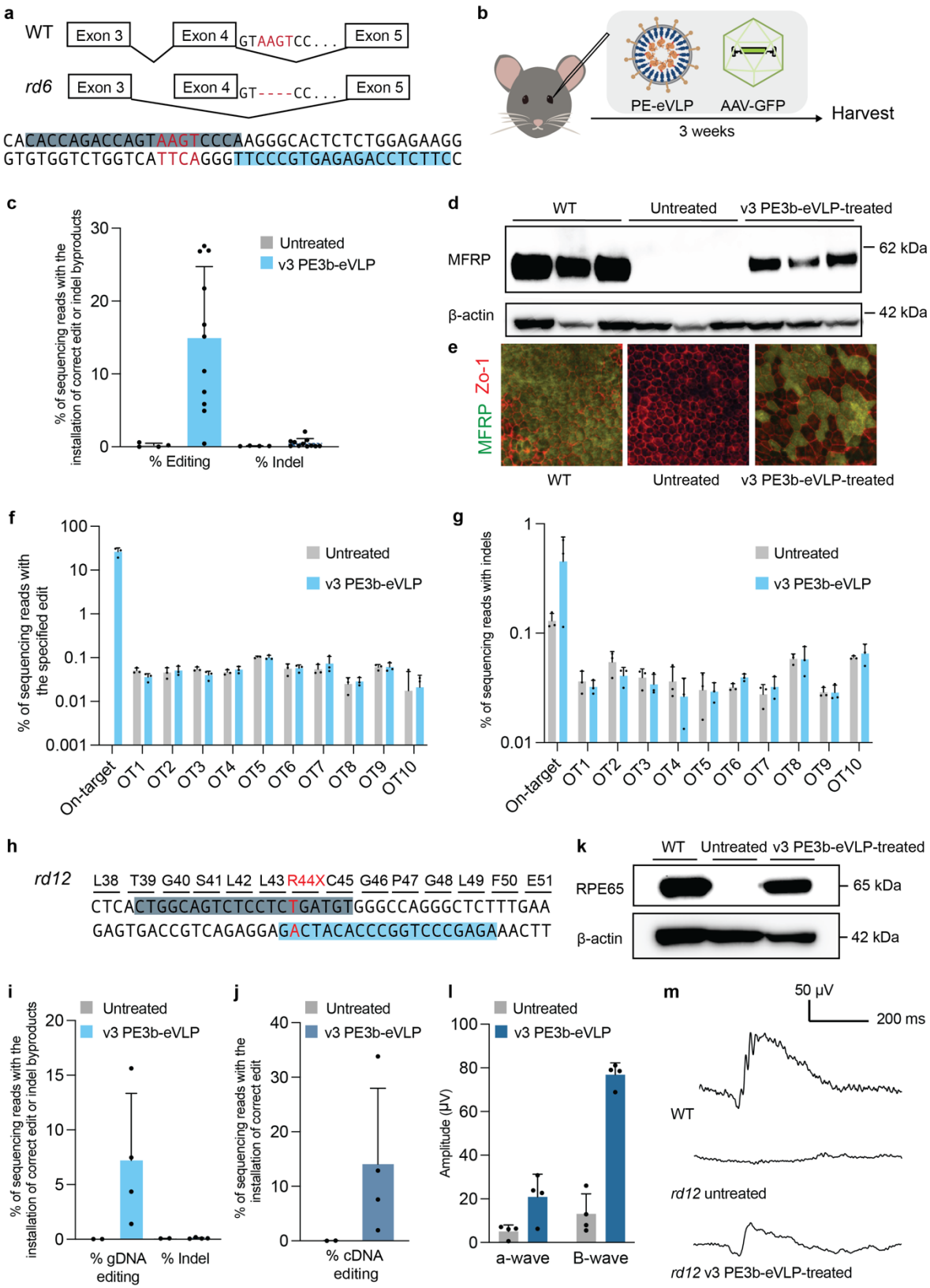

a
WT
Exon 3
Exon 4
GTAAGTCC . . .
Exon 5
rd6
Exon 3
Exon 4
GT----CC . . .
Exon 5
CACACCAGACCAGTAAGTCCCAAGGGCACTCTCTGGAGAAGG
GTGTGGTCTGGTCATTCAGGGTTCCCGTGAGAGACCTCTTCC
b
PE-eVLP
AAV-GFP
3 weeks
Harvest
c
% of sequencing reads with the installation of correct edit or indel byproducts
Untreated
v3 PE3b-eVLP
% Editing
% Indel
d
WT
Untreated
v3 PE3b-eVLP-treated
MFRP
62 kDa
β-actin
42 kDa
e
MFRP
Zo-1
WT
Untreated
v3 PE3b-eVLP-treated
f
% of sequencing reads with the specified edit
Untreated
v3 PE3b-eVLP
On-target
OT1
OT2
OT3
OT4
OT5
OT6
OT7
OT8
OT9
OT10
g
% of sequencing reads with indels
Untreated
v3 PE3b-eVLP
On-target
OT1
OT2
OT3
OT4
OT5
OT6
OT7
OT8
OT9
OT10
h
rd12
L38 T39 G40 S41 L42 L43 R44X C45 G46 P47 G48 L49 F50 E51
CTCACTGGCAGTCTCCTCTGATGTGGGCCAGGGCTCTTTGAA
GAGTGACCGTCAGAGGAGACTACACCCGGTCCCGAGAAACTT
k
WT
Untreated
v3 PE3b-eVLP-treated
RPE65
65 kDa
β-actin
42 kDa
i
% of sequencing reads with the installation of correct edit or indel byproducts
Untreated
v3 PE3b-eVLP
% gDNA editing
% Indel
j
% of sequencing reads with the installation of correct edit
Untreated
v3 PE3b-eVLP
% cDNA editing
l
Amplitude (μV)
Untreated
v3 PE3b-eVLP
a-wave
B-wave
m
50 μV
200 ms
WT
rd12 untreated
rd12 v3 PE3b-eVLP-treated

Figure 4.2. Retinal disease correction *in vivo* with PE-eVLPs. a, An optimized PE3b strategy to correct a 4-bp deletion in *Mfrp* that causes exon 4 skipping and retinal degeneration in the *rd6* mouse model. The mutation is in red, the epegRNA spacer sequence is highlighted in light blue, and the ngRNA spacer sequence is highlighted in dark blue. b, Schematic of subretinal injection of *rd6* mice. 3- to 5-week-old *rd6* mice were injected with v3 PE3b-eVLPs premixed with AAV1-GFP (used to confirm injection efficiency). Tissues were harvested 3 weeks after injection for analysis. c, Prime editing efficiency to correct the 4-bp deletion in *Mfrp* and the associated indel frequency in the genomic DNA harvested from the retinas of *rd6* mice. Bars represent the average values of n=4 (untreated) or n=11 (v3 PE3b-eVLP-treated) mice, with each dot representing individual mice and error bars representing standard deviations. d, Western blot of RPE tissue protein extracts from wild-type C57BL/6J mice, untreated *rd6* mice, and v3 PE3b-eVLP-treated *rd6* mice. e, Immunohistochemistry blot on RPE flatmounts from wild-type C57BL/6J mice, untreated *rd6* mice, and v3 PE3-eVLP-treated *rd6* mice. Flatmounts were stained with anti-MFRP antibody (green) and anti-ZO-1 antibody (red). f, Analysis of PE-dependent editing at the on-target site and top 10 CIRCLE-seq nominated off-target sites associated with the *rd6* epegRNA sequence. g, Analysis of indel byproducts at the on-target site and top 10 CIRCLE-seq nominated off-target sites associated with the *rd6* ngRNA sequence. For f and g, bars represent average values for n=3 (untreated) or n=3 (v3 PE3b-eVLP-treated) mice, with each dot representing individual mice and error bars representing standard deviations. h, The R44X mutation in *Rpe65* exon 3 in the *rd12* mouse model and the optimized PE3b strategy used for correction of this mutation. The mutation is in red, the epegRNA spacer sequence is in light blue, and the ngRNA spacer sequence is in dark blue. i, Prime editing efficiency of *Rpe65* R44X mutation correction and the associated indel frequency in genomic DNA harvested from *rd12* mice. j, Prime editing efficiency of *Rpe65* R44X mutation correction in *Rpe65* RNA collected from *rd12* mice. k, Western blot of RPE tissue protein extracts from wild-type C57BL/6J mice, untreated *rd12* mice, and v3 PE3b-eVLP-treated *rd12* mice. l, Scotopic a- and B-wave amplitudes measured by ERG following

overnight dark adaptation. For i, j and l, bars represent average values for n=4 (untreated) or n=4 (v3 PE3b-eVLP-treated) mice, with each dot representing individual mice and error bars representing standard deviations. m, Representative ERG waveforms from wild-type C57BL/6J mice, untreated *rd12* mice, and v3 PE3-eVLP-treated *rd12* mice. Figure adapted from An *et al* and generated in David R. Liu and Krzysztof Palczewski's laboratory.

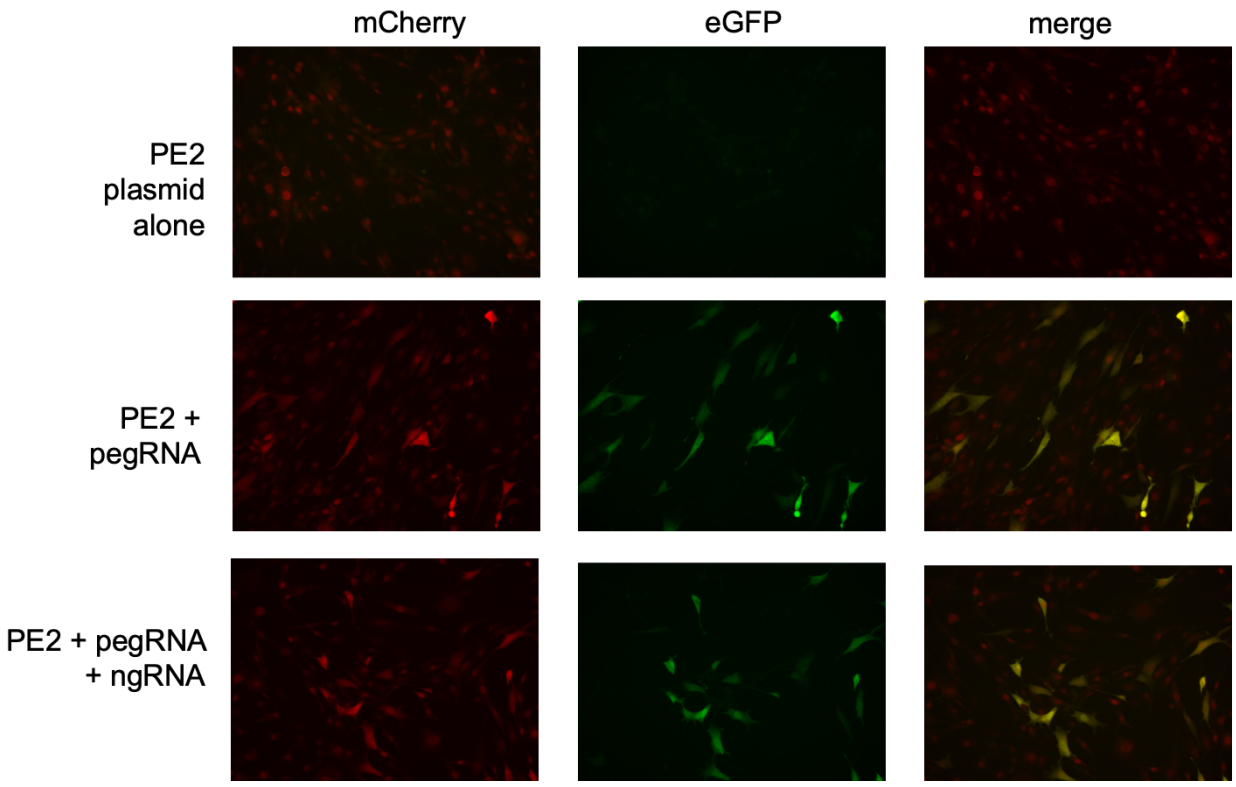


Figure 4.3. A fluorescent reporter *Mfrp*^{rd6} cell line. An NIH/3T3 cell line was constructed via retroviral transduction, where a fragment of the *rd6* genomic locus containing the *rd6* mutation is flanked by mCherry and frameshifted eGFP. Successful prime editing by reversion of the 4 bp deletion restores eGFP expression, as shown when PE2 and the pegRNA or pegRNA/ngRNA combination is co-delivered by plasmid transfection, but not when only PE2 plasmid is delivered.

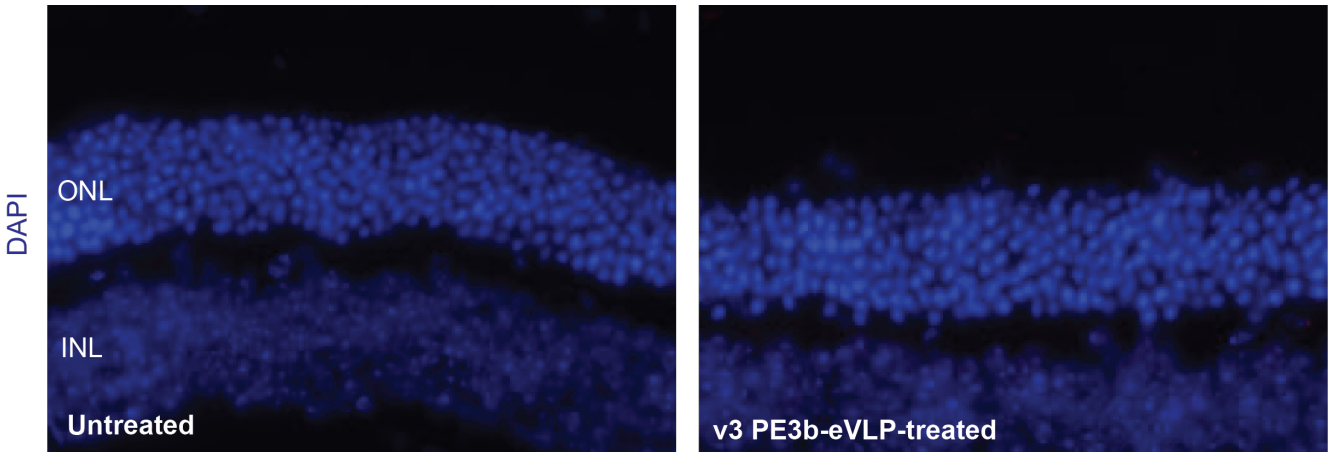


Figure 4.4 Immunohistochemistry blot on eye cryosections of *rd6* mice. Retina cryosections from untreated *rd6* mouse and v3 PE3b-eVLP-treated *rd6* mouse were stained with DAPI (blue).

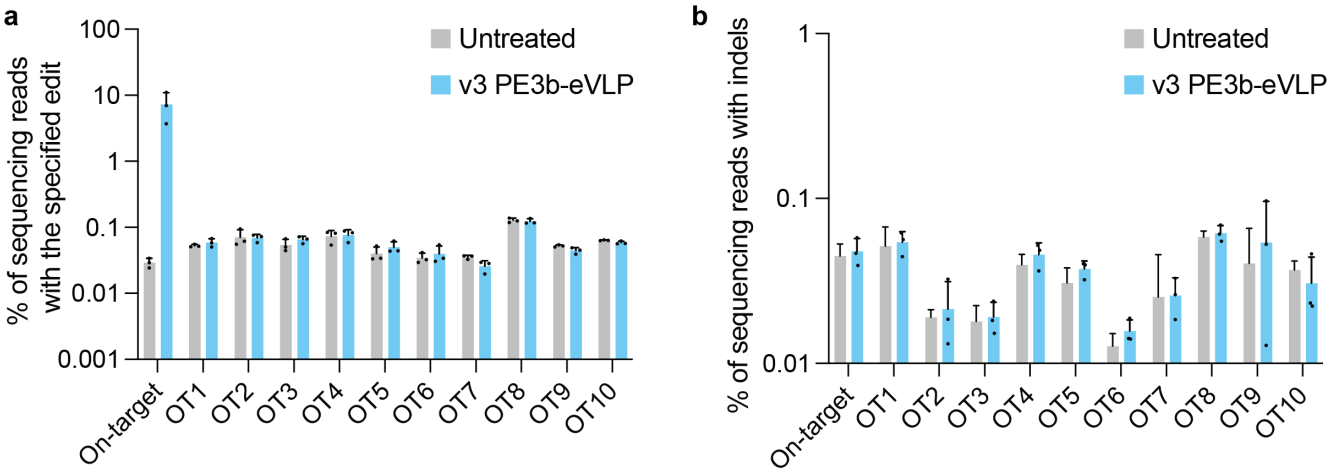


Figure 4.5 Off-target analysis in *rd12* mice. a, Analysis of PE-dependent editing at the on-target site and at the top 10 CIRCLE-seq nominated off-target sites associated with the *rd12* epegRNA sequence. **b**, Analysis of indels at the on-target site and the top 10 CIRCLE-seq nominated off-target sites associated with the *rd12* ngRNA sequence. Bars represent average values for n=3 (untreated) or n=3 (v3 PE3b-eVLP-treated), with each dot representing an individual mouse and error bars representing standard deviation. Figure adapted from An *et al* and generated in David R. Liu's laboratory.

CHAPTER 5

Development of ENVLPE VLPs as an alternative prime editing strategy

This chapter is derived in part from the following manuscript published in *Cell:*

Geilenkeuser, J. *et al*. Engineered Nucleocytosolic Vehicles for Loading of Programmable Editors. Cell 188, 1-19 (2025).

© 2025 the Authors.

CHAPTER 5

Development of ENVLPE VLPs as an alternative prime editing strategy

5.1. Development of ENVLPE VLPs

Contemporaneously to the PE-eVLP study, another group investigated the delivery of prime editors within VLPs. Similarly to the PE-eVLP study, they also realized that the relative instability of epegRNAs was a major hurdle to the efficient packaging and delivery of PE RNP complexes within VLPs.

With the v1 through v3 PE-eVLP architectures, PE protein packaging was conducted *via* covalent fusion of the PE gene to the 3' end of the gag polypeptide, with the exception of the v3b which utilized a coiled-coil peptide domain to recruit the PE[229]. However, these strategies do not actively recruit epegRNAs to be packaged within the eVLP as well. This was partially solved by introducing the aptamer system with the MS2/MCP and COM/com pairs to encourage epegRNA recruitment, as opposed to passive epegRNA-PE interactions[229]. While these increase the probability of epegRNA recruitment, it does not guarantee it.

Therefore, by designing a VLP system that recruits the most unstable component of the complex, the epegRNA, improved PE RNP packaging and delivery could be achieved. In pursuit of this goal, the laboratories of Gil Gregor Westmeyer and Dong-Jiunn Jeffery Truong started with the HIV-1 nucleocapsid, which is also capable of producing VLPs. Similarly to the PE-eVLP strategy, they inserted another aptamer system, the PP7 and PP7 coat protein (PCP) pair, with the PCP domain inserted within the gag domain of the HIV-1 capsid. In conjunction, when the PP7 aptamer was grafted onto the epegRNA scaffold, they demonstrated that they could recruit productive PE RNP complexes into VLPs. Later experiments showed that moving the PP7 sequence to the 3' end of the epegRNA downstream of the RTT and PBS showed additional benefit.

They also reasoned that “nucleocytosolic” shuttling of the gag-PCP construct could increase pegRNA loading, as pegRNAs are transcribed within the locus, but the gag-PCP protein resides within the cytosol. Therefore, by screening combinations of nuclear export and import signals upstream of the PCP domain, they demonstrated that, indeed, pegRNAs are limiting and not easily packaged within the VLP, but with the nucleocytosolic shuttling system, they were able to increase epegRNA packaging and increase PE rates.

Because pegRNAs are unstable, improvements in pegRNA architecture, such as the epegRNA with the tevoPreQ1 knot, increase pegRNA stability and protect them from degradation. Therefore, they chose to implement an additional protection module for the 3’ end of the epegRNA. Another CRISPR-associated protein, Csy4 (also known as Cas6f), from *Psueomonas aeruginosa* was used. Cys4 is an endonuclease used by *P. aeruginosa* to process crRNAs in a sequence-specific manner. Therefore, by adding the Cys4 (C4) motif to the end of the epegRNA downstream of the PP7 domain, but upstream of the tevoPreQ1 domain, the 3’ end of the RNA is bound by Cys4, cleaved, and remains associated, which could improve stability. Importantly, the Cys4 domain can be expressed as a fusion to PE, or as a separate protein with an intervening P2A sequence. This resulted in the VLP architecture they termed Engineered Nucleocytosolic Vehicles for Loading of Programmable Editors, or ENVLPE, with a nucleocytosolic shuttling system, PP7/PCP recruitment of epegRNAs, and Cys4 stablization of epegRNAs. Of note, because the recruitment of RNPs is *via* the gRNA and not as a fusion, the system is highly modular and “hot-swappable”, and these results also apply to base editors, nuclease Cas9, and other systems, such as mRNA delivery *via* PP7 domains within the 3’ UTR.

The PE-eVLP architecture (and ENVLPE architecture) utilized a mixture of wildtype gag-pol and engineered gag-fusions. For PE-eVLPs, because of steric hinderances of these fusions and the dependence on gag-pol proteases for particle maturation, the inclusion of wildtype gag-pol is necessary. However, because the fused domain (PCP) is smaller, and because the recruitment of the RNP complex is not dependent on proteolytic cleavage, it could be possible for

a minimal gag architecture to be engineered. Indeed, omission of the wildtype gag-pol when producing ENVLPE particles only modestly decreased editing efficiency. Thus, they engineered a minimal gag domain by unnecessary elements as described elsewhere with the addition of GCN4 coiled-coil domains to promote gag oligomerization to create a miniaturized VLP, termed miniENVLPE[252]. Of note, similar efforts have been made with other retroviral VLP systems[253]. They tested the addition of the GCN4 domains to regular ENVLPE and noticed an increase in editing efficiency – thus, an ENVLPE^{+} system was created that incorporated this change (summarized in **Figure 5.1**).

5.2 Delivering mRNA to study ENVLPE biodistribution in vivo

The eye has been used as a proving ground for breakthroughs in technology and precision genome editing[105]. Multiple BE and PE strategies been demonstrated in a diverse set of inherited retinal degeneration models, though virally-delivered BE and PE limits the clinical applicability of the studies[80,140,171]. To initially investigate the distribution and delivery efficiency of ENVLPE upon subretinal injection, we applied VSV-G pseudotyped ENVLPE loaded with Cre_{NLS} $mRNA_{PP7}$ to mT/mG mice[62] (**Figure 5.2A**), that indicate Cre recombinase activity as a red-to-green switch. We injected 1.0, 1.5, and 2.0 µl of an ENVLPE solution (2.53×10^{8} particles μl^{-1} in PBS) and, after one week, observed uniform green fluorescence due to reporter activation across the retinal pigment epithelium (RPE) for 17/18 injected eyes (**Figure 5.2B**, **Figure 5.3A**), indicating broad biodistribution and activity after subretinal injection. More importantly, no gross change of the compact RPE layer's pentagonal and hexagonal cell morphology was evident, suggesting ENVLPE was well tolerated. Compared to ENVLPE, ENVLPE^{+} also performed much better as an mRNA delivery tool in a titration experiment in a Cre-dependent green-to-red reporter HEK293 line[63] (**Figure 5.3B**), where a ~4× lower dose of ENVLPE^{+} was able to achieve the same level of color conversion. Therefore, ENVLPE+ was employed to investigate therapeutic genomic editing.

5.3 PE_{Csy4} ENVLPE^{+} in inherited retinal degeneration mouse models

Encouraged by the results from mRNA delivery, we sought to test PE, now using the optimal configuration iPE$_{Csy4}$ ENVLPE^{+}, in mouse models of Leber congenital amaurosis and retinitis pigmentosa via subretinal injection, as recently shown for v3 PE-eVLPs[17] (**Figure 5.2A**). The loss-of-function phenotype in the first mouse model, *rd12*, is caused by a nonsense mutation in exon 3 of *Rpe65*[64] which abolishes the canonical visual cycle and leads to visual impairment. To enable a direct head-to-head comparison with the recently published v3 PE-eVLP systems *in vivo*[17], we employed the identical PE3b strategy for ENVLPE^{+} (including identical spacers and 3' extensions of the pegRNA but adapted to our scaffold and 3'-modifications required for the Csy4/C4 protection) (**Figure 5.2C**).

Three weeks after subretinal injection of equal dosage of both preparations into the RPE of 5–7 week old *rd12* mice with 1 µl VLPs (1 × 10^9 VLPs), light-dependent retinal activity was then measured via electroretinography (ERG) (**Figure 5.2D,E**). ENVLPE^{+} treatment evoked ~5.5-fold higher *b*-wave signal (median 173.5 µV) compared to an equal dose of v3 PE-eVLPs (median 31.52 µV). A response of the comparable magnitude was evoked only after injecting a dose of v3 PE-eVLP that was approximately one order of magnitude higher (13.7×10^9 particles µl^{-1}) (median 102.2 µV, **Figure 5.2D,E**).

Immunoblot analysis of RPE homogenates revealed that the restored RPE65 protein could only be detected in eyes treated with PE3b$_{Csy4}$ ENVLPE^{+}, whereas protein levels in eyes treated with v3 PE3b-eVLP remained below the detection limit (**Figure 5.2F**).

The same was evident when analyzing *Rpe65* exon 3 via targeted amplicon sequencing, where significant successful prime editing events were only apparent for PE3b$_{Csy4}$ ENVLPE^{+} (**Figure 5.2G**) without detectable InDels (**Figure 5.2H**). In comparison, editing levels in v3 PE3b-eVLP condition were under the detection threshold. Across all samples, the ERG response generally correlated with the observed editing rates (**Figure 5.6**).

In *rd12* mice, the absence of RPE65 disrupts the visual cycle, leading to an 11-*cis*-retinal deficiency. High-performance liquid chromatography (HPLC) analysis of retinoids in PE3b$_{Csy4}$

ENVLPE^{+}-treated *rd12* mouse eyes revealed significant restoration of 11-*cis*-retinal after dark adaptation, reaching ~20% of wild-type levels, suggesting a partially restored visual cycle (**Figure 5.2I**), while v3 PE3b-eVLP-treated samples were beyond the limit of detection, though some restoration must have occurred due to the recordable *b*-wave signals (**Figure 5.2D,E**).

We repeated our head-to-head benchmark on a second mouse model, *rd6,* that contains a 4 bp-deletion in the splice donor region of *Mfrp* intron 4 which abolishes protein expression[65] (**Figure S16A**). 5–7 weeks old *rd6* mice were injected with an equal dosage of PE3b$_{Csy4}$ ENVLPE^{+} and v3 PE3b-eVLP (1.6×10^{9} particles μl^{-1} in 1 µl PBS). Three weeks post-injection, we analyzed the protein expression of *Mfrp* in the eye cup via immunoblot and the editing outcomes via targeted amplicon sequencing. Only ENVLPE^{+}-treated eyes showed visibly restored MFRP protein expression (**Figure S16B**) mediated by the restoration of the splice donor site (median 8.6%, **Figure S16C**) with no detectable InDels (**Figure S16D**), while v3 PE3b-eVLP-treated samples were beyond detection limit.

5.4 Discussion

By systematically analyzing VLP methods for delivery of gene-editing RNP complexes, the ENVLPE system identified and addressed three interrelated bottlenecks that limit their performance: First, the formation of guide RNA/Cas complexes in the nucleus is spatially separated from the budding process at the plasma membrane. Second, unbound guide RNAs, especially pegRNAs, are the least stable RNP components in packaging cells. Third, the transport and packaging of the RNP using the Cas protein as an affinity handle limits the efficiency and modularity of the resulting VLPs. Improvements thus have incorporated nuclear localization (NLS) and export (NES) sequences to enable an active nucleocytosolic export of editor-RNP complexes via the aptamer-tagged guide RNAs, which recruits and stabilizes the least stable component of the RNP.

The *in vivo* mouse studies compared HIV-1- and MMLV-based systems under equivoluminal or equimolar conditions, demonstrating potent mRNA delivery and superior "per

particle" editing efficiency with increased RNP loading, surpassing PE-eVLPs. The titer used for equimolar comparison was 1 × 10^9 particles per µl, which is 26-fold (*rd6*) and 40-fold less (*rd12*) than in the referenced study17 (4.2 ×1010). While an ERG response could be detected at this dose, we did not observe *Rpe65* editing or RPE65 protein in v3 PE-eVLP-treated eyes. The variability of the protein levels could potentially be explained by the lack of any kind of enrichment or pre-selection of transduced tissue in our analysis protocol.

5.5 Selected methods

Genetic constructs

The ENVLPE packaging plasmid is based on psPAX2$_{D64V}$ encoding CAG-driven Gag/Gag–Pol with a D64V mutation in the HIV-1 integrase domain. During optimization, Gag/Gag–Pol (psPAX2$_{D64V}$) and shuttling Gag–PCP variants were co-expressed on separate plasmids. Later, we grafted the optimized CAG-driven shuttling Gag–PCP/Gag–Csy4 expression cassettes to yield equimolar expression of Gag/Gag–Pol and Gag–PCP/Gag–Csy4 into psPAX2$_{D64V}$. For CMV-driven ENVLPE$^+$, the CAG promoters were exchanged for CMV promoters taken from pCMV-VSV-G.

VLP production

12.5×10^6 cells were seeded in 50 ml per well in full DMEM with 10% FBS 24 h prior to transfection. The cells were transfected (jetOPTIMUS, Polyplus) with a total of 19.2 µg plasmid DNA using JetOPTIMUS transfection reagent. The reagent volume to DNA mass ratio (V/m) was 1:1 in a total volume of 1.92 ml (fill-up with JetOPTIMUS Buffer, 10 min incubation at room temperature for complex formation).

VLPs were then purified by ultracentrifugation. After 72 hours of expression in a 15 cm dish (12,500,000 cells in 50 ml advanced DMEM), the supernatant was harvested and sterile filtered (0.45 µm). 35 ml of the filtrate was transferred into a Beckman Coultier Ultra-Clear Tube and 3 ml of a 20% sucrose PBS solution was layered below the supernatant. The supernatants were spun for two hours at 26,000 rpm in a Beckman LE-70 ultracentrifuge. The SW28 swinging

bucket rotator was cooled to 4 °C. Pellets were resuspended in 1/1000 of the original volume using PBS supplemented with 10% sucrose and 1× PenStrep.

Animals

Mouse experiments and procedures were approved by the Institutional Animal Care and Use Committee at the University of California, Irvine and conform to the Association for Research in Vision and Ophthalmology Statement for the Use of Animals in Ophthalmic and Vision Research. Breeding colonies of wild-type C57BL/6J (000664), rd6 (003684), and rd12 (005379) were established by purchase from the Jackson Laboratory (Bar Harbor, ME). Mice were housed in the specific pathogen-free vivarium of the University of California, Irvine on a 12 h/12 h light/dark cycle and fed ad libitum. 5-7 week old homozygous mouse littermates were randomly assigned to experimental groups. Both male and female mice were used equally. No mice were involved in previous procedures.

Subretinal injection

Prior to injection, VLPs were clarified by centrifugation at 17,000× g for 1 min at room temperature. Mice were prepared for injection by sequential dilation with 1% tropicamide solution (Somerset Therapeutics #119758) and 2.5% phenylephrine solution (Akorn #118050). Mice were anesthetized with a ketamine xylazine cocktail and GenTeal Severe 0.3% hypromellose gel (Alcon #0065806401) was applied to the corneas. Under a surgical microscope (Zeiss), a corneal incision was made with a disposable 27G beveled needle before a 34G blunt injection needle connected to Silflex tubing (World Precision Instruments # RPE-KIT) was advanced through the incision and into the subretinal space. 1 µl of VLPs were injected at 70 nl s-1, controlled by a UMP3 pump (World Precision Instruments #UMP3-3). Anesthesia was reversed with atipamezole (Zoetis #10000449) and the mice recovered on a heating pad prior to return to their cage.

Electroretinography (ERG)

Mice were dark adapted for 24 hours preceding the ERG recordings. Under a safety light, mice were dilated with topical administration of 1% tropicamide ophthalmic solution (Akorn

#17478-102-12) followed by 10% phenylephrine ophthalmic solution (MWI Animal Health #054243) and underwent anesthesia by isoflurane inhalation. The mouse was placed on a Diagnosys Celeris rodent-ERG device (Diagnosys LCC, Lowell, MA, USA) equipped with a heating pad and hypromellose administration (Akorn #9050-1) for hydration. Ocular stimulator electrodes were placed on the corneas, a ground electrode was placed subdermally in the rear leg and the reference electrode was placed subdermally between the ears. Green-light stimulation (peak emission 544 nm, bandwidth ~160 nm) of -0.3 log (cd s m-2) was recorded from each eye. The responses for 10 stimuli with an inter-stimulus interval of 10 sec were averaged, and the a- and b-wave amplitudes were acquired from the averaged ERG waveform. Data were analyzed with Espion V6 software (Diagnosys LLC).

Retinoid analysis

Mice were dark-adapted for 48 hours prior to sacrifice. Single, whole-eyes were enucleated under dim red light and frozen on dry ice before wrapping in aluminum foil and short-term storage at –80 °C. The whole eyes were unwrapped and allowed to thaw on ice prior to Dounce homogenization in 1 ml of a chilled, sodium phosphate-based buffer containing hydroxylamine and methanol (10 mM sodium phosphate, 100 mM hydroxylamine hydrochloride, and 50% methanol by volume). Following incubation of the homogenates at room temperature for 25 minutes, 2 ml of 3M NaCl and 3 ml of ethyl acetate were added to each homogenate. The tubes were vigorously shaken for 2 minutes to partition the retinoids into the ethyl acetate layer, then centrifuged at 3,220× g in a tabletop centrifuge for 15 min at 20 °C. The top ethyl acetate layer was collected in separate tubes, and an additional 3 ml of ethyl acetate was added to each tube. The shaking and centrifugation steps were then repeated, and the ethyl acetate fractions were consolidated for each sample. Following consolidation, each fraction was dried under vacuum at approximately 32 °C. The dried retinoids were resuspended in 400 µl of hexanes and centrifuged in a tabletop centrifuge at 16,100× g for 15 minutes at 4 °C to pellet undissolved material. All steps prior to loading onto the HPLC were done in darkroom conditions with dim red

illumination. The top 350 µl of each sample were placed into amber HPLC vials and loaded into onto a normal-phase Agilent 1260 Infinity II high-performance liquid chromatograph (Agilent, Santa Clara, CA) equipped with an Agilent Rx-SIL HPLC column (Neta Scientific, Hainesport NJ, cat #: 880975-901). The elution protocol consisted of two steps, one less-polar elution step (99.4% hexanes: 0.6% ethyl acetate) for 20 minutes followed by a more polar elution step (90% hexanes: 10% ethyl acetate) for 25 minutes, followed by a brief shift to the less-polar elution step for 5 minutes. Eluting retinoids were detected spectrophotometrically by monitoring changes in absorbance at 325 nm and 360 nm wavelengths. Retinoids were identified by their elution times and spectra[254]. To quantify individual retinoids in pmol/eye, areas under each retinoid peak were multiplied by conversion factors derived from standard curves for all-*trans*-retinyl esters, syn-11-*cis*-retinal oxime (derivative of syn-11-*cis*-retinal), and all-*trans*-retinal oxime (derivative of all-*trans*-retinal) dissolved in hexanes.

Western blotting

After eyecups were isolated as described above for nucleic acid extraction, eyecups were immersed into 1× RIPA buffer with protease inhibitors (Roche # 04693132001). The eyecups were homogenized mechanically with a pestle before incubation for 20 min on ice. The homogenates were then spun at 4 ºC at 21,300× g for 20 min and supernatants were collected. Homogenates were then cleared of mouse immunoglobulins via incubation for 15 min at 4 ºC with Protein G Dynabeads (Invitrogen # 10003D). Protein lysates were separated on a 4-12% Bis-Tris gel (Invitrogen # NP0323BOX) in 1× MOPS running buffer before fast wet transfer (GenScript eBlot L1 # L00686) to PVDF membranes (Millipore # IPFL00010). The membranes were blocked with 5% non-fat milk in phosphate buffered saline, pH 7.4 with 0.1% Tween-20 (PBS-T) for 1 h at room temperature with constant agitation before incubation with primary antibodies in PBS-T with 1% non-fat milk overnight at 4 ºC with constant agitation. Primary antibodies in this study include anti-RPE65 (1:1,000, clone KPSA1[255], produced in-house), anti-beta-actin (1:2,000, clone 13E5, Cell Signaling Technologies # 4970S), anti-Cas9 (1:5,000, clone 7A9, Biolegend # 844301), and anti-

MFRP (1:1,000, R&D Systems # AF3445). The following day, the membranes were washed 3 times for 10 min each with PBS-T before incubation with secondary antibodies in PBS-T with 1% non-fat milk for 1 h at room temperature with constant agitation. Secondary antibodies in this study include donkey anti-goat IgG HRP (1:5,000, Thermo #A16005), anti-mouse IgG HRP (1:5,000, Cell Signaling Technologies # 7076S), and anti-rabbit IgG HRP (1:5,000, Cell Signaling Technologies # 7074S). The membranes were washed 3 times again for 10 min each with PBS-T before HRP detection with Clarity Max substrate (Bio-Rad # 1705062) and imaging on a Bio-Rad ChemiDoc.

Two-photon imaging

Two-photon excitation imaging was accomplished using our custom TP-imaging system based on a Leica TCSSP8 and equipped with a 1.0 NA 20x water immersion objective and a Vision S (Coherent) Ti:sapphire laser delivering 950 nm 80 MHz pulsing light. To image and spectrally separate GFP and tdTomato, two internal spectral detectors were used with their detection bandwidths set to 490 – 545 nm for GFP, and 590 - 680 nm for tdTomato. Intact mouse eyes were imaged *ex vivo* after euthanasia and enucleation. Leica LASX 4.7.0.28176 and ImageJ (NIH) were used for the reconstruction of 3D stacks and quantification of transfected cells[256,257].

Statistics and reproducibility

Statistics were calculated as specified in each figure using Prism (v.10, GraphPad). Mean and s.d. were calculated across biological replicates. For next-generation sequencing experiments, precision was calculated as the proportion of correct editing events among all editing events (correct/(correct + error) × 100). We made an effort to reduce any biases introduced during the sample preparation by using master mixes and multichannel pipettes. No data were excluded from the analyses except for next-generation sequencing samples for which certain replicates had to be excluded from calculating the mean value due to obvious technical errors (no reads).

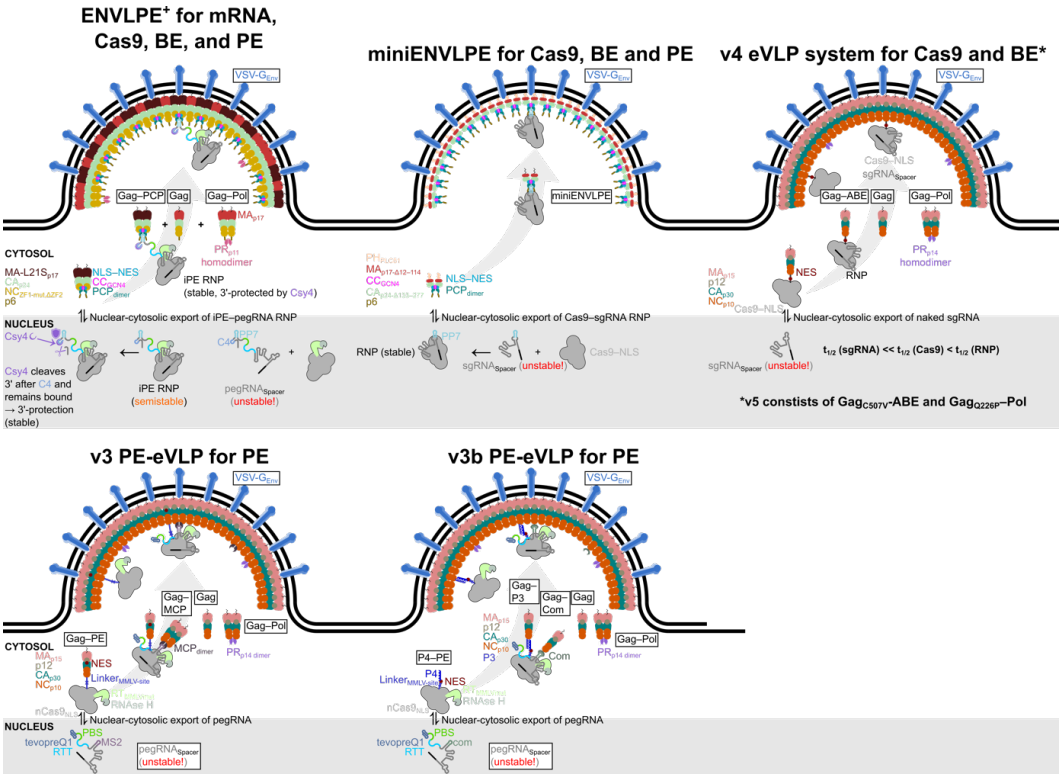


Figure 5.1. Assembly and RNP recruitment mechanisms in ENVLPE and eVLP variants. The Cas9 effector protein binds the stabilized gRNA-Cas-effector ribonucleoprotein (RNP) complex in the nucleus; nucleocytosolic shuttling (NLS-NES) of Gag–PCP enables binding of the fully assembled RNP *via* PCP–PP7 interaction. The system enables modular packaging of various RNP complexes and only requires modification of the (pe)gRNA with a PP7 aptamer. Csy4 cleaves and protects the pegRNA in the RNP complex. v4 eVLPs consist of an MMLV-Gag fusion to a genome-editing effector protein of choice. The fusion protein shuttles between the nucleus and cytosol to package the unprotected gRNA. In contrast to ENVLPE+ , packaging of the Cas *apo*-enzyme (without gRNA) is possible; the genome editor is released after budding only upon proteolytic processing of the Gag polyprotein by the protease encoded in MMLV Gag/Gag–Pol**.** Figure adapted from Geilenkeuser *et al* and generated in J.D. Truong and G. Westmeyer's laboratory.

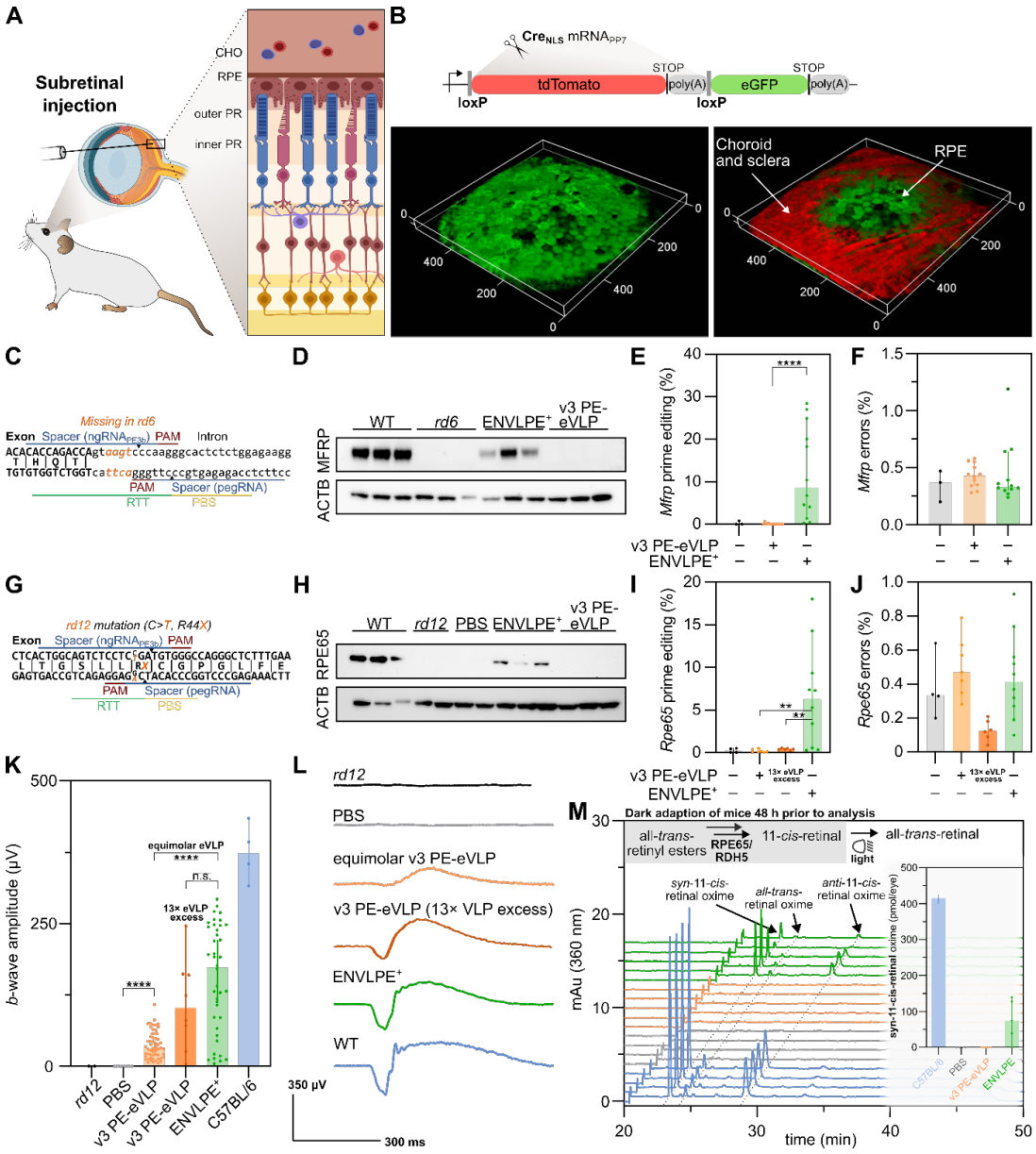


Figure 5.2. Subretinal injection of ENVLPE particles for mRNA delivery into Cre-reporter mice and for PE RNP delivery to mouse models for inherited retinal degeneration.

(A) Depiction of subretinal injection of VLPs into mouse retina. CHO, choroid; RPE, retinal pigment epithelium; PR, photoreceptor. **(B)** Genetic construct of the reporter mouse indicating delivery of mRNA-encoded Cre activity with a red-green switch of fluorescent proteins expressed in RPE. Example 3D rendering of an imaging volume of the posterior portion of the intact eye acquired by 2-photon imaging after subretinal injection of 1.5 µl sample (containing 3.63 × 108

ENVLPE particles). Green fluorescence was observed in 17 out of 18 eyes; additional images are shown in **Figure S14**. **(C)** Schematic diagram of 4 bp deletion in the splice donor region of exon 4 of *Mfrp* in *rd6* mice. **(D)** Immunoblot analysis of MFRP protein levels in *rd6* mouse eyes, three weeks after prime editing. **(E, F)** Analysis of gDNA-editing efficacy and indel rate. Bars represent median with 95% CI (*n* = 12 biological replicates, except for 'untreated' where *n* = 3). Selected statistical comparisons using the Kolmogorov-Smirnov test are shown (****$p < 0.0001$). **(G)** Schematic diagram of the nonsense-mutation in exon 3 of *Rpe65* in *rd12* mice. **(H)** Immunoblot analysis of RPE65 protein levels in *rd12* mice after prime editing. **(I, J)** Analysis of the corresponding editing efficacy and error rate, including indels. Bars represent median with 95% CI (*n* = 4 (untreated); *n* = 7 (eVLP); n = 6 (eVLP 13× excess); n = 10 (ENVLPE+) biological replicates). Selected statistical comparisons using the Kolmogorov-Smirnov test are shown (**$p < 0.01$). **(K**) Scotopic electroretinogram (ERG) *b*-wave amplitudes upon light stimulus of −0.3 log[cd s m−2] flash three weeks after injection of the different VLP systems or controls. Bars represent median with 95% CI (*n* = 2 (*rd12*); *n* = 9 (PBS); *n* = 56 (v3 PE-eVLP light orange); *n* = 8 (v3 PE-eVLP dark orange), *n* = 40 (ENVLPE+); *n* = 10 (C57BL/6) biological replicates). Mice were dark-adapted overnight prior to analysis. Selected statistical comparisons using the Kolmogorov-Smirnov test are shown (****$p < 0.0001$; ns $p > 0.05$). **(L**) Representative ERG traces from (K). **(M)** Schematic diagram of the visual cycle. Extracted whole-eye retinoids were analyzed by HPLC to quantify 11-*cis*-retinal as well as all-*trans*-retinyl esters. The mobile phase for elution consisted of 99.4% hexanes and 0.6% ethyl acetate. Retinoid levels were determined using a standard curve. Results on the right show median and 95% CI for *n* = 4 control samples and *n* = 5 ENVLPE+ and eVLP samples. In D–M, injection volumes were adjusted to equalize the injected VLP titers from v3 PE-eVLP and ENVLPE+ particles per eye. VLP titers were quantified *via* ELISA. Figure adapted from Geilenkeuser *et al* and generated in K. Paczewski, J.D. Truong, and G. Westmeyer's laboratory.

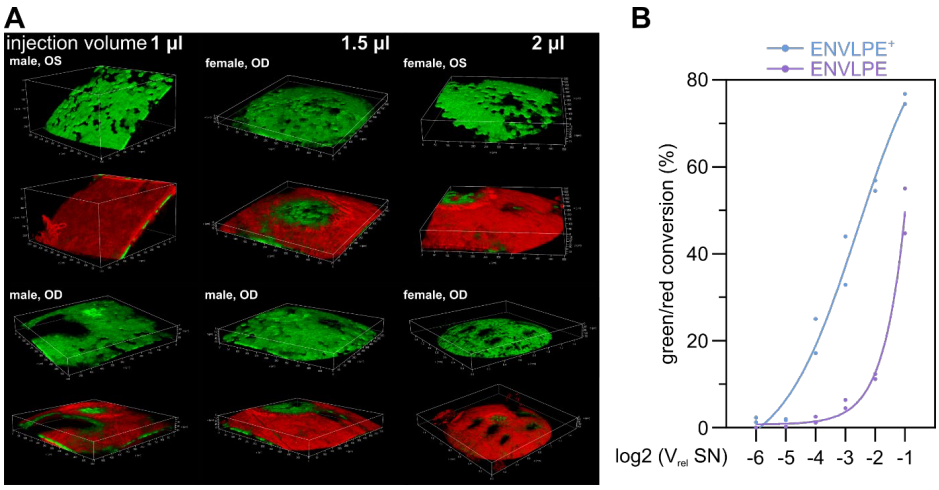


Figure 5.3. Delivery of CreNLS mRNA to activate a red/green-reporter locus. (A) Indicated volumes of CreNLS mRNA-loaded ENVLPE were injected subretinally into the eyes of mT/mG reporter mice (2.53×10^8 particles μl^{-1} in PBS). Two-photon excitation imaging-based 3D reconstruction of the posterior portion of intact mouse eyes are shown, 1 week after subretinal injection. Green fluorescent cells indicate successful reporter activation by Cre in the red/green-reporter locus. **(B)** Quantification of CreNLS mRNA delivery by ENVLPE *vs.* ENVLPE+ to a HEK293T reporter cell line carrying a green/red-reporter locus (inverse signal logic compared to (A)). Log2(VrelSN): relative transduction volumes in 2× dilution series. Figure adapted from Geilenkeuser *et al* and generated in K. Paczewski, J.D. Truong, and G. Westmeyer's laboratory.

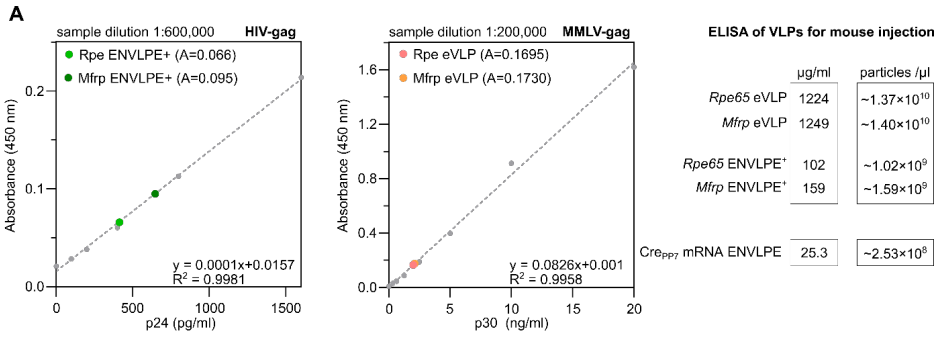


Figure 5.4. Quantification of VLP titers using anti-p24 (HIV-1) or anti-p30 (MMLV) ELISA.

(A) Quantification of ENVLPE+ and v3 PE-eVLP titers after ultracentrifugation prior to subretinal injections. The VLP amount per volume was calculated based on the assumption that 2500 HIV-1 Gag monomers (or 1800 MMLV Gag monomers) form the capsid. Figure adapted from Geilenkeuser *et al* and generated in J.D. Truong and G. Westmeyer's laboratory.

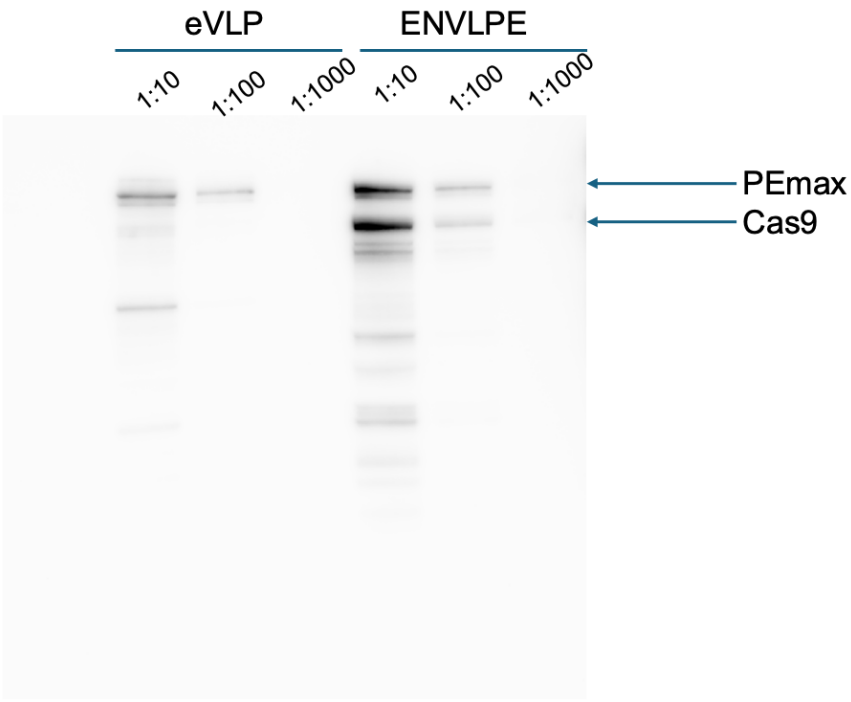


Figure 5.5. eVLP versus ENVLPE anti-Cas9 Western blot. eVLPs and ENVLPE VLPs for MFRP correction were diluted serially in RIPA buffer and then assessed for Cas9/PE content by Western blotting.

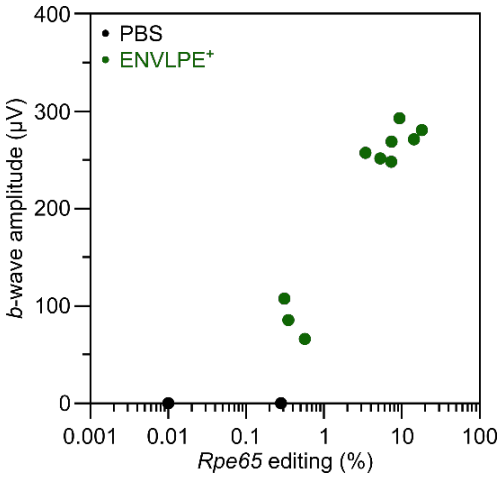


Figure 5.6. Correlation of *in vivo* editing of *Rpe65* in *rd12* mice with corresponding *b*-waves. Correlation plot of *Rpe65* prime editing efficacy and functional restoration quantified by *b*-wave amplitudes in response to a light stimulus after ENVLPE+ -mediated iPECsy4 delivery. Figure adapted from Geilenkeuser *et al* and generated in K. Paczewski, J.D. Truong, and G. Westmeyer's laboratory.

CHAPTER 6

Development of lipid nanoparticles to deliver ABE and PE RNPs

This chapter is derived in part from the following manuscript published in *Nature Biomedical Engineering:*

Holubowicz, R. *et al*. Safer and efficient base editing and prime editing via ribonucleoproteins delivered through optimized lipid-nanoparticle formulations. *Nature Biomedical Engineering* (2024).

© 2024 the Authors.

CHAPTER 6

Development of lipid nanoparticles to deliver ABE and PE RNPs[179]

6.1 Introduction

Monogenic diseases arise from genetic mutations that lead to aberrant or absent gene expression, and many lack appropriate therapies. Advances in molecular biology have enabled several treatment approaches to address this unmet medical need and correct the molecular basis of inherited diseases. Gene augmentation therapy, for example, delivers a wild-type (WT) copy of a mutated gene *via* a viral vector to supplement expression.[258] However, gene augmentation is limited by several major shortcomings, including potential loss of expression over long periods, lack of endogenous gene regulation, the inability to package large transgenes,[259] and low efficacy when treating mutations that act in a dominant manner.[260,261] An alternative approach to gene augmentation is genome editing. By correcting the genomic mutation *in situ*, a one-time treatment could be curative for the lifetime of the patient.[105,224] Of the gene editing techniques, clustered regularly interspaced short palindromic repeats and CRISPR-associated protein 9 (CRISPR/Cas9) editing has shown great promise and has advanced to clinical trials.[262] While these early trials have focused on treating monogenic diseases, it is possible to envision the application of genome editing for the treatment or prevention of common diseases with multifactorial or polygenic causes, such as malignancies,[263,264] cardiovascular disorders,[265] or neurodegenerative diseases.[266]

The CRISPR/Cas9 system used in gene editing trials consists of a Cas9 nuclease that is targeted to a genomic site by a protospacer-adjacent motif (PAM), and guide RNA that focuses the binding of Cas9 on a 20-bp-long DNA protospacer.[267] While CRISPR/Cas9 is easily programmed by the substitution of the guide RNA, the double-stranded DNA cleavage mediated by the nuclease can lead to a heterogeneous pool of editing outcomes, namely random insertions and deletions (indels) by non-homologous end joining (NHEJ), as well as cytotoxicity, p53

pathway activation, and large chromosomal irregularities and rearrangements.[262] Moreover, the efficiency of precise repair *via* homology-directed repair with a donor DNA template is low compared to NHEJ, especially in post-mitotic cells,[268] including major cell types of interest such as neurons.

Two alternatives to genome editing with CRISPR/Cas9 nucleases are base and prime editors, which fuse a DNA effector domain to a partially inactivated Cas9 domain, termed a Cas9 nickase.[61,81,139] These modifications combine the ease of programmability of CRISPR/Cas9 with the precision and direct chemistry of the effector domain of the base or prime editor, while avoiding NHEJ and cytotoxicity caused by double-stranded DNA breaks.[37] Thus, the purity of editing outcomes is much greater for base and prime editors; because the DNA-repair mechanisms that enable base and prime editing are cell-cycle independent, the high editing efficiencies are maintained in post-mitotic cell types when genome editing is performed *in vivo*.[186] CRISPR/Cas9 strategies, and base and prime editing in particular, are suitable approaches for dominant-negative diseases through correction of the pathogenic allele.[166,269] However, bystander editing by base editors is a concern,[270] as it could lead to unintended changes and hamper the therapeutic efficacy for the patient.[270] As well, the potential off-target effects of prime editors have not yet been carefully explored and documented.

One major hurdle that limits the application of base and prime editors is appropriate and efficient delivery of these editing constructs. The current standard for delivery of gene therapy and gene editing constructs is *via* viral vectors. However, the net size of the guide RNA constructs along with the base or prime editors exceeds the packaging limits of most commonly used viral vectors, such as lentiviruses (LV) and adeno-associated viruses (AAVs); indeed, base and prime editors delivered by AAV often are split into two viral vectors.[191] The wildtype LVs and AAVs are immunogenic, and current therapeutic viral vectors have been engineered to be less immunogenic; despite this, they still express base and prime editors over a sustained period, which poses an additional safety issue.[271] Whereas the intended “on-target” site is

thermodynamically favored to be edited, prolonged expression of base and prime editors leads to an increased risk of off-target editing at less-favored sites on the genome and transcriptome,[272] either in a Cas9-dependent [273] or in an effector-dependent manner.[274,275] Prolonged exposure to base editors has been also shown to increase bystander editing.[209] Lastly, there is a non-zero risk of viral genome integration, even when non-integrating viral vectors are used,[276] and this risk could even be worsened by the deployment of Cas9 nucleases and nickases.[168,170] Thus, as sustained expression of CRISPR/Cas9 is unnecessary and only risks unintended editing outcomes, CRISPR/Cas9 should be delivered in a transient manner and rapidly degraded thereafter. Multiple ways of achieving this transient action have been proposed, such as by virus-like particle (VLP) delivery,[209,211,213] mRNA lipid-nanoparticle (LNP) delivery,[277] and by direct ribonucleoprotein (RNP) delivery, either as naked RNP or as a lipoplex with cationic lipid reagents such as Lipofectamine 2000[177,278-280]. Such a variety of approaches has the potential to fine-tune the duration of activity of CRISPR/Cas9 machinery; however, these alternative delivery mechanisms require further refinement.

Conceptually, delivery of preassembled RNPs offers the most rapid onset and the shortest duration of genome editor activity in the cell. Real world human data for AAV-mediated delivery of retinal pigment epithelium-specific 65 kDa protein (RPE65) by voretigene neparvovec (Luxturna®) show that the therapeutic effect may be maintained for 7 years and potentially longer, demonstrating sustained expression of the transgene delivered by AAV.[281] Protein expression after subretinal delivery of the mRNA was detected within 4 hours and lasted for up to 7 days.[282] In the case of RNP, the purified protein is complexed with synthetic guide RNA before direct delivery into cells, thus bypassing the requirement of transcription (AAV, LV) and translation (AAV, LV, mRNA). VLPs that have RNP encapsulated in a viral shell offer the same advantageous activity kinetics as RNP; however, they are not chemically defined, which may complicate their manufacturing and clinical application. Use of purified RNP thus offers the most transient and chemically defined delivery modality for CRISPR/Cas9.

Previously, we reported the successful correction of the causative mutation in the *rd12* mouse model of Leber congenital amaurosis (LCA) through delivery of an adenine base editor (ABE) *via* LV,[80] AAV,[171] and engineered virus-like particles (eVLP).[209] Likewise, we recently delivered prime editor (PE) *via* eVLP and achieved effective and precise correction of the *rd12* mutation [229]. However, we expect that we can create a more defined, clinically relevant formulation of CRISPR/Cas9-based genome editor through optimization of direct delivery of base- and prime-editor RNPs.

Here, following screening of cell-penetrating peptides (CPPs) and commercially available ionizable cationic lipids with pK_a > 6, we demonstrate restoration of visual function in a mouse model of inherited retinal degeneration using purified ABE and PE RNPs encapsulated in lipid nanoparticles LNPs. This success opens the way to create chemically defined and protected delivery technologies for CRISPR/Cas9-mediated genome editing.

6.2 Results

6.2.1 Expression and characterization of Cre, ABE, and PE

The potential for therapeutic benefit from administered proteins hinges upon successful delivery across cellular membranes. A number of agents have been demonstrated to enhance intracellular delivery of genome-editing proteins and RNPs, including CPPs. Accordingly, we genetically fused three different CPPs (TAT, CPP5, and ANTP)[283-286] to the N-terminus of Cre recombinase and ABE8e-SpCas9-NG (hereafter referred to as ABE8e), which recognizes the NG PAM (**Figure 6.1a**). To facilitate purification, we also fused the 1D4 peptide tag [287] to the C-termini of ABE8e and the prime editor protein, PE2 (**Figure 6.1a**). Although Cre recombinase and Cas9-based genome-editing proteins possess distinct physicochemical properties, such as size and charge, we hypothesized that insights from the study of intracellular delivery of Cre recombinase would inform the design of delivery vehicles for ABE8e and PE2.

We first purified Cre recombinase to homogeneity, with or without the N-terminal CPP fusion, through nickel metal-affinity chromatography (Ni-NTA) chromatography (**Figure 6.1b**) and

size exclusion chromatography (SEC, **Figure 6.1c**), and confirmed purity of the product through sodium dodecyl sulfate-polyacrylamide gel electrophoresis (SDS-PAGE) visualized with Coomassie Brilliant Blue (CBB) (**Figure 6.1d**) and anti-Cre Western blot **Figure 6.1e**). ABE8e was similarly purified through affinity chromatography on TALON metal (**Figure 6.1e**) and 1D4 (**Figure 6.1f**) affinity columns and completed with SEC (**Figure 6.1g**); purity was again assessed by SDS-PAGE with CBB staining and anti-Cas9 Western blot (**Figure 6.1h,i**). PE2 was purified in a similar manner as ABE8e, with an additional heparin chromatography step after 1D4 immunoaffinity to maximize separation from impurities (**Figure 6.1j**). We noted that ABE8e after immunoaffinity chromatography still contained contaminating nucleic acids and aggregates; these contaminants were removed effectively by SEC (**Figure 6.1k**). We also noted that ABE8e RNP was more stable than ABE8e protein alone, as determined by differential scanning fluorimetry (DSF), especially when the single guide RNA (sgRNA) was refolded by heating and slow cooling (**Figure 6.1l, Supplementary Figure 6.1a-f**). The ABE RNP was further stabilized by 10% (w/v) sucrose. Like ABE8e, the PE2 RNP complex with an engineered prime-editing guide RNA (epegRNA) was more stable than PE2 protein alone; however, heat-refolding of epegRNA had no additional effect on PE2 RNP stability (**Figure 6.1m, Supplementary Figure 6.1g,h**). PE RNP did not require sucrose to remain soluble. For consistency, we heat-refolded all sgRNAs and epegRNAs used throughout the study. We also assessed the enzymatic activity of our ABE8e and PE2 RNPs through *in vitro* activity assays to ensure our proteins maintained activity following purification. ABE8e RNP displayed high levels of activity as assessed by an *in vitro* deamination assay (**Figure 6.1n,o**), and PE2 RNP similarly displayed high levels of activity as assessed by an *in vitro* reverse-transcriptase extension assay (**Figure 6.1p,q**).

6.2.2 CPPs enable efficient delivery of Cre in vitro *and* in vivo

We first assessed the delivery of Cre recombinase into the HEK293-loxP-GFP-RFP cultured cell line (color switching, “CS”) for a rapid and convenient fluorescent readout of intracellular protein delivery. The CS reporter cell line expresses green fluorescent protein (GFP)

constitutively, while a stop codon upstream of red fluorescent protein (RFP) gene prevents its expression. Upon delivery of Cre, floxed GFP-STOP is excised, enabling RFP expression in place of GFP (**Figure 6.2a**). As a positive control, we delivered Cre recombinase as a lipoplex with Lipofectamine 3000 to confirm the specificity of this cell line, reaching up to 40% conversion of the cells (**Figure 6.2b**). Cre recombinase alone induced low but detectable (up to 4.4%) color-switching from GFP to RFP, indicating an ability of unmodified Cre recombinase to cross cell membranes (**Figure 6.2b,c, Supplementary Figure 6.2a,b**). TAT- and ANTP-CPPs resulted in enhancement of Cre delivery (up to 28% and 45%, respectively), while the CPP5-CPP did not (**Figure 6.2b,c, Supplementary Figure 6.2a,b**). We also delivered Cre as a non-covalent complex with CPP peptide 6xHis-CM18-PTD4,[288] which increased the delivery of Cre to ~6%, and synergistically enhanced the delivery efficiency of CPP-fused Cre proteins (**Figure 6.2b,d, Supplementary Figure 6.3a,b, Supplementary Figure 6.4a,b**). Next, we delivered Cre into mT/mG mice, a global fluorescent reporter strain for monitoring Cre recombinase activity.[215] All cells from the mT/mG mouse constitutively express membrane-targeted tdTomato from the *Rosa26* locus, while a polyadenylation stop signal prevents the expression of enhanced GFP (eGFP). When Cre recombinase is introduced to the cells, the tdTomato and stop signals are excised, enabling eGFP expression (**Figure 6.2e**). We isolated and cultured primary mT/mG fibroblasts and demonstrated that Cre recombinase delivered alone resulted in low tdTomato to eGFP conversion, while Cre protein delivered by Lipofectamine 3000 resulted in higher conversion (**Figure 6.2f,g**). In contrast to the results with the CS line, only the fused ANTP peptide modestly improved delivery of Cre recombinase to the mT/mG fibroblasts (**Figure 6.2f,g**). When injected subretinally into mT/mG mice to evaluate *in vivo* activity (**Figure 6.2h**), the positive controls, AAV1-CMV-Cre, and eVLPs packaging Cre protein, mediated efficient tdTomato to eGFP conversion mainly in the retinal pigment epithelium (RPE), with occasional and scarce eGFP observed in photoreceptors, as detected by two-photon excitation (**Figure 6.2i,j**). The untagged Cre recombinase mediated minimal eGFP expression in the RPE (**Figure 6.2k**). Consistent with

our *in vitro* findings, Cre recombinase delivered subretinally with Lipofectamine 3000, the 6xHis-CM18-PTD4 peptide, or fused CPPs, effected ample eGFP expression in the RPE and photoreceptors **(Figure 6.2l-p**). Notably, although not effective *in vitro*, CPP5-fusion peptide enabled delivery of Cre into the photoreceptors *in vivo* (**Figure 6.2n**).

6.2.3 CPPs are unable to efficiently deliver ABE and PE in vitro and in vivo

As all of the CPPs were effective to some degree in delivering Cre recombinase *in vitro* and *in vivo*, we then applied them for the delivery of ABE and PE to the *rd12* mouse model of Leber congenital amaurosis. In these mice, a nonsense mutation in *Rpe65* abolishes RPE65 expression,[80,171] leading to a lack of visual chromophore production and photoreceptor light detection; but successful base or prime editing rescues this phenotype. To enable efficient *in vitro* screening, we developed a fluorescent *rd12* reporter cell line. We retrovirally transduced NIH/3T3 cells with a construct containing a fragment of the *Rpe65 rd12* cDNA encompassing an in-frame nonsense mutation, which is flanked by mCherry and eGFP. In unedited cells, the stop codon only permits mCherry protein expression, and successful transition by base or prime editing results in the expression of the mCherry-eGFP fusion protein (**Figure 6.3a**). We verified that adenine base editing *via* plasmid transfection of ABE8e with a previously validated *rd12* sgRNA [171] successfully edited the reporter construct and restored eGFP expression, as quantified by next-generation sequencing (22%, **Figure 6.3b**) and flow cytometry (32%, **Figure 6.3c**). Unmodified ABE applied on the *rd12* reporter cells caused low but detectable conversion of the fluorescent reporter (**Figure 6.3c,d**), but in contrast to fusion with Cre recombinase, the fused CPP peptides did not enhance the delivery of ABE *in vitro* (**Figure 6.3d**). However, as we previously observed that sucrose promoted stability of the RNP complex (**Supplementary Figure 6.1c-f**), the addition of sucrose (10% w/v) to the RNP mixture boosted delivery of the ABE8e RNP (**Figure 6.3d**). This was further enhanced 1.5-fold by the addition of the non-covalent 6xHis-CM18-PTD4 peptide, but fused CPPs still did not result in improved delivery efficiency (**Figure 6.3d**). In contrast to ABE, we did not observe a color change in the *rd12* reporter cells when PE was delivered with 2% sucrose, but

we noted activity when delivered with 10% sucrose. As in the case of Cre and ABE, the 6xHis-CM18-PTD4 peptide modestly improved delivery efficiency of PE2 RNP, by approximately 1.6-fold, though overall efficiencies remained low (**Extended Data Figure 6.1a,b**).

We then investigated whether the non-covalent 6xHis-CM18-PTD4 peptide or high sucrose concentration could effectively enable the delivery of ABE8e RNP *in vivo*. Subretinal injection of ABE8e RNP rescued the scotopic dark-adapted flash electroretinography (ERG) b-wave, indicating successful genome editing and restoration of the visual cycle, as untreated *rd12* mice do not exhibit a recordable ERG waveform in response to this light stimulus (**Figure 6.3e,f**). We noted the low-NaCl, high-sucrose formulation effected a more robust rescue, as measured by ERG b-wave amplitudes (**Figure 6.3g**). Consistent with our *in vitro* findings, the rescue of the scotopic flash ERG was promoted by the non-covalent 6xHis-CM18-PTD4 peptide but was not substantially improved by the fused CPPs (**Figure 6.3f,g,j,k**). We sequenced genomic DNA and transcripts isolated from RPE samples from the treated mice and noted up to 2% on-target genomic editing, corresponding to up to 7% on-target base editing in cDNA. The ABE editing outcomes were distributed approximately equally between precise edits and edits with at least one bystander adenine deaminated (**Figure 6.3h,i,l,m**). Notably, purified RNP led to more precise ABE editing than eVLP packaging of the same ABE8e, which led to multiply deaminated adenines.[209]

6.2.4 Optimized lipid nanoparticles enable the effective delivery of ABE and PE RNPs

As an alternative to CPPs, lipid reagents are also suitable for CRISPR/Cas9 RNP delivery.[130] Our preliminary investigations showed that binding of sgRNA by ABE results in change of the net charge from positive (zeta potential of +4.4 mV) to negative (-7.6 mV), which is in line with data published for Cas9 [289] and suggests that ABE RNP can be efficiently captured by cationic lipids as a lipoplex after simple mixing, or into a lipid nanoparticle after microfluidic encapsulation. For example, delivery of ABE RNP *in vitro via* a lipoplex with Lipofectamine 3000 was efficient in the *rd12* reporter cell line at concentrations as low as 20 nM (4.5 μg ml^{-1}) (**Extended Data Figure**

6.2b,c). ABE RNP delivered using Lipofectamine 3000 restored expression of RPE65 in the *rd12* cDNA reporter cell line, and next-generation sequencing analysis showed improved efficiency and precision of ABE editing mediated by RNP compared to plasmid (**Extended Data Figure 6.2d,e**). However, the formulation of ABE8e RNP that was optimal *in vitro* [50 pmol (11.2 μg) RNP per μL of Lipofectamine 3000, 5.6 μg RNP per eye] did not restore the ERG responses in the *rd12* mice. This result might correspond to toxicity of the high dose of Lipofectamine 3000 (50% by volume, 0.5 μL per eye), as we observed substantially higher rescue when we used a 5-fold lower dose of Lipofectamine 3000 with the same amount of ABE RNP (**Extended Data Figure 6.2f,g**). These results indicate that lipid-mediated delivery of ABE RNP *in vivo* is a viable approach; however, we envisioned that a chemically defined formulation that minimizes toxicity is required to maximize the potential of RNP delivery *in vivo*.

To this end, we sought to adapt LNP technology, which has successfully delivered mRNA vaccines and Cas9 nuclease RNP.[289,290] We found that the ABE RNP was transiently stable at pH 6.0 and in 25% ethanol, conditions which are necessary for LNP formulation. To create ABE and PE RNP LNPs, we tested a panel of ionizable lipids in a prototypical lipid mixture consisting of ionizable lipid, 1,2-distearoyl-sn-glycero-3-phosphocholine (DSPC), cholesterol, and 1,2-dimyristoyl-rac-glycero-3-methoxypolyethylene glycol-2000 (DMG-PEG 2000), in a molar ratio of 50:10:38.5:1.5, respectively. In order to avoid inactivation of ABE, we utilized ionizable lipids whose pK_a was above 6.0: 8-[(2-hydroxyethyl)[6-oxo-6-(undecyloxy)hexyl]amino]-octanoic acid, 1-octylnonyl ester (SM102): pK_a = 6.68 [291]; 9-octadecenoic acid, 1,1′-[7-[4-(dipropylamino)butyl]-7-hydroxy-1,13-tridecanediyl] ester (CL4H6): pK_a = 6.25 [292]; 1,2-dioleyloxy-3-dimethylaminopropane (DODMA): pK_a = 6.59 [293], enabling the protonation of the tertiary amine of the ionizable lipids at pH 6.0 to facilitate incorporation of ABE RNP into LNPs during encapsulation (**Supplementary Figure 6.5**, **Figure 6.4a**). We noted that the resultant LNPs were highly monodisperse with a hydrodynamic diameter between 200-250 nm, measured by dynamic light scattering (**Figure 6.4b**). We verified encapsulation of ABE RNP within our LNPs by distinguishing

encapsulated RNP from free ABE RNPs through immunoprecipitation with 1D4 resin and subsequent anti-Cas9 Western blot analysis (**Figure 6.4c,d, Extended Data Figure 6.3a,b**). While free ABE RNPs were bound by the resin and eluted with 1D4 peptide, ABE RNP LNPs were detected in the non-bound fraction (NB). The binding of ABE was epitope-specific, as a B6-30 resin directed against the N-terminus of rhodopsin did not bind ABE (**Extended Data Figure 6.3a**).[294] When the LNPs were tested, the majority of the ABE was found in the NB and in wash fractions (data not shown). Upon elution with Laemmli sample buffer, some RNP was eluted from the 1D4 resin (**Figure 6.4d**), suggesting non-specific binding because no material was eluted from LNP-treated resin when 1D4 peptide was used instead (**Extended Data Figure 6.3a**), and a similar amount of LNP-derived material was eluted with Laemmli sample buffer from non-binding control B6-30 resin (**Extended Data Figure 6.3b)**.

We tested the ABE RNP LNPs on the *rd12* reporter cells and noted that the LNPs effected rapid delivery of active ABE (**Figure 6.4e**). We also noted high conversion efficiency for all three LNPs, nearing 100% for SM102 LNPs (**Figure 6.4f,g**). The LNPs were highly potent, with as little as 20 nM ABE RNP (4.5 μg ml^{-1}) in SM102 LNPs eliciting nearly total conversion of the reporter cells. This result represented a substantial improvement over the lipoplex with Lipofectamine 3000, which peaked at approximately 50% of the cells converted (**Figure 6.4g, Extended Data Figure 6.2c**). We observed high toxicity of DODMA LNPs, which we alleviated by replacement of the 2.5% DSPC within the LNP with 1-stearoyl-2-oleoyl-sn-glycero-3-phospho-L-serine (SOPS) (**Extended Data Figure 6.3c**). The LNPs remained stable for at least 28 days when stored at -80 °C, and for at least 14 days when stored at 4 °C (**Extended Data Figure 6.3d**). We then verified that these LNPs were active *in vivo via* subretinal delivery into *rd12* mice, with all three LNPs effecting a substantial rescue of the ERG b-wave (**Figure 6.4h**). Importantly, although the concentration of ABE in the LNP preparation (2 μM, 0.45 mg ml^{-1}, 450 ng per eye) was at least tenfold lower than the RNPs formulated with sucrose or Lipofectamine 3000 *in vivo* (20-36 μM, 4.5 – 8.1 mg ml^{-1}, 4.5 – 8.1 μg per eye), we registered the most substantial response here, with

the ERG b-wave amplitude reaching up to 265 μV for the SM102 LNP-RNP, whereas the highest amplitude registered for free RNP was 185 μV with added 6xHis-CM18-PTD4 peptide (**Figure 6.3g**), and 200 μV with Lipofectamine 3000 (**Extended Data Figure 6.2g**).

Our experiments *in vitro* and *in vivo* suggested that LNPs made with SM102 were the most effective, but we reasoned that we could further improve the LNP formulation. As modulating PEG lipids can influence biodistribution,[295] we investigated the impact of varying the DMG-PEG 2000 concentration. We also investigated whether we could further optimize the lipid:RNA weight ratio, which was 40:1 in our original formulation. We found that DMG-PEG 2000 lipid is indispensable for encapsulation of the RNP, as LNPs without DMG-PEG 2000 exhibited the highest particle size (**Figure 6.4i**) and were not active *in vitro* (**Figure 6.4j**). We determined that LNPs with 2.5% DMG-PEG 2000 were the most potent *in vitro*, achieving nearly 100% conversion of cells at 5 nM (1.1 μg ml^{-1}) ABE RNP, a concentration 4-fold lower than that for 1.5% DMG-PEG 2000 (**Fig. 4j**). The optimal lipid:RNA weight ratio was at least 40:1 (**Extended Data Figure 6.3e,f**). The ABE RNP was fully encapsulated at the optimal formulation of 40:1 lipid:sgRNA ratio and 2.5% DMG-PEG 2000, as shown by 1D4 immunoassay (**Extended Data Figure 6.3g**) and SEC (**Extended Data Figure 6.3h**). We assessed the structure of our optimized RNP LNPs through cryo-electron microscopy (cryoEM) and confirmed intact and uniform particles with an approximate diameter of 100 nm (**Figure 6.4k**). We further characterized our RNP LNPs through absolute quantification of ABE within the LNPs through targeted proteomics (**Figure 6.4l,m, Supplementary Figure 6.6a-e**). We noted that Cas9 and TadA* deaminase peptides were detected at the same level, indicative of intact, full-length ABE8e protein within the LNPs (**Figure 6.4n**). The ABE RNP LNPs restored expression of RPE65 in the *rd12* cDNA cell line, and rescue *via* RNP was notably higher *via* LNP delivery, compared to Lipofectamine 3000 (**Figure 6.4n**). Next-generation sequencing revealed that the RNP LNPs mediated higher on-target editing, up to 40%, compared to plasmid- or Lipofectamine-delivered RNP treatment, and lower bystander editing compared to plasmids (**Figure 6.4o**). The off-target activity of ABE in the *rd12* cDNA cell line was minimal, as we noted

≤ 0.3% edited alleles in off-target sites, concurrent with almost 60% editing of the on-target adenine (**Figure 6.4p**). When tested *in vivo*, the SM102 LNP-RNP with 2.5% DMG-PEG 2000 resulted in a higher maximal rescue of the ERG b-wave compared to SM102 LNP RNPs with 1.5% DMG-PEG 2000 (368 μV and 265 μV, respectively), approaching response levels registered for WT mice (**Figure 6.4q**).

We also successfully encapsulated the prime editor PE2 within our optimized LNP formulation. Like ABE RNP, PE2 RNP can be efficiently delivered *in vitro* as a lipoplex with Lipofectamine 3000, although it was efficient at higher concentrations of RNP (500 nM (149 μg ml^{-1}) for PE compared to 20-100 nM (4.5 – 22.4 μg ml^{-1}) for ABE, **Extended Data Figure 6.1a,c,d; Extended Data Figure 6.2b,c**). Our initial effort to encapsulate PE2 RNP into LNPs with 1.5% DMG-PEG 2000 was partially successful, as some unencapsulated PE2 protein was detected in the 1D4 immunoprecipitation assay (**Figure 6.5a**)**.** The particle size was also larger than for ABE RNP LNPs (**Figure 6.5b**). Nevertheless, the unoptimized PE RNP LNPs delivered PE into the *rd12* reporter cells with efficiency surpassing Lipofectamine 3000 (**Figure 6.5c**). By increasing the concentration of DMG-PEG 2000 to 2.5%, we no longer detected unencapsulated PE2 (**Figure 6.5a**) and observed robust delivery of PE into the *rd12* reporter cells (**Figure 6.5 c,d**). The cryoEM images of optimized PE RNP LNP revealed the presence of homogenous, well-defined particles (**Figure 6.5e**). We noted that Cas9 and the reverse transcriptase (MMLV-RT) were not detected at equimolar concentrations within our PE2 RNP LNPs, indicating that further improvements may be necessary in LNP formulation and in PE2 purification (**Figure 6.5f**). Nevertheless, the PE RNP LNP restored expression of RPE65 in the cDNA-expression cell line (**Figure 6.5g**). Next-generation sequencing revealed that RNP-mediated prime editing led to exceptional purity of editing outcomes, as we did not notice any unwanted editing of the cells bearing the *Rpe65 rd12* cDNA, while indels were detected in cells transfected with PE and epegRNA plasmids (**Figure 6.5h**). No off-target editing occurred in the cells treated with PE RNP LNP (**Figure 6.5i**). Importantly, using PE2 RNP LNPs, we achieved a comparable magnitude of rescue of the ERG

b-wave in *rd12* mice compared to ABE RNP LNPs, with ERG b-wave amplitudes exceeding 300 μV (**Figure 6.5j**).

6.2.5 In vivo *ABE and PE editing in the* rd12 *mouse model restores visual chemistry and physiology*

After we characterized the LNPs *in vitro* and screened them *in vivo* for the rescue of ERG response in the *rd12* mice, we applied the optimized RNP LNPs to investigate the physiological rescue of the *rd12* inherited retinal degeneration phenotype. As transient exposure to genome-editing RNPs improved our editing purities *in vitro*, we sought to determine the residence time of ABE within the mouse eye. We injected the optimized ABE RNP LNP with SM102 and 2.5% DMG-PEG 2000 subretinally into WT mice and sacrificed individual mice at sequential intervals to determine the kinetics of ABE degradation. We noted that ABE was detectable up to 24 h post-injection in the neural retina, and up to 48 h in the RPE (**Figure 6.6a**). We then delivered our optimized ABE RNP LNP *via* subretinal injection into 3-4-week-old juvenile *rd12* mice. Two weeks after injection, we noted an average of 0.30% precise correction of *Rpe65* genomic DNA by ABE and an average of 0.12% precise correction by PE (**Figure 6.6b**), and an average of 1.25% precise correction in *Rpe65* transcripts by ABE and 1.28% by PE (**Figure 6.6c**). We noted 0.67% bystander editing by ABE in the transcripts, with no indels with either ABE or PE. The base editing efficiency was similar in eyes treated with ABE RNP LNP with 1.5% DMG-PEG 2000 (not shown). We did not detect off-target editing (**Supplementary Figure 6.7a,b**) and we did not note any editing when ABE and PE RNPs were complexed with guide RNAs that did not target the *Rpe65* locus (**Supplementary Figure 6.8a,b**). We also detected restoration of RPE65 in the RPE of the *rd12* mice treated with ABE RNP LNP, according to Western blot (**Figure 6.6d**) and immunostaining of RPE flatmounts (**Figure 6.6f**). Restoration of RPE65 function would lead to the production of 11-*cis*-retinal, the chromophore for photoreceptor-mediated vision. Accordingly, we assayed the retinoids in the whole eyes and detected 11-*cis*-retinal only in *rd12* mice that were treated with either ABE or PE RNP LNPs (**Figure 6.6e**). When we performed scotopic flash ERG

on the treated *rd12* animals, we observed rescue of both the a- and b-wave ERG amplitudes, both of which were not detectable in untreated *rd12* animals (**Figure 6.6g**). Again, we noted no rescue of the ERG flash response upon treatment with ABE and PE RNPs with non-targeting guides (**Supplementary Figure 6.8c,d**). We also demonstrated restoration of intact visual signaling from the eye through the optic nerve. The pupillary light reflex (**Figure 6.6h**) and evoked responses from the super colliculus (SC) and primary visual cortex (V1) (**Figure 6.6i, Extended Data Figure 6.4**), which both require 11-*cis*-retinal and intact neuronal connections, were restored in *rd12* mice treated with ABE or PE RNP LNP. These results collectively demonstrate that a single dose of ABE or PE RNP LNPs can correct the *Rpe65 rd12* mutation and partially restore normal physiology and biochemistry in the *rd12* eye. Further development of ABE and PE RNP geared towards increased editing efficiency will result in a blueprint for chemically defined, effective RNP LNP formulations that allow for the repair of genetic mutations causing dysfunction of the RPE and other tissues.

6.3 Discussion

Genome-editing technologies have opened new avenues in gene therapy, offering potential strategies for addressing both genetic and non-genetic diseases.[224,296,297] Simultaneously, the rapid advances in genome editing have illuminated the critical necessity for precise, safe, and efficient delivery systems. Traditionally, vectors including AAV and LV have been the standard approaches in this domain. However, a growing body of evidence highlights intrinsic limitations associated with these vectors. For AAV vectors, one limitation is their constrained packaging capacity. AAVs can typically accommodate genomes around 4.7 thousand base pairs long, which can be restrictive, especially when attempting to deliver larger genome-editing constructs such as base editing and prime editing systems.[298-300] This limitation necessitates either the truncation of essential elements (e.g. RNaseH); packaging of less active homologs; or the use of dual-vector strategies, which can reduce efficiency and increase complexity. While lentiviral vectors accommodate larger genetic payloads, their use raises other

concerns related to their integration into the host genome.[250] Such integrations, though ensuring long-term expression, can disrupt endogenous genes or regulatory elements, leading to potential genotoxicity.[301-303] Unintended insertions can also potentially activate oncogenes or deactivate tumor suppressor genes, escalating the risk of malignancies.[304,305] Moreover, both AAV and lentiviral vectors can induce immune responses.[306-310] The pre-existing immunity to certain AAV serotypes in the population can render AAV-mediated therapies less effective or even elicit adverse immune reactions and prevent redosing.[308] Similarly, lentiviral vectors can trigger cellular immune responses against transduced cells, impacting the longevity and efficacy of the therapeutic intervention. These challenges underscore the necessity to explore alternative delivery systems that can bypass the constraints and risks associated with AAV and LV. Consequently, non-viral delivery methods such as LNPs, silica nanocapsules, eVLPs, and RNP delivery have been developed.[177,180,209,282,311-316] A major advantage of the approach we propose here is the pharmacologically defined formulation of the RNP LNPs, which offer the most transient exposure to genome-editing agents. Before progressing into clinical trials, a reproducible and manufacturable platform will be required to maximize patient safety and satisfy regulatory requirements. Compared to viral and viral derived platforms, such as AAV and eVLPs, an LNP approach allows for a controllable synthetic therapeutic strategy with definable components, and LNPs could offer more uniform and reproducible synthesis compared to previously described lipoplex formulations which delivered RNPs.[317]

In this study, we have developed methods that utilize CPPs and LNPs to deliver proteins and ribonucleoprotein complexes. CPPs, when used as an excipient rather than fused to the protein, improved delivery of ABE RNP. The amphiphilic, cationic CPP can bridge the interactions between RNP and cell surface receptors and proteoglycans and improve absorption of ABE RNP by the cells [288,318,319], and circumvent intracellular challenges such as endosomal escape. While encouraging, the CPP approach had solubility and efficiency issues, and was ineffective for PE RNP. We decided to use protein-lipid and RNA-lipid interactions to bring RNPs into the cell using

LNP technology, and we ultimately delivered ABE8e and PE2 RNPs to correct the *rd12* mutation *in vitro* and *in vivo.* ABEs have previously been delivered *in vitro* in a variety of cell lines and *in vivo* into the RPE and other tissues as a lipoplex[177,279,280], but the cellular toxicity associated with Lipofectamine-type reagents used to form the lipoplexes suggests that less toxic LNPs could improve the functional outcome of RNP-mediated editing.[320]

Our results show that ABE8e RNP is a useful testing platform for RNP-delivery technology, and the technology developed for ABE RNP delivery can be rapidly adapted for PE. We imagine that this approach could be further extended to cytosine base editors, as encapsulation is dependent primarily on the negatively charged guide RNA. When compared head-to-head *in vivo* in the *rd12* mouse, base editing was more efficient at the target base than prime editing, while prime editing resulted in pure editing outcomes. Consequently, the higher efficiency of ABE means it will be favored over PE if bystander editing does not result in deleterious coding changes. In general, optimization of transient ABE delivery could be more straightforward than PE, due to the lower complexity and higher activity of ABE. We demonstrated that the precision of base editing can be further improved by using more precise, albeit less active variants, for example ABE8e N108Q (**Extended Data Figure 6.2a, Extended Data Figure 6.3i-k**). However, PE is still indispensable as it can perform edits that base editors cannot, including modification of sites containing clustered adenines or cytosines. Our study utilized a PE2 editing strategy without the introduction of a second guide RNA that programs a nick on the unedited strand, the PE3 strategy, which in general increases prime editing efficiency. Like the eVLP platform, LNPs allow RNPs with multiple guide RNAs to be packaged, theoretically allowing for PE3.[289] However, it is unclear if adopting PE3 would improve editing outcomes without unacceptable indel formation.

Our study has identified several challenges associated with the LNP delivery system. One of the primary concerns centers on the low concentration of the active macromolecule. Furthermore, the lipid content, which exceeds the weight of the ribonucleoprotein complex by approximately eight times, could pose potential translational challenges in non-human primates

or humans, and optimization of the LNP to increase payload delivery without inducing immune response may be required. Overall, optimizing the formulation of LNPs and their characteristics is of paramount importance for enhancing delivery efficiency, especially for challenging target tissues such as the RPE. The RPE has specific structural and physiological attributes that can impact the effectiveness of LNP-mediated delivery. Reducing the size of LNPs has been highlighted as a potential strategy to enhance their uptake by cells. Smaller nanoparticles, typically below 100 nm in diameter, have been shown to be more readily internalized by cells, possibly due to more efficient endocytosis.[321] For the RPE, with its tight junctions and unique phagocytic role, smaller LNPs may offer better uptake and retention to maximize LNP delivery. Enhancing the functionality of LNPs is another potential approach.[314] Incorporating specific ligands or targeting moieties that recognize and bind to receptors on the RPE cells could improve LNP uptake.[322] Recent studies have demonstrated the effectiveness of peptides and small molecules that target RPE-specific receptors and increase the internalization of nanoparticles.[313,323] By tailoring the surface properties and composition of LNPs, it could be feasible to exploit the unique biology of the RPE to enhance delivery.

In summary, we learned that inclusion of a fused peptide in a protein sequence can be effective for a small, positively charged protein such as Cre (~40 kDa), but not for a large protein such as ABE (187 kDa protein plus 33 kDa sgRNA per monomer), which, as an RNP, is negatively charged. Recently, another group demonstrated extensive optimization of fused CPPs that enabled the delivery of a nuclease Cas9 RNP *in vitro* and *in vivo* [324]. It is important to note, however, that Cas9 nuclease is a monomer,[325] and thus is a better candidate for CPP-mediated delivery than ABE which dimerizes in solution.[66] This self-association can be noted in our SEC profile in **Fig. 1k**, where the ABE protein has an apparent molecular weight of 480 kDa, 2.6-fold higher than the theoretical molecular weight of 187.1 kDa. Non-covalent CPP can be used to overcome these issues *in vitro*, as demonstrated by us and others.[326,327] We were quite disappointed that high concentrations of ABE were still needed, and out of concern about potential

toxicity and immunogenicity of ABE, we overcame this by encapsulating RNP into LNP. We justified the shift from CPP- to lipid-based delivery by considering the molecular properties of ABE, the most important of which was the negative charge of the RNP that would enable interactions of ABE with cationic lipids. Indeed, in a reporter cell line, the typical cationic lipid reagent Lipofectamine 3000 enabled effective delivery of ABE RNP at a 25-fold lower concentration than with non-covalent CPP and sucrose. As a next step, we explored the chemically defined LNP technology, which proved to be the most effective both *in vitro* and *in vivo*, achieving superior therapeutic effect at a 15-fold lower concentration of ABE than with CPP or Lipofectamine. Importantly, in contrast to ABE, PE was efficiently delivered only as a lipoplex with Lipofectamine 3000 or encapsulated in LNP, not with non-covalent CPP.

We have estimated the approximate number of RNP particles encapsulated per LNP. Two models were considered for this estimation: (1) the solid sphere model, and (2) the liposome model. The solid sphere model posits that lipids, guide RNA, and ABE protein form a compact, water-excluded sphere, and the mass of lipids and RNPs per LNP increases proportionally to volume, cubically with increasing radius. Conversely, the liposome model suggests the formation of a lipid bilayer encapsulating an aqueous interior, thus accommodating ABE proteins within; this model predicts the formation of a higher number of particles, each with fewer protein molecules, due to the internal aqueous space. Here, the mass of lipids and RNPs per LNP increases proportionally to the lipid bilayer area, approximately quadratically with increasing radius of the LNP.

Based on the cryoEM data, we observed condensed product inside the nanoparticles and blebs containing water. Therefore, we favor the liposome model (**Figure 6.4k**). To simplify the estimation, we assume that all the lipids in the liposome form a lipid bilayer. The imaged preparation of LNP contained 928.8 µg of lipids (1447 nmol, $8.71 \cdot 10^{17}$ molecules), 119.7 µg of ABE protein (0.64 nmol, $3.85 \cdot 10^{14}$ molecules) and 23.22 µg of sgRNA. Under the assumption that a surface of a lipid head group is 0.71 nm^2,[328] and an average thickness of a lipid monolayer is 5

nm,[329] we estimated that a liposome whose diameter is 100 nm would require 80,000 lipid molecules per particle, and the preparation would contain $1.09 \cdot 10^{13}$ particles. Knowing that $3.85 \cdot 10^{14}$ ABE RNP molecules were used to prepare the LNPs, we can estimate that there are approximately 35 ABE RNP molecules per particle. This number changes to 87 RNP per LNP when the diameter is determined by particle size analysis (154 nm) and used for the calculation.

According to the solid-sphere model, assuming the density of LNP to be 1 g ml^{-1}, the LNPs would occupy a volume of 1.07 µl. A single 100 nm nanoparticle would have a volume of $5.23 \cdot 10^{-16}$ liter; therefore, $2.05 \cdot 10^{12}$ nanoparticles would encapsulate $3.85 \cdot 10^{14}$ molecules of ABE, approximately 188 RNP molecules per nanoparticle (or 687 for particles of d = 154 nm).

The typical mRNA LNP encapsulation process involving buffer at pH 4 is not compatible with Cas9/ABE/PE RNP, which denatures and precipitates at low pH. In the approach from Siegwart's group, encapsulation of Cas9 RNP is performed in PBS at neutral pH by the addition of a permanently charged lipid DOTAP, which binds RNP and seeds further interactions with other lipids, including the ionizable lipids C12-200, 5A2, or DLin-MC3-DMA, which are uncharged at this pH. Importantly, the Siegwart group's formulations using a variety of lipid mixes suggested that the LNP technology is quite flexible. Due to the complex nature of ABE and PE compared to Cas9 nuclease used in the Siegwart report,[289] (larger ABE and PE, dimerization of ABE, longer guide RNA for PE), and poor solubility of our RNPs in PBS, we decided to develop a unique approach. We found that ABE is soluble and active at pH 6 and higher, enabling us to encapsulate RNPs at pH 6. Based on our experience with liposomes and mRNA nanoparticles, we utilized monoprotic Tris base and acetic acid as the buffer. We included 10% sucrose in all solutions to prevent aggregation of ABE RNP, which occurs at ABE RNP concentrations above 4 µM without sucrose. Next, to provide a driving force for interactions between the positively charged lipids and the negatively charged guide RNA and acidic side chains of ABE/PE, we used ionizable lipids with pKa values significantly above 6.0, so that they would be at least partially protonated and bear significant positive charge at pH 6. We kept the ionic strength of our encapsulation buffer low (10

mM NaCl instead of ~137 mM NaCl plus other salts in PBS) to further strengthen the interactions between lipids and our cargo. All these considerations helped us achieve successful encapsulation of first ABE, and then PE, using three suitable ionizable lipids, SM102, CL4H6 and DODMA. SM102 was chosen for further optimization due to toxicity of DODMA and poor reproducibility with CL4H6, including optimization of the lipid:RNA ratio and PEG content; we settled on and chose the 40:1 weight ratio and 2.5% DMG-PEG 2000 in the lipid mixture.

Comparing the two approaches, the LNPs with permanently cationic lipids made by Wei *et al*.[289] had a particle size of 200 nm or more, and polydispersity index mostly above 0.1 (**Figure 6.2**). Our optimized RNP LNP had a particle size consistently below 200 nm and a polydispersity index predominantly below 0.1. The low diameter of our optimized LNPs formed at pH 6 enables sterile filtration through 0.22 um filters, which is a significant advantage for clinical translation. In terms of activity, Siegwart-group LNPs were effective at a tested concentration of 9 nM RNP, whereas our ABE LNPs and PE LNPs converted 100% of the reporter cells at as low as 5 nM RNP (**Figure 6.4j Figure 6.5c**). Our LNPs can be stored frozen for at least 6 months without loss of activity, which was not demonstrated for SORT LNP. Overall, we conclude that while distinct, our, Siegwart's and others' approaches are viable starting points for further development of Cas9-RNP delivery technology [290], and our formulation is uniquely optimized for the more complex and challenging delivery of ABE- and PE-RNPs.

Despite the challenges with the LNP delivery system, our study presents encouraging functional outcomes. While the observed editing efficiency of *Rpe65* in *rd12* mice was lower than previously reported, a noteworthy restoration of retinal function was evident, as demonstrated by the ERG recordings. Several factors potentially underlie this functional improvement despite the modest genomic correction. A mechanism to consider is the interplay between mRNA transcribed from the corrected *Rpe65* allele and that from the mutant *Rpe65* allele harboring a nonsense mutation. It is well-established that mRNA molecules containing premature termination codons are often subjected to nonsense-mediated decay, a surveillance pathway that degrades aberrant

mRNA transcripts.[330] Thus, mRNA transcribed from the mutant *Rpe65* allele could be selectively targeted and degraded by the nonsense-mediated decay pathway, leading to its reduced levels in the RPE. Concurrently, mRNA derived from the corrected *Rpe65* allele would remain stable and accumulate, effectively compensating for the diminished mutant transcript levels. However, additional experiments are needed to correlate functional *Rpe65* mRNA levels with the zygosity of corrected alleles of *Rpe65* in *rd12* mice.

Supporting evidence from our prior investigation provides additional insight into the functional implications of our current findings. In a previous study, we characterized a novel animal model, the RPE65-P2A-CreERT2 knock-in mouse. Remarkably, the homozygous knock-in mice, despite expressing RPE65 at levels amounting to only 1-5% of their WT counterparts, exhibited ERG responses that were nearly indistinguishable from the WT mice.[331] The editing in our current study also resulted in the partial restoration of vision-dependent outcomes, such as the pupillary light reflex and V1 and SC responses, which are all dependent on visual input to the brain. This observation suggests that achieving high levels of RPE65 correction and expression would not be required for fully restoring retinal function, but a low yet stable level of RPE65 could suffice to produce clinically-relevant outcomes. In essence, while the genomic-correction efficiencies mediated by ABE or PE LNP could be further optimized, restoration of retinal function could be achieved at low editing rates. The nuanced interplay between genomic editing, mRNA stability, and functional restoration provides a compelling rationale for achieving even modest genomic corrections with strategically targeted editors, as they could bring about meaningful therapeutic benefits.

A fundamental gap in our understanding of the cellular uptake and processing mechanisms for LNPs and RNPs limits the efficiency of these systems. Clarifying these mechanisms is crucial for enhancing delivery efficiency. The discrepancies in the delivery efficiencies of Cre, ABE, and PE within our study suggests that optimizing the size of the encapsulated protein, the overall diameter of the LNP, the length of the guide RNA, and the

surface charge of the protein are crucial factors for improving delivery efficiency. In addition to these physical and chemical optimizations, the development of newly evolved genome editors offers further potential to enhance editing efficiency. These advanced editors can be specifically tailored for target-sequence specificity, providing a refined approach to genome modification with potentially higher efficacy and precision.

In conclusion, our results highlight the potential of LNP-mediated delivery of RNPs as an attractive alternative to viral delivery methods in genome-editing applications. We and others previously demonstrated the potential of RNP delivery *via* eVLP, lipoplex, or RNP with Lipofectamine-type cationic lipids. Here, we present chemically defined and adjustable LNPs that are highly reproducible and stable. While before advancing to GMP production for non-human primate and human trials our RNP LNPs require additional optimization, including fully quantitative characterization of encapsulation efficiency, this approach offers major safety and manufacturing advantages. Future endeavors should focus on refining the LNP formulation to enhance delivery and editing efficiency, particularly to target tissues selectively, while also seeking a deeper understanding of the functional consequences of genome editing. There is also a need to develop novel ionizable lipids that would efficiently deliver the RNP with reduced risk of inflammation. This multi-faceted approach will be instrumental in harnessing the full potential of genome-editing technologies and ensuring their safe and effective clinical translation.

6.4 Methods

Animals

Pigmented Gt(ROSA)26Sor$^{tm4(ACTB-tdTomato,-EGFP)Luo}$ (ROSA$^{mT/mG}$) mice were purchased from the Jackson Laboratory (Bar Harbor, ME, USA, JAX 007676) and crossed with BALB/cJ albino mice (JAX 000651) to establish an albino ROSA$^{mT/mG}$ line, referred to as mT/mG mice. The C57BL/6J (”WT", JAX 000664) and *rd12* (JAX 005379) mouse lines were purchased from the Jackson Laboratory and housed in the vivarium at the University of California, Irvine, where they were maintained on a normal mouse chow diet and a 12 h/12 h light/dark cycle. All animal

procedures were approved by the Institutional Animal Care and Use Committee of the University of California, Irvine, and were conducted in accordance with the NIH guidelines for the care and use of laboratory animals, and with the Association for Research in Vision and Ophthalmology Statement for the Use of Animals in Ophthalmic and Visual Research.

Molecular cloning

The N-terminal Cre recombinase fusion proteins were produced from recombinant plasmids based on pTAT-Cre.[285] pTAT-Cre was purchased from Addgene (#35619), and pCPP5-Cre and pN-Cre inserts were synthesized and cloned by GeneWiz (South Plainfield, NJ, USA) and clone into pET-28b. The antennapedia (ANTP) DNA sequence was generated by single-strand oligo annealing, using ANTP-Or_F and ANTP-Or_R primers. The two oligonucleotides were mixed in a 1:1 molar ratio at a total DNA concentration of 80 μM in 50 mM Tris-HCl, pH 7.4, 62.5 mM NaCl, and 10 mM ethylenediaminetetraacetic acid (EDTA). The annealing was done in a thermocycler with an initial heating step of 2 min at 95 °C, and gradual cooling for 45 min to 25 °C. The pANTP-Cre plasmid was obtained by replacing the TAT sequence with ANTP between the NcoI and NdeI cloning sites. The plasmids were propagated in *Escherichia coli* NEB 5-alpha cells (New England Biolabs, Ipswich, MA, USA, C2987H). To produce a positive control Cre eVLP, Cre (Addgene, 123133) was subcloned into pCMV-MMLVgag-3xNES-ABE7.10-NG (Addgene, 181753) *via* USER cloning, and eVLPs were prepared as previously described.[209]

Genes encoding ABE7.10, ABE8e, and PE2 constructs were subcloned into pRha rhamnose-inducible expression vectors *via* USER cloning (NEB). The 1D4 peptide with a preceding tobacco etch virus (TEV) protease recognition site was introduced by PCR site-directed mutagenesis and KLD cloning (NEB #M0554S). Sequences encoding cell penetrating peptides were introduced into ABE using PAGE-purified single-strand oligonucleotides (Sigma-Aldrich, Burlington, MA, USA). The oligonucleotides were annealed at a final concentration of 25 μM in 10 mM Tris-HCl pH 8.0, 50 mM NaCl, 1 mM EDTA, 5 mM $MgCl_2$ by heating at 95 °C for 5 min and slow cooling in a thermocycler. Assembled duplexes were ligated at a 100-fold excess into the protein expression

vectors linearized with FastDigest NdeI (Thermo Fisher, Waltham, MA, USA, FD0584). The ligation mixtures were transformed into NEB5α cells and plated onto LB-agar plates with 25 μg ml^{-1} kanamycin. Candidate clones were identified using colony PCR and confirmed by Sanger sequencing (GeneWiz).

Expression and purification of Cre recombinase

The plasmids were transformed into *Escherichia coli* BL21star (DE3) (Thermo Fisher Scientific, C601003), and the selected clones were grown in Terrific Broth (TB, Thermo Fisher Scientific, 22711-022) with 50 μg ml^{-1} kanamycin (Goldbio, St. Louis, MO, USA, K-120-SL25), overnight at 37 °C with mixing at 190 rpm. The production cultures were inoculated with overnight cultures and incubated at 37 °C with mixing at 190 rpm. After A_{600nm} reached 0.5, protein expression was induced with 0.5 mM isopropyl β-D-1-thiogalactopyranoside (IPTG, Goldbio, I2481C25) and incubation was continued at 20 °C for 16 h. The cells were harvested by centrifugation at 7,000*g* at 4 °C for 10 min, and the pellets were stored at -80 °C until used further for protein purification.

Cre recombinase was kept on ice or refrigerated at 4-8 °C throughout the purification procedure. The cell pellet from a 1.5-liter culture was thawed in a room-temperature water bath, resuspended in the Cre-lysis buffer (50 mM Na phosphate pH 7.4, 1 M NaCl, 1 cOmplete EDTA-free protease inhibitor cocktail tablet (MilliporeSigma, St. Louis, MO, USA, COEDTAF-RO) per 50 ml buffer) and lysed by sonication (125-W pulses (5 sec on / 5 sec off) for 10 min total); or French press (3 passes at up to 15,000 psi). The lysate was centrifuged at 48,500*g* for 15 min and incubated with 1 ml of a suspension of Ni-Sepharose High Performance beads (Cytiva, Uppsala, Sweden, 17526801) in a rotating mixer for 1 h. The resin was centrifuged at 500*g* for 5 min, washed with 40 ml of the Cre-wash buffer (25 mM Na phosphate pH 7.4, 500 mM NaCl), centrifuged again, packed in a Tricorn 5/50 column and connected to a Bio-Rad DuoFlow system (Bio-Rad, Hercules, CA, USA) and perfused at 0.5 ml min^{-1}. The resin was washed with 20 ml of the Cre-wash buffer or until a stable absorbance baseline was observed; then, the proteins were

eluted with 30 ml of a continuous gradient of the Cre-elution buffer (25 mM Na phosphate, pH 7.4, containing 500 mM NaCl, 500 mM imidazole). The fractions containing Cre recombinase that were identified by SDS-PAGE and CBB staining (Quick Coomassie stain, Anatrace, Maumee, OH, USA, GEN-QC-STAIN-1L) were concentrated and subjected to size-exclusion chromatography on a Superdex 200 Increase 10/300 GL column (Cytiva, 28990944), or a HiLoad 16/600 Superdex 200 pg column (28989335), with P500G buffer (sodium phosphate 20 mM pH 7.4, NaCl 500 mM, glycerol 20% (v/v)) as the mobile phase. Fractions containing pure Cre recombinase were concentrated, snap frozen in liquid nitrogen, and stored at -80 °C.

Expression and purification of ABE and PE

E. coli BL21star (DE3) cells (Thermo Fisher Scientific, C601003) were transformed with the expression plasmids and grown overnight on Luria-Bertani (LB)-agar plates with 25 μg ml^{-1} kanamycin; single clones were used to inoculate starter cultures in TB with kanamycin, and grown overnight. One and a half liter of TB with kanamycin was inoculated with 10 ml of starter culture, and the cells were grown at 37 °C with mixing at 190 rpm until they reached an A_{600nm} of 1.5. Then, the cultures were cooled in an ice-water slurry for 30 min – 1 h, and protein expression was induced with 0.8% (w/v) rhamnose (Goldbio, R-105-250). The proteins were expressed at 17 °C with mixing at 190 rpm for 16-24 h. The cells were harvested by centrifugation at 5,000*g*, 10 min, 4 °C, and the pellets were stored at -80 °C.

All protein purification steps were conducted in a cold room (~4-8 °C), or on ice. The thawed cells from a 1.5-liter culture were homogenized with a 40 ml Dounce homogenizer in a lysis buffer (100 mM Bis-Tris Propane, pH 8.0, 1 M NaCl, 20% glycerol (v/v), 5 mM tris(2-carboxyethyl)phosphine (TCEP), 1 cOmplete Ultra EDTA-Free protease inhibitor tablet per 40 ml of the buffer), and lysed by sonication with a Qsonica Q125 sonicator (125 W) with a 1/8-inch microtip at 100% amplitude for a total of 20 min (intermittent pulses: 5 sec on; 5 sec off). The lysate was clarified two times at 4 °C by centrifugation at 48,500*g* for 10 min. ABE was captured on a 3-ml TALON metal-affinity resin (Takara Bio, San Jose, CA, USA, 635502). The resin was

then washed with 100 ml of the lysis buffer without inhibitors, and with 10 ml of the wash buffer (100 mM Bis-Tris Propane, pH 8.0, 500 mM NaCl, 20% glycerol (v/v), 1 mM TCEP). The proteins were eluted with the wash buffer supplemented with 150 mM imidazole.

In a second step, ABE was purified by immunoaffinity chromatography using a 1D4 resin (Sepharose CL-4B resin (Cytiva, 17043001), with immobilized 5-10 mg ml^{-1} 1D4 antibody purified in house). The 1D4 resin (4 ml) was packed in a DWK Life Sciences Kimble™ Kontes™ FlexColumn™. The column was equilibrated with the wash buffer (described above). ABE was loaded by gravity flow. The column was washed with at least 40 ml of the wash buffer at 0.5 ml min^{-1}, and then ABE was eluted with 1 mg ml^{-1} 1D4 peptide in the wash buffer at approximately 1 ml h^{-1}. Fractions containing ABE were pooled, concentrated, and further purified to remove contaminating nucleic acids and aggregates, by size exclusion chromatography on a Superdex 200 Increase 10/300 GL column, or a Superdex 200 16/60 Prep Grade column. The protein was eluted with the ABE storage buffer (4-(2-Hydroxyethyl)-1-piperazine ethanesulfonic acid (HEPES) 10 mM, pH 7.0, 500 mM NaCl, 20% glycerol). The fractions containing pure ABE were concentrated using Amicon Ultra centrifugal filters with 30-kDa molecular weight cut-off membranes (Merck, UFC903024), sterilized by passage through 0.22-µm filters, quantified using UV absorption at 280 nm, divided into aliquots, and snap frozen in a chilled metal block for storage at -80 °C.

PE was purified using a similar procedure as for ABE. Cells expressing PE were lysed using a single pass through the French press and subsequent sonication for 10 min. Metal affinity and immunoaffinity steps were identical as for ABE, except the wash buffer contained 400 mM NaCl. After immunoaffinity chromatography, PE was subjected to heparin-affinity chromatography (HiTrap Heparin HP 5 ml, Cytiva, 17040703) at 0.5 ml min^{-1}. The heparin column was equilibrated with the wash buffer containing 400 mM NaCl. After PE was loaded, the column was washed with at least 50 ml of the wash buffer until the UV baseline was stable, and then bound proteins were eluted with a 200 ml NaCl gradient (0.4 M – 1.0 M). Purest fractions were selected for size

exclusion chromatography on a Superdex 200 16/60 Prep Grade column, with PE-storage buffer (HEPES 10 mM pH 7.0, NaCl 500 mM, glycerol 5% (v/v)) as the eluent. Pure PE was concentrated, filtered, quantified using UV absorption at 280 nm, distributed into aliquots, and snap frozen for storage at -80 °C.

The protein purity was assessed using SDS-PAGE in hand-cast Tris-glycine-SDS discontinuous gels with 4% acrylamide in a stacking gel (pH 6.8) and 10% acrylamide in a resolving gel (pH 8.8) with 2.7% cross-linker (acrylamide:bis-acrylamide ratio of 37.5:1, Bio-Rad 1610158). The samples were mixed with 4x-concentrated Laemmli sample buffer (Bio-Rad 1610747) and supplemented with 50 mM dithiothreitol (DTT, MilliporeSigma D9779), denatured at 70 °C for 10 min and centrifuged before applying on gel. The protein concentration was quantified using UV absorption spectroscopy by measuring absorbance at 280 nm with a Nanodrop ND-1000 spectrophotometer. Separation of contaminating nucleic acids was followed by monitoring the ratio of absorbance at 260 nm to absorbance at 280 nm; a ratio < 0.60 was used as an indication of protein free from nucleic acids. A typical $A_{260\ nm}/A_{280\ nm}$ value for purified ABE and PE was 0.55. Extinction coefficients of the constructs were estimated using the ProtParam tool (https://web.expasy.org/protparam/).

ABE and PE activity assay

Synthetic 60 bp-long DNA oligonucleotides (Sigma) labeled with fluorescein on the strand undergoing deamination were annealed, in a 1:1 ratio in 10 mM Tris pH 8.0, 50 mM NaCl, 1 mM EDTA, by incubation at 95 °C for 5 min, and subsequent slow cooling to 20 °C. End-modified sgRNA and epegRNA were ordered from IDT Technologies (Coralville, IA, USA) with 2′-O-methyl groups on the first three and last three nucleotides, and the first and last three phosphodiester bonds were replaced with phosphorothioate bonds. The guide RNAs were dissolved in nuclease-free water at 37 °C, 15 min, 500 rpm in a thermomixer, and folded by incubation at approximately 75 °C for 5 min, followed by slow cooling. Prepared nucleic acids were quantified using UV absorption spectroscopy by measuring absorbance at 260 nm. Accordingly, an A_{260nm} value of 1.0

corresponded to a DNA concentration of 50 µg/ml, or a RNA concentration of 40 µg/ml. DNA was stored at -20 °C, RNA at -80 °C.

For the ABE enzymatic assay, ABE ribonucleoprotein was assembled by incubation with 1.5-fold molar excess of sgRNA in a reaction buffer (20 mM Bis-Tris Propane, pH 7.5, 100 mM KCl, 2.5 mM $MgSO_4$, 2 mM DTT, 5% glycerol (v/v)) for 15 min at room temperature. Additional 10% (w/v) sucrose was used when RNPs were assembled above 4 µM. Then, ABE was diluted to 1 µM with the reaction buffer, preheated at 37 °C, and 15 ng of DNA substrate (0.02 µM final) was added. The deamination was conducted for 10 – 60 min for ABE8e. The 20-µl reactions were quenched by addition of 30 µl of water preheated to 95 °C and incubated for 2 min at 95 °C. After cooling, the mixtures were treated with 1 µl of RNase A (20 mg/ml) and 1 µl of proteinase K (20 mg/ml) for 15 min at room temperature; then DNA products were purified using an Oligo Clean & Concentrator kit (Zymo Research, Irvine, CA, USA, D4061). Purified DNA was nicked with 5 units of Endonuclease V (EndoV, NEB) for 2-3 h at 37 °C, after which the reaction was quenched by addition of TriTrack DNA-loading dye (1x final) (Thermo Fisher Scientific, R1161) and incubation at 95 °C for 2 min. The cleavage products were analyzed by denaturing polyacrylamide gel electrophoresis with urea (Urea-PAGE) in Bio-Rad MiniProtean continuous hand-cast 15% acrylamide gels in Tris-borate-EDTA (TBE, Bio-Rad 1610770) with 7 M urea and 5% crosslinker (acrylamide:bis-acrylamide ratio of 19:1, Bio-Rad 1610144). The voltage was controlled to maintain at least 42 °C in the electrophoresis chamber. Imaging was done using the ChemiDoc MP system (Bio-Rad). For fluorescein, it was done immediately after electrophoresis, and for the SYBR Gold (Thermo Fisher S11494) – after 30 min staining with 1x dye in 1xTBE.

For the *in vitro* reverse-transcriptase elongation assay of PE, the activity assay was carried out in the same reaction buffer as for ABE, supplemented with 0.5 mM deoxyribonucleotides (dNTP). PE2 RNP was assembled with 1.1-fold molar excess epegRNA, targeting the rd12 locus in the reaction buffer without added sucrose for 15 min at room temperature. Then, reactions were preheated at 37 °C, and 45 ng of fluorescein-labeled substrate was added to a final volume of 15

µl. After 15 min, the reactions were quenched with 1 µl each of proteinase K (20 mg ml^{-1}) and RNase A (20 mg ml^{-1}), denatured at 95 °C for 2 min, supplemented with 6xTriTrack loading dye, and 15 ng of substrate was analyzed by Urea-PAGE, as for ABE.

Differential scanning fluorimetry

ABE and PE proteins were complexed with 1.5-fold molar excess of guide RNA in phosphate-buffered saline (PBS) at room temperature for 15 min to obtain 10 µM RNP. ABE RNP contained an additional 10% (w/v) sucrose. Subsequently, the RNPs were diluted with PBS to 1 µM, SYPRO Orange probe was added to a final concentration of 5x, the samples were aliquoted (10 µl per well) into a 384-well plate (Applied Biosystems, 4483319), and the plate was sealed with optical foil (Applied Biosystems, 4360954). After an additional 15 min incubation, the plate was centrifuged at 1,000*g* for 1 min at room temperature, and was installed in a pre-equilibrated Bio-Rad CFX384 thermocycler. The fluorescence was measured in Förster resonance energy transfer (FRET) mode every 0.2 °C from 20 °C to 95 °C. The rate of change of fluorescence (-dF/dT) was used to estimate the melting temperature (T_m). All samples were run in triplicate, and plots of averaged data are reported.

Mammalian cell culture

HEK293-loxP-GFP-RFP cells (referred to as “CS cell line” GenTarget Inc., San Diego, CA, USA, SC018-Bsd), NIH/3T3 *rd12* cells,[80] and *rd12* reporter cells were maintained in DMEM/F-12 medium with GlutaMAX supplement (Thermo Fisher, Waltham, MA, USA, 10565018) or in DMEM with glutamine (Thermo Fisher, 11965092), both supplemented with 10% FBS (Genesee Scientific, San Diego, CA, USA, 25-514H) and optional 100 U ml^{-1} penicillin-streptomycin (Thermo Fisher, 15140122) (complete medium) in a humidified incubator at 37 °C, 5% CO_2.

Primary fibroblasts were isolated from the skin of P0-P3 Rosa mT/mG mice. The mice were euthanized, the skin separated and washed with PBS containing 100 U ml^{-1} penicillin-streptomycin and 40 µg ml^{-1} gentamicin (Thermo Fisher 15710072). The skins were digested in a 100 mm cell culture dish by 1:1 mixture of 0.25% trypsin without EDTA (Thermo Fisher, 15050065)

and 5 U ml^{-1} dispase (STEMCELL Technologies, Cambridge, MA, USA, 07913) for 1 h at 37 °C, after which the dermis was collected to a new dish and digested with 0.25% collagenase I (Thermo Fisher, 17018029) in serum-free DMEM/F12 for 1 h at 37 °C. The tissue fragments were thoroughly resuspended, filtered through a 70-µm strainer, and extensively washed with DMEM/F12 with 15% FBS and 100 U ml^{-1} penicillin-streptomycin by two centrifugation steps at 180*g*, 5 min, room temperature. The cells were maintained in DMEM/F12 with 15% FBS and passaged every 3-4 days, using 0.05% trypsin-EDTA (Thermo Fisher Scientific, 25300054). After the first passage, the cells were filtered through a 40-µm strainer to remove undigested aggregates that permeated through the 70-µm strainer. Both freshly isolated and cryopreserved cells that were passaged at least twice were used for the experiments. For Cre delivery, medium with 10% FBS was used, and the procedure was the same as for the CS cell line. For protein delivery experiments, the cells were seeded 24 h prior to the experiment in 24-, 48- and 96-well plates to reach 50-70% confluency (approximately 100,000, 50,000 and 25,000 cells per well, respectively, for CS cell line and NIH/3T3 rd12 cells, and 50,000, 24,000 and 10,000 cells per well, respectively, for *rd12* reporter cells and primary fibroblasts).

Delivery of Cre recombinase

The CS cells and primary Rosa mT/mG fibroblasts were plated on 48-well treated tissue-culture plates in complete medium with 10% FBS. Cre recombinase, fused separately with each of the cell-penetrating peptides (CPPs: CPP5 (KLPVM)[286], TAT (RKKRRQRRR)[332], or ANTP (RQIKIWFQNRRMKWKK))[333] was prepared at various final concentrations (0.10, 0.25, 0.50, 0.75 or 1.00 µM, 4.2, 10.5, 21.0, 31.4 or 41.9 µg ml^{-1}, respectively) in 250 µl each of OptiMEM medium (Thermo Fisher, 31985070). Only the 0.5 µM Cre proteins were tested in the primary fibroblasts. For non-covalent complexation with 6xHis-CM18-PTD4 peptide (Genscript),[288] an aliquot of the non-covalent peptide was added to Cre recombinase (free or fused with one of the CPPs) and incubated for 15 min at room temperature. The reporter cells were washed with 180 µl of OptiMEM medium, which was then exchanged with OptiMEM plus one of the various preparations of Cre

recombinase. After 3 h, the medium was exchanged with complete medium. The CS cells and Rosa mT/mG fibroblast cells were maintained post treatment for a total of 24 h and 72 h, respectively. For imaging, the medium was exchanged to FluoroBrite DMEM (Thermo Fisher, A1896701), and the cells were imaged using a Keyence BZ-X810 microscope with GFP and Texas Red optical filters.

Flow cytometry

Cells were washed with PBS (Thermo Fisher, 10010023), detached with 0.05% trypsin (Thermo Fisher Scientific, 25300054), transferred to a 96-well round bottom plate, and centrifuged at 180*g* for 5 min at room temperature. Centrifuged cells were washed with a FACS buffer (PBS with 2% FBS, 100 U ml^{-1} penicillin-streptomycin), centrifuged again and resuspended in the FACS buffer with 1 µg ml^{-1} 4′,6-diamidino-2-phenylindole (DAPI, Thermo Fisher, 62248). The cells were analyzed using a Novocyte Quanteon (Agilent) flow cytometer with Pacific Blue (445/45 nm), FITC (530/30 nm), and PE (586/20 nm) optical filters. Cells were gated on forward and side scatter, viability *via* DAPI exclusion, and single cells (**Supplementary Figure 6.9**).

Subretinal injections

Cre proteins with or without fused cell-penetrating peptides were diluted in OptiMEM to 10 µM. 6xHis-CM18-PTD4 peptide was optionally added to Cre in ten-fold excess and incubated for at least 15 min before injection. A lipoplex of Cre with Lipofectamine 3000 was injected at 10 µM, with 2% Lipofectamine 3000 by volume (419 ng Cre per eye, 0.02 µl Lipofectamine 3000 per eye). AAV2/1-Cre (Addgene, 105537-AAV1, $1.8 \cdot 10^{10}$ vg) or vesicular stomatitis virus G glycoprotein (VSV-G) pseudotyped eVLP-Cre (concentrated by ultracentrifugation 1,000-fold as described [209]) were injected as a positive control for mT/mG mice. Mice were anesthetized by intraperitoneal injection of a cocktail consisting of 20 mg ml^{-1} ketamine and 1.60 mg ml^{-1} xylazine in PBS at a dose of 100 mg kg^{-1} of ketamine and 8 mg kg^{-1} of xylazine, and their pupils were dilated by topical administration of 1% tropicamide ophthalmic solution (Akorn, 17478-102-12) and 10% phenylephrine ophthalmic solution (MWI Animal Health, 054243). The corneas were hydrated with

GenTeal Severe Lubricant Eye Gel (0.3% Hypromellose, Alcon). Subretinal injections were performed using an ophthalmic surgical microscope (Zeiss). An incision was made through the cornea adjacent to the limbus at the nasal side, using a 27-gauge needle. A 34-gauge blunt-end needle (World Precision Instruments, NF34BL-2), connected to an RPE-KIT (World Precision Instruments RPE-KIT) with SilFlex tubing (World Precision Instruments; SILFLEX-2), was inserted through the corneal incision while avoiding the lens and advanced into the subretinal space. Each mouse received a 1 µl injection per eye, and volume and rate were controlled with a UMP3 UltraMicroPump (World Precision Instruments, UMP3-4). After surgery, the mice were placed on a heating pad and anesthesia was reversed with intraperitoneal atipamezole (2.5 mg kg^{-1}, MWI Animal Health #032800). Triple antibiotic ophthalmic ointment (neomycin, polymyxin, and bacitracin) was administered to the cornea to promote recovery.

Two-photon imaging of mouse eyes

After sacrifice, intact enucleated mouse eyes were submerged in room temperature PBS. Pulsing IR light from a Ti:sapphire laser (Coherent, Vision S, Santa Clara, CA; tunable between 690 and 1050 nm) was set to 950 nm and attenuated in a controlled, variable manner with an electro-optic modulator (EOM). To image and spectrally separate GFP and tdTomato, two internal spectral detectors were used with their detection bandwidths set to 490 – 545 nm for GFP, and 590 - 680 nm for tdTomato. A 1.0 NA 20x Leica objective was used for the imaging.[257,334]

Generation of the *rd12* reporter cell line

The *rd12* reporter construct was synthesized by GenScript according to the following strategy: 198 bp of the mouse *Rpe65* cDNA was flanked by 5'-mCherry and 3'-eGFP, and the whole construct was inserted into the pcDNA3.1/(Zeo)+ backbone with BamHI and XhoI restriction sites (mCherry-*rd12*-eGFP). The mCherry-*rd12*-eGFP construct was then subcloned into pMXs-IRES-Blasticidin *via* double digestion of the backbone with BamHI and XhoI. The downstream sequence of the internal ribosomal entry site (IRES) and blasticidin-resistance gene enabled co-expression of the reporter and selectable marker. The *rd12* reporter cell line was

generated by transduction of NIH/3T3 cells with retrovirus obtained from Phoenix-Eco cells, transfected with pMXs-mCherry-*rd12*-eGFP-IRES-Blasticidin [335,336] according to a previously published protocol.[337] Transduced cells were then selected with blasticidin for 10 days (5 μg ml^{-1} Thermo Scientific # R25001). The surviving cells were sorted using flow cytometry to select high-expressing mCherry-positive clones and then seeded into 96-well plates for clonal selection. Single colonies were screened for proper expression and editability *via* Gene Juice (Millipore Sigma #70967-3) co-transfection of pCMV-NG-SpCas9-ABE7.10max and pSPgRNA-*rd12*-A6, and *via* proper co-expression of mCherry and eGFP. Finally, the clones were sequenced. No additional characterization was performed on the sorted cells.

Delivery of ABE and PE *in vitro*

ABE RNP was assembled by incubation of up to 20 μM ABE for at least 15 min at room temperature with 1.1-fold excess of sgRNA in OptiMEM medium supplemented with 10% (w/v) sucrose. The sgRNA used for experiments in cell lines and *in vivo* contained additional modifications as described, and was supplied by IDT.[311] 6xHis-CM18-PTD4 peptide was dissolved in 100 mM HEPES, pH 8.0 to achieve a peptide concentration of 10 mM; the final pH of this stock solution was approximately 7.0. 6xHis-CM18-PTD4 peptide was diluted to 400 μM with water, added to ABE RNP, and incubated for an additional 15 min. CPP fusions of ABE with or without 6xHis-CM18-PTD4 peptide were diluted to their final concentrations in OptiMEM, containing 2% sucrose or 10% sucrose; and 100 μl of each of the mixtures was applied on the cells in a 48-well plate that had been washed with OptiMEM medium. After 3 h, the medium was exchanged with 250 μl of complete medium.

To assemble Lipofectamine 3000 lipoplexes, 0.5 μl of Lipofectamine 3000 per well of a 48-well plate or 0.2 μl per well of a 96-well plate was diluted with OptiMEM containing 10% (w/v) sucrose to 12.5 and 5 μl per well, respectively; the ABE RNPs diluted with OptiMEM with 10% (w/v) sucrose to 12.5 μl (48-well) or 5 μl (96-well) were then added to the diluted lipids and incubated for 15 min at room temperature. A lipoplex of ABE with Lipofectamine 3000 in a volume of 25 μl

was added to the cells with 225 µl fresh complete medium in a 48-well plate, or 10 µl was added to the cells with 90 µl medium in a 96-well plate. The cells were incubated for 48 h before analysis. Plasmid DNA transfections were done in 48-well plates using 160 ng pCMV-NG-SpCas9-ABE, 80 ng pSPgRNA-*rd12*-A6, and 0.75 µl Lipofectamine 3000 per well, following the manufacturer's protocol. PE was delivered *in vitro,* similarly as ABE, but without sucrose, unless otherwise noted. Activities of ABE and PE in the *rd12* reporter cell line were analyzed by fluorescence microscopy and flow cytometry, as described above for Cre delivery.

Rescue of RPE65 expression was analyzed using NIH/3T3 cells stably expressing *Rpe65 rd12* cDNA, as previously described.[80] The ABE and PE were applied on these cells, and after 48 h, the cells were detached using trypsin and washed three times with PBS. One-tenth of the cell suspension was lysed with 10 mM Tris pH 7.5, 0.05% SDS with 0.02 mg ml^{-1} proteinase K for 1 h at 37 °C, then the proteinase K was inactivated at 85 °C for 45 min. The lysate was used as a template for PCR, and the products were subjected to next-generation sequencing. The remaining cells were lysed in 1x RIPA buffer (Cell Signaling Technology, 9806) with 1x cOmplete Ultra EDTA-free protease inhibitors (Roche) for 1 h on a rotator in a cold room, and then centrifuged at 17,000 – 21,400*g* for 20 min at 4 °C, and the supernatant was used for analysis. Protein concentration in the extracts was measured using the BCA assay (Thermo Fisher Scientific, 23252), and the extracts were subjected to Western blotting.

Next-generation sequencing

Complementary DNA (cDNA) was synthesized from RNA with the High Capacity RNA-to-cDNA kit (Thermo Fisher 4387406), according to manufacturer's instructions. 0.5 – 1 µl of the isolated genomic DNA or cDNA was used as input for the first of two PCR reactions (PCR1). Genomic loci were amplified in PCR1, using Phusion Plus polymerase (Thermo Fisher Scientific F631S). PCR1 was performed as follows: 98 °C for 30 sec; 30 cycles at 98 °C for 10 sec, 60 °C for 20 sec, and 72 °C for 30 sec; 72 °C for 5 min. PCR1 products were confirmed on a 2% agarose gel. One microliter of PCR1 was used as input for PCR2 to install Illumina barcodes. PCR2 was

conducted for nine cycles of amplification using a Phusion HS II kit (Life Technologies). Following PCR2, samples were pooled, and gel-purified in a 1% agarose gel using a Qiaquick Gel Extraction Kit (Qiagen). Library concentration was quantified using the Qubit High-Sensitivity Assay Kit (Thermo Fisher Scientific). Samples were sequenced on an Illumina MiSeq instrument (paired-end read, read 1: 200–280 cycles, read 2: 0 cycles) using an Illumina MiSeq 300 v2 Kit (Illumina).

High-throughput sequencing data analysis

Sequencing reads were demultiplexed using the MiSeq Reporter software (Illumina) and were analyzed using CRISPResso2 as previously described.[226,275] Batch analysis mode (one batch for each unique amplicon and sgRNA combination analyzed) was used in all cases. Reads were filtered according to minimum average quality score (Q > 30) prior to analysis. The following quantification window parameters were used: -w 20 -wc -10. Base editing efficiencies are reported as the percentage of sequencing reads containing a given base conversion at a specific position. Prism 10 (GraphPad) was used to generate dot plots and bar plots.

Western blotting

Protein was analyzed *via* Western blotting and detected using mouse anti-RPE65 antibody (produced in house)[255] or mouse anti-SpCas9 (clone 7A9, Biolegend #844302), diluted 1:1,000 in 5% non-fat dry milk in PBS (Bio-Rad, 1610780) with 0.1% Tween 20 (MilliporeSigma, P9416) (PBST). The lysates (7-10 µg total protein) were separated by SDS-PAGE, transferred to a polyvinylidene fluoride (PVDF) membrane (MilliporeSigma, IPVH00010), blocked for 1 h with 5% non-fat dry milk in PBST at room temperature, and incubated with the primary antibodies overnight in the cold room. After washing 4 times with PBST for 5 min each, the blots were incubated for 1 h at room temperature with a horseradish peroxidase (HRP)-linked horse anti-mouse antibody (Vector Laboratories, Newark, CA, USA, PI-2000-1), diluted 1:2,500 in 5% non-fat dry milk in PBST. The signals were detected with SuperSignal West Pico Plus Chemiluminescent substrate (Thermo Fisher 34577). Next, the antibodies were stripped from the membrane with 0.2 M glycine pH 2.2, 0.1% SDS, 1% Tween 20; then, the membranes were washed, blocked, and re-probed

for 1 h at room temperature using rabbit anti-β-actin polyclonal antibody (1:2,000; Cell Signaling Technology; 4970S). Goat anti-rabbit IgG with HRP (1:2,500; Cell Signaling Technology; 7074S) was used as the secondary antibody before developing the blots, as described above.

Delivery of ABE *in vivo*

ABE was diluted into OptiMEM containing additional sucrose (10 or 25% (w/v) final, as indicated); or into the ABE storage buffer containing high salt concentration (390 mM NaCl final) without added sucrose. To form RNPs, ABE was added to guide RNA dissolved in water and incubated for 15 min at room temperature. For combination with five-fold molar excess of 6xHis-CM18-PTD4 peptide, ABE RNPs were added to a peptide stock solution diluted to 1 mM. In the case of Lipofectamine 3000, ABE RNPs were added to the undiluted reagent. RNPs were incubated with the reagents for at least 15 min at room temperature before subretinal injection into *rd12* mice as described.

RPE dissociation, genomic DNA and RNA, and lysate preparation

Mouse eyes were dissected under a light microscope to separate the posterior eyecup (containing RPE, choroid, and sclera) from the retina and anterior segment. Each posterior eyecup was immediately immersed in RLT Plus (Qiagen). RPE, choroid, and scleral cells were detached from the posterior eyecup by gentle pipetting, followed by removal of the remaining posterior eyecup. Cells were then processed for genomic DNA and RNA using the AllPrep DNA/RNA Micro kit according to manufacturer instructions (Qiagen 80284). To prepare the protein lysate from the mouse RPE tissue, the dissected mouse posterior eyecup was transferred to a microcentrifuge tube containing 40 µl of ice-cold RIPA buffer with protease inhibitors, and homogenized with a motorized tissue grinder (Fisher Scientific K749540-0000), incubated on ice for 20 min, and then centrifuged for 20 min at 21,000*g* at 4 °C. The resulting supernatant was pre-cleared with Dynabeads Protein G (Thermo Fisher 10003D) by rotation at 4 °C for 15 min to remove immunoglobulin contaminants from blood prior to loading on the gel.

Immunohistochemistry of RPE flatmounts and cryosections

Mouse eyes were enucleated and fixed with 4% paraformaldehyde in PBS for 20 min at room temperature and washed three times in PBS for 5 min each. To make RPE flatmounts, the anterior segment and retina were removed from the posterior eyecup under a dissecting microscope, and four radial cuts were made toward the optic nerve to flatten the eyecup into an RPE flatmount. Samples were permeabilized and blocked in 0.1% Triton X-100 (Sigma-Aldrich, T8532) with 3% normal goat serum (NGS) in PBS for 30 min and incubated with the following primary antibodies in PBS, 0.1% Triton X-100 and 3% NGS: mouse anti-RPE65 antibody (1:100; in-house) and rabbit anti-ZO-1 polyclonal antibody (1:100; Invitrogen, 61-7300) overnight at 4 °C. The next day, samples were washed three times in PBS for 5 min each and then incubated with the appropriate secondary antibodies in PBS, 0.1% Triton X-100 and 3% NGS, including Alexa Fluor 555-conjugated goat anti-mouse IgG (1:200; Thermo Fisher; A11032) and Alexa Fluor 647-conjugated goat anti-rabbit IgG (1:200; Thermo Fisher) for 2 h at room temperature in the dark. The secondary antibodies were then removed, and the flatmounts were incubated in DAPI (1 μg ml^{-1}, Thermo Fisher, 62248) in PBS for 10 min. Samples were washed three times in PBS for 5 min each. The samples were then mounted with VECTASHIELD HardSet Antifade Mounting Medium (Vector Labs H-1400-10) and imaged on a Keyence BZ-X810 All-in-One fluorescence microscope.

Electroretinography (ERG)

Prior to ERG recording, mice were dark adapted for 1 week. Under a safety light, mice were anesthetized by isoflurane inhalation, and their pupils were dilated with topical administration of 1% tropicamide ophthalmic solution (Akorn; 17478-102-12) and 10% phenylephrine ophthalmic solution (MWI Animal Health #054243), followed by hypromellose (Akorn; 9050-1) for hydration. The mouse was placed on a heated Diagnosys Celeris rodent-ERG device (Diagnosys LCC, Lowell, MA, USA). Ocular stimulator electrodes were placed on the corneas, the reference electrode was positioned subdermally between the ears, and a ground electrode was placed in the rear leg. The eyes were stimulated with a green-light stimulus (peak emission 544 nm,

bandwidth ~160 nm) of -0.3 log (cd s m^{-2}). The responses for 10 stimuli with an inter-stimulus interval of 10 sec were averaged, and the a- and b-wave amplitudes were acquired from the averaged ERG waveform. Data were analyzed with Espion V6 software (Diagnosys LLC). For the RNP LNP optimization study, eyes that received LNP and had no ERG response after treatment were excluded from the analyses.

Pupillary light reflex

The pupillary light reflex (PLR) was characterized in mice (n = 5 for each group) using the A2000 computerized pupillometer (Neuroptics, San Clemente, CA, USA). Mice were dark-adapted for 6 h prior to recordings in a dark room. This pupilometer system consists of a sensing device equipped with two infrared cameras that independently record and track dynamics of each pupil. The light profile consisted of four white-light stimuli (1.2 log, $10^{1.2}$ W m^{-2}), each for 500 msec. For the duration of the PLR testing routine, mice were kept under isoflurane anesthesia. The experiments were carried out under scotopic conditions, with no background illumination from the pupillometer, with the infrared cameras as the primary light source. The maximum size of the pupil after dark adaptation was quantified at 2 min after anesthesia and was used to establish baseline size. The pupil response was expressed as percent constriction of the pupil when compared to baseline. Captured digital movies of pupil responses were recorded using the Active Presenter software (v. 9.1.3; Atomi Systems, Inc, Hanoi, Vietnam), and the videos were subsequently decomposed into individual frames using Adobe Premiere Rush program (v. 10.0.1; Adobe Systems, Inc., San Jose, CA, USA) for manual verification of pupil dynamics and calculation of absolute pupil diameters from the recorded images.

Retinoid analysis

Mice were dark adapted for 2 days before eye enucleation. Eyes were homogenized in 1 ml of a 10 mM sodium phosphate buffer (pH 8.0) containing 50% methanol (v/v) (Sigma–Aldrich; 34860-1L-R) and 100 mM hydroxylamine, pH 8.0 (Sigma–Aldrich; 159417-100G). After 15 min incubation at room temperature, 2 ml of 3 M NaCl was added. The resulting sample was extracted

twice with 3 ml ethyl acetate (Fisher Scientific; E195-4). Then, the combined organic phase was dried *in vacuo* and reconstituted in 250 µl hexane. Extracted retinoids (100 µl) were separated on a normal-phase HPLC column (Zorbax Sil; 5 µm; 4.6 mm × 250 mm; Agilent Technologies) connected to an Agilent Infinity 1260 HPLC system equipped with a diode-array detector. Separation was achieved with a mobile phase of 0.6% ethyl acetate in hexane (Fisher Scientific; H302-4) at a flow rate of 1.4 ml min^{-1} for 17 min, followed by a step increase to 10% ethyl acetate in hexane for an additional 25 min. Retinoids were detected by monitoring absorbance at 325 nm and 360 nm using Agilent ChemStation software.

Encapsulation of ABE and PE LNPs

RNPs were assembled by mixing 10 µM purified ABE or PE with synthetic sgRNA (ABE) or epegRNA (PE) at a 1:1.1 molar ratio. The buffer for ABE was HEPES 10 mM, pH 7.0, NaCl 500 mM, glycerol 20% (v/v); for PE, the buffer was HEPES 10 mM, pH 7.0, NaCl 500 mM, glycerol 5% (v/v); and guide RNA was dissolved in water. Proteins were diluted, supplemented with 10% (w/v) sucrose from 50% (w/v) stock in water, and added to guide RNA. Final composition of the buffer in which RNPs were assembled was HEPES 2.8 mM, pH 7.0, NaCl 140 mM, sucrose 10% (w/v), glycerol 5.6% (v/v) (ABE); or glycerol 1.4% (v/v) (PE). The RNPs were incubated at room temperature for at least 15 min. Transient turbidity, which cleared during incubation, was observed. Immediately before encapsulation, RNPs were diluted to 0.711 µM in a 50 mM Tris-acetate buffer, pH 6.0, with 10% (w/v) sucrose, to achieve a final concentration of NaCl of 10 mM. The lipids used to encapsulate pre-formed RNPs were comprised of an ionizable cationic lipid (either CL4H6 (Cayman Chemical, Ann Arbor, MI, USA, 37279), SM102 (Broadpharm, San Diego, CA, USA, BP-25499), or DODMA (Avanti Polar Lipids, Alabaster, AL, USA, 890899), all of which have pK_as > 6.0 at 6.25, 6.68 and 6.59 respectively), and co-lipids DSPC (Avanti Polar Lipids, 850365), cholesterol (Avanti Polar Lipids, 700100), and DMG-PEG 2000 (Avanti Polar Lipids, 880151) (**Supplementary Figure 6.5**) at a molar composition of 50/10/38.5/1.5, respectively, to encapsulate pre-formed RNPs. For optimization of DMG-PEG 2000 lipid content from 1.5 to 10

mole%, the concentration of cholesterol was decreased accordingly. In some formulations, 2.5 mole% of SOPS (18:0-18:1 PS, Avanti Polar Lipids 840039C) was used with 7.5 mole% of DSPC. In brief, the lipids were dissolved in ethanol and rapidly combined with preformed RNP at a volume ratio of 1:3 (ethanol:aqueous) and a total lipid:guide RNA weight ratio of 40:1 (approximate total lipid:protein weight ratio of 7.75:1). The combination was performed by microfluidic mixing using a Precision NanoSystems Ignite device (Precision NanoSystems, Vancouver, BC, Canada). Immediately after mixing, the formed LNPs were dialyzed two times for 2 h each at room temperature, against 20 mM Tris, 4.3 mM Na acetate, pH 7.4, 10% (w/v) sucrose (TAS buffer), to remove the ethanol and deprotonate the ionizable cationic lipid at neutral pH. Final concentration of protein was approximately 0.53 μM (0.10 mg ml^{-1} ABE8e, 0.13 mg ml^{-1} PE), and of guide RNA – 0.59 μM (0.02 mg ml^{-1} sgRNA, 0.03 mg ml^{-1} epegRNA). The LNPs were transferred to ice and concentrated to no less than one fifth initial volume, using an Amicon Ultra centrifugal filter with molecular weight cutoff of 30 kDa (Merck, UFC903024); the concentrated LNPs were distributed into aliquots, quickly frozen on a pre-cooled metal block, and stored at -80 °C. The percent recovery and concentration factor of the LNPs were estimated using SDS-PAGE electrophoresis and CBB staining. Fluorescence intensity of Coomassie dye bound to protein was measured using ChemiDoc MP imager, and analyzed using ImageLab software version 6.1.0 (Bio-Rad). Doses of RNP LNP are reported *in vitro* as a final concentration of RNP and *in vivo* as RNP concentration and injected volume.

Particle-size distribution analysis

Particle-size distribution was measured using a Malvern Zetasizer Advance Nano (Malvern Panalytical, Malvern, UK). Twenty microliters of freshly dialyzed LNP were diluted to 200 μl with TAS buffer and subjected to particle-size distribution measurement in triplicates. The particle size distributions were processed by the accompanying software to calculate average particle diameter and polydispersity index (PdI).

Cryoelectron-microscopic imaging of LNPs

LNP samples were concentrated 3-4 times in an Amicon Ultra 0.5 device with a 10 kDa molecular weight cutoff. LNP solution (2.5 µl) was applied onto a Quantifoil 200 mesh grid coated with a thin carbon film (Ted Pella). Grids were blotted for 2 sec with filter paper, then plunged into liquid ethane using a manual plunger. The image was collected on a FEI Tecnai TF20 high resolution Transmission Electron Microscope equipped with a K2 Direct-Detection Camera at an accelerating voltage of 200 kV.

ABE encapsulation immunoassay

LNPs were diluted 1:3 in an immunoprecipitation buffer (HEPES 10 mM, pH 7.0, NaCl 150 mM, sucrose 10% (w/v)), and 80 µl of diluted LNPs were incubated with 20 µl of 1D4 resin for 30 min in a cold room in an overhead mixer. As a control, pre-formed free RNP was diluted in the TAS buffer to the approximate concentration of RNP in a prepared LNP, and also incubated with 20 µl of 1D4 resin. Samples were then centrifuged at 700*g* for 5 min at 4 °C. The supernatant was filtered with centrifugation at 200*g* for 2 min through a 30-µm polyethylene filter. Pelleted resin was resuspended in 500 µl of the immunoprecipitation buffer and washed by centrifugation at 700*g* for 5 min. The supernatant was discarded, and the washing process was repeated four separate times to ensure thorough washing. To elute the RNP, 80 µl of the elution buffer (1 mg ml^{-1} of 1D4 peptide in the immunoprecipitation buffer) was introduced to the resin, and the samples were incubated overnight in a cold room in an overhead mixer. After incubation, the samples were centrifuged and filtered as described above. Filtered samples were then analyzed by Western blot, as described.

Size exclusion chromatography of ABE LNP

The LNPs containing ABE8e RNP or free ABE8e RNP (112 µg RNP in both) were diluted into 500 µl of 1x PBS (Corning, 46-013-CM) with 0.001% Pluronic F-68 (Gibco, 24040032), filtered on a pre-washed 0.22-µm cellulose acetate centrifugal filter (Corning, 8160) and resolved on a HiPrep 16/60 Sephacryl S-500 HR column (Cytiva, 28935606) at a flow rate of 0.4 ml min^{-1}. One

milliliter fractions were collected and analyzed by Western blot with anti-Cas9 antibodies as described.

Quantification of ABE and PE by mass spectrometry

Deionized water in all experiments was generated using a Milli-Q water-purification system (Millipore Corporation, Bedford, USA). Formic acid (FA), ammonium bicarbonate (NH_4HCO_3) and acetonitrile (ACN) of MS grade were purchased from Fisher chemical (Fair Lawn, NJ, USA). Iodoacetic acid (IAA) and DTT were of analytical grade and supplied by Millipore Corporation (Bedford, USA). Sequencing-grade modified trypsin was provided by Promega (Madison, WI, USA). Stable-isotope-labeled peptides (SIL peptides) were synthesized with alkylated cysteines by GenScript (Piscataway, NJ, USA). The stock solutions of all the peptides were prepared by accurately weighing the synthetic peptides and then dissolving them in water or dimethyl sulfoxide (DMSO) following the manufacturer's instructions. The SIL peptides were diluted in water before adding to the samples.

The samples were diluted with 50 mM ammonium bicarbonate and reduced with 10 mM DTT for 1 h at 56 °C, and alkylated with 20 mM iodoacetic acid for 30 min at room temperature in the dark. Then, the stable-isotope-labeled peptides (SIL peptides) were spiked into protein samples, and then free trypsin was added at a trypsin to protein ratio of 1:50 and incubated overnight at 37 °C. Trypsin activity was inhibited by acidification with 0.1% FA, and the samples were then desalted using a C18 desalting column (Nest). After drying completely by speed vacuum, peptides were dissolved in 0.1% formic acid. The samples were analyzed using LC-MS/MS using a Vanquish LC instrument (Thermo Fisher Scientific), coupled in-line with a Q Exactive mass spectrometer (Thermo Fisher Scientific), with an ESI source. Mobile phase A was composed of 0.1% FA in water, and mobile phase B was comprised of 0.1% FA in acetonitrile. The total flow rate was 0.4 ml min^{-1}. Peptides were separated with a 25-min gradient on an Acquity UPLC® BEH C18 column (1.7 μm, 2.1 mm × 100 mm, Waters Corporation). The acquisition method combined a full scan method with a time-scheduled sequential parallel-analysis monitoring (PRM) method. For PRM,

MS2 scan parameters were set to select the m/z ratio of the natural peptides of Cas9, TadA deaminase, and reverse transcriptase, and their corresponding SIL peptides, with defined elution time windows. MS1 scans were acquired at the m/z range of 300–1000, mass resolution of 70,000, automatic gain control (AGC) target of 1e6, and maximum ion injection time of 50 msec. The PRM scans were acquired at a resolution of 17,500, AGC target value of 1e5, maximum ion injection time of 50 msec, isolation window of 2.0 m/z.

Local field potential and single unit recordings, visual stimulation, and data analysis

Mice were initially anesthetized with 2% isoflurane in a mixture of N_2O/O_2 (70%/30%) and then placed into a stereotaxic apparatus. A small, custom-made plastic chamber was glued (Vetbond, St. Paul, MN, US) to the exposed skull. After one day of recovery, re-anesthetized animals were placed in a custom-made hammock, maintained under isoflurane anesthesia (1-2% in O_2), and multiple single tungsten electrodes were inserted into a small craniotomy above the V1 and SC. Once the electrodes were inserted, the chamber was filled with sterile agar and sealed with sterile bone wax. During recording sessions, animals were kept under isoflurane anesthesia (0.5 – 1% in 30% O_2). EEG and EKG scans were monitored throughout the experiments, and body temperature was maintained with a heating pad (Harvard Apparatus, Holliston, MA).

Data were acquired using a 32-channel Scout recording system (Ripple, UT, USA). The local field potential (LFP) from multiple locations was bandpass filtered from 0.1 Hz to 250 Hz and stored with spiking data on a computer with a 1-kHz sampling rate. The LFP signal was cut according to stimulus time stamps and averaged across trials for each recording location to calculate visually evoked potentials (VEP).[80,338-340] The evoked potential across all layers was recorded, and the most robust response was used for comparisons between groups at the same SC or V1 layer.

The spike signal was bandpass filtered from 500 Hz to 7 kHz and stored in a computer hard drive at a 30 kHz sampling frequency. Spikes were sorted online in Trellis software (Ripple, UT, USA) while performing visual stimulation. Visual stimuli were generated in Matlab (Mathworks, USA) using Psychophysics Toolbox [341-343] and displayed on a gamma-corrected LCD monitor (55

inches, 60 Hz; 1920 x 1080 pixels; 52 cd m^{-2} mean luminance). Stimulus onset times were corrected for LCD-monitor delay using a photodiode and microcontroller (in-house design).

Vision was assessed using protocols published in our previous work.[80,339,344,345] Cells were first tested with 100 repetitions of a 500 msec bright flash of light (105 cd m^{-2}) for the presence of the visually evoked responses. When cells showed signs of robust visually driven activity, we used further drifting grating stimuli to assess the properties of the spatiotemporal receptive fields. Briefly, each cell was evaluated for orientation selectivity, optimal stimulus size, optimal spatial frequency, optimal temporal frequency, and contrast sensitivity. Recorded tuning curves were further normalized between 0 and 1 for visual purposes and plotted together for comparison. Data are presented as mean ± SEM. The level of statistical significance was set at $P < 0.05$ for two-tailed Mann-Whitney U-tests. The figures show single recording locations from the SC and V1 recordings as examples. Offline data analysis and statistics were performed in Matlab (Mathworks, USA).

Tuning curves were calculated based on the average spike rate. Optimal visual parameters were chosen as the maximum response value. Orientation tuning was measured in degrees at the half-width at half-height (HWHH; 1.18 x σ) based on fits to Gaussian distributions using equation (1):

$$R_{O_s} = baseline + R_p e^{\frac{-(O_s - O_p)^2}{2\sigma^2}} + R_n e^{\frac{-(O_s - O_p + 180)^2}{2\sigma^2}} \qquad (1),$$

where O_s is the stimulus orientation, R_{Os} is the response to different orientations, O_p is the preferred orientation, R_p and R_n are the responses at the preferred and non-preferred direction, σ is the tuning width, and “baseline” is the offset of the Gaussian distribution. Gaussian fits were estimated without subtracting spontaneous activity.[345]

The optimal spatial and temporal frequency was extracted from the data fitted to Gaussian distributions using equation (2):[345]

$$R_{\frac{SF}{TF}} = baseline + R_{pref} e^{\frac{-\left(\frac{SF}{TF} - \frac{SF}{TF}_{pref}\right)^2}{2\sigma^2}}, \qquad (2)$$

Where $R_{SF/TF}$ is the estimated response, and R_{pref} indicates response at a preferred spatial or temporal frequency. SF/TF indicates spatial or temporal frequency, σ is the standard deviation of the Gaussian, and the baseline is the Gaussian offset.

Statistical analyses

Unless otherwise stated, the data are presented as mean ± s.d., and statistical analyses were performed using GraphPad Prism 10.0. *P < 0.05; **P < 0.01; ***P < 0.001; ****P < 0.0001; ns, P ≥ 0.05.

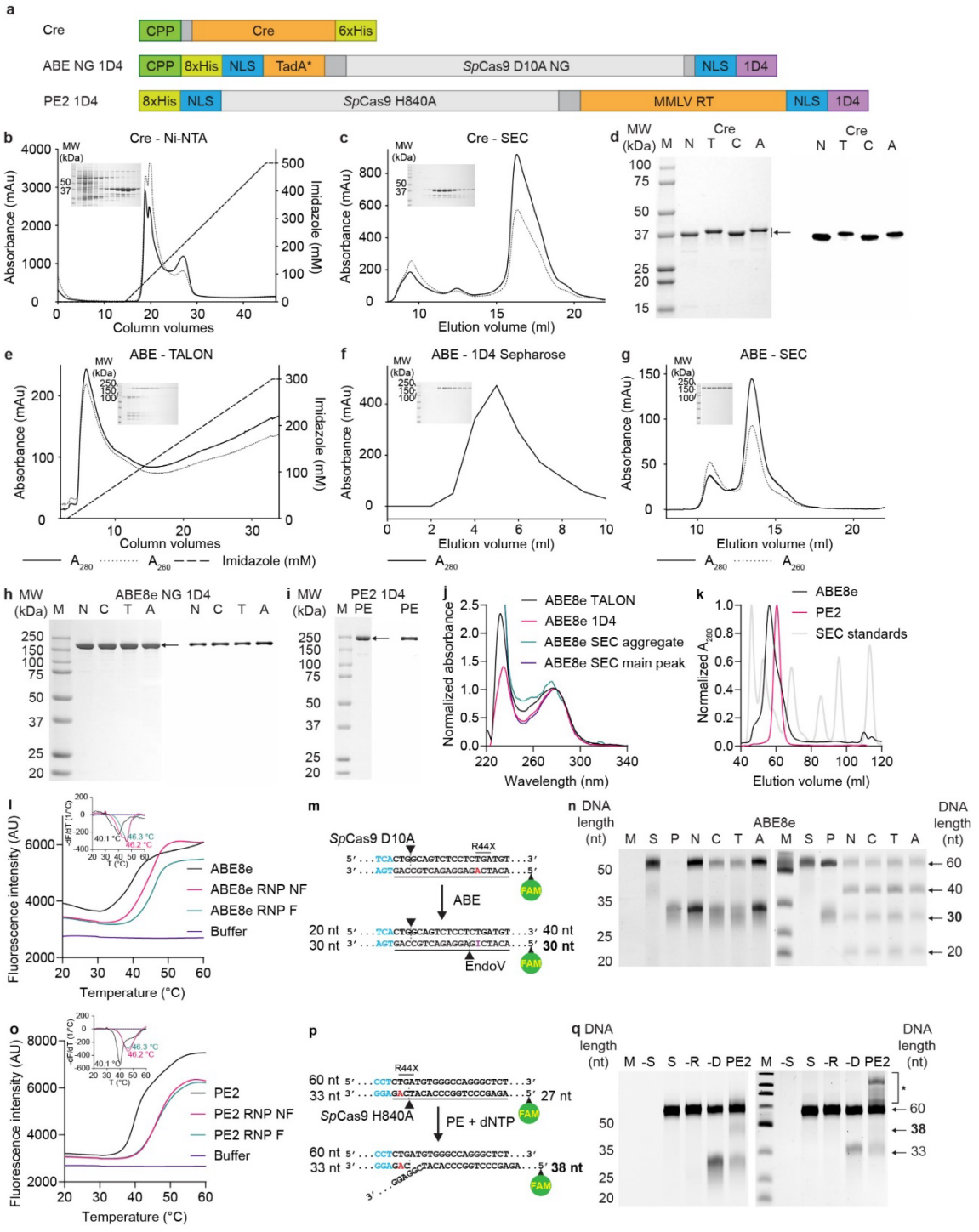


Figure 6.1. Purification and characterization of genome-editing proteins. (**a**) Schematic cartoon of protein constructs utilized in this study. CPP = cell-penetrating peptide; 1D4 = 9 amino acid C-terminal 1D4 rhodopsin peptide; MMLV RT = Moloney murine leukemia virus reverse transcriptase; NLS = nuclear localization signal; TadA* 8e = engineered tRNA deaminase. (**b,c**)

Metal-affinity chromatography (Ni-NTA, **b**), and size-exclusion chromatography (SEC, **c**) purification of Cre recombinase. Insets show SDS-PAGE gels of collected fractions stained with Coomassie Brilliant Blue. (**d**) SDS-PAGE (left) and Western blot analysis (right) of purified Cre recombinase. M = molecular weight marker; N = N-Cre-His; T = TAT-Cre-His; C = CPP5-Cre-His; A = ANTP-Cre-His. (**e-g**) Metal-affinity chromatography (TALON), immunoaffinity chromatography (1D4), and SEC, representing purification of ABE proteins. Insets show SDS-PAGE gels of collected fractions stained with Coomassie Brilliant Blue. (**h,i**) SDS-PAGE (left) and Western blot (right) analyses of purified ABE and PE proteins. (**j**) Absorbance spectra of the fractions collected during purification of ABE, showing gradual removal of contaminating nucleic acids by decreasing absorbance at 260 nm relative to 280 nm. (**k**) SEC of ABE and PE proteins relative to SEC standards consisting of blue dextran (2,000 kDa, determining void column volume), thyroglobulin (670 kDa), γ-globulin (158 kDa), ovalbumin (44 kDa), myoglobin (17 kDa), and vitamin B12 (1.35 kDa, determining accessible column volume). (**l**) Averaged (n = 3) differential scanning fluorimetry (DSF) denaturation profiles of ABE with guide RNA in PBS containing 10% (w/v) sucrose. Inserts show rate of change of fluorescence intensity (-dF/dT) and melting temperatures. NF = non-folded guide RNA; F = folded guide RNA. (**m**) A schematic diagram of the ABE activity assay. (**n**) Denaturing PAGE gels imaged for fluorescein (left) and SYBR Gold (right), demonstrating activity of ABE *in vitro*. M = DNA standard; S = substrate; N = ABE without fused cell penetrating peptide; C = CPP5-ABE; T = TAT-ABE; A = ANTP-ABE. (**o**) Averaged (n = 3) DSF profiles of PE with guide RNA in PBS. Inserts show rate of change of fluorescence intensity (-dF/dT) and melting temperatures. (**p**) A schematic diagram of the PE activity assay. (**q**) Denaturing PAGE gel imaged for fluorescein (left) and SYBR Gold (right), demonstrating activity of PE. “-S” = no substrate control; “S” = substrate-only control; “-R” = no epegRNA control; “-D” = no dNTP control; PE2 = sample containing PE RNP and dNTP. Asterisk indicates products extended beyond the reverse transcriptase template. Data generated by Rafal Holubowicz and Roman Smidak.

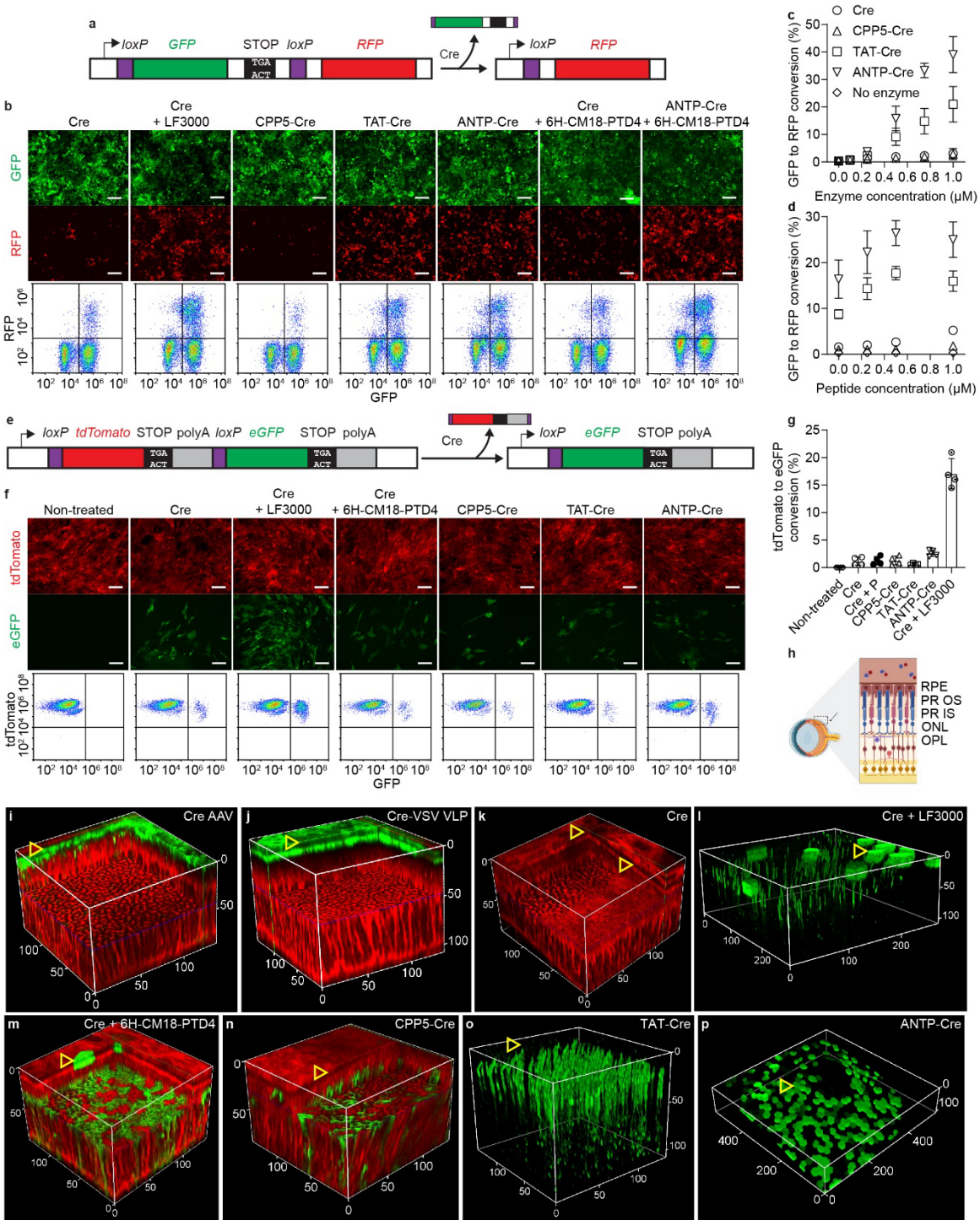


Figure 6.2. Direct protein delivery of Cre recombinase mediated by cell-penetrating peptides. (**a**) Schematic cartoon of color-switch Cre reporter cell line. GFP is constitutively

expressed, while a stop codon prevents expression of RFP. Upon Cre-mediated excision of GFP and the stop codon, RFP expression replaces expression of GFP. (**b**) Various formulations of cell-penetrating CRE mediate excision of the GFP gene and induce expression of RFP measured by microscopy (upper) and flow cytometry (lower). From left to right: purified Cre recombinase delivered alone; with Lipofectamine 3000 (LF3000); with fused CPP5 covalent cell-penetrating peptide; with fused TAT; with fused ANTP; with 6xHis-CM18-PTD4 non-covalent cell-penetrating peptide (6H-CM18-PTD4); with fused ANTP cell-penetrating peptide and 6xHis-CM18-PTD4 peptide. Scale bar represents 200 μm. (**c**) Quantification of Cre-mediated GFP to RFP conversion as a function of direct protein delivery with Cre recombinase alone or with fused cell-penetrating peptides, as measured by flow cytometry. Circle represents Cre alone, triangle represents CPP5-fused Cre recombinase, square represents TAT-fused Cre recombinase, inverted triangle represents ANTP-fused Cre recombinase. Three biological replicates with 2 analytical replicates each, mean ± s.d. 1 μM corresponds to 41.9 μg ml^{-1}. (**d**) Quantification of enhancement of Cre-mediated GFP to RFP conversion with increasing concentrations of 6xHis-CM18-PTD4 peptide at a protein concentration of 0.5 μM. Symbols are consistent with panel c. Three biological replicates with 2 analytical replicates each, mean ± s.d. (**e**) Schematic cartoon of genetic construct of mT/mG Cre reporter-mouse model. In the mice, tdTomato is constitutively expressed, while a stop signal prevents expression of eGFP. Upon Cre-mediated excision of tdTomato and the stop signal, eGFP expression replaces expression of tdTomato. (**f**) Protein delivery to skin fibroblasts isolated from the mT/mG Cre-reporter mice, as observed with a fluorescent microscope and quantified by flow cytometry, 72 h post-delivery. Scale bar represents 100 μm. (**g**) Quantification by flow cytometry of Cre-recombinase delivery into mT/mG Cre reporter-mouse primary fibroblasts. Two separate experiments with 2 analytical replicates each, mean ± s.d. (**h**) Schematic cartoon representing retinal cross-section orientation. RPE = retinal pigment epithelium; PR OS = photoreceptor outer segment; PR IS = photoreceptor inner segment; ONL = outer nuclear layer;

OPL = outer plexiform layer. Generated in Biorender. (**i-p**) Cre-mediated tdTomato to eGFP expression, 1 week after subretinal delivery of Cre recombinase measured by two-photon excitation microscopy. The RPE layer is orientated toward the top, denoted with open yellow triangles. Scale is provided in micrometers. (**i**) AAV2/1-CMV-Cre; (**j**) VSV-G pseudotyped Cre-eVLP; (**k**) Cre recombinase alone; (**l**) Cre recombinase delivered with Lipofectamine 3000; (**m**) Cre recombinase delivered with 6xHis-CM18-PTD4 peptide; (**n**) CPP5-fused Cre recombinase; (**o**) TAT-fused Cre recombinase; (**p**) ANTP-fused Cre recombinase. Data generated by Grazyna Palczewska, Rafal Holubowicz, and Roman Smidak.

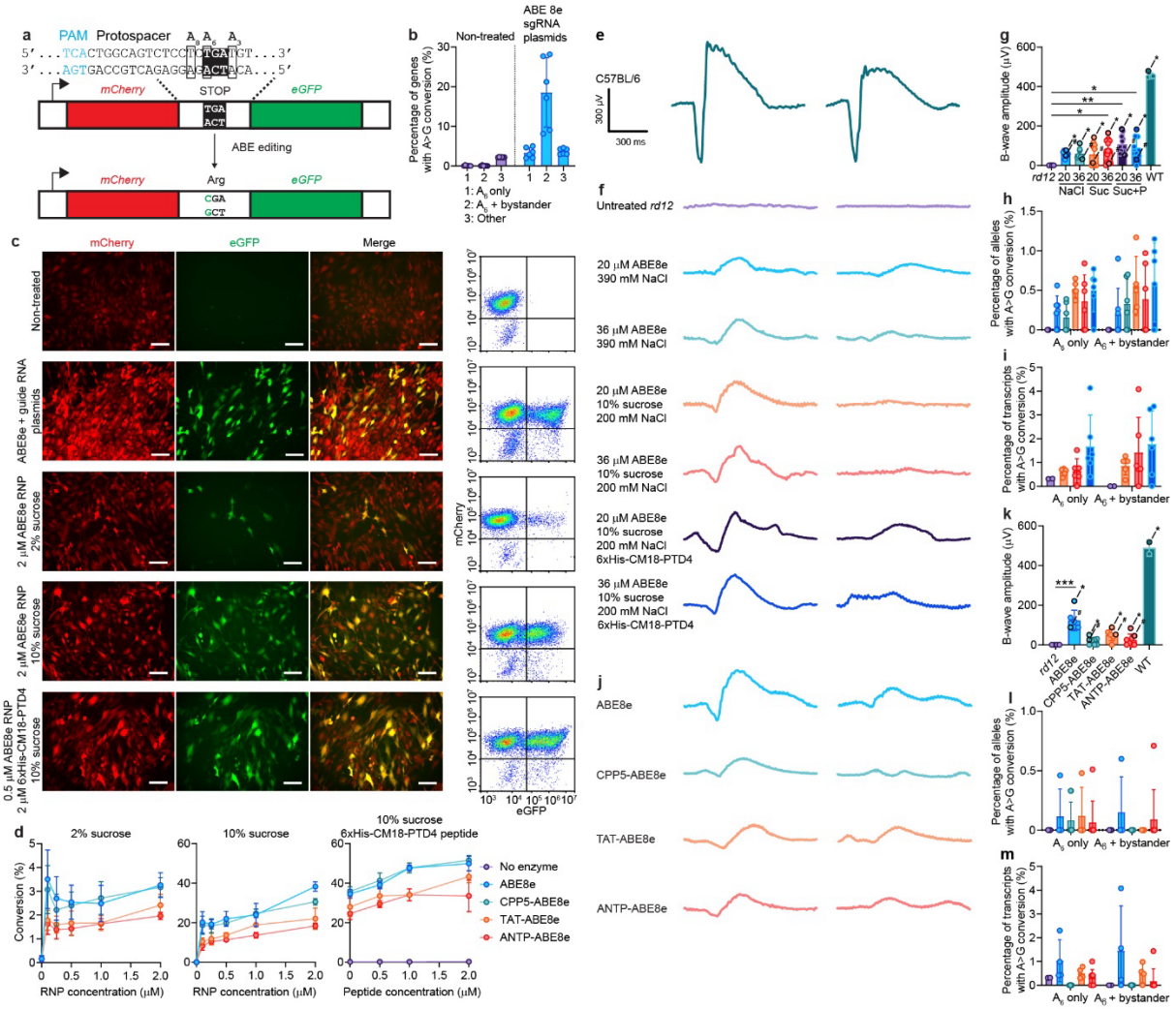


Figure 6.3. Cell-penetrating peptide-mediated delivery of ABE *in vitro* and *in vivo*. (**a**) Schematic cartoon of fluorescent *rd12* reporter. Under the control of the CMV promoter, a gene expresses both mCherry and eGFP, with an intervening sequence from the *Rpe65 rd12* genomic sequence. The *rd12* mutation (c.130C > T; p.R44X) prevents expression of eGFP, but successful base editing restores the reading frame and co-expression of mCherry and eGFP. (**b**) Quantification of successful base editing of *rd12* reporter cells, 48 h after co-transfection of CMV-ABE8e-NG and sgRNA plasmids. Three biological replicates with 2 analytical replicates each, mean ± s.d. (**c**) Assessment by fluorescence microscopy and flow cytometry of ABE delivery to *rd12* reporter cells, 48 h post-treatment; mCherry and eGFP co-expression indicate successful

delivery. Scale bar represents 100 μm. (**d**) Concentration-dependence of efficiency of delivery of ABE in the presence of 2% (w/v) sucrose, 10% (w/v) sucrose; and of 0.5 μM ABE with 10% (w/v) sucrose and 6xHis-CM18-PTD4 peptide. 1 μM corresponds to 224 μg ml^{-1}. Two biological replicates with 2 analytical replicates each, mean ± s.d. **(e)** Electroretinography (ERG) response curves from WT mice. (**f**) ERG response curves from *rd12* mice, two-weeks post-treatment with ABE8e NG RNP in the presence of high and low NaCl and sucrose, with and without 6xHis-CM18-PTD4 peptide. The left curves represent the highest responding eye from each treatment group, indicated with a star on the graph, while the right curves represent a low responding eye from each treatment group, indicated with a hash. (**g**) Quantification of ERG responses (b-wave amplitude) from *rd12* mice whose response curves are shown in panel e. ABE RNP concentrations are given in μM. 20 μM corresponds to 4.5 μg ABE RNP per eye, 36 μM – to 8.1 μg per eye. At least 6 eyes, mean ± s.d., Kruskal-Wallis test with Dunn's multiple comparisons test, $*P < 0.05$; $**P < 0.01$. (**h,i**) Quantification of genomic DNA editing (**h**) and cDNA transcripts containing the edit (**i**) in ABE-treated mice, whose responses are summarized in panel f. The colors are consistent with panel **g**. (**j**) ERG response curves from *rd12* mice, 2 weeks post-treatment with ABE8e RNP with or without fused cell-penetrating peptides. (**k**) Quantification of ERG responses (b-wave amplitude) from *rd12* mice whose response curves are shown in the panel j. The mice received 4.5 μg ABE RNP per eye. At least 6 eyes, mean ± s.d., Kruskal-Wallis test with Dunn's multiple comparisons test, $***P < 0.001$. (**l,m**) Quantification of genomic DNA editing (**l**) and resulting proportion of transcripts containing the edit (**m**) in CPP-ABE treated mice, whose responses are summarized in panel j. The colors are consistent with panel k. Data generated with assistance from Rafal Holubowicz, Elliot H. Choi, and Carolline R. Menezes.

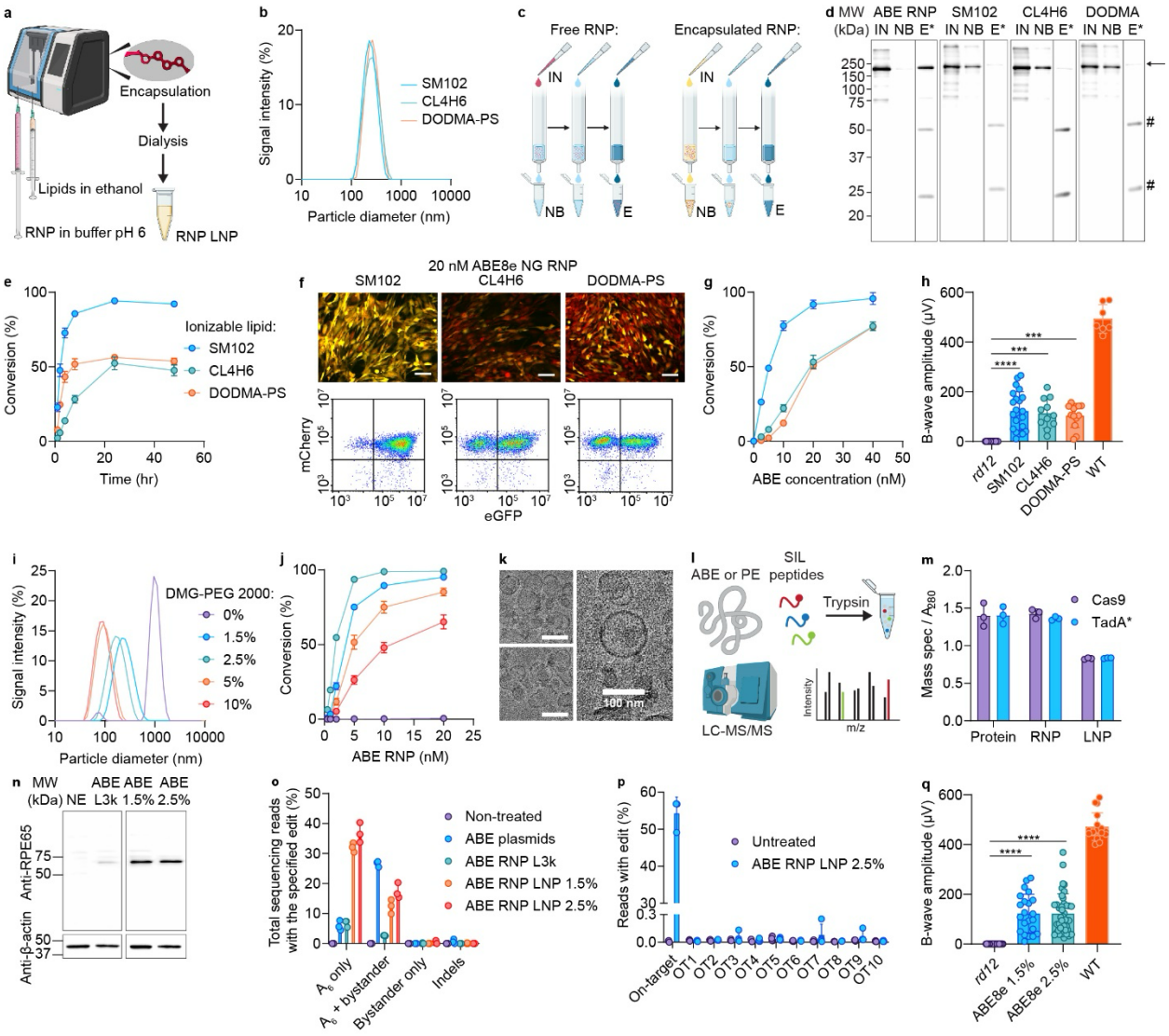


Figure 6.4. Lipid nanoparticle delivery of ABE RNPs. (**a**) Schematic cartoon of encapsulation of RNP into LNP. (**b**) Size-distribution analysis of ABE RNP LNP, with 1.5% DMG-PEG 2000 and ionizable lipids: SM102 (diameter d = 228 nm, polydispersity index PdI = 0.072); CL4H6 (d = 235 nm, PdI = 0.132); DODMA (d = 249 nm, PdI = 0.079). Averaged plots are shown, n = 3 replicates. (**c**) A scheme of the immunoprecipitation of ABE RNP, free (red) or encapsulated into LNP (yellow), on a 1D4 resin. IN = input; NB = non bound; E = eluate. (**d**) Western blot analysis of the immunoprecipitation of ABE RNP, free and encapsulated into LNPs containing 1.5% DMG-PEG 2000 and ionizable lipids SM102, CL4H6, or DODMA. The band corresponding to ABE is

indicated with an arrow. Bound material was eluted using a Laemmli sample buffer with DTT, and bands corresponding to the mouse 1D4 antibody stripped from the resin alongside ABE are indicated with hashes (see also **Fig S8a, b**). (**e**) Delivery of ABE RNP by LNP after incubation of the *rd12* reporter cells with the LNPs for 1 – 48 h, quantified by flow cytometry. The concentration of ABE RNP was 20 nM, 4.5 μg ml^{-1}. Two biological replicates with 2 analytical replicates each, mean ± s.d. (**f**) Fluorescence microscopy and flow cytometry results demonstrating delivery of ABE by LNP to the *rd12* reporter cells, measured 24 h after treatment. Scale bar represents 100 μm. (**g**) Quantification of delivery of ABE RNP as LNP after incubation of the *rd12* reporter cells with 1 – 40 nM ABE RNP for 24 h. Two biological replicates with 2 analytical replicates each, mean ± s.d. (**h**) Summary of ERG b-wave responses of *rd12* mice treated with 1 μl ABE RNP LNP per eye. The concentration of ABE RNP in the LNP was approximately 2.3 μM (SM102, CL4H6, 515 ng per eye) and approximately 1.8 μM (DODMA, 403 ng per eye). At least 10 eyes, mean ± s.d, Kruskal-Wallis test with Dunn's multiple comparisons test, ***$P < 0.001$; ****$P < 0.0001$. (**i**) Size-distribution analysis of ABE RNP LNP with ionizable lipid SM102 and 0 - 10% DMG-PEG 2000. Average of 3 replicates. (**j**) Delivery of ABE RNP LNP with 0 - 10% DMG-PEG 2000, quantified by flow cytometry. The colors are consistent with panel i. Two biological replicates with 2 analytical replicates each, mean ± s.d. (**k**) Cryoelectron-microscopic image of optimized ABE RNP LNP containing ionizable lipid SM102 and 2.5% DMG-PEG 2000. (**l**) Schematic cartoon of targeted quantification of ABE and PE using mass spectrometry. (**m**) MS Quantification of ABE8e protein, RNP, and LNP with 2.5% DMG-PEG 2000 using peptides targeting Cas9 and evolved adenosine deaminase TadA*, relative to quantification by absorbance at 280 nm. Protein concentration in LNP was estimated by correcting for dilution throughout the encapsulation and dialysis. Three analytical replicates, mean ± s.d. (**n**) Rescue of expression of RPE65 in a cell line expressing *Rpe65 rd12* cDNA by ABE RNP, delivered with Lipofectamine 3000 (L3k) or *via* LNP containing ionizable lipid SM102 and 1.5 - 2.5% DMG-PEG 2000. (**o**) Next-generation sequencing analysis of ABE-editing outcomes in the cells with cDNA encoding *Rpe65 rd12*, treated with ABE

delivered on a plasmid with Lipofectamine 3000 (L3k) or as LNP. Three analytical replicates, mean ± s.d. (**p**) Off-target analysis of *Rpe65 rd12* cDNA cells. (**q**) ERG b-wave responses of *rd12* mice treated with 1 µl ABE RNP LNP per eye, with ionizable lipid SM102 and 1.5 or 2.5% DMG-PEG 2000. The RNP concentrations were approximately 2.3 and 2.5 µM, respectively, and the doses 515 ng and 560 ng RNP per eye, respectively. At least 8 eyes, mean ± s.d, Kruskal-Wallis test with Dunn's multiple comparisons test, ****$P < 0.0001$. Data generated by Rafal Holubowicz, Omar Medani, J. Noah Workman, Carolline R. Menezes, and Jiin H. Felgner.

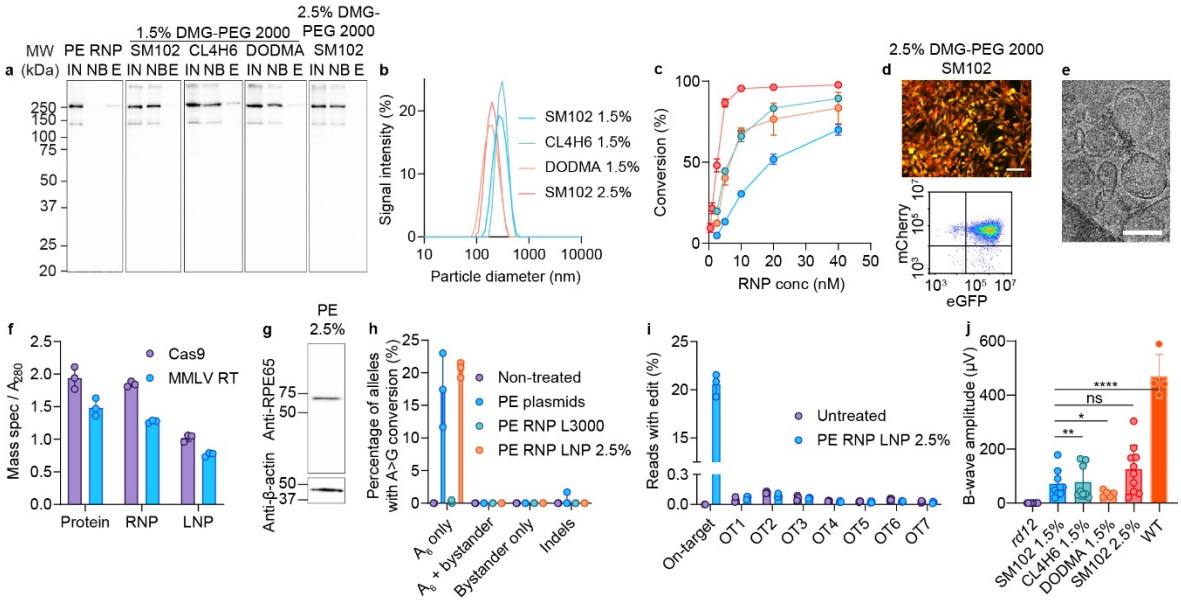


Figure 6.5. Lipid nanoparticle delivery of PE. (**a**) Immunoprecipitation-encapsulation assay of PE2 RNP LNP. (**b**) Particle size distribution of PE2 RNP LNP prepared with 1.5% DMG-PEG 2000 and ionizable lipids SM102 (d = 270 nm, PdI = 0.068), CL4H6 (d = 298 nm, PdI = 0.024), or DODMA (d = 176 nm, PdI = 0.096), and with 2.5% DMG-PEG 2000 and ionizable lipid SM102 (d = 194 nm, PdI = 0.040). Average plots are shown, n = 3 replicates. (**c,d**) Delivery of PE2 RNP LNP to *rd12* reporter cells, analyzed by flow cytometry and fluorescence microscopy. Representative microscopic image is shown for *rd12* reporter cells, treated with 20 nM PE2 RNP LNP with 2.5% DMG-PEG 2000. 20 nM corresponds to 6 μg ml^{-1}. Scale bar represents 100 μm. Two biological replicates with two analytical replicates each, mean ± s.d. (**e**) Cryoelectron-microscopic image of PE2 RNP LNP, containing ionizable lipid SM102 and 2.5% DMG-PEG 2000. The scale bar represents 100 nm. (**f**) Mass spectrometric quantification of PE2 as protein, RNP, and LNP. Three analytical replicates, mean ± s.d. (**g**) PE-mediated rescue of expression of RPE65 in a cell line transformed with cDNA encoding *Rpe65 rd12*. LNP with 2.5% DMG-PEG 2000 was used, and RNP concentration was 20 nM, 6 μg ml^{-1}. (**h**) Next-generation sequencing analysis of PE-editing outcome in the cells with cDNA encoding *Rpe65 rd12*. Three analytical replicates, mean ± s.d. (**i**) Off-target analysis of *Rpe65 rd12* cells treated with PE RNP LNP. (**j**) Restoration

of visual function in *rd12* mice treated with 1.6 uM (CL4H6, 476 ng RNP per eye), 2.0 μM (SM102, DODMA, 596 ng RNP per eye) or 2.2 μM (SM102 with 2.5% DMG-PEG 2000, 655 ng RNP per eye) PE2 LNP, 1 μl per eye, as evidenced by ERG. At least 5 eyes, mean ± s.d. Kruskal-Wallis test with Dunn's multiple comparisons test, $*P < 0.05$; $**P < 0.01$; $****P < 0.0001$; ns, $P \geq 0.05$. Data generated by Rafal Holubowicz, Omar Medani, J. Noah Workman, Carolline R. Menezes, and Jiin H. Felgner.

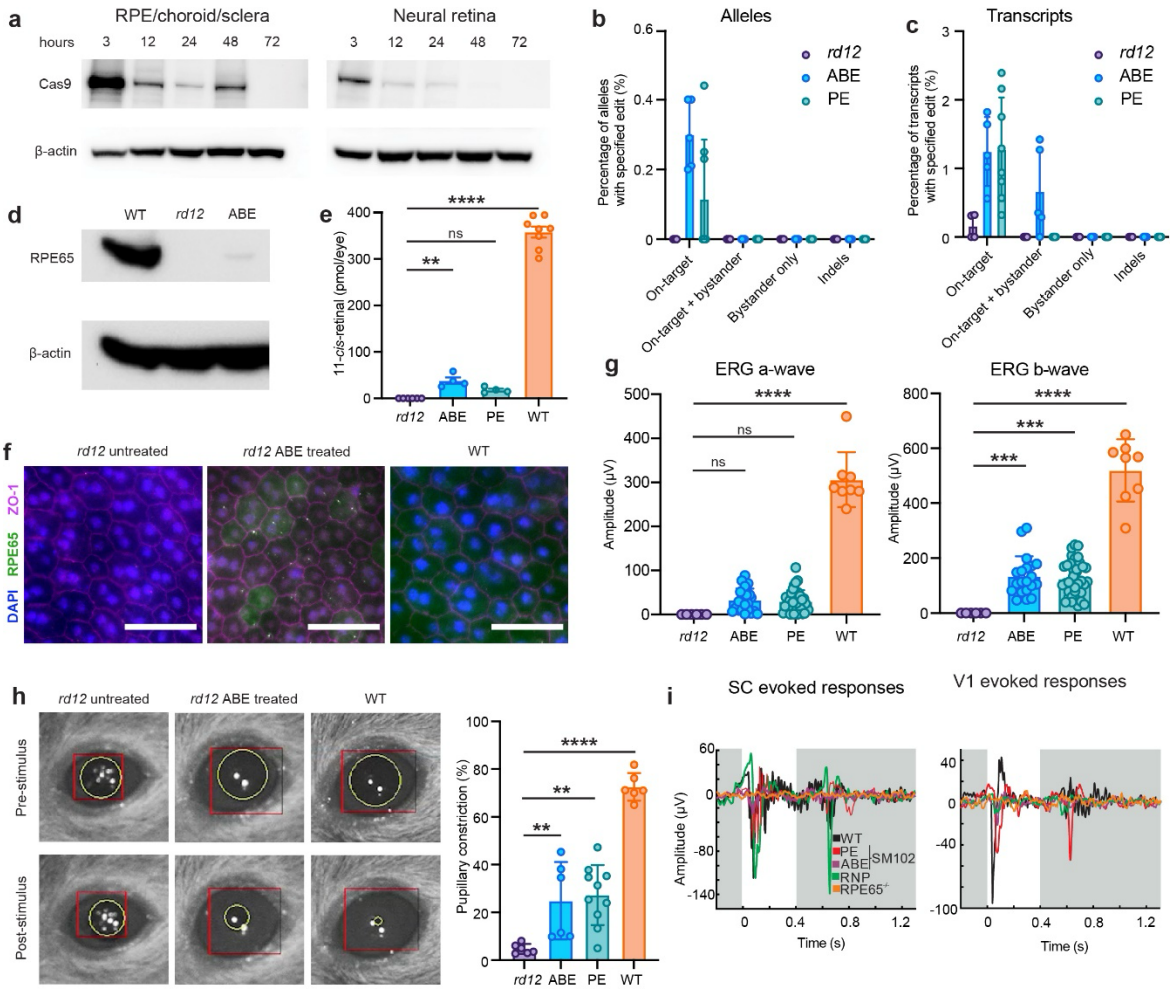
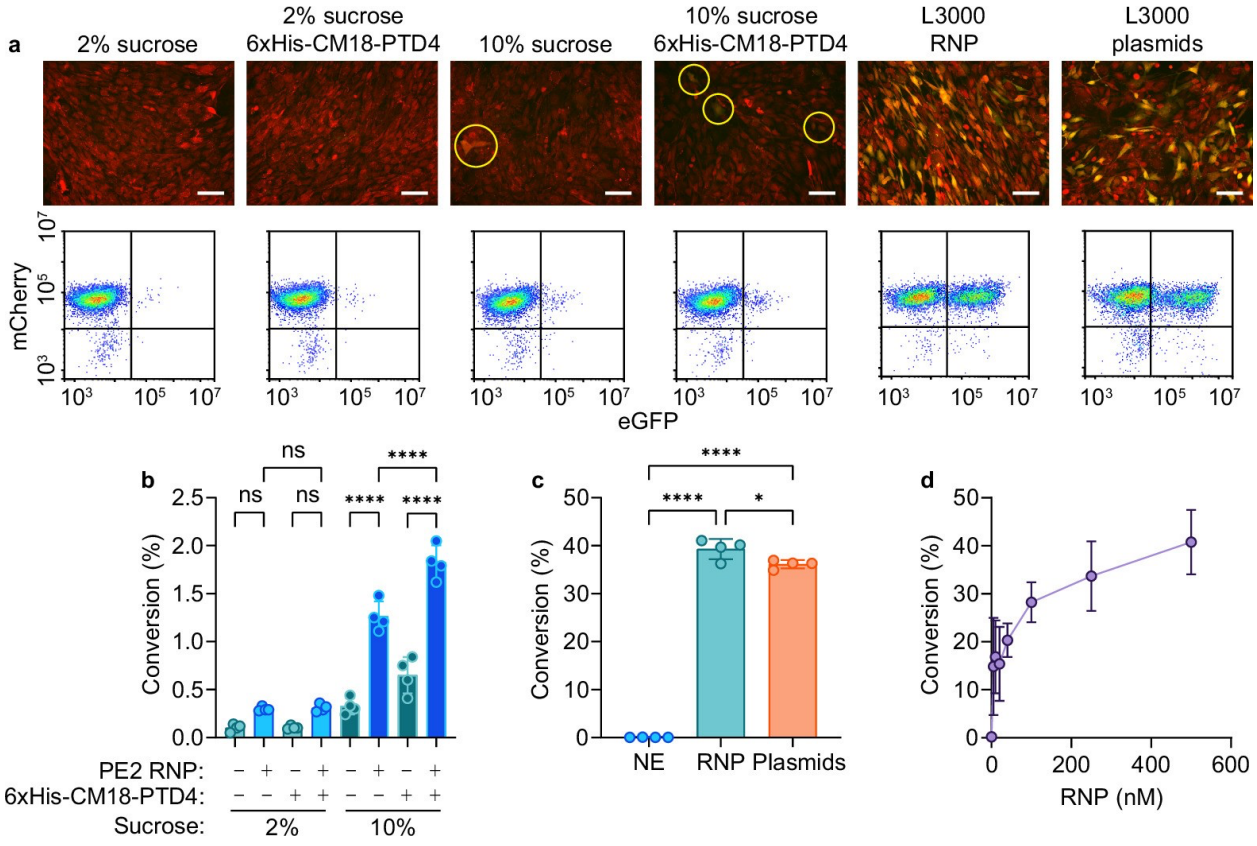


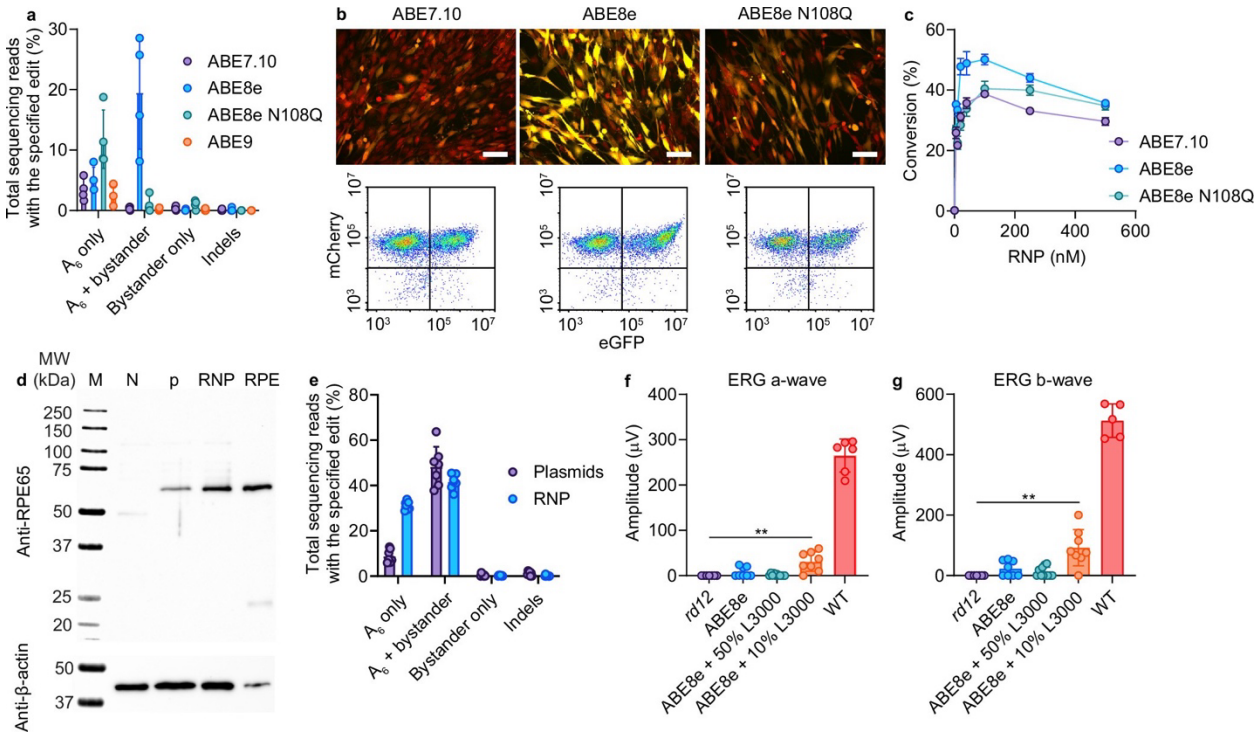
Figure 6.6. *In vivo* physiology and chemistry of *Rpe65* correction. (**a**) ABE RNP LNP degradation kinetics after subretinal injection into WT mice; anti-Cas9 Western blot analysis of RPE/choroid/sclera and neural retina lysates collected at the indicated hours post-injection. (**b,c**) Next-generation sequencing of genomic DNA (**b**) and of transcripts (**c**) to document *Rpe65*-editing outcomes after treatment with ABE RNP LNP or PE RNP LNP. (**d**) Anti-RPE65 Western blot analysis of RPE/choroid/sclera lysates from WT, untreated *rd12*, and ABE-RNP-LNP-treated *rd12*. (**e**) HPLC quantification of 11-*cis*-retinal in whole eyes from dark-adapted untreated *rd12* mice, ABE-RNP-LNP- and PE-RNP-LNP-treated *rd12* mice, and WT mice. (**f**) RPE flatmounts of *rd12* untreated, ABE-RNP-LNP-treated *rd12*, and WT mice stained for RPE65 (green) and counterstained with ZO-1 (magenta) and DAPI (blue). (**g**) Scotopic flash ERG a-wave (left) and

b-wave (right) amplitudes for *rd12* mice treated with ABE RNP LNP or PE RNP LNP, compared to untreated *rd12* and WT mice. (**h**) Pupillary light response (PLR) after a $10^{1.2}$ W m^{-2} stimulus for ABE-RNP-LNP- and PE-RNP-LNP-treated *rd12* mice, compared to untreated *rd12* and WT mice. Data quantified as pupil diameter constriction post-stimulus compared to pupil diameter pre-stimulus in dark-adapted animals. Representative frames (left), and summarized data (right). (**i**) Representative SC (left) and V1 (right) responses from WT mice (black), *rd12* mice treated with free ABE RNP (green), ABE RNP LNP (purple), or PE RNP LNP (red), and untreated *rd12* mice (orange). The mice received 1 µl of 2.5 µM ABE RNP (560 ng) or 2.2 µM PE RNP (655 ng) per eye. All data plotted as mean ± s.d., analyzed by Kruskal-Wallis test with Dunn's multiple comparisons test, **P* < 0.05; ***P* < 0.01; ****P*<0.001; *****P* < 0.0001; ns, *P* ≥ 0.05. Data generated with assistance from Paul Z. Chen, Carolline R. Menezes, and Andrzej Foik.



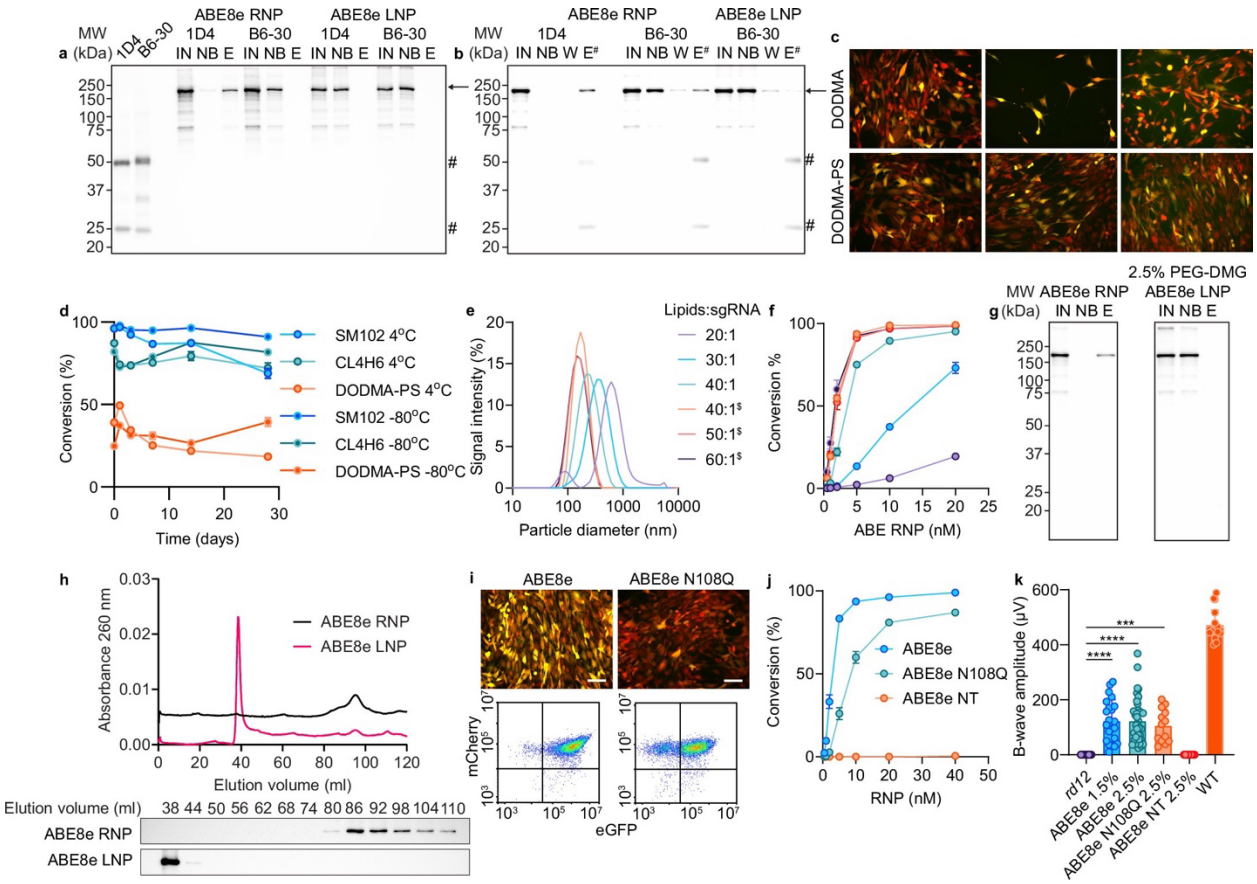
Extended Data Figure 6.1: Delivery of PE RNP into *rd12* reporter cells. (a) Analysis of delivery of 500 nM PE2 RNP (149 µg ml^{-1}), with epegRNA targeting *Rpe65 rd12*, into the *rd12* reporter cells using 2% (w/v) sucrose or 10% (w/v) sucrose, and with or without added cell-penetrating peptide 6xHis-CM18-PTD4; or using Lipofectamine 3000 (L3000). In parallel, the *rd12* reporter cells were transfected with PE2 and *rd12* epegRNA plasmids (right-most panel). The cells were analyzed using fluorescence microscopy and flow cytometry. Faint-yellow cells that were modified with PE2 RNP are highlighted with yellow circles. Scale bar: 100 µm. (b) Delivery of PE2 RNP using 10% sucrose and 6xHis-CM18-PTD4 peptide, quantified using flow cytometry. Two biological replicates with two analytical replicates each, mean ± s.d. One-way ANOVA with Tukey's multiple comparisons test. ****$P < 0.0001$; ns, $P > 0.05$. (c) Comparison of efficiency of delivery of PE2 with Lipofectamine 3000 as RNP, and as a pair of PE and epegRNA plasmids. *P < 0.05; ****P < 0.0001. One-way ANOVA with Tukey's multiple comparisons test. NE = minus enzyme control with Lipofectamine 3000 alone. (d) Titration of *rd12* reporter cells with increasing PE RNP

and constant L3000, quantified by flow cytometry. Four biological replicates with 2 analytical replicates each, mean ± s.d. Data generated by Rafal Holubowicz and Roman Smidak.



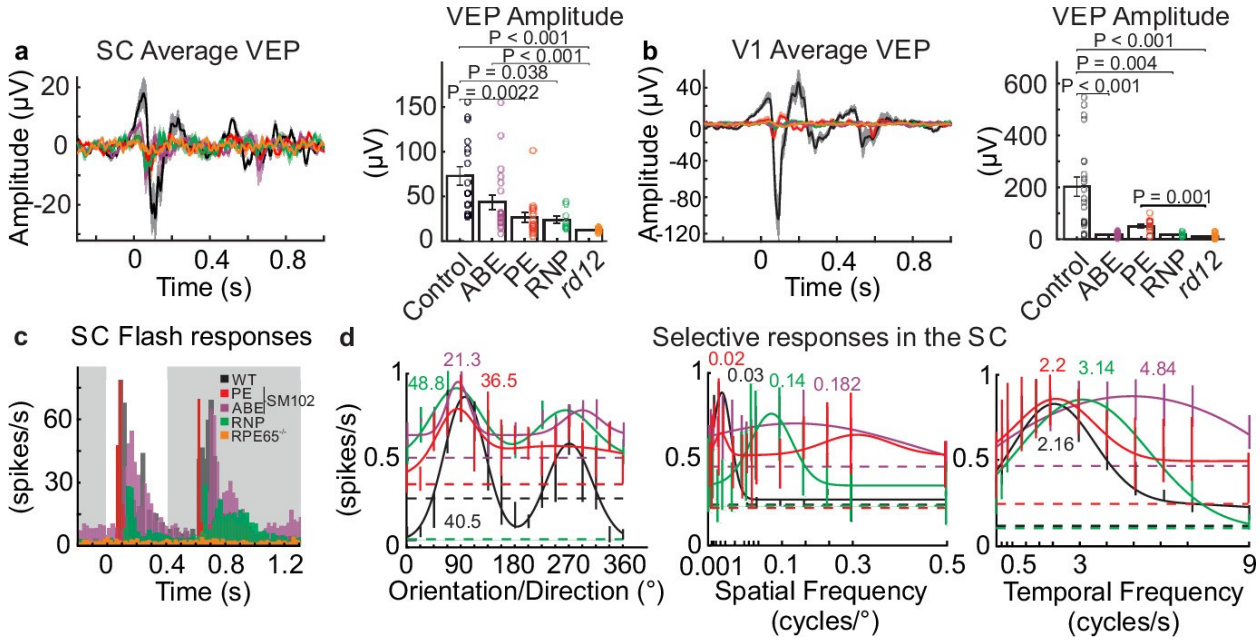
Extended Data Figure 6.2: Delivery of ABE using Lipofectamine 3000. (**a**) Analysis of ABE editing of *rd12* reporter cells transfected with plasmids encoding ABE NG variants and guide RNA targeting *Rpe65 rd12*. Two biological replicates with 2 analytical replicates each, mean ± s.d. (**b,c**) ABE RNPs were delivered to *rd12* reporter cells using Lipofectamine 3000. Efficiency of delivery was analyzed using (**b**) fluorescence microscopy (100 nM, 22.4 μg ml^{-1} RNP shown here) and (**c**) flow cytometry. Scale bar: 100 μm. Two biological replicates with 2 analytical replicates each, mean ± s.d. (**d**) Rescue of RPE65 protein expression in NIH/3T3-*rd12* cells by delivery of ABE and guide RNA plasmids (p), or 100 nM ABE RNP using Lipofectamine 3000 (RNP). Mouse retinal pigment epithelium (RPE) extract was used as a positive control. M = molecular weight marker; N = untreated cells. (**e**) NGS analysis of editing of NIH/3T3-*rd12* cells treated with ABE. Two biological replicates with at least 3 analytical replicates each, mean ± s.d. (**f,g**) Rescue of visual function in *rd12* mice injected with 25 μM ABE8e RNP (5.6 μg per eye), 23.6 μM ABE8e RNP with 50%(v/v) Lipofectamine 3000 (4.5 μg per eye), or 23.6 μM ABE8e RNP with 10%(v/v) Lipofectamine 3000. Injected material additionally contained 25% (w/v) sucrose. At least 8 eyes,

mean ± s.d, Kruskal-Wallis test with Dunn's multiple comparisons test, $^{**}P < 0.01$. Data generated by Rafal Holubowicz, Paul Z. Chen, Carolline R. Menezes, and Omar Medani.

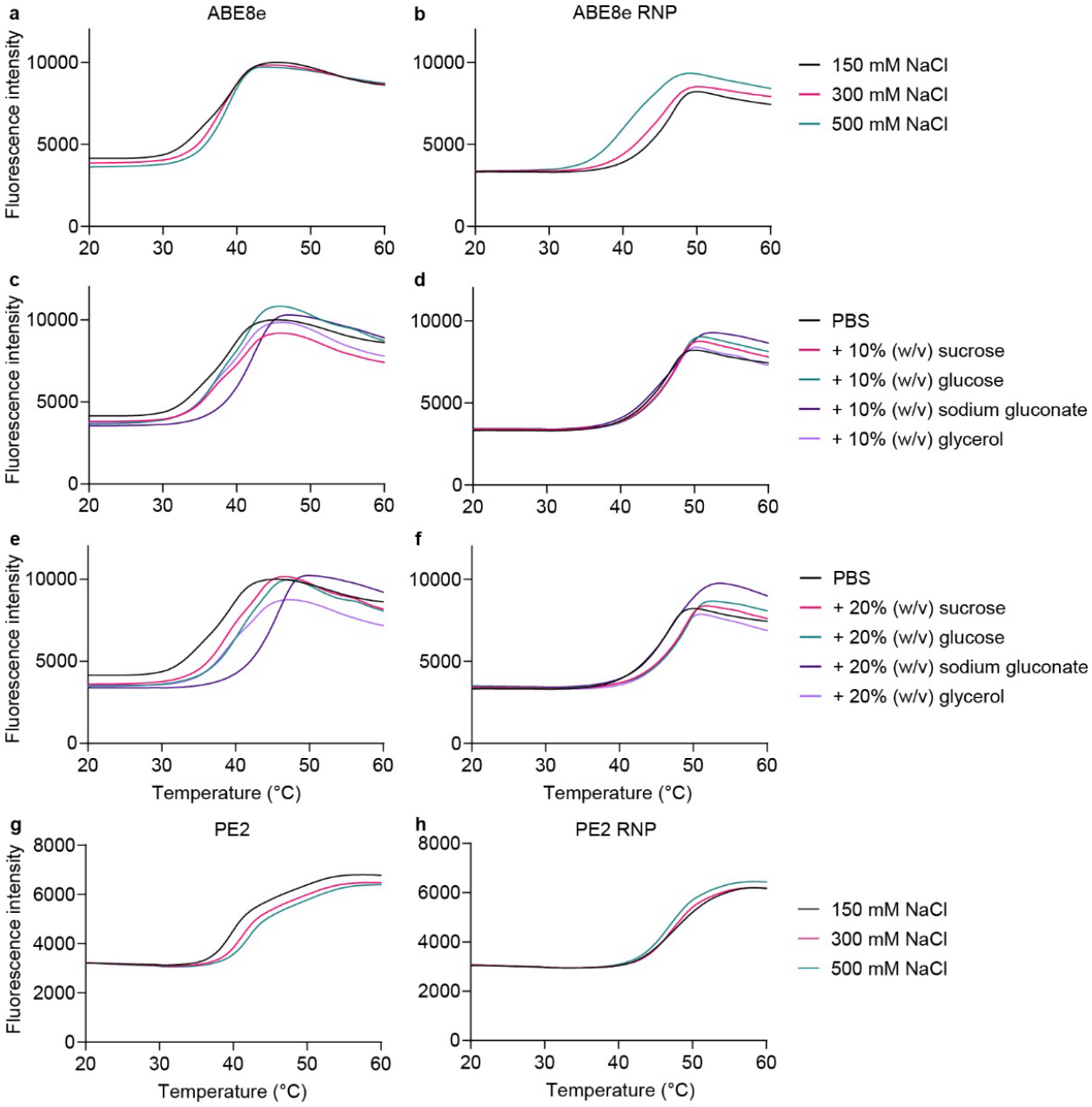


Extended Data Figure 6.3: Optimization of ABE RNP LNPs. (**a**,**b**) Immunoprecipitation of ABE RNP, free or encapsulated in the LNP with SM102 ionizable lipid and 1.5% DMG-PEG 2000, using 1D4 resin or control B6-30 resin. Elution was done using 1 mg ml^{-1} 1D4 peptide (E) or using Laemmli sample buffer with DTT (E*). 1D4 and B6-30 resins treated with Laemmli sample buffer alone served as additional controls. The arrow (at the right) indicates the band corresponding to ABE; hash marks correspond to bands from mouse 1D4 and B6-30 antibodies detected by equine anti-mouse secondary HRP-linked antibody. (**c**) Relative cytotoxicity of LNP with ionizable lipid DODMA, with or without SOPS, demonstrated using fluorescence-microscopic images from three transfection experiments at 20 nM RNP (4.5 μg ml^{-1}). (**d**) Stability (upon storage at 4 °C or -80 °C) of ABE RNP LNP made with 50% ionizable lipid and 1.5% DMG-PEG 2000, as tested with *rd12* reporter cells and 20 nM ABE RNP. Three replicates, mean ± s.d. (**e**,**f**) Particle size distribution and delivery efficiency of ABE RNP LNP made with various lipid:RNA weight ratios. Asterisks

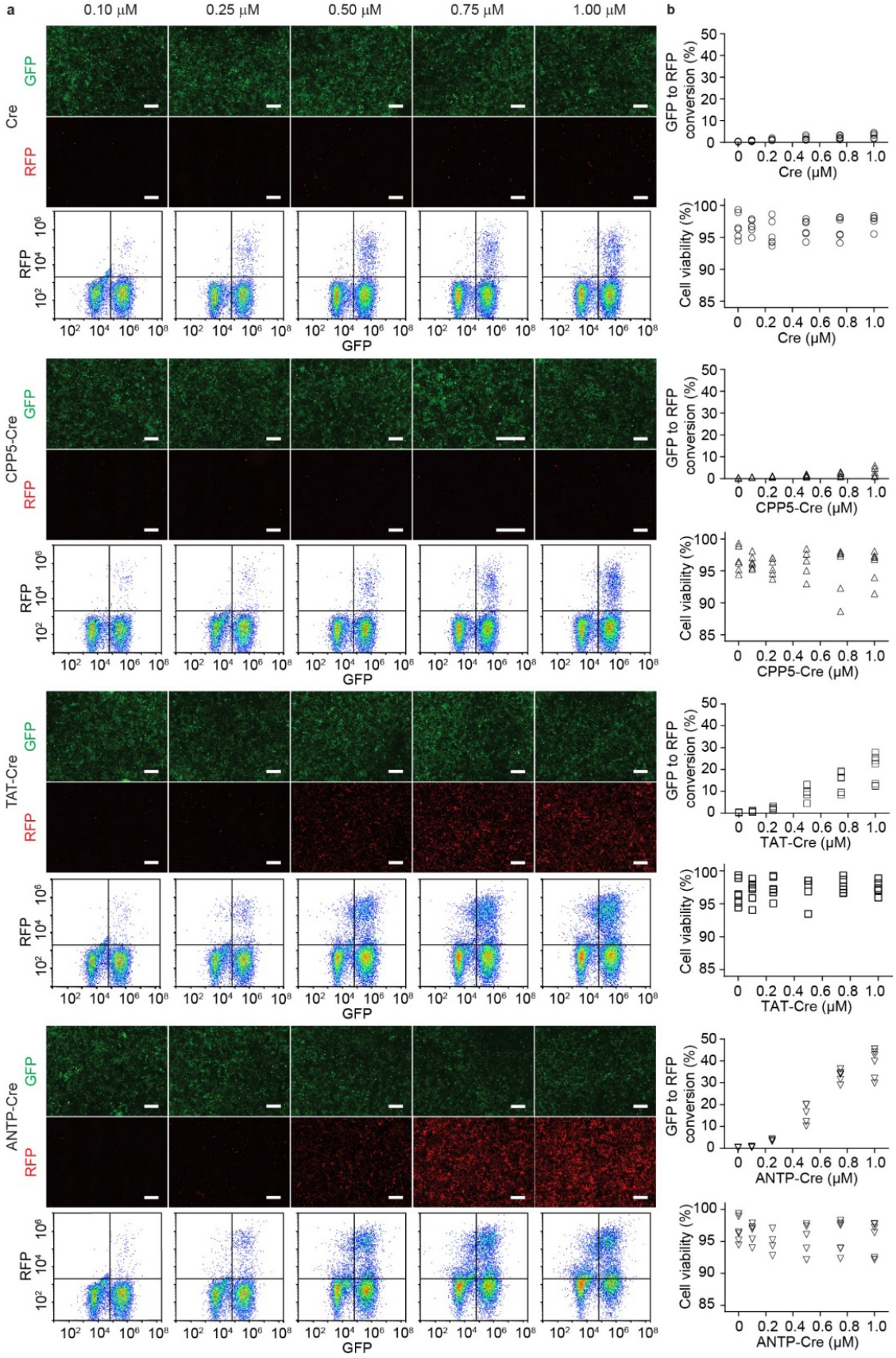
denote 2.5% DMG-PEG 2000; otherwise, the concentration was 1.5%. Plots shown in panels **e** and **f** represent data that were averaged from n = 3 replicates, mean ± s.d. (**g**) Encapsulation of ABE RNP into LNPs with ionizable lipid SM102 and 2.5% DMG-PEG 2000. (**h**) Size exclusion chromatograms of ABE8e RNP (black) and ABE8e RNP LNP with SM102 lipid and 2.5% DMG-PEG2000, 40:1 lipid:sgRNA ratio (red) resolved on a Sephacryl S-500 HR column (top) and anti-Cas9 blots of collected fractions (bottom). (**i,j**) ABE editing in the *rd12* reporter cells, using ABE RNP LNP visualized *via* fluorescence microscopy (here, 20 nM ABE8e RNP) and quantified by flow cytometry. Scale bar: 100 μm. Three replicates. (**k**) ERG responses of *rd12* mice treated with ABE8e LNPs made using ionizable lipid SM102 and 1.5 – 2.5% DMG-PEG 2000 (2.3 and 2.5 μM, 515 and 560 ng, respectively), ABE8e N108Q LNPs made with 2.5% DMG-PEG 2000 (2.3 μM, 515 ng), or ABE8e LNPs with non-targeting guide RNA (2.5 μM, 560 ng), 1 μl per eye. At least 8 eyes, mean ± s.d, Kruskal-Wallis test with Dunn's multiple comparisons test, ***$P < 0.001$; ****$P < 0.0001$. Data generated by Rafal Holubowicz, Paul Z. Chen, Carolline R. Menezes, and Omar Medani.



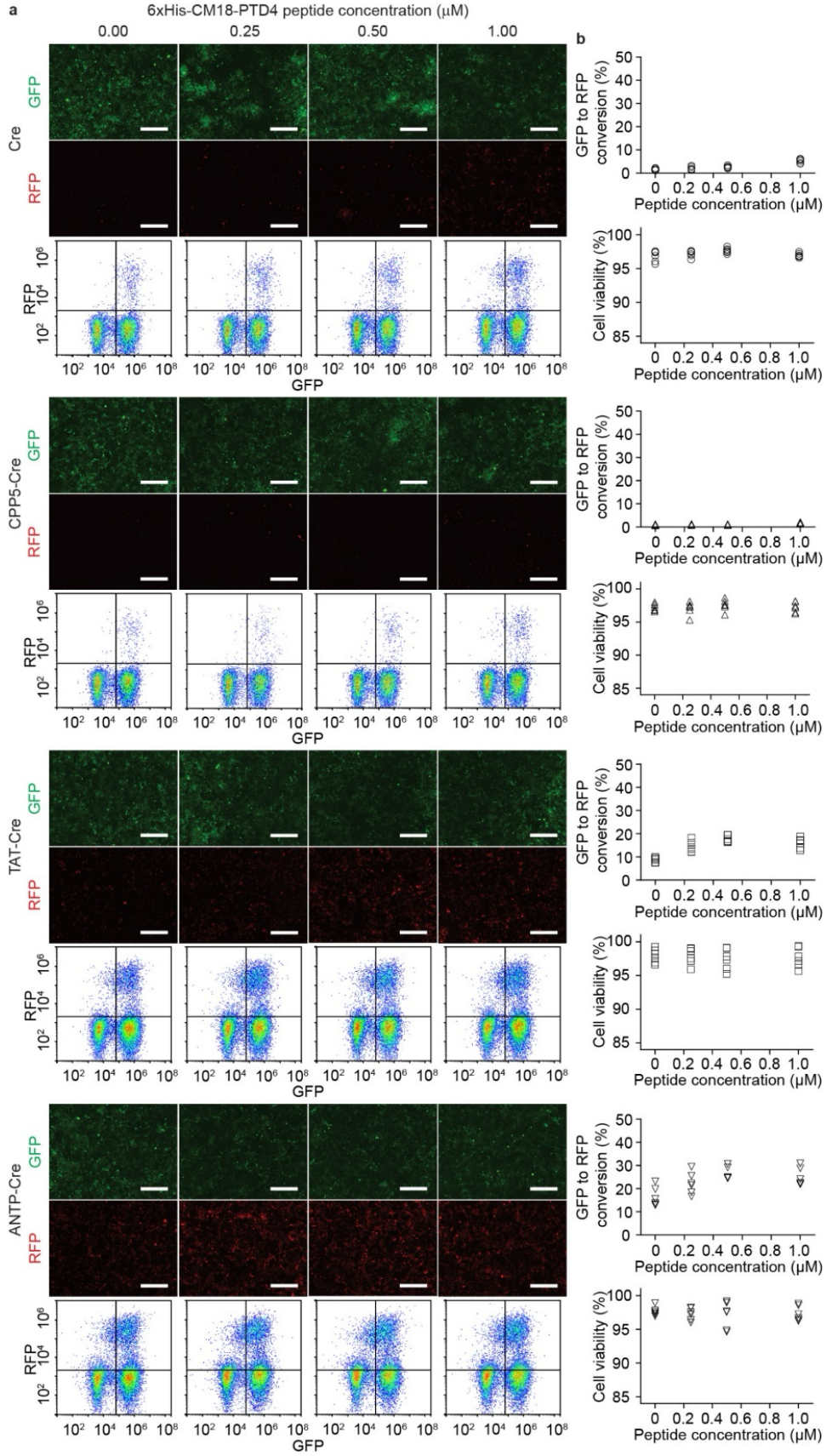
Extended Data Figure 6.4: Treatment with editor-containing nanoparticles restores visual responses in *rd12* mice. (**a**) Visually evoked potentials (VEPs) in the superior colliculus (SC) for untreated WT mice (black); *rd12* mice treated with free RNP (green); *rd12* mice treated with ABE RNP LNP (purple); *rd12* mice treated with PE RNP LNP (red); and untreated *rd12* mice (orange). Bar plots represent the summary of the VEPs from all tested animals. (**b**) Same analysis as in (A) performed for the primary visual cortex (V1). (**c**) Overlapped examples of histograms for single-neuron flash responses. (**d**) Single-cell examples of selective neurons recorded in the SC. The tuning curves present orientation-selective cells, spatial frequency, and temporal frequency tuning curves for the tested mice. Numbers on the graphs indicate HWHH, optimal spatial frequency, and optimal temporal frequency. Data generated by Andrzej Foik.



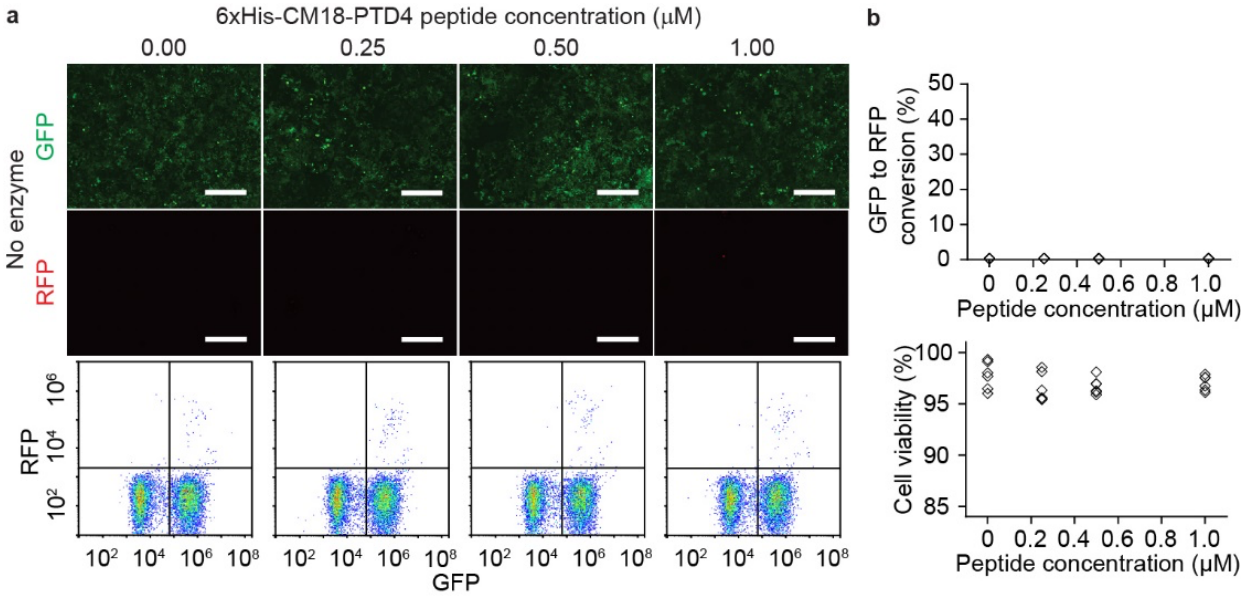
Supplementary Figure 6.1. Differential-scanning fluorimetry profiles of ABE and PE. ABE8e and PE2 proteins, with or without respective guide RNAs, were incubated with increasing concentrations of NaCl, and with optional additives. Plots were averaged from n = 3 replicates. Data generated by Rafal Holubowicz.


a
0.10 μM
0.25 μM
0.50 μM
0.75 μM
1.00 μM
Cre
CPP5-Cre
TAT-Cre
ANTP-Cre
GFP
RFP
RFP
GFP
b
GFP to RFP conversion (%)
Cell viability (%)
Cre (μM)
CPP5-Cre (μM)
TAT-Cre (μM)
ANTP-Cre (μM)

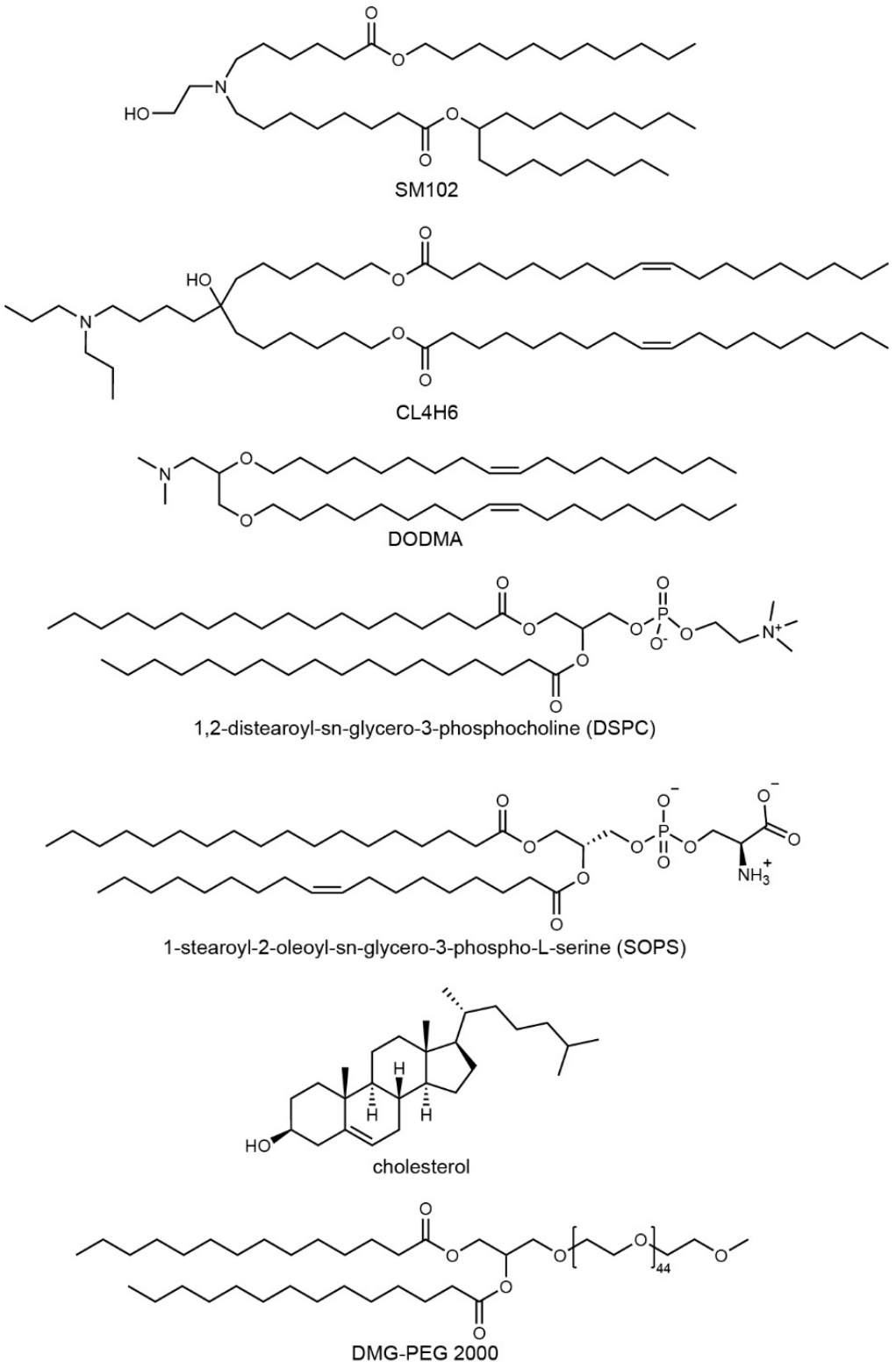
Supplementary Figure 6.2. Titration of HEK293-loxP-GFP-RFP cells with CPP-fused Cre. Cre recombinase, with and without fused cell-penetrating peptides, was delivered to the HEK293-loxP-GFP-RFP cells; and delivery efficiency was analyzed by (**a**) fluorescence microscopy and (**b**) flow cytometry. Cell viability was assessed using inclusion of DAPI. Scale bar: 200 μm. Three experiments with two replicates each, mean ± s.d. Data generated by Rafal Holubowicz.


a
6xHis-CM18-PTD4 peptide concentration (μM)
0.00
0.25
0.50
1.00
Cre
CPP5-Cre
TAT-Cre
ANTP-Cre
GFP
RFP
GFP
RFP
b
GFP to RFP conversion (%)
Peptide concentration (μM)
Cell viability (%)
Peptide concentration (μM)

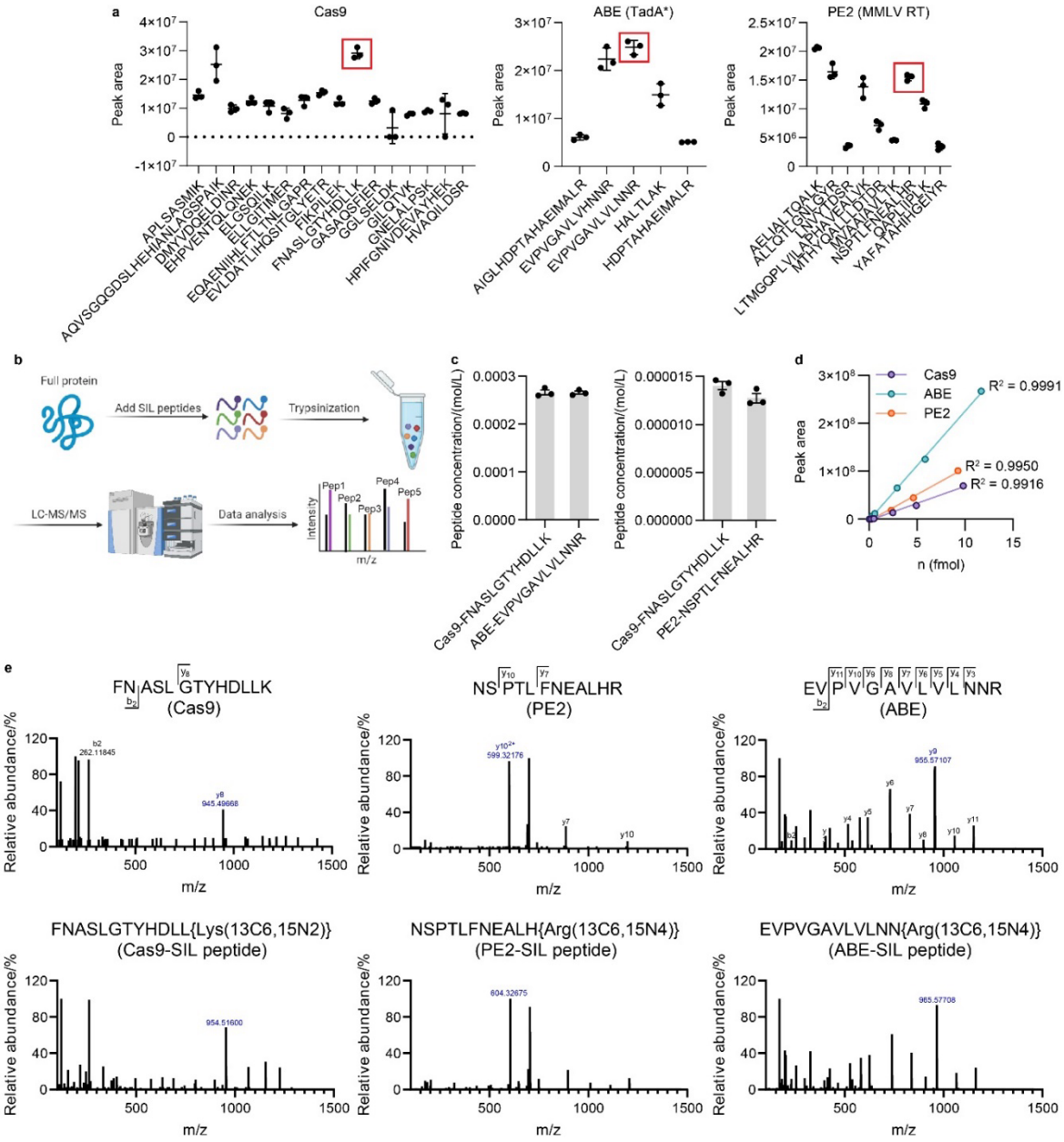
Supplementary Figure 6.3. Titration of HEK293-loxP-GFP-RFP cells with Cre and 6xHis-CM18-PTD4 peptide. Cre recombinase (0.5 μM) with additional 6xHis-CM18-PTD4 peptide was delivered to the HEK293-loxP-GFP-RFP cells, and delivery efficiency was analyzed by (**a**) fluorescence microscopy and (**b**) flow cytometry. Cell viability was assessed according to inclusion of DAPI. Scale bar: 200 μm. Three experiments with two replicates each, mean ± s.d. Data generated by Rafal Holubowicz.



Supplementary Figure 6.4. Minus-enzyme controls for HEK293-loxP-GFP-RFP cells with 6xHis-CM18-PTD4 peptide. The cells were treated with OptiMEM medium without or with additional 6xHis-CM18-PTD4 peptide, analogous to the experiments with Cre recombinase, and analyzed by (**a**) fluorescence microscopy and (**b**) flow cytometry. Scale bar: 200 μm. Three experiments with two replicates each, mean ± s.d. Data generated by Rafal Holubowicz.

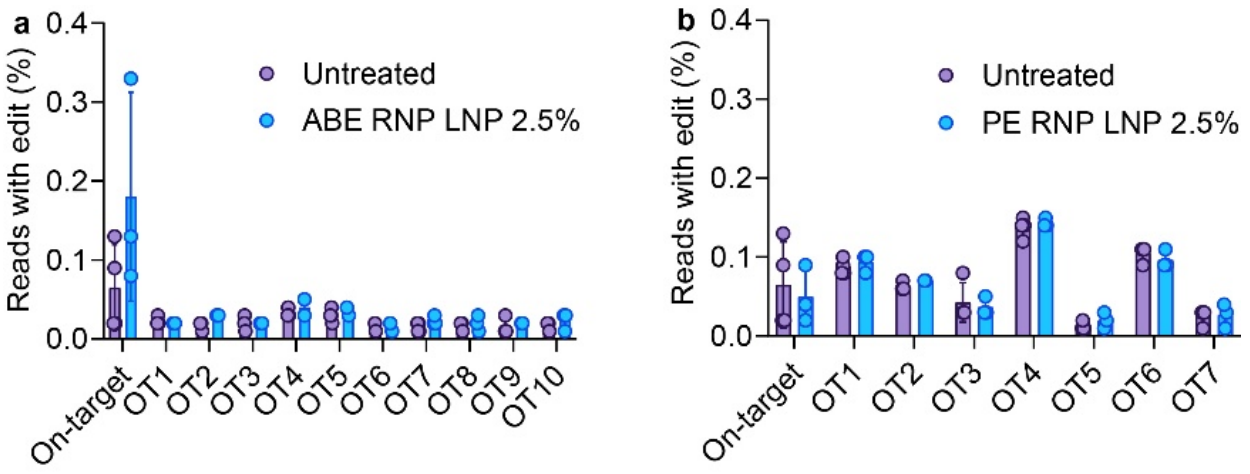


Supplementary Figure 6.5. Structures of lipids used in the study.

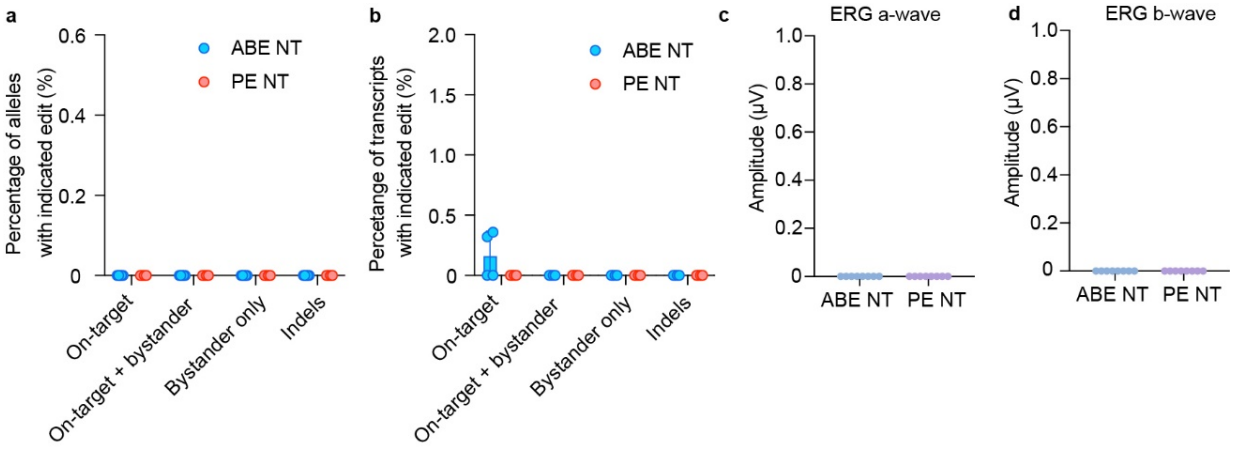


Supplementary Figure 6.6. Mass spectrometric quantification of ABE and PE. (**a**) Reproducibly detected tryptic peptides of Cas9, ABE, and PE2. The peptides selected for quantification are highlighted. (**b**) Workflow for absolute quantification of protein abundance with stable-isotope–labeled (SIL) peptides. Created in BioRender, BioRender.com/z14j704. (**c**) Repeatability of SIL peptide-based quantification in LNP samples. (**d**) Linear response of SIL peptide-based quantification of Cas9, ABE, and PE2. (**e**) The MS2 spectra of the peptides and

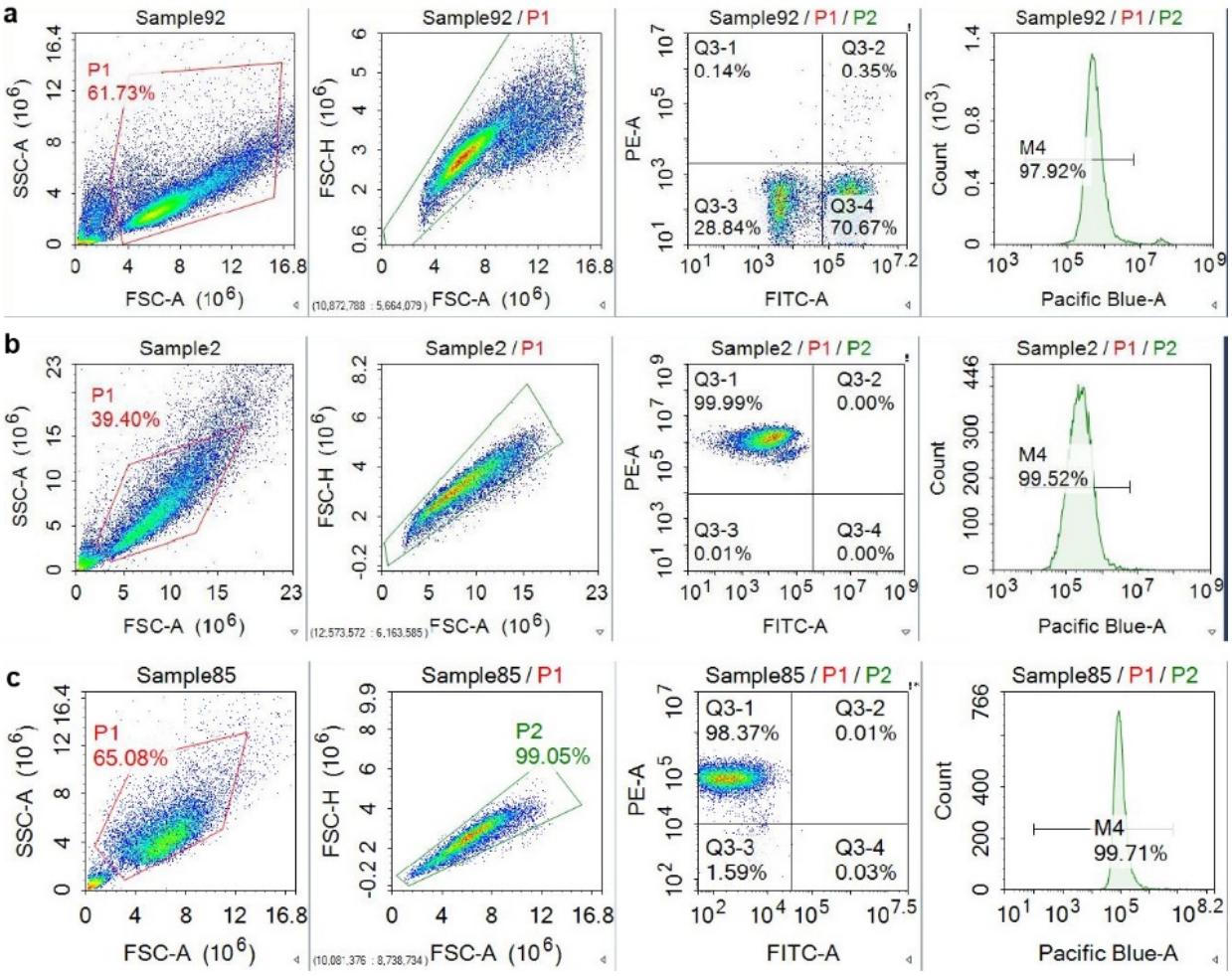
related SIL peptides for quantification of Cas9, ABE, and PE2. Data generated by Rafal Holubowicz and Fangyuan Gao.



Supplementary Figure 6.7. Off-target analysis of rd12 mice treated with ABE- and PE RNP LNP. (a) Quantification of deamination of target A6 (on-target) or adenosine closest to A5 (off-targets) in genomic DNA isolated from RPE cells of *rd12* mice treated with ABE RNP LNP, 560 ng per eye. **(b)** Quantification of target edit (on-target) or most edited nucleotide (off-targets) in genomic DNA isolated from RPE cells of *rd12* mice treated with PE RNP LNP. Data generated by J. Noah Workman.



Supplementary Figure 6.8. Non-targeting ABE and PE RNP LNPs do not result in correction of *Rpe65* or restore scotopic flash ERG responses. (**a, b**) Next-generation sequencing of **(a)** genomic DNA and (**b**) transcripts to document *Rpe65*-editing outcomes after treatment of *rd12* mice with non-targeting ABE8e RNP LNP or nontargeting PE2 RNP LNP made with 2.5% DMG-PEG 2000. (**c, d**) Scotopic flash ERG a-wave and b-wave amplitudes for *rd12* mice treated with non-targeting ABE RNP LNP and non-targeting PE RNP LNP. The mice received 560 ng of ABE RNP or 655 ng of PE RNP per eye. Data generated in part with assistance from Rafal Holubowicz, Carolline R. Menezes, and Paul Z. Chen.



Supplementary Figure 6.9. Flow cytometry gating strategies. (**a**) HEK293-loxP-GFP-RFP cells, (**b**) mT/mG fibroblasts, (**c**) *rd12* reporter cells. The cells were gated on forward and side scatter (FSC-A and CCS-A, respectively) to select intact cells; and forward scatter area (FSC-A) and height (FSC-H) to isolate single cells. Fluorescence of GFP was quantified using a FITC filter (530/30 nm), and fluorescence of RFP, tdTomato, and mCherry was quantified using a PE filter (586/20 nm). Cell viability was estimated by DAPI exclusion using a Pacific Blue filter (445/45 nm). Data generated by Rafal Holubowicz.

CHAPTER 7

Conclusions and future directions

CHAPTER 7

Conclusions and future directions

7.1 Summary of the work

In summary, the body of work presented here offers proof of concept for the editing of multiple IRD mouse models and novel delivery vehicles for the delivery of genome editing agents. Through *in vitro* modeling and screening of ABE and PE strategies, we selected maximally efficient combinations of editors and guide RNAs to correct mutations associated with retinitis pigmentosa, Leber congenital amaurosis, and nanophthalmos. We also developed novel delivery technologies that promise to improve on the specificity and safety of genome editors by spatially and temporally minimizing the presence of genome editors. We hope that these will offer new therapeutic options to patients with IRDs who currently do not have molecularly targeted therapies to halt or reverse retinal degeneration. Combined with early detection, genetic diagnosis, and an improved understanding of the molecular mechanisms of disease, precision medicine has the potential to revolutionize the management and treatment of editing. In particular, advances in long read sequencing, which will allow for geneticists to assess intronic and structural variants, as well as interpret phase and compound heterozygosity, will offer a clearer picture of the molecular cause of disease[346]. With decreased sequencing cost, and the use of base and prime editors to perform saturation editing and phenotype assessment of disease genes, clinical geneticists should be able to identify and classify the vast majority of IRD cases[347-350].

7.2 Ethics of genome editing

Thus far, the field of genome editing has moved rapidly and provided a path forward for the treatment of IRDs and other genetic disorders. When it comes to the correction of somatic mutations that cause debilitating diseases, such as IRDs, sickle cell anemia, and lysosomal storage disorders, it is relatively straightforward to approve the use of genome editing to alleviate these medical burdens. However, the ethics of genome editing are less straightforward for non-

somatic cell editing. Should embryos be screened for rare inherited diseases? Should these be attempted to be corrected *in vitro* before implantation? Should these be treated *in utero*? The side effects of somatic gene editing are confined to the cells, tissues, and ultimately, the body of the patient receiving the treatment, but genome engineering at the embryo or germline could have wide-reaching, unintended, and unappreciated consequences. For instance, evidence of large chromosomal translocations and rearrangements was missed by targeted amplicon sequencing of off-target sites, but growing evidence has shown that these structural changes occur with both nuclease, base, and prime editing[351]. It will be difficult to clear the much higher bar of safety in pre-implantation or germline gene editing, but perhaps this is a milestone which should not ever be breached. In addition, genome editing for polygenic and more nuanced genetic diseases, or risk variants that slightly modify the risk of developing a disease, should be carefully studied and considered before being applied to larger population for diseases such as high blood pressure, diabetes, dementia, and cardiovascular disease. This conversation needs to happen with stakeholders from all facets of society, including ethicists, government regulators, scientists, physicians, and common citizens.

Genome editing should also take natural genetic variation into consideration. The reference human genome cannot capture the diversity of human sequences, and single nucleotide variations that are uncommon or not represented in reference sequences could lead to surprisingly high off-target effects. For example, a CRISPR strategy targeting the *BCL11A* enhancer for sickle cell and beta-thalassemia, which are genetic diseases common in populations of African ancestry, has a top off-target site in a genetic variant that is found in ~4% of populations of African ancestry[352]. This off-target site would otherwise not have been found when assessing off-targets in a reference genome, highlighting that more sequencing of diverse patient populations to form larger genome variant databases, direct sequencing of patients enrolled in clinical trials, and consideration of natural and global genetic variation need to happen in genome editing approaches.

7.3 Challenges in scaling genome editing

A major hurdle for the application of genome editing is the cost and complexity of bringing therapies to market for rare and orphan diseases[353]. It has been estimated to cost, on average, over $1.1 billion USD to bring a product through preclinical, clinical trials, and FDA approval[354]. Even with cell and gene therapies (CGT) that can cost millions of dollars, it is difficult to see how this can be feasible for IRDs, where many mutations have only a handful to a few hundred patients. A solution could be the formation of nonprofit or academic institution driven CGT programs that do not seek to make a profit on their products, but instead seek to offer access for patients who need them. Programs spearheaded by pharmaceutical companies, such as the EDIT-101 product for *CEP290*-associated LCA, were discontinued for business reasons, despite potentially promising responses in patients in the phase I clinical trial[355]. Another potential solution is enabled by the biochemistry of CRISPR systems itself, where therapies for different IRDs or different mutations within the same gene only differ by their guide RNA, while the delivery systems and enzymes (e.g. VLPs, LNPs, and PEs) remain the same across therapies. Currently, each new guide RNA and editor combination requires a separate investigational new drug (IND) application and separate review and approval. An overarching IND or approval for these gene editing therapies where only the guide is changed, along with additional testing in human organoids or patient tissues for off-target analysis could enable these therapies for rare diseases, though there will be legal and ethical challenges to ensure public safety[353]. Notably, with appropriate safeguards, because these are personalized medicines for a small patient population with an unmet medical need, the risk for abuse of the approval process and to public health could be minimal. If one or several gene editing therapies are approved, the safety and risk profile for these could establish the foundation for more therapies in the future, as Luxturna did for gene augmentation therapies.

A more ambitious approach would be to move in a mutation-independent direction. For instance, mutations in *USH2A* are responsible for Usher syndrome type 2 and RP, and a high

proportion of mutations are found within exon 13[356]. Combined with the knowledge that exon 13 can be skipped with minimal impact to the usherin protein, therapeutics that can mediate exon 13 skipping by gene editing or anti-sense oligonucleotides could cover all patients with exon 13 mutations. Even more excitingly, prime editing approaches, such as twin PE and programmable addition via site-specific targeting elements (PASTE)[93], could re-write entire exons. Smaller exons could be directly rewritten to wildtype sequences by PE and twin PE. For smaller genes like peripherin-2 (*PRPH2*) with 3 exons, a suite of 3 genome editing tools, one covering each exon, could theoretically cover all patients with coding mutations in *PRPH2*. Other strategies could include installation of an integrase landing pad by prime editing, followed by the knock-in of an entire wildtype cDNA or wildtype exons. By combining patient populations, this would increase the effective patient pool that could be treated with a single gene editing product.

7.4 Immunogenicity of gene editing

A major concern with the clinical application of gene therapy and gene-editing tools in the clinic is the potential for development of an immune or inflammatory response to the vector. While very rare, uncontrolled immune activation after patient dosing, in severe cases, can lead to organ failure or even death of the patient. Thus, before clinical application, the immune response to the gene editing vector must be carefully evaluated to ensure patient safety. Vectors and cargoes can also be dose limiting, possibly resulting in gene editing at levels that are insufficient for a therapeutic effect.

Inflammatory responses to gene therapy could be due to the delivery vehicle or to the cargo. Although AAVs have been engineered to reduce their immunogenicity, pre-clinical and clinical data have suggested that unwanted immune responses to AAVs occur over time in a payload-independent manner.[271,357] One study of AAV in non-human primates reported the presence of sub-foveal deposits, concentric macular rings, and outer retinal disruption.[358] In multiple clinical trials of gene-augmentation therapies with AAV, the major complication has been inflammation resulting in uveitis, necessitating steroid and immunosuppressive treatment. This

response could be due to new innate and adaptive immune responses, or to preexisting immunity, as many humans demonstrate preexisting humoral immunity to several AAV serotypes. Immune cells of the myelomonocytic lineage, such as neutrophils, are innate cells that are among the first responders to infection and inflammation. Less is known about the immune response to non-viral delivery methodologies. In addition to responses targeted at the delivery vector, immune responses to the cargo are possible. As the Cas9 effectors most commonly used in gene-editing experiments are proteins derived from normal microbiome commensal bacteria (*e.g.*, *Streptococcus pyogenes, Staphylococcus aureus*), evidence of preexisting cellular and humoral immunity has been demonstrated in over half of human donor samples.[359] The presence of bacterial and viral proteins, such as ABE-deaminases and PE-RTs, could also trigger adaptive immune responses. The implications for human gene therapy from the immunological perspective are not entirely clear. It is anticipated that immune responses will be stronger against prolonged expression of Cas9 (*e.g.*, from AAV) compared with transient delivery (*e.g.*, from RNP or mRNA), though anti-CRISPR immune activity has not yet been conclusively demonstrated. Thus, thorough profiling of the relative immune responses to each delivery modality and cargo needs to be performed to establish safety profiles for each construct, as damaging inflammation could limit or preclude safe gene editing therapy.

7.5 Challenges of delivery and promising new technologies

The safe and efficient clinical application of CRISPR hinges on refined and novel non-viral delivery methods. Further development of non-viral technologies such as eVLPs, ENVLPE VLPs, and LNPs will continue to enable CRISPR translation. VLPs will require additional investment of quality control and assessment of biosafety, due to how they are produced in HEK293 lines. The low but non-zero risk of incorporation of cellular proteins and nucleic acids in VLPs needs to be carefully understood and mitigated. Other improvements in purification and minimization of aggregation will also go a long way to increase their use as a pharmacological grade therapy. For LNPs, further characterization of how LNPs enter the cell and perform endolysosomal escape, as

well as improvements in encapsulation and efficiency will help create better LNPs that deliver RNP or mRNA.

Most non-viral delivery methods easily target the RPE. This was demonstrated in this work in both LNP and VLP form. The more critical unmet need in this field is the efficient and reproducible transduction of rod and cone photoreceptors, as numerous IRDs that affect photoreceptors could benefit from gene editing technologies. The editing rates and delivery for the LNP and VLPs described in this work were moderate, as some resulted in photoreceptor delivery as assessed by Cre activity, but overall editing efficiencies were still low in comparison with AAV delivery. Barriers to photoreceptor delivery likely include competition with the RPE for particles, because the RPE is highly phagocytic and could require RPE intake saturation before significant photoreceptor delivery is observed. The nuclei and soma of the photoreceptors are also highly packed, and there could be a physical limitation in how many particles can reach the ONL. Further engineering and size minimization could decrease the particle size of LNPs and VLPs (>100 nm) to approximately the size of AAVs (~25 nm), which could be crucial to penetrate the tissue. Related efforts are already underway to engineer VLPs, and it could involve AI-designed capsids that enforce a smaller radius or more extreme curvature[253]. Similarly, interactions of LNPs and VLPs with components of the extracellular space could impeded free trafficking of these particles, and decoration or modulation of the surface of LNPs and VLPs with lipids, targeting proteins and peptides, or small molecules, could increase their tissue penetration and cell type specificity. Other novel delivery systems and editing strategies, such as bridge RNAs[98], mRNA VLPs[360], bacterial contractile injection syringes[361], and bacterial toxin-conjugated RNPs[362], could also show more tropism and bias toward photoreceptors, though these are less advanced and require further development; some of these systems cannot package their guide RNA, and some have not even been shown to work in mammalian cells yet. However, it is clear that the space of non-viral delivery has not yet been fully explored, and there could be different

delivery modalities employed, each of which could be more favorable for a different cell type or editing technology.

7.6 Further development of base and prime editors

In general, further development of base and prime editors will likely improve editing outcomes for these CRISPR 2.0 and 3.0 technologies. New base editors, including those that do not simply perform transition mutations, but that could be reprogrammed to perform transversions, could increase the applicability of base editors. Other deaminases could also prove to be useful, such as those with higher precision, or those which can target mitochondrial mutations[363,364]. The creation of bespoke deaminases, which could eliminate bystander effects, or be evolved to recognize specific sequence contexts, could also improve deaminases by bringing their editing product purities closer to those of PEs. This is similar to how reverse transcriptases and Cas9 are now being evolved to fit different editing needs[85,365].

Additional understanding of the mechanisms of PEs could increase their editing efficiency *in vivo*. For example, low intracellular dNTP concentrations were identified as a potential limiting factor for PE efficiency[366]. Additional, structurally guided studies on PE mechanisms could begin to address why pegRNA scaffold reverse transcription and incorporation happen and strategies that minimize this possibility[81,367]. Careful understanding of ABE and PE off-target effects, both Cas-dependent and Cas-independent, will increase confidence in their safety profile. Adaptation of genome-wide assays, such as the UDiTaS techniques, will allow for the investigation of rare but potentially serious off-target events[368]. Lastly, the engineering of PEs to further increase the efficiency of very large sequence insertions and rewriting could transform genetic medicine and enable large-scale genome engineering.

REFERENCES

1 Sanger, F. *et al.* Nucleotide sequence of bacteriophage phi X174 DNA. *Nature* **265**, 687-695 (1977). https://doi.org/10.1038/265687a0

2 Maxam, A. M. & Gilbert, W. A new method for sequencing DNA. *Proc Natl Acad Sci U S A* **74**, 560-564 (1977). https://doi.org/10.1073/pnas.74.2.560

3 Shendure, J. *et al.* DNA sequencing at 40: past, present and future. *Nature* **550**, 345-353 (2017). https://doi.org/10.1038/nature24286

4 Nurk, S. *et al.* The complete sequence of a human genome. *Science* **376**, 44-53 (2022). https://doi.org/10.1126/science.abj6987

5 Blaese, R. M. *et al.* T lymphocyte-directed gene therapy for ADA- SCID: initial trial results after 4 years. *Science* **270**, 475-480 (1995). https://doi.org/10.1126/science.270.5235.475

6 F, D. I. F., Micheli, G. & Camilloni, G. Restriction enzymes and their use in molecular biology: An overview. *J Biosci* **44** (2019).

7 Urnov, F. D., Rebar, E. J., Holmes, M. C., Zhang, H. S. & Gregory, P. D. Genome editing with engineered zinc finger nucleases. *Nature reviews. Genetics* **11**, 636-646 (2010). https://doi.org/10.1038/nrg2842

8 Durai, S. *et al.* Zinc finger nucleases: custom-designed molecular scissors for genome engineering of plant and mammalian cells. *Nucleic Acids Res* **33**, 5978-5990 (2005). https://doi.org/10.1093/nar/gki912

9 Isalan, M. Zinc-finger nucleases: how to play two good hands. *Nat Methods* **9**, 32-34 (2011). https://doi.org/10.1038/nmeth.1805

10 Shamshirgaran, Y., Liu, J., Sumer, H., Verma, P. J. & Taheri-Ghahfarokhi, A. Tools for Efficient Genome Editing; ZFN, TALEN, and CRISPR. *Methods Mol Biol* **2495**, 29-46 (2022). https://doi.org/10.1007/978-1-0716-2301-5_2

11 Ishino, Y., Shinagawa, H., Makino, K., Amemura, M. & Nakata, A. Nucleotide sequence of the iap gene, responsible for alkaline phosphatase isozyme conversion in Escherichia coli, and identification of the gene product. *J Bacteriol* **169**, 5429-5433 (1987). https://doi.org/10.1128/jb.169.12.5429-5433.1987

12 Barrangou, R. *et al.* CRISPR provides acquired resistance against viruses in prokaryotes. *Science* **315**, 1709-1712 (2007). https://doi.org/10.1126/science.1138140

13 Jinek, M. *et al.* A programmable dual-RNA-guided DNA endonuclease in adaptive bacterial immunity. *Science* **337**, 816-821 (2012). https://doi.org/10.1126/science.1225829

14 Cong, L. *et al.* Multiplex genome engineering using CRISPR/Cas systems. *Science* **339**, 819-823 (2013). https://doi.org/10.1126/science.1231143

15 Mali, P. *et al.* RNA-guided human genome engineering via Cas9. *Science* **339**, 823-826 (2013). https://doi.org/10.1126/science.1232033

16 Kurata, M. *et al.* Highly multiplexed genome engineering using CRISPR/Cas9 gRNA arrays. *PloS one* **13**, e0198714 (2018). https://doi.org/10.1371/journal.pone.0198714

17 Niu, D. *et al.* Inactivation of porcine endogenous retrovirus in pigs using CRISPR-Cas9. *Science* **357**, 1303-1307 (2017). https://doi.org/10.1126/science.aan4187

18 Wang, J. Y. & Doudna, J. A. CRISPR technology: A decade of genome editing is only the beginning. *Science* **379**, 251-+ (2023). https://doi.org/10.1126/science.add8643
19 Makarova, K. S. *et al.* Evolutionary classification of CRISPR-Cas systems: a burst of class 2 and derived variants. *Nature reviews. Microbiology* **18**, 67-83 (2020). https://doi.org/10.1038/s41579-019-0299-x
20 Wiegand, T., Karambelkar, S., Bondy-Denomy, J. & Wiedenheft, B. Structures and Strategies of Anti-CRISPR-Mediated Immune Suppression. *Annu Rev Microbiol* **74**, 21-37 (2020). https://doi.org/10.1146/annurev-micro-020518-120107
21 Jiang, F. & Doudna, J. A. CRISPR-Cas9 Structures and Mechanisms. *Annu Rev Biophys* **46**, 505-529 (2017). https://doi.org/10.1146/annurev-biophys-062215-010822
22 Degtev, D. *et al.* Engineered PsCas9 enables therapeutic genome editing in mouse liver with lipid nanoparticles. *Nat Commun* **15**, 9173 (2024). https://doi.org/10.1038/s41467-024-53418-8
23 Xu, X. *et al.* Engineered miniature CRISPR-Cas system for mammalian genome regulation and editing. *Mol Cell* **81**, 4333-4345 e4334 (2021). https://doi.org/10.1016/j.molcel.2021.08.008
24 Yoon, P. H. *et al.* Structure-guided discovery of ancestral CRISPR-Cas13 ribonucleases. *Science* **385**, 538-543 (2024). https://doi.org/10.1126/science.adq0553
25 Altae-Tran, H. *et al.* The widespread IS200/IS605 transposon family encodes diverse programmable RNA-guided endonucleases. *Science* **374**, 57-65 (2021). https://doi.org/10.1126/science.abj6856
26 Karvelis, T. *et al.* Transposon-associated TnpB is a programmable RNA-guided DNA endonuclease. *Nature* **599**, 692-696 (2021). https://doi.org/10.1038/s41586-021-04058-1
27 Li, Z. *et al.* Engineering a transposon-associated TnpB-omegaRNA system for efficient gene editing and phenotypic correction of a tyrosinaemia mouse model. *Nat Commun* **15**, 831 (2024). https://doi.org/10.1038/s41467-024-45197-z
28 Marquart, K. F. *et al.* Effective genome editing with an enhanced ISDra2 TnpB system and deep learning-predicted omegaRNAs. *Nat Methods* **21**, 2084-2093 (2024). https://doi.org/10.1038/s41592-024-02418-z
29 Xiang, G. *et al.* Evolutionary mining and functional characterization of TnpB nucleases identify efficient miniature genome editors. *Nat Biotechnol* **42**, 745-757 (2024). https://doi.org/10.1038/s41587-023-01857-x
30 Saito, M. *et al.* Fanzor is a eukaryotic programmable RNA-guided endonuclease. *Nature* **620**, 660-668 (2023). https://doi.org/10.1038/s41586-023-06356-2
31 Hu, J. H. *et al.* Evolved Cas9 variants with broad PAM compatibility and high DNA specificity. *Nature* **556**, 57-63 (2018). https://doi.org/10.1038/nature26155
32 Nishimasu, H. *et al.* Engineered CRISPR-Cas9 nuclease with expanded targeting space. *Science* **361**, 1259-1262 (2018). https://doi.org/10.1126/science.aas9129
33 Walton, R. T., Christie, K. A., Whittaker, M. N. & Kleinstiver, B. P. Unconstrained genome targeting with near-PAMless engineered CRISPR-Cas9 variants. *Science* **368**, 290-296 (2020). https://doi.org/10.1126/science.aba8853

34 Kleinstiver, B. P. *et al.* High-fidelity CRISPR-Cas9 nucleases with no detectable genome-wide off-target effects. *Nature* **529**, 490-495 (2016). https://doi.org/10.1038/nature16526
35 Vakulskas, C. A. *et al.* A high-fidelity Cas9 mutant delivered as a ribonucleoprotein complex enables efficient gene editing in human hematopoietic stem and progenitor cells. *Nat Med* **24**, 1216-1224 (2018). https://doi.org/10.1038/s41591-018-0137-0
36 Miller, S. M. *et al.* Continuous evolution of SpCas9 variants compatible with non-G PAMs. *Nat Biotechnol* **38**, 471-481 (2020). https://doi.org/10.1038/s41587-020-0412-8
37 Newby, G. A. *et al.* Base editing of haematopoietic stem cells rescues sickle cell disease in mice. *Nature* **595**, 295-302 (2021). https://doi.org/10.1038/s41586-021-03609-w
38 Alves, C. R. R. *et al.* Optimization of base editors for the functional correction of SMN2 as a treatment for spinal muscular atrophy. *Nat Biomed Eng* **8**, 118-131 (2024). https://doi.org/10.1038/s41551-023-01132-z
39 Segurado, O. G., Jiang, R. & Pipe, S. W. Challenges and opportunities when transitioning from in vivo gene replacement to in vivo CRISPR/Cas9 therapies – a spotlight on hemophilia. *Expert Opinion on Biological Therapy* **22**, 1091-1098 (2022). https://doi.org/10.1080/14712598.2022.2090241
40 Doudna, J. A. & Charpentier, E. The new frontier of genome engineering with CRISPR-Cas9. *Science* **346** (2014). https://doi.org/10.1126/science.1258096
41 Hsu, Patrick D., Lander, Eric S. & Zhang, F. Development and Applications of CRISPR-Cas9 for Genome Engineering. *Cell* **157**, 1262-1278 (2014). https://doi.org/10.1016/j.cell.2014.05.010
42 Sander, J. D. & Joung, J. K. CRISPR-Cas systems for editing, regulating and targeting genomes. *Nature Biotechnology* **32**, 347-355 (2014). https://doi.org/10.1038/nbt.2842
43 Hustedt, N. & Durocher, D. The control of DNA repair by the cell cycle. *Nature Cell Biology* **19**, 1-9 (2017). https://doi.org/10.1038/ncb3452
44 Bassuk, A. G., Zheng, A., Li, Y., Tsang, S. H. & Mahajan, V. B. Precision Medicine: Genetic Repair of Retinitis Pigmentosa in Patient-Derived Stem Cells. *Scientific Reports* **6**, 19969-19969 (2016). https://doi.org/10.1038/srep19969
45 Bohrer, L. *et al.* Correction of NR2E3 Associated Enhanced S-cone Syndrome Patient-specific iPSCs using CRISPR-Cas9. *Genes* **10**, 278-278 (2019). https://doi.org/10.3390/genes10040278
46 Cai, Y. *et al.* In vivo genome editing rescues photoreceptor degeneration via a Cas9/RecA-mediated homology-directed repair pathway. *Science Advances* **5** (2019). https://doi.org/10.1126/sciadv.aav3335
47 Greenwald, D. L., Cashman, S. M. & Kumar-Singh, R. Engineered Zinc Finger Nuclease–Mediated Homologous Recombination of the Human Rhodopsin Gene. *Investigative Opthalmology & Visual Science* **51**, 6374-6374 (2010). https://doi.org/10.1167/iovs.10-5781

48 Jo, D. H. *et al.* CRISPR-Cas9–mediated therapeutic editing of Rpe65 ameliorates the disease phenotypes in a mouse model of Leber congenital amaurosis. *Science Advances* **5** (2019). https://doi.org/10.1126/sciadv.aax1210
49 Overlack, N., Goldmann, T., Wolfrum, U. & Nagel-Wolfrum, K. Gene Repair of an Usher Syndrome Causing Mutation by Zinc-Finger Nuclease Mediated Homologous Recombination. *Investigative Opthalmology & Visual Science* **53**, 4140-4140 (2012). https://doi.org/10.1167/iovs.12-9812
50 Vagni, P. *et al.* Gene Editing Preserves Visual Functions in a Mouse Model of Retinal Degeneration. *Frontiers in Neuroscience* **13** (2019). https://doi.org/10.3389/fnins.2019.00945
51 Yanik, M. *et al.* In vivo genome editing as a potential treatment strategy for inherited retinal dystrophies. *Progress in Retinal and Eye Research* **56**, 1-18 (2017). https://doi.org/10.1016/j.preteyeres.2016.09.001
52 Cox, D. B. T., Platt, R. J. & Zhang, F. Therapeutic genome editing: prospects and challenges. *Nature Medicine* **21**, 121-131 (2015). https://doi.org/10.1038/nm.3793
53 Suzuki, K. *et al.* In vivo genome editing via CRISPR/Cas9 mediated homology-independent targeted integration. *Nature* **540**, 144-149 (2016). https://doi.org/10.1038/nature20565
54 McVey, M. & Lee, S. E. MMEJ repair of double-strand breaks (director's cut): deleted sequences and alternative endings. *Trends in Genetics* **24**, 529-538 (2008). https://doi.org/https://doi.org/10.1016/j.tig.2008.08.007
55 Sakuma, T., Nakade, S., Sakane, Y., Suzuki, K.-I. T. & Yamamoto, T. MMEJ-assisted gene knock-in using TALENs and CRISPR-Cas9 with the PITCh systems. *Nature Protocols* **11**, 118-133 (2016). https://doi.org/10.1038/nprot.2015.140
56 Bakondi, B. *et al.* In Vivo CRISPR/Cas9 Gene Editing Corrects Retinal Dystrophy in the S334ter-3 Rat Model of Autosomal Dominant Retinitis Pigmentosa. *Molecular Therapy* **24**, 556-563 (2016). https://doi.org/10.1038/mt.2015.220
57 Li, P. *et al.* Allele-Specific CRISPR-Cas9 Genome Editing of the Single-Base P23H Mutation for Rhodopsin-Associated Dominant Retinitis Pigmentosa. *The CRISPR Journal* **1**, 55-64 (2018). https://doi.org/10.1089/crispr.2017.0009
58 Tsai, Y.-T. *et al.* Clustered Regularly Interspaced Short Palindromic Repeats-Based Genome Surgery for the Treatment of Autosomal Dominant Retinitis Pigmentosa. *Ophthalmology* **125**, 1421-1430 (2018). https://doi.org/10.1016/j.ophtha.2018.04.001
59 Maeder, M. L. *et al.* 687. Therapeutic Correction of an LCA-Causing Splice Defect in the CEP290 Gene by CRISPR/Cas-Mediated Genome Editing. *Molecular Therapy* **23**, S273-S274 (2015). https://doi.org/10.1016/S1525-0016(16)34296-4
60 Maeder, M. L. *et al.* Development of a gene-editing approach to restore vision loss in Leber congenital amaurosis type 10. *Nature Medicine* **25**, 229-233 (2019). https://doi.org/10.1038/s41591-018-0327-9
61 Komor, A. C., Kim, Y. B., Packer, M. S., Zuris, J. A. & Liu, D. R. Programmable editing of a target base in genomic DNA without double-stranded DNA cleavage. *Nature* **533**, 420-424 (2016). https://doi.org/10.1038/nature17946

62 Nishida, K. *et al.* Targeted nucleotide editing using hybrid prokaryotic and vertebrate adaptive immune systems. *Science* **353** (2016). https://doi.org/10.1126/science.aaf8729
63 Gaudelli, N. M. *et al.* Programmable base editing of A•T to G•C in genomic DNA without DNA cleavage. *Nature* **551**, 464-471 (2017). https://doi.org/10.1038/nature24644
64 Koblan, L. W. *et al.* Improving cytidine and adenine base editors by expression optimization and ancestral reconstruction. *Nat Biotechnol* **36**, 843-846 (2018). https://doi.org/10.1038/nbt.4172
65 Richter, M. F. *et al.* Phage-assisted evolution of an adenine base editor with improved Cas domain compatibility and activity. *Nat Biotechnol* **38**, 883-891 (2020). https://doi.org/10.1038/s41587-020-0453-z
66 Lapinaite, A. *et al.* DNA capture by a CRISPR-Cas9-guided adenine base editor. *Science* **369**, 566-571 (2020). https://doi.org/10.1126/science.abb1390
67 Arantes, P. R. *et al.* Dimerization of the deaminase domain and locking interactions with Cas9 boost base editing efficiency in ABE8e. *Nucleic Acids Res* **52**, 13931-13944 (2024). https://doi.org/10.1093/nar/gkae1066
68 Neugebauer, M. E. *et al.* Evolution of an adenine base editor into a small, efficient cytosine base editor with low off-target activity. *Nat Biotechnol* **41**, 673-685 (2023). https://doi.org/10.1038/s41587-022-01533-6
69 Anzalone, A. V., Koblan, L. W. & Liu, D. R. Genome editing with CRISPR–Cas nucleases, base editors, transposases and prime editors. *Nature Biotechnology* **38**, 824-844 (2020). https://doi.org/10.1038/s41587-020-0561-9
70 Kurt, I. C. *et al.* CRISPR C-to-G base editors for inducing targeted DNA transversions in human cells. *Nature Biotechnology* **39**, 41-46 (2021). https://doi.org/10.1038/s41587-020-0609-x
71 Zhao, D. *et al.* Glycosylase base editors enable C-to-A and C-to-G base changes. *Nature Biotechnology* **39**, 35-40 (2021). https://doi.org/10.1038/s41587-020-0592-2
72 Stone, E. M. *et al.* Clinically Focused Molecular Investigation of 1000 Consecutive Families with Inherited Retinal Disease. *Ophthalmology* **124**, 1314-1331 (2017). https://doi.org/10.1016/j.ophtha.2017.04.008
73 Jacobson, S. G. *et al.* Improvement and Decline in Vision with Gene Therapy in Childhood Blindness. *New England Journal of Medicine* **372**, 1920-1926 (2015). https://doi.org/10.1056/NEJMoa1412965
74 Xiong, W. *et al.* AAV cis -regulatory sequences are correlated with ocular toxicity. *Proceedings of the National Academy of Sciences* **116**, 5785-5794 (2019). https://doi.org/10.1073/pnas.1821000116
75 Suh, S. *et al.* Restoration of visual function in adult mice with an inherited retinal disease via adenine base editing. *Nature Biomedical Engineering* **5**, 169-178 (2021). https://doi.org/10.1038/s41551-020-00632-6
76 Choi, E. H. *et al.* In vivo base editing rescues cone photoreceptors in a mouse model of early-onset inherited retinal degeneration. *Nature Communications* **13**, 1830 (2022). https://doi.org/10.1038/s41467-022-29490-3
77 Cideciyan, A. V. *et al.* Human retinal gene therapy for Leber congenital amaurosis shows advancing retinal degeneration despite enduring visual

improvement. *Proceedings of the National Academy of Sciences* **110** (2013). https://doi.org/10.1073/pnas.1218933110

78 Bainbridge, J. W. B. *et al.* Long-Term Effect of Gene Therapy on Leber's Congenital Amaurosis. *New England Journal of Medicine* **372**, 1887-1897 (2015). https://doi.org/10.1056/NEJMoa1414221

79 Jang, H.-K. *et al.* High-purity production and precise editing of DNA base editing ribonucleoproteins. *Science Advances* **7**, eabg2661 (2021). https://doi.org/doi:10.1126/sciadv.abg2661

80 Suh, S. *et al.* Restoration of visual function in adult mice with an inherited retinal disease via adenine base editing. *Nat Biomed Eng* **5**, 169-178 (2021). https://doi.org/10.1038/s41551-020-00632-6

81 Anzalone, A. V. *et al.* Search-and-replace genome editing without double-strand breaks or donor DNA. *Nature* **576**, 149-157 (2019). https://doi.org/10.1038/s41586-019-1711-4

82 Hussmann, J. A. *et al.* Mapping the genetic landscape of DNA double-strand break repair. *Cell* **184**, 5653-5669 e5625 (2021). https://doi.org/10.1016/j.cell.2021.10.002

83 Chen, P. J. *et al.* Enhanced prime editing systems by manipulating cellular determinants of editing outcomes. *Cell* **184**, 5635-5652 e5629 (2021). https://doi.org/10.1016/j.cell.2021.09.018

84 Nelson, J. W. *et al.* Engineered pegRNAs improve prime editing efficiency. *Nat Biotechnol* **40**, 402-410 (2022). https://doi.org/10.1038/s41587-021-01039-7

85 Doman, J. L. *et al.* Phage-assisted evolution and protein engineering yield compact, efficient prime editors. *Cell* **186**, 3983-4002 e3926 (2023). https://doi.org/10.1016/j.cell.2023.07.039

86 Yan, J. *et al.* Improving prime editing with an endogenous small RNA-binding protein. *Nature* **628**, 639-647 (2024). https://doi.org/10.1038/s41586-024-07259-6

87 Truong, D. J. *et al.* Exonuclease-enhanced prime editors. *Nat Methods* **21**, 455-464 (2024). https://doi.org/10.1038/s41592-023-02162-w

88 Davis, J. R. *et al.* Efficient prime editing in mouse brain, liver and heart with dual AAVs. *Nat Biotechnol* **42**, 253-264 (2024). https://doi.org/10.1038/s41587-023-01758-z

89 Jang, H. *et al.* Application of prime editing to the correction of mutations and phenotypes in adult mice with liver and eye diseases. *Nature Biomedical Engineering* **6**, 181-194 (2022). https://doi.org/10.1038/s41551-021-00788-9

90 Anzalone, A. V. *et al.* Programmable deletion, replacement, integration and inversion of large DNA sequences with twin prime editing. *Nat Biotechnol* **40**, 731-740 (2022). https://doi.org/10.1038/s41587-021-01133-w

91 Lin, Q. *et al.* High-efficiency prime editing with optimized, paired pegRNAs in plants. *Nat Biotechnol* **39**, 923-927 (2021). https://doi.org/10.1038/s41587-021-00868-w

92 Jiang, T., Zhang, X. O., Weng, Z. & Xue, W. Deletion and replacement of long genomic sequences using prime editing. *Nat Biotechnol* **40**, 227-234 (2022). https://doi.org/10.1038/s41587-021-01026-y

93 Fell, C. W., Schmitt-Ulms, C., Tagliaferri, D. V., Gootenberg, J. S. & Abudayyeh, O. O. Precise kilobase-scale genomic insertions in mammalian cells using PASTE. *Nat Protoc* (2024). https://doi.org/10.1038/s41596-024-01090-z
94 Pandey, S. *et al.* Efficient site-specific integration of large genes in mammalian cells via continuously evolved recombinases and prime editing. *Nat Biomed Eng* (2024). https://doi.org/10.1038/s41551-024-01227-1
95 Strecker, J. *et al.* RNA-guided DNA insertion with CRISPR-associated transposases. *Science* **365**, 48-53 (2019). https://doi.org/10.1126/science.aax9181
96 Klompe, S. E., Vo, P. L. H., Halpin-Healy, T. S. & Sternberg, S. H. Transposon-encoded CRISPR-Cas systems direct RNA-guided DNA integration. *Nature* **571**, 219-225 (2019). https://doi.org/10.1038/s41586-019-1323-z
97 Ferreira da Silva, J. *et al.* Click editing enables programmable genome writing using DNA polymerases and HUH endonucleases. *Nat Biotechnol* (2024). https://doi.org/10.1038/s41587-024-02324-x
98 Durrant, M. G. *et al.* Bridge RNAs direct programmable recombination of target and donor DNA. *Nature* **630**, 984-993 (2024). https://doi.org/10.1038/s41586-024-07552-4
99 Hiraizumi, M. *et al.* Structural mechanism of bridge RNA-guided recombination. *Nature* **630**, 994-1002 (2024). https://doi.org/10.1038/s41586-024-07570-2
100 Hohman, T. C. Hereditary retinal dystrophy. *Handbook of Experimental Pharmacology* **242**, 337-367 (2017). https://doi.org/10.1007/164_2016_91/TABLES/1
101 Travis, G. H., Golczak, M., Moise, A. R. & Palczewski, K. Diseases caused by defects in the visual cycle: retinoids as potential therapeutic agents. *Annu Rev Pharmacol Toxicol* **47**, 469-512 (2007). https://doi.org/10.1146/annurev.pharmtox.47.120505.105225
102 Palczewski, K. & Kiser, P. D. Shedding new light on the generation of the visual chromophore. *Proc Natl Acad Sci U S A* **117**, 19629-19638 (2020). https://doi.org/10.1073/pnas.2008211117
103 Cremers, F., Boon, C., Bujakowska, K. & Zeitz, C. Special Issue Introduction: Inherited Retinal Disease: Novel Candidate Genes, Genotype–Phenotype Correlations, and Inheritance Models. *Genes* **9**, 215-215 (2018). https://doi.org/10.3390/genes9040215
104 Sahel, J. A., Marazova, K. & Audo, I. Clinical Characteristics and Current Therapies for Inherited Retinal Degenerations. *Cold Spring Harbor Perspectives in Medicine* **5**, a017111-a017111 (2015). https://doi.org/10.1101/cshperspect.a017111
105 Suh, S., Choi, E. H., Raguram, A., Liu, D. R. & Palczewski, K. Precision genome editing in the eye. *Proc Natl Acad Sci U S A* **119**, e2210104119 (2022). https://doi.org/10.1073/pnas.2210104119
106 Benati, D., Patrizi, C. & Recchia, A. Gene editing prospects for treating inherited retinal diseases. *Journal of Medical Genetics* **57**, 437-437 (2020). https://doi.org/10.1136/jmedgenet-2019-106473

107 Georgiou, M., Fujinami, K. & Michaelides, M. Inherited retinal diseases: Therapeutics, clinical trials and end points—A review. *Clinical & Experimental Ophthalmology* **49**, 270-288 (2021). https://doi.org/10.1111/ceo.13917
108 Frangoul, H. *et al.* CRISPR-Cas9 Gene Editing for Sickle Cell Disease and β-Thalassemia. *New England Journal of Medicine* **384**, 252-260 (2021). https://doi.org/10.1056/NEJMoa2031054
109 Gillmore, J. D. *et al.* CRISPR-Cas9 In Vivo Gene Editing for Transthyretin Amyloidosis. *New England Journal of Medicine* **385**, 493-502 (2021). https://doi.org/10.1056/NEJMoa2107454
110 Ou, X., Ma, Q., Yin, W., Ma, X. & He, Z. CRISPR/Cas9 Gene-Editing in Cancer Immunotherapy: Promoting the Present Revolution in Cancer Therapy and Exploring More. *Frontiers in Cell and Developmental Biology* **9** (2021). https://doi.org/10.3389/fcell.2021.674467
111 Russell, S. *et al.* Efficacy and safety of voretigene neparvovec (AAV2-hRPE65v2) in patients with RPE65 -mediated inherited retinal dystrophy: a randomised, controlled, open-label, phase 3 trial. *The Lancet* **390**, 849-860 (2017). https://doi.org/10.1016/S0140-6736(17)31868-8
112 Nuzbrokh, Y., Ragi, S. D. & Tsang, S. H. Gene therapy for inherited retinal diseases. *Annals of Translational Medicine* **9**, 1278-1278 (2021). https://doi.org/10.21037/atm-20-4726
113 Greig, J. A. *et al.* Loss of transgene expression limits liver gene therapy in primates. *bioRxiv*, 2022.2003.2024.485675 (2022). https://doi.org/10.1101/2022.03.24.485675
114 Surace, E. M. & Auricchio, A. Versatility of AAV vectors for retinal gene transfer. *Vision Research* **48**, 353-359 (2008). https://doi.org/10.1016/j.visres.2007.07.027
115 ClinicalTrials.gov. Identifier NCT02416622, Safety and Efficacy of rAAV-hRS1 in Patients With X-linked Retinoschisis (XLRS). (Bethesda, MD, 2015).
116 Cukras, C. *et al.* Retinal AAV8-RS1 Gene Therapy for X-Linked Retinoschisis: Initial Findings from a Phase I/IIa Trial by Intravitreal Delivery. *Molecular Therapy* **26**, 2282-2294 (2018). https://doi.org/10.1016/j.ymthe.2018.05.025
117 Ladha, R., Caspers, L. E., Willermain, F. & de Smet, M. D. Subretinal Therapy: Technological Solutions to Surgical and Immunological Challenges. *Frontiers in Medicine* **9** (2022). https://doi.org/10.3389/fmed.2022.846782
118 Gao, J., Hussain, R. M. & Weng, C. Y. Voretigene Neparvovec in Retinal Diseases: A Review of the Current Clinical Evidence . *Clinical Ophthalmology* **Volume 14**, 3855-3869 (2020). https://doi.org/10.2147/OPTH.S231804
119 Znoiko, S. L., Crouch, R. K., Moiseyev, G. & Ma, J.-x. Identification of the RPE65 Protein in Mammalian Cone Photoreceptors. *Investigative Ophthalmology & Visual Science* **43**, 1604-1609 (2002).
120 Parker, M. A. *et al.* Three-Year Safety Results of SAR422459 (EIAV-ABCA4) Gene Therapy in Patients With ABCA4-Associated Stargardt Disease: An Open-Label Dose-Escalation Phase I/IIa Clinical Trial, Cohorts 1-5. *American Journal of Ophthalmology* **240**, 285-301 (2022). https://doi.org/10.1016/j.ajo.2022.02.013
121 Arsenijevic, Y., Berger, A., Udry, F. & Kostic, C. Lentiviral Vectors for Ocular Gene Therapy. *Pharmaceutics* **14** (2022). https://doi.org/10.3390/pharmaceutics14081605

122 Chung, D. C. *et al.* Long-term Effect of Voretigene Neparvovec on the Full-Field Light Sensitivity Threshold Test of Patients with RPE65 Mutation-Associated Inherited Retinal Dystrophy – Post Hoc Analysis of Phase I trial data. *Investigative Ophthalmology & Visual Science* **60**, 3398-3398 (2019).
123 Maguire, A. M. *et al.* Durability of Voretigene Neparvovec for Biallelic RPE65-Mediated Inherited Retinal Disease. *Ophthalmology* **128**, 1460-1468 (2021). https://doi.org/10.1016/j.ophtha.2021.03.031
124 Kenjo, E. *et al.* Low immunogenicity of LNP allows repeated administrations of CRISPR-Cas9 mRNA into skeletal muscle in mice. *Nat Commun* **12**, 7101 (2021). https://doi.org/10.1038/s41467-021-26714-w
125 Han, J. P. *et al.* In vivo delivery of CRISPR-Cas9 using lipid nanoparticles enables antithrombin gene editing for sustainable hemophilia A and B therapy. *Science Advances* **8**, eabj6901 https://doi.org/10.1126/sciadv.abj6901
126 Qiu, M. *et al.* Lipid nanoparticle-mediated codelivery of Cas9 mRNA and single-guide RNA achieves liver-specific in vivo genome editing of Angptl3. *Proceedings of the National Academy of Sciences* **118**, e2020401118 (2021). https://doi.org/10.1073/pnas.2020401118
127 Finn, J. D. *et al.* A Single Administration of CRISPR/Cas9 Lipid Nanoparticles Achieves Robust and Persistent In Vivo Genome Editing. *Cell Reports* **22**, 2227-2235 (2018). https://doi.org/10.1016/j.celrep.2018.02.014
128 Rothgangl, T. *et al.* In vivo adenine base editing of PCSK9 in macaques reduces LDL cholesterol levels. *Nature Biotechnology* **39**, 949-957 (2021). https://doi.org/10.1038/s41587-021-00933-4
129 Musunuru, K. *et al.* In vivo CRISPR base editing of PCSK9 durably lowers cholesterol in primates. *Nature* **593**, 429-434 (2021). https://doi.org/10.1038/s41586-021-03534-y
130 Zuris, J. A. *et al.* Cationic lipid-mediated delivery of proteins enables efficient protein-based genome editing in vitro and in vivo. *Nat Biotechnol* **33**, 73-80 (2015). https://doi.org/10.1038/nbt.3081
131 Kim, K. *et al.* Genome surgery using Cas9 ribonucleoproteins for the treatment of age-related macular degeneration. *Genome Research* **27**, 419-426 (2017). https://doi.org/10.1101/gr.219089.116
132 de Cogan, F. *et al.* Topical Delivery of Anti-VEGF Drugs to the Ocular Posterior Segment Using Cell-Penetrating Peptides. *Investigative Ophthalmology & Visual Science* **58**, 2578-2590 (2017). https://doi.org/10.1167/iovs.16-20072
133 Johnson, L. N., Cashman, S. M. & Kumar-Singh, R. Cell-penetrating peptide for enhanced delivery of nucleic acids and drugs to ocular tissues including retina and cornea. *Mol Ther* **16**, 107-114 (2008). https://doi.org/10.1038/sj.mt.6300324
134 Pescina, S. *et al.* Cell penetrating peptides in ocular drug delivery: State of the art. *Journal of Controlled Release* **284**, 84-102 (2018). https://doi.org/https://doi.org/10.1016/j.jconrel.2018.06.023
135 LeCher, J. C., Nowak, S. J. & McMurry, J. L. Breaking in and busting out: cell-penetrating peptides and the endosomal escape problem. **8**, 131-141 (2017). https://doi.org/doi:10.1515/bmc-2017-0023
136 Del'Guidice, T. *et al.* Membrane permeabilizing amphiphilic peptide delivers recombinant transcription factor and CRISPR-Cas9/Cpf1 ribonucleoproteins in

hard-to-modify cells. *PLOS ONE* **13**, e0195558 (2018). https://doi.org/10.1371/journal.pone.0195558
137 Kim, Y. G., Cha, J. & Chandrasegaran, S. Hybrid restriction enzymes: zinc finger fusions to Fok I cleavage domain. *Proc Natl Acad Sci U S A* **93**, 1156-1160 (1996). https://doi.org/10.1073/pnas.93.3.1156
138 Boch, J. *et al.* Breaking the code of DNA binding specificity of TAL-type III effectors. *Science* **326**, 1509-1512 (2009). https://doi.org/10.1126/science.1178811
139 Gaudelli, N. M. *et al.* Programmable base editing of A*T to G*C in genomic DNA without DNA cleavage. *Nature* **551**, 464-471 (2017). https://doi.org/10.1038/nature24644
140 Du, S. W. *et al.* In vivo photoreceptor base editing ameliorates rhodopsin-E150K autosomal-recessive retinitis pigmentosa in mice. *Proc Natl Acad Sci U S A* **121**, e2416827121 (2024). https://doi.org/10.1073/pnas.2416827121
141 Gulati, S. & Palczewski, K. Structural view of G protein-coupled receptor signaling in the retinal rod outer segment. *Trends Biochem Sci* **48**, 172-186 (2023). https://doi.org/10.1016/j.tibs.2022.08.010
142 Palczewski, K. *et al.* Crystal structure of rhodopsin: A G protein-coupled receptor. *Science* **289**, 739-745 (2000). https://doi.org/10.1126/science.289.5480.739
143 Ripps, H. The color purple: milestones in photochemistry. *FASEB J* **22**, 4038-4043 (2008). https://doi.org/10.1096/fj.08-1202ufm
144 Böll, F. Zur Anatomie und Physiologie der Retina. *Monatsber. Akad. Wiss, Berlin* pp. 783-788 (1876).
145 Hong, J. D. & Palczewski, K. A short story on how chromophore is hydrolyzed from rhodopsin for recycling. *Bioessays* **45**, e2300068 (2023). https://doi.org/10.1002/bies.202300068
146 Palczewski, K. G protein-coupled receptor rhodopsin. *Annu Rev Biochem* **75**, 743-767 (2006). https://doi.org/10.1146/annurev.biochem.75.103004.142743
147 Calvert, P. D., Strissel, K. J., Schiesser, W. E., Pugh, E. N., Jr. & Arshavsky, V. Y. Light-driven translocation of signaling proteins in vertebrate photoreceptors. *Trends Cell Biol* **16**, 560-568 (2006). https://doi.org/10.1016/j.tcb.2006.09.001
148 Pearring, J. N., Salinas, R. Y., Baker, S. A. & Arshavsky, V. Y. Protein sorting, targeting and trafficking in photoreceptor cells. *Prog Retin Eye Res* **36**, 24-51 (2013). https://doi.org/10.1016/j.preteyeres.2013.03.002
149 Skiba, N. P. *et al.* Absolute Quantification of Photoreceptor Outer Segment Proteins. *J Proteome Res* **22**, 2703-2713 (2023). https://doi.org/10.1021/acs.jproteome.3c00267
150 Filipek, S., Stenkamp, R. E., Teller, D. C. & Palczewski, K. G protein-coupled receptor rhodopsin: a prospectus. *Annu Rev Physiol* **65**, 851-879 (2003). https://doi.org/10.1146/annurev.physiol.65.092101.142611
151 Liang, Y. *et al.* Rhodopsin signaling and organization in heterozygote rhodopsin knockout mice. *J Biol Chem* **279**, 48189-48196 (2004). https://doi.org/10.1074/jbc.M408362200
152 Fotiadis, D. *et al.* Atomic-force microscopy: Rhodopsin dimers in native disc membranes. *Nature* **421**, 127-128 (2003). https://doi.org/10.1038/421127a

153 Gunkel, M. *et al.* Higher-order architecture of rhodopsin in intact photoreceptors and its implication for phototransduction kinetics. *Structure* **23**, 628-638 (2015). https://doi.org/10.1016/j.str.2015.01.015
154 Suda, K., Filipek, S., Palczewski, K., Engel, A. & Fotiadis, D. The supramolecular structure of the GPCR rhodopsin in solution and native disc membranes. *Mol Membr Biol* **21**, 435-446 (2004). https://doi.org/10.1080/09687860400020291
155 Kevany, B. M. & Palczewski, K. Phagocytosis of retinal rod and cone photoreceptors. *Physiology (Bethesda)* **25**, 8-15 (2010). https://doi.org/10.1152/physiol.00038.2009
156 Young, R. W. The renewal of photoreceptor cell outer segments. *J Cell Biol* **33**, 61-72 (1967). https://doi.org/10.1083/jcb.33.1.61
157 Young, R. W. The renewal of rod and cone outer segments in the rhesus monkey. *J Cell Biol* **49**, 303-318 (1971). https://doi.org/10.1083/jcb.49.2.303
158 Dryja, T. P. *et al.* A point mutation of the rhodopsin gene in one form of retinitis pigmentosa. *Nature* **343**, 364-366 (1990). https://doi.org/10.1038/343364a0
159 Sullivan, L. S. *et al.* Prevalence of disease-causing mutations in families with autosomal dominant retinitis pigmentosa: a screen of known genes in 200 families. *Invest Ophthalmol Vis Sci* **47**, 3052-3064 (2006). https://doi.org/10.1167/iovs.05-1443
160 Leenders, M., Gaastra, M., Jayagopal, A. & Malone, K. E. Prevalence estimates and genetic diversity for autosomal dominant retinitis pigmentosa due to RHO, c.68C>A (p.P23H) variant. *Am J Ophthalmol* (2024). https://doi.org/10.1016/j.ajo.2024.08.038
161 Athanasiou, D. *et al.* The molecular and cellular basis of rhodopsin retinitis pigmentosa reveals potential strategies for therapy. *Prog Retin Eye Res* **62**, 1-23 (2018). https://doi.org/10.1016/j.preteyeres.2017.10.002
162 Yan, A. L., Du, S. W. & Palczewski, K. Genome editing, a superior therapy for inherited retinal diseases. *Vision Res* **206**, 108192 (2023). https://doi.org/10.1016/j.visres.2023.108192
163 Liu, C.-H. *et al.* A Mutation-Independent CRISPR/Cas9-based 'Knockout and Replace' Strategy to Treat Rhodopsin-Associated Autosomal Dominant Retinitis Pigmentosa. *Invest Ophth Vis Sci* **63**, 3474-3474 (2022).
164 Cideciyan, A. V. *et al.* Mutation-independent rhodopsin gene therapy by knockdown and replacement with a single AAV vector. *Proc Natl Acad Sci U S A* **115**, E8547-E8556 (2018). https://doi.org/10.1073/pnas.1805055115
165 Wu, W. H. *et al.* CRISPR genome surgery in a novel humanized model for autosomal dominant retinitis pigmentosa. *Mol Ther* **30**, 1407-1420 (2022). https://doi.org/10.1016/j.ymthe.2022.02.010
166 Li, P. *et al.* Allele-Specific CRISPR-Cas9 Genome Editing of the Single-Base P23H Mutation for Rhodopsin-Associated Dominant Retinitis Pigmentosa. *CRISPR J* **1**, 55-64 (2018). https://doi.org/10.1089/crispr.2017.0009
167 Chen, P. J. & Liu, D. R. Prime editing for precise and highly versatile genome manipulation. *Nat Rev Genet* **24**, 161-177 (2023). https://doi.org/10.1038/s41576-022-00541-1

168 Hanlon, K. S. *et al.* High levels of AAV vector integration into CRISPR-induced DNA breaks. *Nat Commun* **10**, 4439 (2019). https://doi.org/10.1038/s41467-019-12449-2
169 Suchy, F. P. *et al.* Genome engineering with Cas9 and AAV repair templates generates frequent concatemeric insertions of viral vectors. *Nat Biotechnol* (2024). https://doi.org/10.1038/s41587-024-02171-w
170 Simpson, B. P., Yrigollen, C. M., Izda, A. & Davidson, B. L. Targeted long-read sequencing captures CRISPR editing and AAV integration outcomes in brain. *Mol Ther* **31**, 760-773 (2023). https://doi.org/10.1016/j.ymthe.2023.01.004
171 Choi, E. H. *et al.* In vivo base editing rescues cone photoreceptors in a mouse model of early-onset inherited retinal degeneration. *Nat Commun* **13**, 1830 (2022). https://doi.org/10.1038/s41467-022-29490-3
172 Jo, D. H. *et al.* Visual function restoration in a mouse model of Leber congenital amaurosis via therapeutic base editing. *Molecular therapy. Nucleic acids* **31**, 16-27 (2023). https://doi.org/10.1016/j.omtn.2022.11.021
173 Liu, Z. *et al.* Efficient Rescue of Retinal Degeneration in Pde6a Mice by Engineered Base Editing and Prime Editing. *Adv Sci (Weinh)* **11**, e2405628 (2024). https://doi.org/10.1002/advs.202405628
174 Su, J. *et al.* In vivo base editing rescues photoreceptors in a mouse model of retinitis pigmentosa. *Molecular therapy. Nucleic acids* **31**, 596-609 (2023). https://doi.org/10.1016/j.omtn.2023.02.011
175 Wu, Y. *et al.* AAV-mediated base-editing therapy ameliorates the disease phenotypes in a mouse model of retinitis pigmentosa. *Nat Commun* **14**, 4923 (2023). https://doi.org/10.1038/s41467-023-40655-6
176 Muller, A. *et al.* High-efficiency base editing in the retina in primates and human tissues. *Nat Med* (2025). https://doi.org/10.1038/s41591-024-03422-8
177 Jang, H. K. *et al.* High-purity production and precise editing of DNA base editing ribonucleoproteins. *Sci Adv* **7** (2021). https://doi.org/10.1126/sciadv.abg2661
178 Pulman, J. *et al.* Direct delivery of Cas9 or base editor protein and guide RNA complex enables genome editing in the retina. *Molecular therapy. Nucleic acids* **35**, 102349 (2024). https://doi.org/10.1016/j.omtn.2024.102349
179 Holubowicz, R. *et al.* Safer and efficient base editing and prime editing via ribonucleoproteins delivered through optimized lipid-nanoparticle formulations. *Nat Biomed Eng* (2024). https://doi.org/10.1038/s41551-024-01296-2
180 Kabra, M. *et al.* Nonviral base editing of KCNJ13 mutation preserves vision in a model of inherited retinal channelopathy. *J Clin Invest* **133** (2023). https://doi.org/10.1172/JCI171356
181 Zhang, N. *et al.* Autosomal recessive retinitis pigmentosa E150K opsin mice exhibit photoreceptor disorganization. *J Clin Invest* **123**, 121-137 (2013). https://doi.org/10.1172/JCI66176
182 Kumaramanickavel, G. *et al.* Missense rhodopsin mutation in a family with recessive RP. *Nat Genet* **8**, 10-11 (1994). https://doi.org/10.1038/ng0994-10
183 Azam, M. *et al.* A homozygous p.Glu150Lys mutation in the opsin gene of two Pakistani families with autosomal recessive retinitis pigmentosa. *Mol Vis* **15**, 2526-2534 (2009).

184 Saqib, M. A. *et al.* Homozygosity mapping reveals novel and known mutations in Pakistani families with inherited retinal dystrophies. *Sci Rep* **5**, 9965 (2015). https://doi.org/10.1038/srep09965
185 Van Schil, K. *et al.* Autosomal recessive retinitis pigmentosa with homozygous rhodopsin mutation E150K and non-coding cis-regulatory variants in CRX-binding regions of SAMD7. *Sci Rep* **6**, 21307 (2016). https://doi.org/10.1038/srep21307
186 Newby, G. A. & Liu, D. R. In vivo somatic cell base editing and prime editing. *Mol Ther* **29**, 3107-3124 (2021). https://doi.org/10.1016/j.ymthe.2021.09.002
187 Zhu, L. *et al.* Autosomal recessive retinitis pigmentosa and E150K mutation in the opsin gene. *J Biol Chem* **281**, 22289-22298 (2006). https://doi.org/10.1074/jbc.M602664200
188 Qin, H. *et al.* Vision rescue via unconstrained in vivo prime editing in degenerating neural retinas. *J Exp Med* **220** (2023). https://doi.org/10.1084/jem.20220776
189 Mathis, N. *et al.* Predicting prime editing efficiency and product purity by deep learning. *Nat Biotechnol* **41**, 1151-1159 (2023). https://doi.org/10.1038/s41587-022-01613-7
190 Sousa, A. A. *et al.* Systematic optimization of prime editing for the efficient functional correction of CFTR F508del in human airway epithelial cells. *Nat Biomed Eng* (2024). https://doi.org/10.1038/s41551-024-01233-3
191 Levy, J. M. *et al.* Cytosine and adenine base editing of the brain, liver, retina, heart and skeletal muscle of mice via adeno-associated viruses. *Nat Biomed Eng* **4**, 97-110 (2020). https://doi.org/10.1038/s41551-019-0501-5
192 Yan, W. *et al.* Mouse Retinal Cell Atlas: Molecular Identification of over Sixty Amacrine Cell Types. *J Neurosci* **40**, 5177-5195 (2020). https://doi.org/10.1523/JNEUROSCI.0471-20.2020
193 Tsai, S. Q. *et al.* CIRCLE-seq: a highly sensitive in vitro screen for genome-wide CRISPR-Cas9 nuclease off-targets. *Nat Methods* **14**, 607-614 (2017). https://doi.org/10.1038/nmeth.4278
194 Maeder, M. L. *et al.* Development of a gene-editing approach to restore vision loss in Leber congenital amaurosis type 10. *Nat Med* **25**, 229-233 (2019). https://doi.org/10.1038/s41591-018-0327-9
195 Leveillard, T. *et al.* Identification and characterization of rod-derived cone viability factor. *Nat Genet* **36**, 755-759 (2004). https://doi.org/10.1038/ng1386
196 Xue, Y. *et al.* Chromophore supply modulates cone function and survival in retinitis pigmentosa mouse models. *Proc Natl Acad Sci U S A* **120**, e2217885120 (2023). https://doi.org/10.1073/pnas.2217885120
197 Nickell, S., Park, P. S., Baumeister, W. & Palczewski, K. Three-dimensional architecture of murine rod outer segments determined by cryoelectron tomography. *J Cell Biol* **177**, 917-925 (2007). https://doi.org/10.1083/jcb.200612010
198 Lyubarsky, A. L., Daniele, L. L. & Pugh, E. N., Jr. From candelas to photoisomerizations in the mouse eye by rhodopsin bleaching in situ and the light-rearing dependence of the major components of the mouse ERG. *Vision Res* **44**, 3235-3251 (2004). https://doi.org/10.1016/j.visres.2004.09.019

199 Ghaemmaghami, S. *et al.* Global analysis of protein expression in yeast. *Nature* **425**, 737-741 (2003). https://doi.org/10.1038/nature02046
200 Schwanhausser, B. *et al.* Global quantification of mammalian gene expression control. *Nature* **473**, 337-342 (2011). https://doi.org/10.1038/nature10098
201 Pugh, E. N., Jr. & Lamb, T. D. Amplification and kinetics of the activation steps in phototransduction. *Biochim Biophys Acta* **1141**, 111-149 (1993). https://doi.org/10.1016/0005-2728(93)90038-h
202 Saari, J. C., Garwin, G. G., Van Hooser, J. P. & Palczewski, K. Reduction of all-trans-retinal limits regeneration of visual pigment in mice. *Vision Res* **38**, 1325-1333 (1998). https://doi.org/10.1016/s0042-6989(97)00198-3
203 Rodieck, R. W. *The first steps in seeing*. (Sinauer Associates, 1998).
204 Lebherz, C., Maguire, A., Tang, W., Bennett, J. & Wilson, J. M. Novel AAV serotypes for improved ocular gene transfer. *J Gene Med* **10**, 375-382 (2008). https://doi.org/10.1002/jgm.1126
205 Pulagam, L. P. & Palczewski, K. Electrostatic compensation restores trafficking of the autosomal recessive retinitis pigmentosa E150K opsin mutant to the plasma membrane. *J Biol Chem* **285**, 29446-29456 (2010). https://doi.org/10.1074/jbc.M110.151407
206 Hu, S. *et al.* In vivo adenine base editing ameliorates Rho-associated autosomal dominant retinitis pigmentosa. *Journal of genetics and genomics = Yi chuan xue bao* (2024). https://doi.org/10.1016/j.jgg.2024.12.012
207 Arbab, M. *et al.* Base editing rescue of spinal muscular atrophy in cells and in mice. *Science* **380**, eadg6518 (2023). https://doi.org/10.1126/science.adg6518
208 Kliegman, M. *et al.* A roadmap for affordable genetic medicines. *Nature* (2024). https://doi.org/10.1038/s41586-024-07800-7
209 Banskota, S. *et al.* Engineered virus-like particles for efficient in vivo delivery of therapeutic proteins. *Cell* **185**, 250-265 e216 (2022). https://doi.org/10.1016/j.cell.2021.12.021
210 Kaczmarczyk, S. J., Sitaraman, K., Young, H. A., Hughes, S. H. & Chatterjee, D. K. Protein delivery using engineered virus-like particles. *Proc Natl Acad Sci U S A* **108**, 16998-17003 (2011). https://doi.org/10.1073/pnas.1101874108
211 Mangeot, P. E. *et al.* Genome editing in primary cells and in vivo using viral-derived Nanoblades loaded with Cas9-sgRNA ribonucleoproteins. *Nat Commun* **10**, 45 (2019). https://doi.org/10.1038/s41467-018-07845-z
212 Hamilton, J. R. *et al.* In vivo human T cell engineering with enveloped delivery vehicles. *Nat Biotechnol* **42**, 1684-1692 (2024). https://doi.org/10.1038/s41587-023-02085-z
213 Hamilton, J. R. *et al.* Targeted delivery of CRISPR-Cas9 and transgenes enables complex immune cell engineering. *Cell Rep* **35**, 109207 (2021). https://doi.org/10.1016/j.celrep.2021.109207
214 Fitzgerald, K. *et al.* A Highly Durable RNAi Therapeutic Inhibitor of PCSK9. *N Engl J Med* **376**, 41-51 (2017). https://doi.org/10.1056/NEJMoa1609243
215 Muzumdar, M. D., Tasic, B., Miyamichi, K., Li, L. & Luo, L. A global double-fluorescent Cre reporter mouse. *Genesis* **45**, 593-605 (2007). https://doi.org/10.1002/dvg.20335

216 Cideciyan, A. V. Leber congenital amaurosis due to RPE65 mutations and its treatment with gene therapy. *Prog Retin Eye Res* **29**, 398-427 (2010). https://doi.org/10.1016/j.preteyeres.2010.04.002
217 den Hollander, A. I., Roepman, R., Koenekoop, R. K. & Cremers, F. P. Leber congenital amaurosis: genes, proteins and disease mechanisms. *Prog Retin Eye Res* **27**, 391-419 (2008). https://doi.org/10.1016/j.preteyeres.2008.05.003
218 Sodi, A. *et al.* RPE65-associated inherited retinal diseases: consensus recommendations for eligibility to gene therapy. *Orphanet J Rare Dis* **16**, 257 (2021). https://doi.org/10.1186/s13023-021-01868-4
219 Pang, J. J. *et al.* Retinal degeneration 12 (rd12): a new, spontaneously arising mouse model for human Leber congenital amaurosis (LCA). *Mol Vis* **11**, 152-162 (2005).
220 Zhong, Z. *et al.* Seven novel variants expand the spectrum of RPE65-related Leber congenital amaurosis in the Chinese population. *Mol Vis* **25**, 204-214 (2019).
221 Puppo, A. *et al.* Retinal transduction profiles by high-capacity viral vectors. *Gene Ther* **21**, 855-865 (2014). https://doi.org/10.1038/gt.2014.57
222 Richter, M. F. *et al.* Phage-assisted evolution of an adenine base editor with improved Cas domain compatibility and activity. *Nat Biotechnol* (2020). https://doi.org/10.1038/s41587-020-0453-z
223 Huang, T. P. *et al.* Circularly permuted and PAM-modified Cas9 variants broaden the targeting scope of base editors. *Nat Biotechnol* **37**, 626-631 (2019). https://doi.org/10.1038/s41587-019-0134-y
224 Anzalone, A. V., Koblan, L. W. & Liu, D. R. Genome editing with CRISPR-Cas nucleases, base editors, transposases and prime editors. *Nat Biotechnol* **38**, 824-844 (2020). https://doi.org/10.1038/s41587-020-0561-9
225 Jo, D. H. *et al.* (2021). https://doi.org/10.1101/2021.01.07.425822
226 Clement, K. *et al.* CRISPResso2 provides accurate and rapid genome editing sequence analysis. *Nat Biotechnol* **37**, 224-226 (2019). https://doi.org/10.1038/s41587-019-0032-3
227 Lazzarotto, C. R. *et al.* CHANGE-seq reveals genetic and epigenetic effects on CRISPR–Cas9 genome-wide activity. *Nature Biotechnology* **38**, 1317-1327 (2020). https://doi.org/10.1038/s41587-020-0555-7
228 Golczak, M., Kiser, P. D., Lodowski, D. T., Maeda, A. & Palczewski, K. Importance of Membrane Structural Integrity for RPE65 Retinoid Isomerization Activity. *Journal of Biological Chemistry* **285**, 9667-9682 (2010). https://doi.org/10.1074/jbc.M109.063941
229 An, M. *et al.* Engineered virus-like particles for transient delivery of prime editor ribonucleoprotein complexes in vivo. *Nat Biotechnol* (2024). https://doi.org/10.1038/s41587-023-02078-y
230 Huang, X. *et al.* Exploitation of enhanced prime editing for blocking aberrant angiogenesis. *J Adv Res* (2024). https://doi.org/10.1016/j.jare.2024.07.006
231 She, K. *et al.* Dual-AAV split prime editor corrects the mutation and phenotype in mice with inherited retinal degeneration. *Signal Transduct Target Ther* **8**, 57 (2023). https://doi.org/10.1038/s41392-022-01234-1

232 Jang, H. *et al.* Application of prime editing to the correction of mutations and phenotypes in adult mice with liver and eye diseases. *Nat Biomed Eng* **6**, 181-194 (2022). https://doi.org/10.1038/s41551-021-00788-9
233 Peabody, D. S. The RNA binding site of bacteriophage MS2 coat protein. *Embo J* **12**, 595-600 (1993). https://doi.org/10.1002/j.1460-2075.1993.tb05691.x
234 Hawes, N. L. *et al.* Retinal degeneration 6 (rd6): a new mouse model for human retinitis punctata albescens. *Invest Ophthalmol Vis Sci* **41**, 3149-3157 (2000).
235 Kameya, S. *et al.* Mfrp, a gene encoding a frizzled related protein, is mutated in the mouse retinal degeneration 6. *Hum Mol Genet* **11**, 1879-1886 (2002). https://doi.org/10.1093/hmg/11.16.1879
236 Ayala-Ramirez, R. *et al.* A new autosomal recessive syndrome consisting of posterior microphthalmos, retinitis pigmentosa, foveoschisis, and optic disc drusen is caused by a MFRP gene mutation. *Mol Vis* **12**, 1483-1489 (2006).
237 Doman, J. L., Sousa, A. A., Randolph, P. B., Chen, P. J. & Liu, D. R. Designing and executing prime editing experiments in mammalian cells. *Nat Protoc* **17**, 2431-2468 (2022). https://doi.org/10.1038/s41596-022-00724-4
238 Kim, D. Y., Moon, S. B., Ko, J. H., Kim, Y. S. & Kim, D. Unbiased investigation of specificities of prime editing systems in human cells. *Nucleic Acids Res* **48**, 10576-10589 (2020). https://doi.org/10.1093/nar/gkaa764
239 Liu, Y. *et al.* Efficient generation of mouse models with the prime editing system. *Cell Discov* **6**, 27 (2020). https://doi.org/10.1038/s41421-020-0165-z
240 Schene, I. F. *et al.* Prime editing for functional repair in patient-derived disease models. *Nat Commun* **11**, 5352 (2020). https://doi.org/10.1038/s41467-020-19136-7
241 Geurts, M. H. *et al.* Evaluating CRISPR-based prime editing for cancer modeling and CFTR repair in organoids. *Life Sci Alliance* **4** (2021). https://doi.org/10.26508/lsa.202000940
242 Park, S. J. *et al.* Targeted mutagenesis in mouse cells and embryos using an enhanced prime editor. *Genome Biol* **22**, 170 (2021). https://doi.org/10.1186/s13059-021-02389-w
243 Gao, P. *et al.* Prime editing in mice reveals the essentiality of a single base in driving tissue-specific gene expression. *Genome Biol* **22**, 83 (2021). https://doi.org/10.1186/s13059-021-02304-3
244 Lin, J. *et al.* Modeling a cataract disorder in mice with prime editing. *Molecular therapy. Nucleic acids* **25**, 494-501 (2021). https://doi.org/10.1016/j.omtn.2021.06.020
245 Jin, S. *et al.* Genome-wide specificity of prime editors in plants. *Nat Biotechnol* **39**, 1292-1299 (2021). https://doi.org/10.1038/s41587-021-00891-x
246 Habib, O., Habib, G., Hwang, G. H. & Bae, S. Comprehensive analysis of prime editing outcomes in human embryonic stem cells. *Nucleic Acids Res* **50**, 1187-1197 (2022). https://doi.org/10.1093/nar/gkab1295
247 Gao, R. *et al.* Genomic and Transcriptomic Analyses of Prime Editing Guide RNA-Independent Off-Target Effects by Prime Editors. *CRISPR J* **5**, 276-293 (2022). https://doi.org/10.1089/crispr.2021.0080

248 Liang, S. Q. *et al.* Genome-wide profiling of prime editor off-target sites in vitro and in vivo using PE-tag. *Nat Methods* (2023). https://doi.org/10.1038/s41592-023-01859-2
249 Chandler, R. J., Sands, M. S. & Venditti, C. P. Recombinant Adeno-Associated Viral Integration and Genotoxicity: Insights from Animal Models. *Hum Gene Ther* **28**, 314-322 (2017). https://doi.org/10.1089/hum.2017.009
250 Dong, W. & Kantor, B. Lentiviral Vectors for Delivery of Gene-Editing Systems Based on CRISPR/Cas: Current State and Perspectives. *Viruses* **13** (2021). https://doi.org/10.3390/v13071288
251 Schellekens, H. Bioequivalence and the immunogenicity of biopharmaceuticals. *Nat Rev Drug Discov* **1**, 457-462 (2002). https://doi.org/10.1038/nrd818
252 Accola, M. A., Strack, B. & Gottlinger, H. G. Efficient particle production by minimal Gag constructs which retain the carboxy-terminal domain of human immunodeficiency virus type 1 capsid-p2 and a late assembly domain. *J Virol* **74**, 5395-5402 (2000). https://doi.org/10.1128/jvi.74.12.5395-5402.2000
253 Ngo, W. *et al.* Mechanism-guided engineering of a minimal biological particle for genome editing. *Proc Natl Acad Sci U S A* **122**, e2413519121 (2025). https://doi.org/10.1073/pnas.2413519121
254 Garwin, G. G. & Saari, J. C. High-performance liquid chromatography analysis of visual cycle retinoids. *Methods Enzymol* **316**, 313-324 (2000). https://doi.org/10.1016/s0076-6879(00)16731-x
255 Golczak, M., Kiser, P. D., Lodowski, D. T., Maeda, A. & Palczewski, K. Importance of membrane structural integrity for RPE65 retinoid isomerization activity. *J Biol Chem* **285**, 9667-9682 (2010). https://doi.org/10.1074/jbc.M109.063941
256 Palczewska, G. *et al.* Noninvasive two-photon optical biopsy of retinal fluorophores. *Proc Natl Acad Sci U S A* **117**, 22532-22543 (2020). https://doi.org/10.1073/pnas.2007527117
257 Palczewska, G. *et al.* Noninvasive two-photon microscopy imaging of mouse retina and retinal pigment epithelium through the pupil of the eye. *Nat Med* **20**, 785-789 (2014). https://doi.org/10.1038/nm.3590
258 High, K. A. & Roncarolo, M. G. Gene Therapy. *N Engl J Med* **381**, 455-464 (2019). https://doi.org/10.1056/NEJMra1706910
259 Colella, P., Ronzitti, G. & Mingozzi, F. Emerging Issues in AAV-Mediated In Vivo Gene Therapy. *Mol Ther Methods Clin Dev* **8**, 87-104 (2018). https://doi.org/10.1016/j.omtm.2017.11.007
260 Muhuri, M., Levy, D. I., Schulz, M., McCarty, D. & Gao, G. Durability of transgene expression after rAAV gene therapy. *Mol Ther* **30**, 1364-1380 (2022). https://doi.org/10.1016/j.ymthe.2022.03.004
261 Naso, M. F., Tomkowicz, B., Perry, W. L., 3rd & Strohl, W. R. Adeno-Associated Virus (AAV) as a Vector for Gene Therapy. *BioDrugs* **31**, 317-334 (2017). https://doi.org/10.1007/s40259-017-0234-5
262 Wang, J. Y. & Doudna, J. A. CRISPR technology: A decade of genome editing is only the beginning. *Science* **379**, eadd8643 (2023). https://doi.org/10.1126/science.add8643

263 Qiu, H. Y., Ji, R. J. & Zhang, Y. Current advances of CRISPR-Cas technology in cell therapy. *Cell Insight* **1**, 100067 (2022). https://doi.org/10.1016/j.cellin.2022.100067
264 Huang, L. *et al.* CRISPR-Mediated Base Editing: Promises and Challenges for a Viable Oncotherapy Strategy. *Hum Gene Ther* **34**, 669-681 (2023). https://doi.org/10.1089/hum.2023.045
265 Lee, R. G. *et al.* Efficacy and Safety of an Investigational Single-Course CRISPR Base-Editing Therapy Targeting PCSK9 in Nonhuman Primate and Mouse Models. *Circulation* **147**, 242-253 (2023). https://doi.org/10.1161/CIRCULATIONAHA.122.062132
266 Amado, D. A. & Davidson, B. L. Gene therapy for ALS: A review. *Mol Ther* **29**, 3345-3358 (2021). https://doi.org/10.1016/j.ymthe.2021.04.008
267 Knott, G. J. & Doudna, J. A. CRISPR-Cas guides the future of genetic engineering. *Science* **361**, 866-869 (2018). https://doi.org/10.1126/science.aat5011
268 Scully, R., Panday, A., Elango, R. & Willis, N. A. DNA double-strand break repair-pathway choice in somatic mammalian cells. *Nat Rev Mol Cell Biol* **20**, 698-714 (2019). https://doi.org/10.1038/s41580-019-0152-0
269 Koblan, L. W. *et al.* In vivo base editing rescues Hutchinson-Gilford progeria syndrome in mice. *Nature* **589**, 608-614 (2021). https://doi.org/10.1038/s41586-020-03086-7
270 Lavrov, A. V., Varenikov, G. G. & Skoblov, M. Y. Genome scale analysis of pathogenic variants targetable for single base editing. *BMC Med Genomics* **13**, 80 (2020). https://doi.org/10.1186/s12920-020-00735-8
271 Chan, Y. K. *et al.* Engineering adeno-associated viral vectors to evade innate immune and inflammatory responses. *Sci Transl Med* **13** (2021). https://doi.org/10.1126/scitranslmed.abd3438
272 Grunewald, J. *et al.* Transcriptome-wide off-target RNA editing induced by CRISPR-guided DNA base editors. *Nature* **569**, 433-437 (2019). https://doi.org/10.1038/s41586-019-1161-z
273 Davis, K. M., Pattanayak, V., Thompson, D. B., Zuris, J. A. & Liu, D. R. Small molecule-triggered Cas9 protein with improved genome-editing specificity. *Nat Chem Biol* **11**, 316-318 (2015). https://doi.org/10.1038/nchembio.1793
274 Rees, H. A., Wilson, C., Doman, J. L. & Liu, D. R. Analysis and minimization of cellular RNA editing by DNA adenine base editors. *Sci Adv* **5**, eaax5717 (2019). https://doi.org/10.1126/sciadv.aax5717
275 Doman, J. L., Raguram, A., Newby, G. A. & Liu, D. R. Evaluation and minimization of Cas9-independent off-target DNA editing by cytosine base editors. *Nat Biotechnol* **38**, 620-628 (2020). https://doi.org/10.1038/s41587-020-0414-6
276 Raguram, A., Banskota, S. & Liu, D. R. Therapeutic in vivo delivery of gene editing agents. *Cell* **185**, 2806-2827 (2022). https://doi.org/10.1016/j.cell.2022.03.045
277 Gillmore, J. D. *et al.* CRISPR-Cas9 In Vivo Gene Editing for Transthyretin Amyloidosis. *N Engl J Med* **385**, 493-502 (2021). https://doi.org/10.1056/NEJMoa2107454

278 Gao, X. *et al.* Treatment of autosomal dominant hearing loss by in vivo delivery of genome editing agents. *Nature* **553**, 217-221 (2018). https://doi.org/10.1038/nature25164
279 Yeh, W. H., Chiang, H., Rees, H. A., Edge, A. S. B. & Liu, D. R. In vivo base editing of post-mitotic sensory cells. *Nat Commun* **9**, 2184 (2018). https://doi.org/10.1038/s41467-018-04580-3
280 Rees, H. A. *et al.* Improving the DNA specificity and applicability of base editing through protein engineering and protein delivery. *Nat Commun* **8**, 15790 (2017). https://doi.org/10.1038/ncomms15790
281 Leroy, B. P. *et al.* Gene Therapy for Inherited Retinal Disease: Long-Term Durability of Effect. *Ophthalmic Res* **66**, 179-196 (2023). https://doi.org/10.1159/000526317
282 Patel, S., Ryals, R. C., Weller, K. K., Pennesi, M. E. & Sahay, G. Lipid nanoparticles for delivery of messenger RNA to the back of the eye. *J Control Release* **303**, 91-100 (2019). https://doi.org/10.1016/j.jconrel.2019.04.015
283 Kang, Q. *et al.* Cell-penetrating peptide-driven Cre recombination in porcine primary cells and generation of marker-free pigs. *PloS one* **13**, e0190690 (2018). https://doi.org/10.1371/journal.pone.0190690
284 Chien, W. M., Liu, Y. & Chin, M. T. Genomic DNA recombination with cell-penetrating peptide-tagged cre protein in mouse skeletal and cardiac muscle. *Genesis* **52**, 695-701 (2014). https://doi.org/10.1002/dvg.22782
285 Wadia, J. S., Stan, R. V. & Dowdy, S. F. Transducible TAT-HA fusogenic peptide enhances escape of TAT-fusion proteins after lipid raft macropinocytosis. *Nat Med* **10**, 310-315 (2004). https://doi.org/10.1038/nm996
286 Gomez, J. A. *et al.* Cell-Penetrating Penta-Peptides (CPP5s): Measurement of Cell Entry and Protein-Transduction Activity. *Pharmaceuticals (Basel)* **3**, 3594-3613 (2010). https://doi.org/10.3390/ph3123594
287 Molday, L. L. & Molday, R. S. 1D4: a versatile epitope tag for the purification and characterization of expressed membrane and soluble proteins. *Methods Mol Biol* **1177**, 1-15 (2014). https://doi.org/10.1007/978-1-4939-1034-2_1
288 Del'Guidice, T. *et al.* Membrane permeabilizing amphiphilic peptide delivers recombinant transcription factor and CRISPR-Cas9/Cpf1 ribonucleoproteins in hard-to-modify cells. *PloS one* **13**, e0195558 (2018). https://doi.org/10.1371/journal.pone.0195558
289 Wei, T., Cheng, Q., Min, Y. L., Olson, E. N. & Siegwart, D. J. Systemic nanoparticle delivery of CRISPR-Cas9 ribonucleoproteins for effective tissue specific genome editing. *Nat Commun* **11**, 3232 (2020). https://doi.org/10.1038/s41467-020-17029-3
290 Onuma, H., Sato, Y. & Harashima, H. Lipid nanoparticle-based ribonucleoprotein delivery for in vivo genome editing. *J Control Release* **355**, 406-416 (2023). https://doi.org/10.1016/j.jconrel.2023.02.008
291 Hassett, K. J. *et al.* Optimization of Lipid Nanoparticles for Intramuscular Administration of mRNA Vaccines. *Mol Ther Nucleic Acids* **15**, 1-11 (2019). https://doi.org/10.1016/j.omtn.2019.01.013
292 Sato, Y. *et al.* Understanding structure-activity relationships of pH-sensitive cationic lipids facilitates the rational identification of promising lipid nanoparticles

for delivering siRNAs in vivo. *J Control Release* **295**, 140-152 (2019). https://doi.org/10.1016/j.jconrel.2019.01.001
293 Carrasco, M. J. *et al.* Ionization and structural properties of mRNA lipid nanoparticles influence expression in intramuscular and intravascular administration. *Commun Biol* **4**, 956 (2021). https://doi.org/10.1038/s42003-021-02441-2
294 Adamus, G. *et al.* Anti-rhodopsin monoclonal antibodies of defined specificity: characterization and application. *Vision Res* **31**, 17-31 (1991). https://doi.org/10.1016/0042-6989(91)90069-h
295 Cheng, X. & Lee, R. J. The role of helper lipids in lipid nanoparticles (LNPs) designed for oligonucleotide delivery. *Adv Drug Deliv Rev* **99**, 129-137 (2016). https://doi.org/10.1016/j.addr.2016.01.022
296 Porteus, M. H. A New Class of Medicines through DNA Editing. *N Engl J Med* **380**, 947-959 (2019). https://doi.org/10.1056/NEJMra1800729
297 Choi, E. H. *et al.* Genome editing in the treatment of ocular diseases. *Exp Mol Med* **55**, 1678-1690 (2023). https://doi.org/10.1038/s12276-023-01057-2
298 Wu, Z., Yang, H. & Colosi, P. Effect of genome size on AAV vector packaging. *Mol Ther* **18**, 80-86 (2010). https://doi.org/10.1038/mt.2009.255
299 Van Vliet, K. M., Blouin, V., Brument, N., Agbandje-McKenna, M. & Snyder, R. O. The role of the adeno-associated virus capsid in gene transfer. *Methods Mol Biol* **437**, 51-91 (2008). https://doi.org/10.1007/978-1-59745-210-6_2
300 Bennett, A., Mietzsch, M. & Agbandje-McKenna, M. Understanding capsid assembly and genome packaging for adeno-associated viruses. *Future Virol* **12**, 283-297 (2017). https://doi.org/10.2217/fvl-2017-0011
301 Montini, E. *et al.* Hematopoietic stem cell gene transfer in a tumor-prone mouse model uncovers low genotoxicity of lentiviral vector integration. *Nat Biotechnol* **24**, 687-696 (2006). https://doi.org/10.1038/nbt1216
302 Montini, E. *et al.* The genotoxic potential of retroviral vectors is strongly modulated by vector design and integration site selection in a mouse model of HSC gene therapy. *J Clin Invest* **119**, 964-975 (2009). https://doi.org/10.1172/JCI37630
303 Zychlinski, D. *et al.* Physiological promoters reduce the genotoxic risk of integrating gene vectors. *Mol Ther* **16**, 718-725 (2008). https://doi.org/10.1038/mt.2008.5
304 Themis, M. *et al.* Oncogenesis following delivery of a nonprimate lentiviral gene therapy vector to fetal and neonatal mice. *Mol Ther* **12**, 763-771 (2005). https://doi.org/10.1016/j.ymthe.2005.07.358
305 Babaei, S., Akhtar, W., de Jong, J., Reinders, M. & de Ridder, J. 3D hotspots of recurrent retroviral insertions reveal long-range interactions with cancer genes. *Nat Commun* **6**, 6381 (2015). https://doi.org/10.1038/ncomms7381
306 Louis Jeune, V., Joergensen, J. A., Hajjar, R. J. & Weber, T. Pre-existing anti-adeno-associated virus antibodies as a challenge in AAV gene therapy. *Hum Gene Ther Methods* **24**, 59-67 (2013). https://doi.org/10.1089/hgtb.2012.243
307 Chen, M. *et al.* Immune profiling of adeno-associated virus response identifies B cell-specific targets that enable vector re-administration in mice. *Gene Ther* **30**, 429-442 (2023). https://doi.org/10.1038/s41434-022-00371-0

308 Boutin, S. *et al.* Prevalence of serum IgG and neutralizing factors against adeno-associated virus (AAV) types 1, 2, 5, 6, 8, and 9 in the healthy population: implications for gene therapy using AAV vectors. *Hum Gene Ther* **21**, 704-712 (2010). https://doi.org/10.1089/hum.2009.182
309 Follenzi, A., Santambrogio, L. & Annoni, A. Immune responses to lentiviral vectors. *Curr Gene Ther* **7**, 306-315 (2007). https://doi.org/10.2174/156652307782151515
310 Bennett, J. Immune response following intraocular delivery of recombinant viral vectors. *Gene Ther* **10**, 977-982 (2003). https://doi.org/10.1038/sj.gt.3302030
311 Finn, J. D. *et al.* A Single Administration of CRISPR/Cas9 Lipid Nanoparticles Achieves Robust and Persistent In Vivo Genome Editing. *Cell Rep* **22**, 2227-2235 (2018). https://doi.org/10.1016/j.celrep.2018.02.014
312 Gautam, M. *et al.* Lipid nanoparticles with PEG-variant surface modifications mediate genome editing in the mouse retina. *Nat Commun* **14**, 6468 (2023). https://doi.org/10.1038/s41467-023-42189-3
313 Herrera-Barrera, M. *et al.* Peptide-guided lipid nanoparticles deliver mRNA to the neural retina of rodents and nonhuman primates. *Sci Adv* **9**, eadd4623 (2023). https://doi.org/10.1126/sciadv.add4623
314 Chen, G. *et al.* A biodegradable nanocapsule delivers a Cas9 ribonucleoprotein complex for in vivo genome editing. *Nat Nanotechnol* **14**, 974-980 (2019). https://doi.org/10.1038/s41565-019-0539-2
315 Madigan, V., Zhang, F. & Dahlman, J. E. Drug delivery systems for CRISPR-based genome editors. *Nat Rev Drug Discov* **22**, 875-894 (2023). https://doi.org/10.1038/s41573-023-00762-x
316 Liang, X. *et al.* Rapid and highly efficient mammalian cell engineering via Cas9 protein transfection. *J Biotechnol* **208**, 44-53 (2015). https://doi.org/10.1016/j.jbiotec.2015.04.024
317 Wang, M. *et al.* Efficient delivery of genome-editing proteins using bioreducible lipid nanoparticles. *Proc Natl Acad Sci U S A* **113**, 2868-2873 (2016). https://doi.org/10.1073/pnas.1520244113
318 Luo, Z. *et al.* The heparin-binding domain of HB-EGF as an efficient cell-penetrating peptide for drug delivery. *J Pept Sci* **22**, 689-699 (2016). https://doi.org/10.1002/psc.2932
319 Shin, T. H. *et al.* Enhancement of the tumor penetration of monoclonal antibody by fusion of a neuropilin-targeting peptide improves the antitumor efficacy. *Mol Cancer Ther* **13**, 651-661 (2014). https://doi.org/10.1158/1535-7163.MCT-13-0748
320 Sun, D. *et al.* Non-viral Gene Therapy for Stargardt Disease with ECO/pRHO-ABCA4 Self-Assembled Nanoparticles. *Mol Ther* **28**, 293-303 (2020). https://doi.org/10.1016/j.ymthe.2019.09.010
321 Hassett, K. J. *et al.* Impact of lipid nanoparticle size on mRNA vaccine immunogenicity. *J Control Release* **335**, 237-246 (2021). https://doi.org/10.1016/j.jconrel.2021.05.021
322 Bohley, M., Dillinger, A. E., Tamm, E. R. & Goepferich, A. Targeted drug delivery to the retinal pigment epithelium: Untapped therapeutic potential for retinal

diseases. *Drug Discov Today* **27**, 2497-2509 (2022). https://doi.org/10.1016/j.drudis.2022.05.024

323 Sun, D. *et al.* Stable Retinoid Analogue Targeted Dual pH-Sensitive Smart Lipid ECO/pDNA Nanoparticles for Specific Gene Delivery in the Retinal Pigment Epithelium. *ACS Appl Bio Mater* **3**, 3078-3086 (2020). https://doi.org/10.1021/acsabm.0c00130

324 Chen, K. *et al.* Engineering self-deliverable ribonucleoproteins for genome editing in the brain. *Nat Commun* **15**, 1727 (2024). https://doi.org/10.1038/s41467-024-45998-2

325 Camperi, J., Moshref, M., Dai, L. & Lee, H. Y. Physicochemical and Functional Characterization of Differential CRISPR-Cas9 Ribonucleoprotein Complexes. *Anal Chem* **94**, 1432-1440 (2022). https://doi.org/10.1021/acs.analchem.1c04795

326 Foss, D. V. *et al.* Peptide-mediated delivery of CRISPR enzymes for the efficient editing of primary human lymphocytes. *Nat Biomed Eng* **7**, 647-660 (2023). https://doi.org/10.1038/s41551-023-01032-2

327 Zhang, Z. *et al.* Efficient engineering of human and mouse primary cells using peptide-assisted genome editing. *Nat Biotechnol* **42**, 305-315 (2024). https://doi.org/10.1038/s41587-023-01756-1

328 Israelachvili, J. N. & Mitchell, D. J. A model for the packing of lipids in bilayer membranes. *Biochim Biophys Acta* **389**, 13-19 (1975). https://doi.org/10.1016/0005-2736(75)90381-8

329 Regan, D., Williams, J., Borri, P. & Langbein, W. Lipid Bilayer Thickness Measured by Quantitative DIC Reveals Phase Transitions and Effects of Substrate Hydrophilicity. *Langmuir* **35**, 13805-13814 (2019). https://doi.org/10.1021/acs.langmuir.9b02538

330 Chang, Y. F., Imam, J. S. & Wilkinson, M. F. The nonsense-mediated decay RNA surveillance pathway. *Annu Rev Biochem* **76**, 51-74 (2007). https://doi.org/10.1146/annurev.biochem.76.050106.093909

331 Choi, E. H. *et al.* An inducible Cre mouse for studying roles of the RPE in retinal physiology and disease. *Jci Insight* **6** (2021). https://doi.org/10.1172/jci.insight.146604

332 Wender, P. A. *et al.* The design, synthesis, and evaluation of molecules that enable or enhance cellular uptake: peptoid molecular transporters. *Proc Natl Acad Sci U S A* **97**, 13003-13008 (2000). https://doi.org/10.1073/pnas.97.24.13003

333 Pooga, M. *et al.* Cell penetrating PNA constructs regulate galanin receptor levels and modify pain transmission in vivo. *Nat Biotechnol* **16**, 857-861 (1998). https://doi.org/10.1038/nbt0998-857

334 Palczewska, G., Kern, T. S. & Palczewski, K. Noninvasive Two-Photon Microscopy Imaging of Mouse Retina and Retinal Pigment Epithelium. *Methods Mol Biol* **1834**, 333-343 (2019). https://doi.org/10.1007/978-1-4939-8669-9_21

335 Kitamura, T. *et al.* Retrovirus-mediated gene transfer and expression cloning: powerful tools in functional genomics. *Exp Hematol* **31**, 1007-1014 (2003).

336 Onishi, M. *et al.* Applications of retrovirus-mediated expression cloning. *Exp Hematol* **24**, 324-329 (1996).

337 Chelstowska, S., Widjaja-Adhi, M. A. K., Silvaroli, J. A. & Golczak, M. Impact of LCA-Associated E14L LRAT Mutation on Protein Stability and Retinoid Homeostasis. *Biochemistry* **56**, 4489-4499 (2017). https://doi.org/10.1021/acs.biochem.7b00451
338 Foik, A. T. *et al.* Retinal origin of electrically evoked potentials in response to transcorneal alternating current stimulation in the rat. *Invest Ophthalmol Vis Sci* **56**, 1711-1718 (2015). https://doi.org/10.1167/iovs.14-15617
339 Kordecka, K., Foik, A. T., Wierzbicka, A. & Waleszczyk, W. J. Cortical Inactivation Does Not Block Response Enhancement in the Superior Colliculus. *Frontiers in systems neuroscience* **14**, 59 (2020). https://doi.org/10.3389/fnsys.2020.00059
340 Lewandowski, D. *et al.* Inhibition of ceramide accumulation in AdipoR1-/- mice increases photoreceptor survival and improves vision. *JCI Insight* **7**, e156301 (2022). https://doi.org/10.1172/jci.insight.156301
341 Pelli, D. G. The VideoToolbox software for visual psychophysics: transforming numbers into movies. *Spat Vis* **10**, 437-442 (1997).
342 Brainard, D. H. The Psychophysics Toolbox. *Spat Vis* **10**, 433-436 (1997).
343 Kleiner, M., Brainard, D. & Pelli, D. What's new in Psychtoolbox-3? *Perception* **36**, 14-14 (2007).
344 Foik, A. T., Scholl, L. R., Lean, G. A. & Lyon, D. C. Visual Response Characteristics in Lateral and Medial Subdivisions of the Rat Pulvinar. *Neuroscience* **441**, 117-130 (2020). https://doi.org/10.1016/j.neuroscience.2020.06.030
345 Foik, A. T. *et al.* Detailed Visual Cortical Responses Generated by Retinal Sheet Transplants in Rats with Severe Retinal Degeneration. *J Neurosci* **38**, 10709-10724 (2018). https://doi.org/10.1523/JNEUROSCI.1279-18.2018
346 Nakamichi, K. *et al.* Targeted long-read sequencing enriches disease-relevant genomic regions of interest to provide complete Mendelian disease diagnostics. *Jci Insight* **9** (2024). https://doi.org/10.1172/jci.insight.183902
347 Ely, Z. A. *et al.* A prime editor mouse to model a broad spectrum of somatic mutations in vivo. *Nat Biotechnol* **42**, 424-436 (2024). https://doi.org/10.1038/s41587-023-01783-y
348 Erwood, S. *et al.* Saturation variant interpretation using CRISPR prime editing. *Nat Biotechnol* **40**, 885-895 (2022). https://doi.org/10.1038/s41587-021-01201-1
349 Buckley, M. *et al.* Saturation genome editing maps the functional spectrum of pathogenic VHL alleles. *Nat Genet* **56**, 1446-1455 (2024). https://doi.org/10.1038/s41588-024-01800-z
350 Sahu, S. *et al.* Saturation genome editing-based clinical classification of BRCA2 variants. *Nature* (2025). https://doi.org/10.1038/s41586-024-08349-1
351 Hwang, G. H. *et al.* Large DNA deletions occur during DNA repair at 20-fold lower frequency for base editors and prime editors than for Cas9 nucleases. *Nat Biomed Eng* (2024). https://doi.org/10.1038/s41551-024-01277-5
352 Cancellieri, S. *et al.* Human genetic diversity alters off-target outcomes of therapeutic gene editing. *Nat Genet* **55**, 34-43 (2023). https://doi.org/10.1038/s41588-022-01257-y

353 Kliegman, M. *et al.* A roadmap for affordable genetic medicines. *Nature* **634**, 307-314 (2024). https://doi.org/10.1038/s41586-024-07800-7
354 Wouters, O. J., McKee, M. & Luyten, J. Estimated Research and Development Investment Needed to Bring a New Medicine to Market, 2009-2018. *Jama* **323**, 844-853 (2020). https://doi.org/10.1001/jama.2020.1166
355 Medicine, E. "Editas Medicine Announces Clinical Data Demonstrating Proof of Concept of EDIT-101 from Phase 1/2 BRILLIANCE Trial." (2022).
356 Toualbi, L., Toms, M. & Moosajee, M. USH2A-retinopathy: From genetics to therapeutics. *Exp Eye Res* **201**, 108330 (2020). https://doi.org/10.1016/j.exer.2020.108330
357 Xiong, W. *et al.* AAV cis-regulatory sequences are correlated with ocular toxicity. *Proc Natl Acad Sci U S A* **116**, 5785-5794 (2019). https://doi.org/10.1073/pnas.1821000116
358 Sin, T. N. *et al.* Safety and efficacy of CRISPR-mediated genome ablation of VEGFA as a treatment for choroidal neovascularization in nonhuman primate eyes. *Mol Ther* (2024). https://doi.org/10.1016/j.ymthe.2024.09.027
359 Charlesworth, C. T. *et al.* Identification of preexisting adaptive immunity to Cas9 proteins in humans. *Nature Medicine* **25**, 249-+ (2019). https://doi.org/10.1038/s41591-018-0326-x
360 Segel, M. *et al.* Mammalian retrovirus-like protein PEG10 packages its own mRNA and can be pseudotyped for mRNA delivery. *Science* **373**, 882-889 (2021). https://doi.org/10.1126/science.abg6155
361 Kreitz, J. *et al.* Programmable protein delivery with a bacterial contractile injection system. *Nature* **616**, 357-364 (2023). https://doi.org/10.1038/s41586-023-05870-7
362 Tian, S. *et al.* Targeted intracellular delivery of Cas13 and Cas9 nucleases using bacterial toxin-based platforms. *Cell Rep* **38**, 110476 (2022). https://doi.org/10.1016/j.celrep.2022.110476
363 Mok, B. Y. *et al.* A bacterial cytidine deaminase toxin enables CRISPR-free mitochondrial base editing. *Nature* **583**, 631-+ (2020). https://doi.org/10.1038/s41586-020-2477-4
364 Yi, Z. Y. *et al.* Strand-selective base editing of human mitochondrial DNA using mitoBEs. *Nature biotechnology* **42** (2024). https://doi.org/10.1038/s41587-023-01791-y
365 Weber, Y. *et al.* Enhancing prime editor activity by directed protein evolution in yeast. *Nat Commun* **15**, 2092 (2024). https://doi.org/10.1038/s41467-024-46107-z
366 Liu, P. *et al.* Increasing intracellular dNTP levels improves prime editing efficiency. *Nat Biotechnol* (2024). https://doi.org/10.1038/s41587-024-02405-x
367 Shuto, Y. *et al.* Structural basis for pegRNA-guided reverse transcription by a prime editor. *Nature* **631**, 224-231 (2024). https://doi.org/10.1038/s41586-024-07497-8
368 Giannoukos, G. *et al.* UDiTaS, a genome editing detection method for indels and genome rearrangements. *BMC genomics* **19**, 212 (2018). https://doi.org/10.1186/s12864-018-4561-9